

# **Characterisation of disuse-related osteoporosis in an animal model of spinal cord injury**

---

**Jonathan Williams**

A thesis presented for the degree of  
Engineering Doctorate (EngD)



**University of  
Strathclyde**  
Engineering

Department of Biomedical Engineering

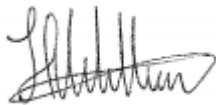
March 18<sup>th</sup>, 2019

## *Declaration*

This thesis is the result of the author's original research. It has been composed by the author and has not been previously submitted for examination which has led to the award of a degree.

The copyright of this thesis belongs to the author under the terms of the United Kingdom Copyright Acts as qualified by University of Strathclyde Regulation 3.50. Due acknowledgement must always be made of the use of any material contained in, or derived from, this thesis.

**Signed:**

A handwritten signature in black ink, appearing to read 'Jonathan Anthony Williams', written in a cursive style.

Jonathan Anthony Williams

**Date:** 18/03/2019

## *Abstract*

Injury to the spinal cord can result in paralysis below the level of injury. A secondary complication of the removal of muscle-driven bone stimulation is the development of rapid osteoporosis in the bones of the paralysed limbs. The severe deterioration of both bone quantity and quality means that spinal cord injury (SCI) patients are at a significantly higher risk of fragility fractures in the lower extremities than the able-bodied population. These fractures occur most commonly around the knee (distal femur and proximal tibia). This thesis presents a characterisation of the time-course effects a complete SCI has on the fracture-prone distal femur in a rat model. The aims are to characterise the quality and distribution of bone and to provide a uniquely detailed description of its response to SCI at various time points post-injury. Bone quality is assessed using i) *ex vivo* micro-Computed Tomography ( $\mu$ CT) for global and site-specific analysis of both trabecular and cortical bone morphometry and densitometry, and ii) three-point bending and torsional mechanical testing to provide whole-bone structural and material level properties.

Evidence is presented that SCI-induced osteoporosis is site-specific within the same appendicular bone. A rapid and severe deterioration of metaphyseal trabecular bone was observed, after just 2 weeks trabecular volume fraction (BV/TV) had decreased by 59% compared to age-matched sham-operated controls. This resulted in a compromised structure composed of on average 53% fewer and 15% thinner trabeculae compared to control. At later time points post-SCI there were no further significant reductions in metaphyseal BV/TV, although significant microstructural changes did occur. On the other hand, the more distally located epiphyseal trabecular bone was structurally more resistant to SCI-induced osteoporosis. There was a 23% decrease in BV/TV at 2 weeks post-SCI compared to control, characterised by a 15% decrease in trabecular thickness, thus unlike metaphyseal trabecular structures, the epiphyseal structure's connectivity was

maintained. At later time points post-SCI there was a growth-related increase in epiphyseal BV/TV.

Rapid changes to cortical bone were also seen, with distal-metaphyseal regions experiencing the most severe decrease in cortical area at 2 weeks post-SCI compared to control. The varying degrees of change in the amount of both trabecular and cortical bone appears concomitant with each region's bone surface to volume ratio. Analysis of more chronic time points post-SCI (6, 10 and 16 weeks) highlights that caution must be exercised when interpreting results from rodent studies. The analysis performed here indicates that SCI-induced bone changes are a combination of bone loss and suppressed bone growth. No difference in cortical tissue mineral density was observed between SCI and control groups at any time-points assessed, indicating that the decreases in whole-bone mechanical properties observed due to SCI were primarily a result of changes to the spatial distribution of bone.

Cumulatively, this thesis illustrates that SCI-induced osteoporosis has detrimentally affected the spatial distribution of both trabecular and cortical bone in site-specific ways, but the bone material itself does not appear affected.



## *Table of Contents*

<i>Declaration</i> .....	<i>i</i>
<i>Abstract</i> .....	<i>ii</i>
<i>Table of Contents</i> .....	<i>iv</i>
<i>List of Tables</i> .....	<i>x</i>
<i>List of Figures</i> .....	<i>xii</i>
<i>Acknowledgements</i> .....	<i>xviii</i>
<i>Thesis Outline</i> .....	<i>xix</i>
<i>Publications</i> .....	<i>xx</i>
<i>Abbreviations</i> .....	<i>xxi</i>
<b>CHAPTER 1 INTRODUCTION</b> .....	<b>1</b>
<i>1.1 Aims and Objectives</i> .....	<i>4</i>
<b>CHAPTER 2 LITERATURE REVIEW</b> .....	<b>5</b>
<b>2.1 Bone</b> .....	<b>5</b>
2.1.1 <i>Bone's Hierarchical Organisation</i> .....	5
2.1.2 <i>Structure of Load Bearing Long Bones</i> .....	6
2.1.2.1 <i>Cortical Bone</i> .....	8
2.1.2.2 <i>Trabecular Bone</i> .....	9
2.1.3 <i>Bone Cells</i> .....	11
2.1.3.1 <i>Osteoblasts</i> .....	11
2.1.3.2 <i>Osteocytes</i> .....	11
2.1.3.3 <i>Osteoclasts</i> .....	12
2.1.4 <i>Modelling and Remodelling</i> .....	12
2.1.4.1 <i>Modelling</i> .....	12
2.1.4.2 <i>Remodelling</i> .....	14
<b>2.2 Mechanical Adaptation of Bone</b> .....	<b>15</b>
2.2.1 <i>Dynamic Loading Drives Bone Adaptation</i> .....	16
2.2.2 <i>Dose-response Relationship</i> .....	17
2.2.3 <i>Strain Environment</i> .....	17
<b>2.3 Theory: The Mechanical Adaptation of Bone</b> .....	<b>19</b>

2.3.1	<i>The Mechanostat</i>	20
2.3.2	<i>Mechanical Usage Windows</i>	21
2.3.3	<i>The Utah Paradigms Predictions for SCI</i>	22
<b>2.4</b>	<b><i>Bone Quantity and Quality</i></b>	<b>24</b>
2.4.1	<i>Osteoporosis</i>	24
2.4.1.1	<i>Operational Definition</i>	25
2.4.2	<i>Bone Quality</i>	26
2.4.2.1	<i>Geometric Characterisation</i>	27
2.4.2.2	<i>Mechanical Characterisation</i>	27
2.4.2.3	<i>Density Characterisation</i>	28
<b>2.5</b>	<b><i>Assessment of Bone Mass</i></b>	<b>28</b>
2.5.1	<i>Micro-computed Tomography</i>	28
2.5.1.1	<i>Theory</i>	30
2.5.1.2	<i>μCT Scanner</i>	32
2.5.2	<i>Dual-energy X-ray Absorptiometry</i>	34
2.5.3	<i>Peripheral Quantitative Computed Tomography</i>	35
<b>2.6</b>	<b><i>Spinal Cord Injury</i></b>	<b>35</b>
2.6.1	<i>The Phases of SCI</i>	36
2.6.2	<i>Secondary Complications</i>	37
2.6.3	<i>Fracture Risk</i>	37
2.6.4	<i>Non-mechanical Agents</i>	38
2.6.5	<i>Clinical Studies of SCI-induced Osteoporosis</i>	39
2.6.5.1	<i>Histomorphometric Analysis</i>	40
2.6.5.2	<i>Cross-sectional DXA Study Findings</i>	41
2.6.5.3	<i>Prospective DXA Study Findings</i>	41
2.6.5.4	<i>Summary of DXA Findings</i>	42
2.6.5.5	<i>Cross-sectional pQCT Study Findings</i>	43
2.6.5.6	<i>Prospective pQCT Study Findings</i>	44
2.6.6	<i>Animal Models of SCI-induced Osteoporosis</i>	49
2.6.6.1	<i>The Rat as a Model of SCI-induced Bone Loss</i>	49
2.6.6.2	<i>Cross-sectional Rat Study Findings</i>	50
2.6.6.3	<i>Cortical Bone</i>	51
2.6.6.4	<i>Trabecular Bone</i>	53
2.6.6.5	<i>Time-course Rat Study Findings</i>	55
<b>CHAPTER 3</b>	<b><i>MATERIALS AND METHODS</i></b>	<b>59</b>
<b>3.1</b>	<b><i>Animal Model</i></b>	<b>59</b>
3.1.1	<i>Surgery and Post-operative Care</i>	60
3.1.2	<i>Preparation of Bones</i>	61

<b>3.2 Micro-Computed Tomography</b> .....	<b>62</b>
3.2.1 Image Acquisition .....	62
3.2.2 Reconstruction .....	64
3.2.2.1 Beam Hardening .....	64
3.2.2.2 Ring Artefacts.....	66
3.2.2.3 Mis-alignment .....	67
3.2.2.4 Mottle .....	67
3.2.2.5 Contrast Limits.....	68
3.2.2.6 Oversize Scan.....	68
3.2.2.7 Summary of Reconstruction Parameters.....	69
3.2.3 Image Co-registration.....	69
Step 1: Definition of Reference Dataset.....	70
Step 2: Acquire Global Shape .....	70
Step 3: Co-registration of Global Shape.....	71
Step 4: Application of Transform to Original.....	72
3.2.4 Segmentation.....	73
3.2.4.1 Trabecular Bone Segmentation.....	74
3.2.4.2 Cortical Bone Segmentation .....	81
3.2.5 Volume of Interest Section .....	82
3.2.5.1 Location of VOI.....	82
3.2.5.2 Size of VOI .....	84
3.2.5.3 Trabecular VOIs .....	85
3.2.5.4 Cortical VOI.....	86
3.2.6 Morphometric Analysis .....	87
3.2.6.1 3D Analysis .....	88
3.2.6.2 2D Analysis .....	90
3.2.7 Densiometric Analysis.....	93
3.2.7.1 Mineral Density Calibration.....	93
<b>3.3 Mechanical Testing</b> .....	<b>95</b>
3.3.1 Three-point Bending .....	95
3.3.2 Torsion .....	96
3.3.2.1 Preparation/Embedding.....	96
3.3.2.2 Torsion/Twist Testing.....	97
3.3.3 Femoral Neck Fracture.....	98
<b>3.4 Statistical Analysis</b> .....	<b>99</b>
3.4.1 2D Morphometric Distributions.....	99
3.4.2 3D Morphometric Parameters .....	100
3.4.3 Correlations .....	101
<b>CHAPTER 4 RESULTS</b> .....	<b>102</b>
<b>4.1 Overall Macroscopic Changes to the Femur</b> .....	<b>102</b>

4.1.1 <i>Muscle and Bone Mass</i> .....	102
4.1.2 <i>Femur Length</i> .....	103
<b>4.2 <i>Trabecular Bone Morphometry</i>.....</b>	<b>104</b>
4.2.1 <i>Variation in Trabecular Bone as a Function of Length</i> .....	105
4.2.2 <i>The Effects of Growth Throughout the Distal Femur</i> .....	107
4.2.3 <i>The Effects of Spinal Cord Injury Throughout the Distal Femur</i> .....	110
4.2.4 <i>Direct 3D Trabecular Morphometry</i> .....	116
4.2.4.1 <i>Metaphyseal Secondary Spongiosa</i> .....	117
4.2.4.2 <i>Metaphyseal Primary Spongiosa</i> .....	122
4.2.4.3 <i>Epiphyseal Trabecular Bone</i> .....	127
<b>4.3 <i>Cortical Bone Morphometry</i>.....</b>	<b>135</b>
4.3.1 <i>2D Morphometric Distributions</i> .....	136
4.3.1.1 <i>Variation of Cortical Bone as a Function of Bone Length</i> .....	136
4.3.1.2 <i>The Effects of Growth on Cortical Bone</i> .....	137
4.3.1.3 <i>The Effects of Spinal Cord Injury on Cortical Bone</i> .....	139
4.3.2 <i>Direct 3D Morphometry</i> .....	141
4.3.2.1 <i>Comparison of Distal-metaphysis and Mid-diaphysis</i> .....	141
4.3.2.2 <i>Acute Cortical Bone Changes</i> .....	142
4.3.2.3 <i>More Chronic Cortical Bone Changes</i> .....	146
4.3.3 <i>Tissue Mineral Density</i> .....	152
4.3.4 <i>Cortical Porosity</i> .....	154
<b>4.4 <i>Mechanical Tests</i> .....</b>	<b>157</b>
4.4.1 <i>Three-Point Bend Test</i> .....	157
4.4.1.1 <i>Whole Bone Mechanical Properties</i> .....	158
4.4.1.2 <i>Material-level Mechanical Properties</i> .....	160
4.4.2 <i>Torsion Test</i> .....	161
4.4.2.1 <i>Whole Bone Mechanical Properties</i> .....	162
4.4.2.2 <i>Material-level Mechanical Properties</i> .....	163
4.4.3 <i>Femoral Neck Fracture</i> .....	164
<b>CHAPTER 5 DISCUSSION.....</b>	<b>169</b>
<b>5.1 <i>Development of Global Analysis Tool</i>.....</b>	<b>169</b>
<b>5.2 <i>Longitudinal Bone Growth</i>.....</b>	<b>171</b>
<b>5.3 <i>Muscle and Bone Mass</i>.....</b>	<b>172</b>
<b>5.4 <i>Trabecular Bone Distributions</i>.....</b>	<b>174</b>
5.4.1 <i>Bone Growth – Control Femurs</i> .....	174
5.4.1.1 <i>Metaphyseal Trabecular Bone</i> .....	175

5.4.1.2 Epiphyseal Trabecular Bone.....	177
5.4.2 Effects of SCI on Trabecular Bone .....	178
<b>5.5 3D Trabecular Morphometric Analysis .....</b>	<b>180</b>
5.5.1 Site-specific Differences.....	180
5.5.2 The Structural Effects of Growth .....	181
<b>5.6 Cortical Bone Distributions .....</b>	<b>190</b>
<b>5.7 3D Cortical Morphometric Analysis .....</b>	<b>190</b>
5.7.1 Appositional Bone Growth.....	190
5.7.2 Effects of SCI on Cortical Bone .....	192
5.7.2.1 Diaphyseal Bone .....	193
5.7.2.2 Metaphyseal Bone .....	194
<b>5.8 Porosity.....</b>	<b>195</b>
<b>5.9 Tissue Mineral Density.....</b>	<b>196</b>
<b>5.10 Mechanical Tests .....</b>	<b>198</b>
5.10.1 Three Point Bend .....	198
5.10.2 Torsion Tests.....	202
5.10.3 Femoral Neck Fracture.....	204
<b>5.11 CTX-I.....</b>	<b>204</b>
<b>5.12 Limitations.....</b>	<b>205</b>
<b>CHAPTER 6 CONCLUSIONS AND FUTURE WORK .....</b>	<b>207</b>
<b>6.1 Conclusions .....</b>	<b>207</b>
<b>6.2 Future Work.....</b>	<b>208</b>
<b>APPENDIX A - TRABECULAR MORPHOMETRIC PARAMETERS</b>	
<b>.....</b>	<b>211</b>
<b>A.1 Metric Parameters .....</b>	<b>211</b>
A.1.1 Bone Volume, Total Volume & Bone Volume Fraction .....	211
A.1.2 Bone Surface Area & Bone Surface to Volume Ratio .....	212
A.1.3 Trabecular Thickness, Separation & Number.....	213
<b>A.2 Non-metric Parameters .....</b>	<b>214</b>
A.2.1 Trabecular Bone Pattern Factor .....	214
A.2.2 Structure Model Index .....	216

A.2.3 <i>Fractal Dimension</i> .....	217
A.2.4 <i>Degree of Anisotropy and Structural Orientation</i> .....	219
A.2.4.1 <i>Mean Intercept Length</i> .....	220
A.2.4.2 <i>Ellipsoid Fitting and Eigen Analysis</i> .....	221
A.2.5 <i>Connectivity Density</i> .....	224
<b>APPENDIX B – CORTICAL MORPHOMETRIC PARAMETERS</b>	<b>225</b>
B.1 <i>Cortical Thickness (Ct.Th)</i> .....	225
B.2 <i>Cortical, Total and Marrow Areas (Ct.Ar, Tt.Ar and Ma.Ar)</i> .....	226
B.3 <i>Periosteal and Endocortical Perimeters (Ps.Pm and Ec.Pm)</i> .....	227
B.4 <i>Polar Moment of Area (J)</i> .....	227
B.5 <i>Eccentricity (Ecc)</i> .....	229
<b>APPENDIX C – VALIDATION OF 2D MORPHOMETRIC DISTRIBUTIONS</b>	<b>230</b>
C.1 <i>Validation of Scripts</i> .....	230
C.2 <i>Comparison of Methods</i> .....	231
<b>APPENDIX D – MATERIAL LEVEL TORSIONAL PROPERTIES</b>	<b>236</b>
.....	
<b>APPENDIX E – CTX-I EXPERIMENT</b>	<b>238</b>
<b>APPENDIX F – EFFECTS OF GROWTH ON TRABECULAR COMPARTMENTS</b>	<b>240</b>
<b>REFERENCES</b> .....	<b>241</b>

## *List of Tables*

Table 1.1. The ASIA impairment scale.....	2
Table 2.1. World Health Organisation’s definition of osteoporosis.....	25
Table 2.2. Summary of cross-sectional pQCT studies.....	47
Table 2.3. Summary of longitudinal pQCT studies.....	48
Table 2.4. Summary of cross-sectional $\mu$ CT studies.....	57
Table 3.1. Experimental design.....	60
Table 3.2. Optimised parameters used to reconstruct projection images.....	69
Table 3.3. 3D trabecular bone morphometric parameters.....	89
Table 3.4. 3D cortical bone morphometric parameters.....	90
Table 3.5. 2D trabecular morphometric distribution parameters.....	91
Table 3.6. 2D cortical morphometric distribution parameters.....	92
Table 4.1. 3D trabecular morphology for metaphyseal secondary spongiosa, metaphyseal primary spongiosa and epiphyseal secondary spongiosa VOIs.....	132
Table 4.2. 3D cortical morphometric parameters for distal-metaphyseal and mid- diaphyseal VOIs.....	150
Table 4.3. 3D cortical tissue mineral density for the distal-metaphyseal and mid- diaphyseal VOIs.....	156
Table 4.4. 3D cortical porosity parameters for the distal-metaphysis.....	156
Table 4.5. Whole-bone and material-level mechanical properties of the femur, from three-point bend, torsion and femoral neck fracture tests.....	167
Table 5.1. Comparison of main confounding variables in $\mu$ CT studies of bone loss in rat SCI models.....	188
Table C.1. Comparison of MATLAB- and CTAn-determined morphometric parameters.....	231
Table C.2. Comparison of 2D slice-by-slice and gold standard approaches for trabecular bone area fraction.....	233

Table C.3. Comparison of 2D slice-by-slice and gold standard approach for total cortical bone area.....	235
---	-----

Table E.1 Blood serum CTX-I levels.....	239
---	-----



## *List of Figures*

Figure 2.1. The hierarchical structure of bone.....	6
Figure 2.2. Schematic of the structure of a load bearing bone.....	7
Figure 2.3. Schematic of cortical bone.....	9
Figure 2.4. $\mu$ CT images of trabecular bone.....	10
Figure 2.5. Schematics of the effects of modelling on bone growth.....	13
Figure 2.6. Schematic of cortical bone drifts.....	14
Figure 2.7. Schematics of the cell activity behind bone modelling and remodelling.....	14
Figure 2.8. Dynamic loading drives bone adaptation.....	16
Figure 2.9. Dose-response relationship between dynamic strain magnitude and change in bone mass.....	17
Figure 2.10. Strain rate and frequency of loading are important factors in bone adaptability.....	18
Figure 2.11. Schematic of the negative feedback inherent in Frost's mechanostat.....	20
Figure 2.12. Schematic of the four mechanical usage windows of the mechanostat.....	21
Figure 2.13. Schematic of disuse pattern osteopenia in a skeletally mature load bearing long bone.....	23
Figure 2.14. Schematic of the fundamental principle of CT: An n-dimensional object can be reconstructed from its (n - 1) projections.....	29
Figure 2.15. Comparison between quantitative histomorphology and $\mu$ CT-derived quantitative morphometry, with respect to trabecular separation.....	30
Figure 2.16. Schematic of X-ray interactions with matter.....	31
Figure 2.17. Schematic of geometry of a $\mu$ CT scanner.....	33
Figure 2.18. Dual-energy X-ray Absorptiometry-based assessment of the femoral neck.....	34
Figure 2.19. Schematic lateral view of human adult spinal cord and vertebra, with examples of the muscles innervated at different levels.....	36
Figure 2.20. Radiographs of a distal femur fragility fracture.....	38
Figure 2.21. Examples DXA and pQCT images of fracture prone long bones.....	40
Figure 2.22. Example pQCT in able-bodied and SCI subjects.....	44
Figure 2.23. Comparison between ex vivo $\mu$ CT images in rats and in vivo pQCT images in humans.....	50
Figure 2.24. $\mu$ CT images of the effects of SCI-induced osteoporosis on metaphyseal cortical bone in a rat model of SCI.....	52

Figure 2.25. $\mu$ CT images of the effects of SCI-induced osteoporosis on metaphyseal trabecular bone in the distal femur and proximal tibia of a rat model of SCI.....	54
Figure 2.26. $\mu$ CT images highlighting the site-specific effects of SCI in distal femoral metaphyseal and epiphyseal VOIs in a rat model of SCI.....	55
Figure 3.1. Schematic of a rat skeleton.....	61
Figure 3.2. Set-up for ex vivo $\mu$ CT scanning of the rat femur.....	62
Figure 3.3. Scanned region of the femur.....	63
Figure 3.4. The effects of beam hardening and correction.....	65
Figure 3.5. The effects of ring artefacts and correction.....	66
Figure 3.6. The effects of mis-alignment and correction.....	67
Figure 3.7. The effects of mottle and correction.....	68
Figure 3.8. Manual alignment of a representative reference distal femur.....	70
Figure 3.9. 2D Schematic showing the image processing steps needed to acquire the overall shape of the femur.....	71
Figure 3.10. Overview of co-registration.....	72
Figure 3.11. Result of co-registration.....	73
Figure 3.12. Global threshold for segmentation of bone tissue from softer tissues.....	75
Figure 3.13. Removal of white speckle noise from $\mu$ CT dataset.....	75
Figure 3.14. Defining of bone's total cross-sectional.....	76
Figure 3.15. Set-up of image, ROI and internal ROI for segmentation algorithm.....	77
Figure 3.16. Application of bitwise NOT operator.....	77
Figure 3.17. Application of bitwise AND operator.....	78
Figure 3.18. Removal of white speckle noise (2).....	79
Figure 3.19. Application of morphological closing.....	79
Figure 3.20. Application of morphological erosion for trabecular segmentation.....	80
Figure 3.21. Effect of reloading original image into marrow cavity ROI.....	80
Figure 3.22. Application of morphological erosion for cortical segmentation.....	81
Figure 3.23. Effect of the subtraction of the marrow cavity on the ROI.....	82
Figure 3.24. Effect of reloading the original image into cortical bone ROI.....	82
Figure 3.25. Comparison of the extent of the growth plate and primary spongiosa at 2 and 16-weeks post sham surgery.....	84

Figure 3.26. Schematic of the three trabecular and two cortical VOIs selected for 3D morphometric analysis.....	87
Figure 3.27. Comparison of 3D and 2D approaches to morphometric analysis of $\mu$ CT scanned trabecular bone.....	88
Figure 3.28. Representative trabecular and cortical VOIs over which 2D morphometric distributions were determined.....	93
Figure 3.29. Mineral density calibration phantoms.....	94
Figure 3.30. Mineral density calibration.....	94
Figure 3.31. Three-point bend experimental set-up.....	96
Figure 3.32. Embedding for torsion testing.....	97
Figure 3.33. Torsion test experimental set-up.....	98
Figure 3.34. Femoral neck fracture experimental set-up.....	99
Figure 4.1. Gross anatomical measurements of sublesional limbs.....	103
Figure 4.2. The entire trabecular bone structure of the distal femur.....	104
Figure 4.3. 2D $\mu$ CT trabecular morphometric distributions for 10-week control distal femurs.....	105
Figure 4.4. Cross-sectional segmented trabecular bone slices with Tb.Th <sub>2D</sub> mapped, for a representative 10-week control distal femur.....	107
Figure 4.5. 2D $\mu$ CT trabecular morphometric distributions indicating the effects of growth on the distal femur in anatomical time and space.....	108
Figure 4.6. Cross-sectional segmented trabecular bone slices with Tb.Th <sub>2D</sub> mapped indicating the effects of growth on the distal femur.....	109
Figure 4.7. 2D $\mu$ CT trabecular morphometric distributions of the distal femoral trabecular structure indicating the effects of SCI-induced osteoporosis.....	111
Figure 4.8. Representative 16-week control and SCI distal femoral trabecular bone structures with 3D Tb.Th mapped.....	113
Figure 4.9. Trabecular bone extent.....	114
Figure 4.10. Cross-sectional segmented trabecular bone slices with Tb.Th <sub>2D</sub> mapped, indicating the effects of SCI-induced osteoporosis.....	115
Figure 4.11. Trabecular bone volume fraction (BV/TV) for metaphyseal secondary spongiosa.....	117
Figure 4.12. Directly-assessed morphometric indices for metaphyseal secondary spongiosa.....	118
Figure 4.13. Representative metaphyseal secondary spongiosa VOIs with Tb.Th and Tb.Sp mapped.....	119

Figure 4.14. Connectivity density and bone surface to volume ratio for metaphyseal secondary spongiosa.....	120
Figure 4.15. Structure model index and degree of anisotropy for metaphyseal secondary spongiosa.....	121
Figure 4.16. Directly-assessed morphometric indices for metaphyseal primary spongiosa.....	123
Figure 4.17. Representative metaphyseal primary spongiosa VOIs with Tb.Th and Tb.Sp mapped.....	125
Figure 4.18. Connectivity density, bone surface to volume ratio, structure model index and degree of anisotropy for metaphyseal primary spongiosa.....	126
Figure 4.19. Directly-assessed morphometric indices for epiphyseal secondary spongiosa.....	128
Figure 4.20. Representative epiphyseal secondary spongiosa VOIs with Tb.Th and Tb.Sp mapped.....	129
Figure 4.21. Connectivity density, bone surface to volume ratio, structure model index and degree of anisotropy for epiphyseal secondary spongiosa.....	130
Figure 4.22. Linear correlation between trabecular number and trabecular volume fraction.....	131
Figure 4.23. A representative 10-week control cortical bone (85 – 40% bone length) VOI.....	135
Figure 4.24. 2D $\mu$ CT cortical morphometric distributions for 10-week control femurs.....	137
Figure 4.25. 2D $\mu$ CT cortical morphometric distributions indicating the effects of growth on the distal femur in anatomical time and space.....	138
Figure 4.26. 2D $\mu$ CT cortical morphometric distributions indicating the effects of SCI-induced osteoporosis.....	140
Figure 4.27. The variation of 3D cortical bone morphometric properties for distal-metaphyseal cortical bone.....	143
Figure 4.28. The variation of 3D cortical bone morphometric properties for mid-diaphyseal cortical bone.....	144
Figure 4.29. Representative distal-metaphyseal and mid-diaphyseal VOIs.....	145
Figure 4.30. Representative 2 and 16-week control and SCI distal femurs.....	149
Figure 4.31. SCI does not affect cortical tissue mineral density.....	153
Figure 4.32. The variation of pore volume fraction for distal-metaphyseal cortical bone VOIs.....	155
Figure 4.33. Three-point bend fractures.....	157
Figure 4.34. Three-point bend-derived load-displacement graphs.....	158

Figure 4.35. Three-point bend determined whole-bone mechanical properties.....	159
Figure 4.36. Linear correlation between three-point bend derived maximum load and mid-diaphyseal cortical area.....	160
Figure 4.37. Three-point bend determined material level mechanical properties.....	160
Figure 4.38. A representative spiral fracture from the torsion test.....	161
Figure 4.39. Torsion test-derived torque-angular displacement graphs.....	162
Figure 4.40. Torsion test determined whole-bone mechanical properties.....	163
Figure 4.41. Torsion test determined material level mechanical properties.....	164
Figure 4.42. Femoral neck fracture test-derived median value load-displacement graphs.....	165
Figure 4.43. Peak fracture force of the right femoral neck.....	166
Figure A.1. Schematic of trabecular bone area fraction.....	212
Figure A.2. Schematic of trabecular bone surface area.....	212
Figure A.3. Schematics of trabecular thickness and separation.....	214
Figure A.4. Schematic of trabecular pattern factor.....	216
Figure A.5. Schematics of the structure model index.....	217
Figure A.6. The Sierpinski triangle.....	218
Figure A.7. Schematic of the box-counting employed to determine the fractal dimension.....	219
Figure A.8. Schematics of isotropic and anisotropic trabecular bone.....	220
Figure A.9. Schematic of the 3D mean intercept length analysis.....	221
Figure A.10. Visualisation of the MIL distribution.....	222
Figure B.1. Cortical thickness calculation.....	225
Figure B.2. Cortical, total and marrow area calculations.....	226
Figure B.3. Moments of area calculation.....	228
Figure B.4. Eccentricity of an ellipse.....	229
Figure D.1. Schematics of non-prismatic models of the femoral diaphysis.....	240
Figure D.2. Schematic of multi-prismatic approach.....	240

Figure E.1. Blood serum CTX-I levels results.....	242
Figure F.1. The effects of growth on trabecular bone compartments .....	243

## *Acknowledgements*

To begin, I thank Sylvie Coupaud for her supervision, time, insight, guidance, support and encouragement throughout this journey. Also, to Elizabeth Tanner, her support and encyclopaedic knowledge of authors and their papers, ideas and thought-provoking discussions have been invaluable. Thanks also to James Windmill for use and tutelage on the Centre for Ultrasonic Engineering's  $\mu$ CT scanner.

More thanks should be given to John Riddell, for the provision of rat bones and guidance without which this project would not be possible. Recognition should also go to his cohort of MRes students who were involved in their collection.

My two months at Lund University, Sweden (where the torsion tests were performed) was a real highlight. Working with a world class team of researcher was an inspiration. Thank you to Hanna Isaksson and her research team for being welcoming, I learnt a lot.

In the early stages of this study I learnt a lot from Carmen Huesa, now at the University of Edinburgh, who also provided great advice and performed the CTX-I assay.

I must acknowledge my EngD cohort; Mynie, Scott, Josh, Audrey, George, Jacob and Pretheepan, amongst others for the good times and camaraderie throughout this process. Trips to the Ark will not be the same with you all departing.

Second to last, my family. Mum and Dad, I swear that I will be around more now that this beast is off my back.

Finally, Zlata, thank you for putting up with me through thick and thin. On to the next adventures together!

## *Thesis Outline*

**Chapter 1 - Introduction:** The thesis begins by describing the epidemiology, classification and complications resulting from spinal cord injury (SCI), before focusing on the secondary complication of interest; bone loss and associated increased fracture risk. This chapter ends by stating the aims and objectives of the thesis.

**Chapter 2 – Background & Literature Review:** This chapter provides an overview of the relevant areas of bone research (including bone structure, composition, adaptability and how it can be assessed, particular attention is placed on X-ray attenuation-based imaging techniques) and spinal cord injury (SCI) (including an overview of both clinical and animal studies of bone changes post-SCI), to provide the context of this thesis and its significance to the field.

**Chapter 3 – Materials & Methods:** This chapter introduces the rat SCI and sham models, experimental design and describes the techniques (*ex vivo* micro-Computed Tomography and mechanical testing), methodologies and measurement parameters used to characterise the bone quantity and quality in the model.

**Chapter 4 - Results:** In this chapter the major findings are presented. Including the overall macroscopic changes to the femur, overall and site-specific changes to trabecular and cortical bone morphometry and densitometry, and changes to the mechanical properties of cortical bone as a result of growth and SCI-induced osteoporosis

**Chapter 5 - Discussion:** Here the analyses of all experimental results are brought together and discussed, to provide an overall assessment of SCI on the fracture-prone distal femur.

**Chapter 6 Summary & Conclusions:** A summary of the main conclusions of this thesis are provided here.



## *Publications*

### Manuscripts

J.A. Williams, J.F.C Windmill, K.E Tanner, J.S. Riddell and S. Coupaud. Global and site-specific changes in bone in a rat model of spinal cord injury induced osteoporosis. Paper submitted to *BoneKEy Reports* (2019).

J.A. Williams, J.F.C. Windmill, M.J. Turunen, H. Isaksson, C. Huesa, J.S. Riddell, K.E. Tanner and S. Coupaud. Time course changes in structural, mechanical and material properties of bone in a rat model of spinal cord injury-related disuse osteoporosis. Paper in preparation for *Calcified Tissue International* (2019).

### Conference Abstracts

J.A. Williams, J.F.C. Windmill, J.S Riddell, K.E. Tanner, S. Coupaud. (2016) Microstructural analysis of disuse-related osteoporosis in an animal model of spinal cord injury, *Bone Research Society Annual Meeting 2016*, Frontiers Abstract, Page 178. <http://doi.org/10.3389/978-2-88919-974-7>

J.A. Williams, J.F.C. Windmill, J.S Riddell, K.E. Tanner, S. Coupaud. Site-specific changes in bone in a rat model of spinal cord injury. *In Proc. 2018 Black Forest Forum in Seoul, Journal of Musculoskeletal and Neuronal Interactions*, Book 2, Pages 111 – 121, October 2018.

## *Abbreviations*

$\mu$ CT – micro-Computed Tomography  
A – Anterior  
aBMD – areal Bone Mineral Density  
AC – Attenuation Coefficient  
ANOVA – Analysis of Variance  
ASIA – American Spinal Injury Association  
BA/TA – Trabecular Bone Area Fraction  
BMC – Bone Mineral Content  
BMD – Bone Mineral Density  
BMU – Bone Multicellular Unit  
BS – Bone Surface Area  
BS/BV – Bone Surface to Bone Volume Fraction  
BV – Bone Volume  
BV/TV – Trabecular Bone Volume Fraction  
CaHA – Calcium Hydroxyapatite  
CCD – Charge Coupled Device  
Conn.D – Connectivity Density  
CNS – Central Nervous System  
CT – Computed Tomography  
Ct.Ar – Cortical Area  
Ct.Th – Cortical Thickness  
CTX-I – C-Terminal Telopeptide Crosslinks of Type I Collagen  
D – Distal  
DA – Degree of Anisotropy  
DF – Distal Femur  
DOI – Duration of Injury  
DPD – Deoxypyridinoline  
DXA – Dual-Energy X-ray Absorptiometry  
Ecc – Eccentricity

Ec.Pm – Endocortical Perimeter  
EIA – Enzyme Immunoassay  
ESS – Epiphyseal Secondary Spongiosa  
FD – Fractal Dimension  
FRAX – Fracture Risk Assessment Tool  
HA – Hydroxyapatite  
J – Second Polar Moment of Area  
L – Lateral  
LMTA – Low Melting Temperature Alloy  
M – Medial  
Ma.Ar – Marrow/Medullary Area  
MES – Minimum Effective Strain  
MESm – Modelling Minimum Effective Strain  
MESr – Remodelling Minimum Effective Strain  
MIL – Mean Intercept Length  
MPS – Metaphyseal Primary Spongiosa  
MSS – Metaphyseal Secondary Spongiosa  
NSCISC – National Spinal Cord Injury Statistical Center  
NLI – Neurological Level of Injury  
ns – Non-Significant  
NTX-1 – N-Terminal Cross-Linking Telopeptide of Type I Collagen  
PBS – Phosphorus Buffered Saline  
Po – Posterior  
Po.Dm – Pore Diameter  
Po.N – Pore Number  
Po.V – Pore Volume  
Po.V/TV – Pore Volume Fraction  
P-A – Posterior-Anterior  
pQCT – peripheral Quantitative Computed Tomography  
Pr – Proximal  
Ps.Pm - Periosteal Perimeter

PT – Proximal Tibia  
PVE – Partial Volume Effect  
PYD – Post-Yield Displacement  
QUENSIU – Queen Elizabeth National Spinal Injuries Unit  
ROI – Region of Interest  
SD – Standard Deviation  
SCI – Spinal Cord Injury  
SE – Standard Error  
SMI – Structure Model Index  
Tb.E – Trabecular Extent  
Tb.N – Trabecular Number  
Tb.Pf – Trabecular Pattern Factor  
Tb.Sp – Trabecular Separation  
Tb.Th – Trabecular Thickness  
TMD – Tissue Mineral Density  
TPVML – Typical Peak Voluntary Mechanical Load  
TRAP – Tartrate-Resistant Acid Phosphatase  
Tt.Ar – Total Area Enclosed by the Periosteum  
TV – Total Volume  
vBMD – volumetric Bone Mineral Density  
VOI – Volume of Interest  
WHO – World Health Organisation  
Z – Atomic Number



## **Chapter 1 Introduction**

Injury to the spinal cord can result in complete or partial paralysis below the level of injury. The extent is dependent on the level and completeness of the injury. The higher the level of the spinal cord injury (SCI), i.e. the nearer to the brainstem, the more muscle groups and organs affected, and the more complete the injury, i.e. the extent of damage to the spinal cord, the more severe the effects on motor and sensory function.

The global incidence rate of traumatic SCI is estimated to be ~23 per million people per year (regional data for North America ~40 per million and Western Europe ~ 16 per million) (Lee et al., 2013). It is a common misconception that SCI primarily affects young men, due to sporting injuries and motor vehicle accidents. The reality is, due to ageing populations, that the mean age at time of traumatic SCI in developed countries has significantly increased over the last few decades. In Scotland the mean age at time of traumatic SCI is 52.6 years with the main cause being falls (McCaughey et al., 2016), while in the USA it is ~ 43 years, with motor vehicle accidents followed closely by falls being the main causes (NSCISC, 2019). In both regions, males account for approximately 75% - 80% of new cases.

SCIs can broadly be divided into two types: incomplete and complete. In incomplete SCIs, the spinal cord is only partly severed, thus the cord's ability to relay motor and/or sensory information is not totally lost. A complete injury on the other hand occurs when the cord has been fully severed, resulting in complete and permanent loss of function below the level of injury. Patients with SCI are further classified as either paraplegic or tetraplegic. Paraplegia occurs when a traumatic SCI (lesion) is sustained within the thoracic, lumbar or sacral segment of the cord, resulting in potentially impaired function to the lower extremities (e.g. legs and/or trunk), however control of upper limbs is

maintained. Tetraplegia (or quadriplegia) results from higher level SCIs, within the cervical region, function of the upper extremities as well as the lower extremities is affected. Incomplete injuries are the most common type, the National Spinal Cord Injury Statistical Center (NSCISC) reports that incomplete tetraplegia (48% of cases) was the most frequent form of SCI since 2015, followed by incomplete paraplegia (20% of cases) (NSCISC, 2019). Table 1.1 provides the proportion of Scottish patients presenting with each of the AISA scores between 2009 and 2013.

**Table 1.1.** The ASIA impairment scale (Kirshblum et al., 2011), with proportion of patients with each score for the Queen Elizabeth National Spinal Injuries Unit (QENSIU) between 2009 and 2013 (McCaughey et al., 2016).

ASIA Score	Completeness	Definition	Prevalence
<b>A</b>	Complete	No sensory or motor function is preserved in the sacral segments S4-S5.	25.9%
<b>B</b>	Incomplete	Sensory but not motor function is preserved below the NLI and includes the sacral segments S4-S5, & no motor function is preserved > 3 levels below the motor level on either side of body	5.9%
<b>C</b>	Incomplete	Motor function is preserved below the NLI, and more than half of key muscles below the NLI have a muscle grade < 3.	28.6 %
<b>D</b>	Incomplete	Motor function is preserved below the NLI, and at least half of key muscles below the NLI have a muscle grade >3.	39.5%
<b>E</b>	Normal	Sensory and motor function is normal.	

NLI – Neurological Level of Injury

In addition to some form of paralysis, secondary complications resulting from SCI can include cardiovascular and respiratory complications, endocrine and metabolic disorders, chronic pain and spasticity (Sezer, 2015). These complications are generally more severe in tetraplegia than in paraplegia. Muscular paralysis below the level of injury leads to rapid muscle atrophy, the removal of muscle-driven dynamic stimulation, and reduced

levels of physical activity which all reduce mechanical loading of bone, leading to rapid osteoporosis in the sublesional bones (Alexandre & Vico, 2011).

This SCI-induced osteoporosis results in rapid and severe deterioration of both bone quantity and quality (Garland et al., 1992). Patients with SCI are at a significantly higher risk of bone fractures than the able-bodied population. An overall fracture incidence of 2.2% per year has been reported, with an average time to first fracture post-SCI of 8.9 years (Zehnder et al., 2004), while Vestergaard et al. (1998) states that the overall sublesional long bone fracture rate is twice that of the able-bodied population. The lower extremities are those most susceptible to fracture, particularly the trabecular-rich knee region (distal femur, proximal tibia) (Cirnigliaro et al., 2017). In a retrospective study documenting the fracture characteristics of 107 traumatic SCI patients, Frotzler et al. (2015) reported 156 long bone fractures, with 61% of the fractures occurred in the femur, 45% of which occurred within the distal femur. Of the remaining 39% of fractures which occurred in the tibia, 42% occurred within the proximal tibia, giving a total of 44% of fractures occurring around the knee. These fractures are typically the result of low energy events, such as transferring from bed to wheelchair. These are therefore termed “fragility fractures”, that is fractures that occur in the absence of major trauma, and take much longer to heal, if indeed they do heal at all (Frotzler et al., 2015). Fragility fracture risk increases with time post-SCI, this combined with an increasing standard of care and consequent increasing life expectancy of SCI patients, means that likelihood of a fracture after SCI is increasing. Although a number of imaging based studies have been performed to characterise sublesional bone loss in patients with SCI (Eser et al., 2004; Frotzler et al., 2008; Coupaud et al, 2015), only a limited understanding of the structural and mechanical property changes can be ascertained.

Thus, the goal of this thesis was to establish the structural changes that occur at a fracture-prone site as a result of SCI-induced osteoporosis in a rat model. Bone changes in rat



models of SCI have previously been characterised (Jiang et al., 2007a; Jiang et al., 2007b; Liu et al., 2008; Morse et al., 2008; Yarrow et al., 2014; Minematsu et al., 2014; 2016; Beggs et al., 2015; Lin et al., 2015). Although these studies are generally single time point in design, or if they are multi-time point, contain certain study limitations exists (e.g. bone loss is evaluated for only a few weeks, and/or only one test and/or type of bone is analysed). At the time of writing no published study has analysed the time course of changes to both trabecular and cortical bone following complete-SCI in a rat model.

### ***1.1 Aims and Objectives***

The aim of this thesis is to characterise the time course effects of a complete SCI on the appendicular skeleton, in particular, the fracture-prone distal femur in a rat model.

The objectives were to:

- i) Quantify the time course structural, densitometric and mechanical changes in bone after SCI,
- ii) Quantify the confounding effects of growth,
- iii) Develop and use tools to assess the site-specific response of bone to SCI-induced osteoporosis.

## **Chapter 2 Literature Review**

This literature review chapter provides an overview of the relevant areas of bone research and spinal cord injury, to provide the context of this thesis and its significance to the field. It starts with introducing bone, with emphasis on load bearing long bones, describing their hierarchical organisation, formation and biological mechanisms responsible for growth, repair and adaptation. The second and third sections describe the mechanical adaptation of bone in terms of experiments and theoretical model respectively. The fourth section introduces the concept of bone quality and its relation to osteoporosis, while the fifth discusses X-ray based imaging techniques for quantification of both bone quantity and quality. The final section provides an overview of spinal cord injury, its classification, phases, epidemiology and associated secondary complications. This section ends with a review of both clinical and animal studies of SCI-induced osteoporosis.

### ***2.1 Bone***

Bone is a rigid multi-functional organ that exists within the skeletal system that also comprises cartilage, tendon and ligament. It plays roles in structural support and protection of the body, provides lever arms for muscles to allow locomotion, and is actively involved in both mineral homeostasis and haematopoiesis. This thesis focuses on one bone in particular, the femur, which is a load bearing long bone, whose chief function is to carry voluntary mechanical loads for life, without spontaneous fracture.

#### ***2.1.1 Bone's Hierarchical Organisation***

Bone has been described as a “composite of a composite of a composite” (Katz, 1971), due to its hierarchical structure, spanning from nano- to the milli-metre domain (Figure 2.1). On the nanoscale there are organic and inorganic components. A flexible collagenous phase is mineralised with stiff nanocrystals of apatite, this is the lowest level

composite. On the microscale, collagen fibrils are formed and interspersed with thin, elongated mineral. On gradually increasing length scales, the mineralised fibrils arrange into higher levels of organisation, firstly forming into fibres, subsequently lamella, which in turn configure osteons and at the macroscopic whole bone scale forming cortical and trabecular bone (Rho et al., 1998). This organisation is local, depending on the surface it forms on, the rate of formation and location. The overall composition of living bone by weight comprises approximately 30% organic matter (20 - 25 % type I collagen, the remainder non-collagenous proteins), 60% inorganic matter (predominantly hydroxyapatite ( $\text{Ca}_{10}(\text{PO}_4)_6(\text{OH}_2)$ )) and 10 % bound water (Gong et al., 1964; Behari, 1991). The configuration of healthy bone's compositional components at these length scales provide it with the structural and material level properties to resist failure (Gupta & Zioupos, 2008).

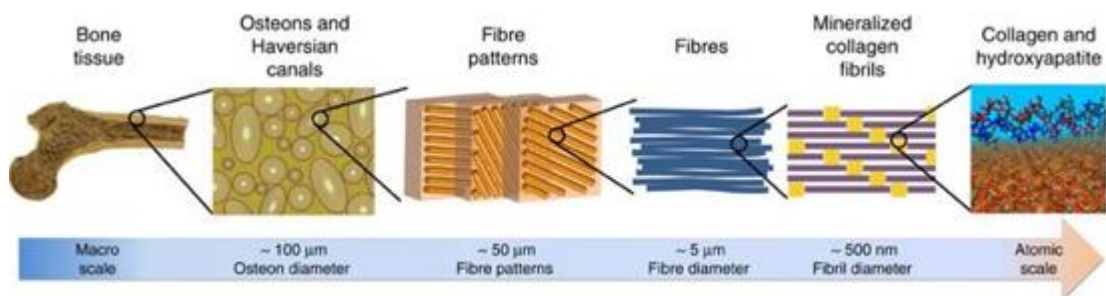


**Figure 2.1.** The hierarchical structure of bone, from the atomic scale to the macroscale of the skeleton. Reprinted with permission from Nair et al. (2013).

### 2.1.2 Structure of Load Bearing Long Bones

On the whole bone scale, two types of bone can be recognised. Cortical (or compact) bone is the dense outer surface of bone, while trabecular (or cancellous) bone is the porous honeycomb-like interconnected network of bony rods and plates (Figure 2.2). Load bearing long bone's macroscopic structure comprises a hollow shaft of cortical bone, termed the diaphysis. The proximal and distal ends of the diaphysis are both contiguous

with a widened area termed the metaphysis, which contains the growth plate, trabecular bone and an outer covering of cortical bone (Figure 2.2). Longitudinal growth occurs at the growth plate. The rounded ends of the bones are termed the epiphyses, the interior of which is filled with trabecular bone, that is contained by a thin covering of cortical bone. These rounded ends are part of a joint, so their surfaces are covered in layers of articular cartilage to aid in movement. At this scale there are four distinct envelopes/surfaces, which are defined by their location. These are the periosteal, endocortical, trabecular and intracortical surfaces (Figure 2.2). The periosteum is the outer membranous surface layer of the diaphysis, it is well vascularised and innervated and contains bone forming cells and has roles in growth and repair. The endosteum (endocortical or inner surface), is the surface surrounding the medullary cavity, it is not covered in a membrane, but is covered with bone lining cells, and is in close contact with bone marrow. Trabecular surfaces, like the endosteum, are exposed to all the elements of the marrow cavity, they have a very high surface area to volume ratio compared to the endosteum, and thus are more metabolically active. Intracortical surfaces are the surfaces of Haversian canals, the basic functional unit of cortical bone.

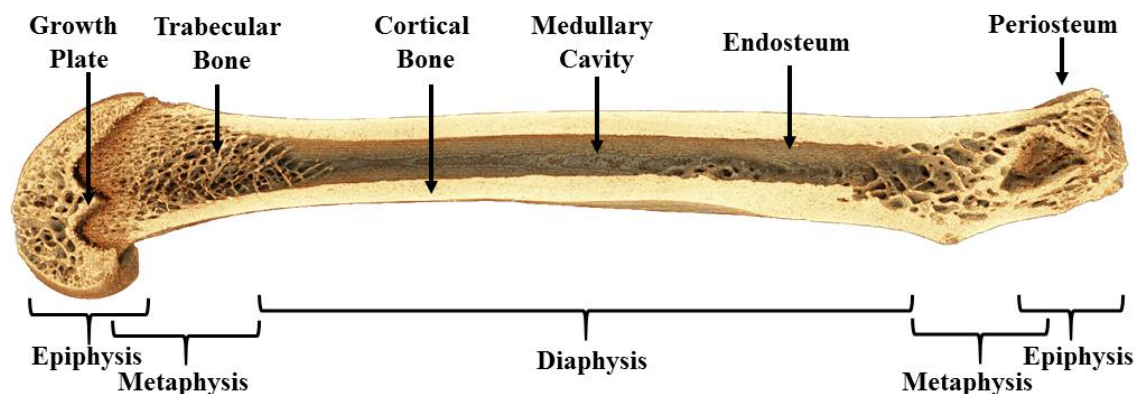


**Figure 2.2.** Schematic of the structure of a load bearing long bone, indicating the main regions, types and surfaces of bone. ( $\mu$ CT scanned femur from a 10-week control rat).

### *2.1.2.1 Cortical Bone*

Cortical bone is the dense and compact bone that contains both trabecular bone and bone marrow. It accounts for approximately 80% of the weight of the mature healthy human skeleton, with a typical porosity at the microscopic level of less than 5% (Burr & Allen, 2013). It is most well defined within the diaphysis, while narrows to a thin containing layer at the epiphyses and metaphyses. Its microstructure comprises of Haversian systems (or osteons), which in cross-section appear approximately circular in shape (Figure 2.3). Starting from the centre, they contain a Haversian canal, a tube-like channel that contains a blood vessel and nerve. Surrounding the Haversian canal are up to 8 concentric layers of lamellae (Vashishth et al., 2001), each sequential lamella have alternating fibre orientations (Rho et al., 1998). These Haversian systems run in parallel to the primary loading axis of the bone. Between each lamella layer are small holes termed lacunae, each containing an osteocyte (Figure 2.3). Perpendicular to and joining the Haversian canals are further canals termed Volkmann canals that supply blood in this transverse direction. (Figure 2.3). Haversian systems are found in human bone and many other high-order species, but smaller animals such as the rat lack well-formed Haversian systems (Jee & Yao, 2001).

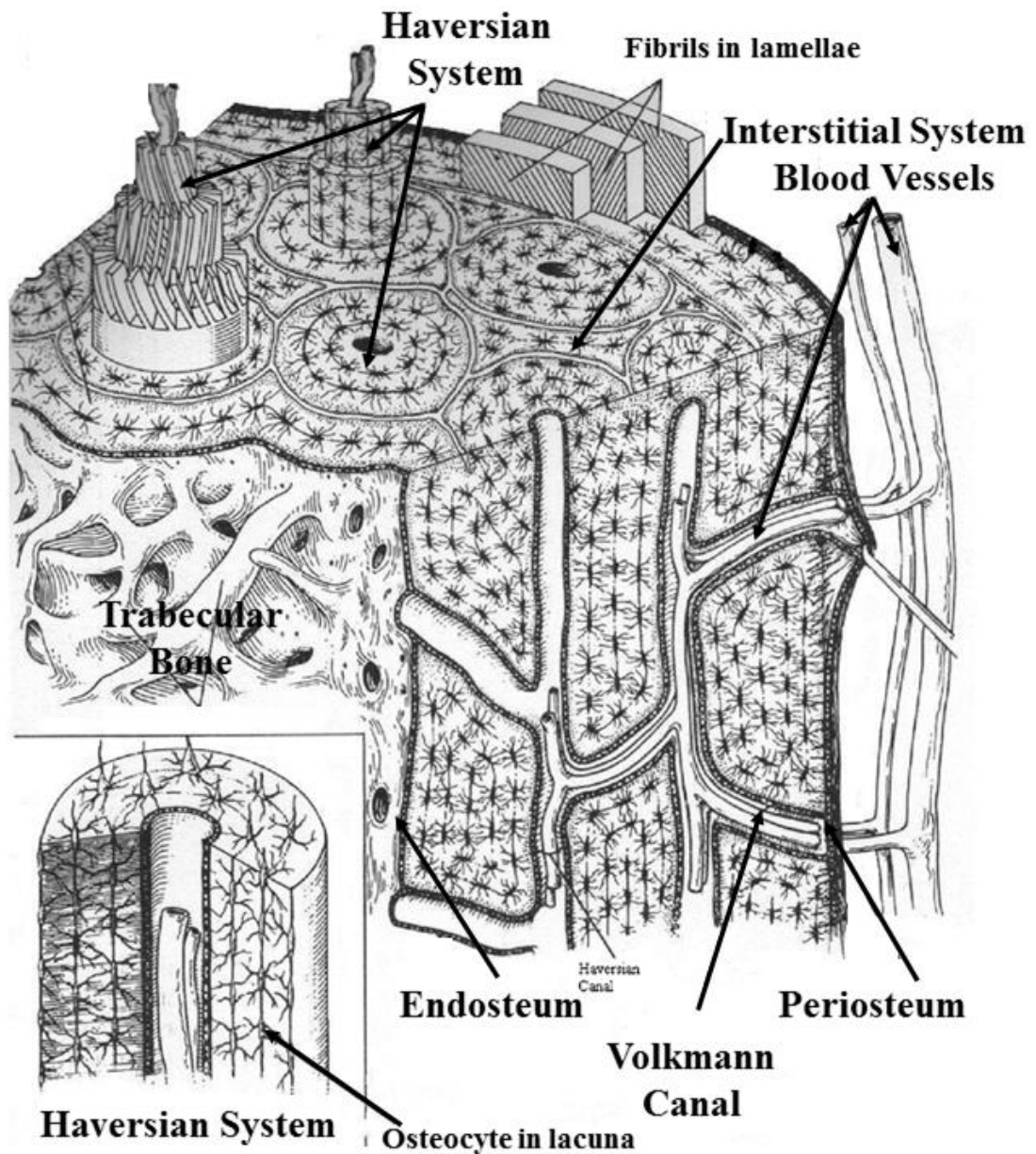


**Figure 2.3.** Schematic representation of cortical bone structure, indicating the individual Haversian systems, circumferential lamella, periosteum, endosteum, trabecular bone and blood vessels. Adapted from Buckwalter et al. (1995).

### 2.1.2.2 Trabecular Bone

Trabecular (or cancellous) bone is a porous interconnected network of rod and plate-like struts of bone termed trabeculae (Figure 2.4). It is classified as bone with a solid volume fraction of less than 70%, above this it would be classified as cortical bone (Gibson, 1985). It thus is lightweight, providing a good strength to weight ratio. Unlike cortical

bone it does not contain osteons, but lamellar bone, with minimal blood vessels. It thus receives nutrients directly from the bone marrow, through canaliculi that are open on its surface. It has on average approximately twenty times higher surface area to volume ratio than cortical bone and is adjacent to hematopoietic marrow. This provides a vast substrate for cellular interactions and as such is much more metabolically active, is remodelled more and on average is younger than cortical bone (Parfitt, 2002). Thus, trabecular bone responds much more rapidly than cortical bone to mechanical stimuli and is closely aligned to the directions of principal stress (Wolff, 1891). In long bones trabecular structures are found primarily within the epiphyses and metaphyses (Figure 2.2). Epiphyseal trabecular bone is located in the rounded ends of a long bone, directly beneath articular cartilage and acts as a natural shock absorber, attenuating forces generated at the joint during motion, while the metaphyseal trabecular bone transmits the remaining load to the diaphysis (Burr & Allen, 2013). Nowhere in the body do trabecular structures operate on their own, they are always enclosed by a shell of cortical bone.

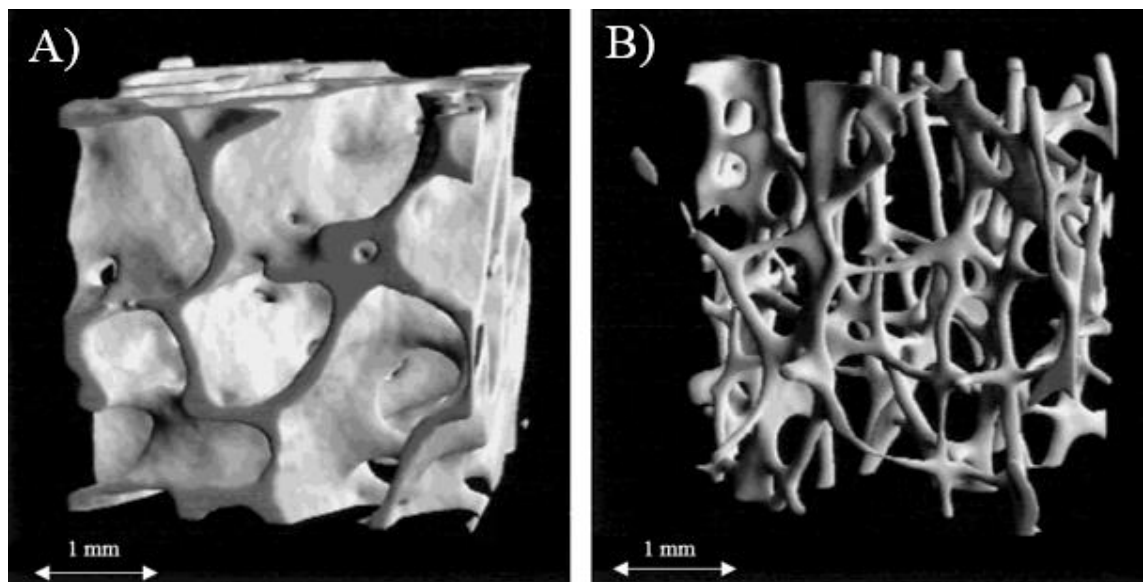


**Figure 2.4.**  $\mu$ CT images of A) high BV/TV trabecular bone with predominantly plate-like architecture from the femoral head B) low BV/TV trabecular bone with rod-like architecture from the lumbar spine. Adapted from Hildebrand et al. (1999).

### *2.1.3 Bone Cells*

At the macroscale bone appears inert, but in fact on the microscale bone is a dynamic organ, continuously being broken down, rebuilt, repaired and modified. The bone cells are responsible for this dynamic behaviour, they are the osteoblasts, osteoclasts and osteocytes and form a continuous covering of all exposed bone surfaces.

#### *2.1.3.1 Osteoblasts*

Osteoblasts are the predominant bone forming cells. They differentiate from mesenchymal stem cells located in the bone marrow. They are located only on bone surfaces and function mainly to produce new bone matrix and influence its mineralisation. Osteoblasts have three fates: i) during inactivity they remain on the bone surface and become quiescent lining cells that lie flat on the bone matrix, ii) whilst actively forming bone matrix they can encase themselves within the matrix, becoming osteocytes, iii) they can disappear from the formation site.

#### *2.1.3.2 Osteocytes*

Osteocytes are mature bone cells embedded in the bone matrix. In mature human skeletons, they make up greater than 90% of the bone cell population (Mellon & Tanner, 2012). The cell bodies have up to 50 long spindly cytoplasmic processes that branch out. These processes contact with neighbouring osteocyte processes through microscopic tunnels termed canaliculi. Thus they form a network, believed to be involved in the activation of remodelling through the detection of strain-induced signals within the bone (Bonewald, 2011).



### *2.1.3.3 Osteoclasts*

Osteoclasts are the main cells involved in bone resorption. They arise from hematopoietic stem cells. They are large multinucleated cells found on bone surfaces, conducting bone resorption within a ruffled zone that is securely attached to the bone surface. Bone mineral is dissolved by secretion of hydrochloric acid, while the extracellular matrix is subsequently degraded through secretion of proteolytic enzymes (Väänänen et al., 1998).

### *2.1.4 Modelling and Remodelling*

Skeletal features exist at birth, thus during skeletal development which begins during embryogenesis and continues postnatally, bone's structure and composition follow a genetic blueprint (Karsenty & Wagner, 2002). Long bones form through endochondral ossification. As the name suggests this is bone formation within a hyaline cartilage template. There are two distinct biological mechanisms that function on the cartilaginous embryonic skeleton; modelling and remodelling. During life these mechanisms govern bone turnover. Throughout skeletal growth turnover rate is high, within the first year it is close to 100%, by the start of adolescence it has declined to approximately 10% per year, it then continues at this rate or lower for the rest of life (Buckwalter et al., 1995).

#### *2.1.4.1 Modelling*

Modelling is the cellular process that assembles bone during the developmental stages and is also chiefly responsible for longitudinal and appositional (radial) growth throughout adolescence. It is a two-stage process; activation followed by either formation of bone via osteoblasts (formation drift), or resorption of bone via osteoclasts (resorption drift) and can take place on periosteal, endocortical and trabecular surfaces (Figure 2.7A). Formation and resorption drifts play vital roles in maintaining bone structure during the growth of load bearing bones. Longitudinal growth arises due to endochondral

ossification at the proximal and distal growth plates, thus to maintain the overall shape and curvature, both types of modelling must act globally in a simultaneous and coordinated manner on the metaphyseal bone surfaces to continually reshape the bone (Figure 2.5A). Radial growth of the diaphysis is achieved via rapid formation drifts on the periosteal surface, which is countered by resorption drifts acting on the endocortical surface (Figure 2.5B).

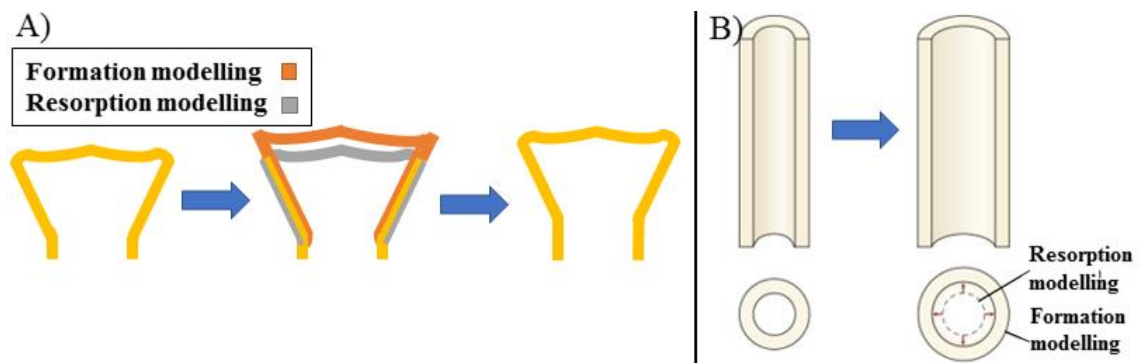


**Figure 2.5.** The effects of modelling on bone growth. A) With longitudinal bone growth, coordinated formation and resorption drifts on the distal femoral metaphysis preserve shape. B) With radial bone growth, formation modelling on periosteal and resorption modelling on endosteal surfaces results overtime in preservation of cortical thickness. Adapted from Burr & Allen (2013).

In contrast to uniform radial growth, cortical drifts can be asymmetric. These drifts occur through coordinated action of formation and resorption drifts on surfaces. Formation drifts occur on one periosteal and endocortical surface, while resorption drifts occur on the opposing two surfaces (Figure 2.6). These drifts are active during adolescence, but can also occur in extreme mechanical loading scenarios (Frost, 2004). Trabecular bone also undergoes modelling, resulting in the translation in anatomical space of struts for more effective load transmission (Burr & Allen, 2013). Modelling activities are at their highest during growth, the adult skeleton does undergo modelling, but is much less prominent than remodelling.

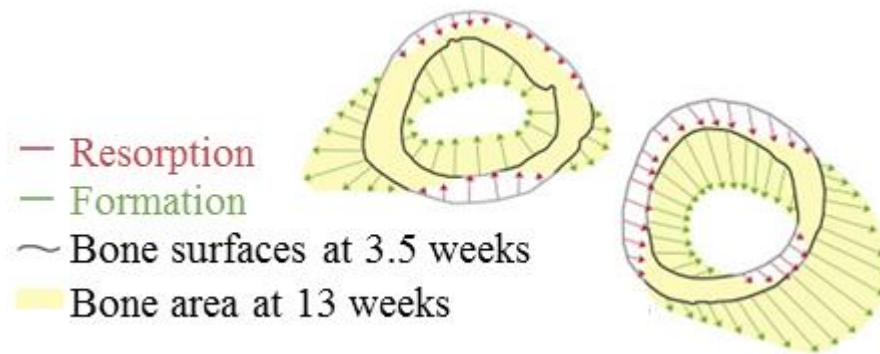


**Figure 2.6.** Schematic cross-sections of the mouse radius and ulna, and the transformation through modelling (cortical drifts) from 3.5 weeks of age to 13 weeks of age. Adapted from Burr and Allen (2013).

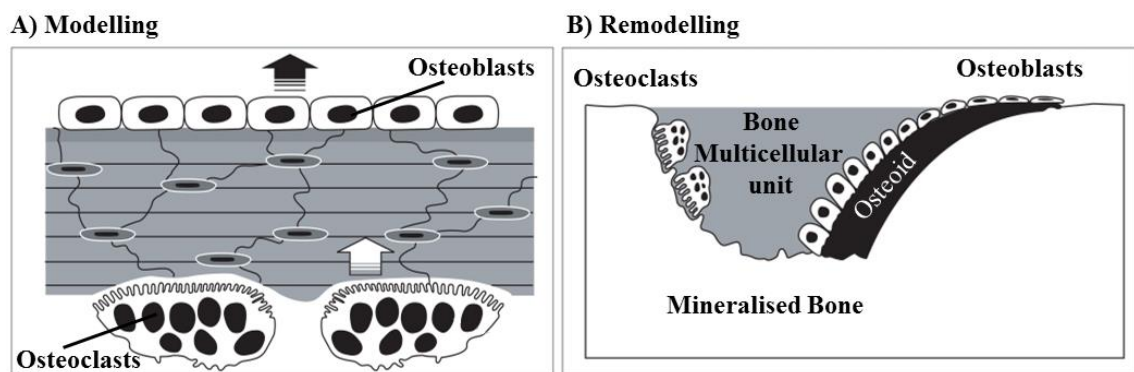


**Figure 2.7.** Schematic of the functions of bone cells in A) modelling, where osteoblastic and osteoclastic activity is not linked, rapid change in the spatial distribution of bone can occur and B) remodelling, where osteoblastic activity is linked to previous osteoclastic activity, minimal changes in the spatial distribution of bone occur in adults, unless there is an imbalance in bone cell activity. Adapted from Bone Health and Osteoporosis: A Report of the Surgeon General (2004).

#### 2.1.4.2 Remodelling

Remodelling is a distinct cellular process from modelling, where bone resorption and formation are coupled in discrete small packets on bone surfaces (Figure 2.7B). It is the only known process that replaces old bone with new bone. It occurs on all four bone surfaces (periosteal, endocortical, trabecular and Haversian). The structural integrity of bone is not only determined by the genetic blueprint, the skeletal features that exist at birth are a baseline from which bone adapts to its mechanical environment. Remodelling

is the process by which bone adapts to changing loads and also provides the ability to repair micro or even major damage (Hadjidakis & Androulakis, 2006).

This re-sculpting of bone is mediated by a coordinated packet of osteoclasts, osteoblasts and associated blood vessels, termed a Bone Multicellular Unit (BMU) (Figure 2.7B). Within the BMU, osteoclasts resorb old bone and subsequently osteoblasts lay down new bone, in the resorbed bone cavity. The function of remodelling is to serve as the mechanism for ensuring that the structural integrity of bone is high enough not to cause spontaneous fracture during normal loading. Abnormalities within modelling and remodelling are the sources of bone fragility.

## ***2.2 Mechanical Adaptation of Bone***

Bone is a living material, that adapts its structure and material properties to the mechanical conditions to which it is subjected, i.e. bone is optimised for its function ('fit for purpose'). This adaptability of bone to mechanical stimulus has been considered for over 100 years. Julius Wolff in 1892 proposed that the architecture of bone was determined by the loads imposed on it (Wolff, 1891, translated into English 1986). This idea was refined by D'Arcy Thompson in 1917, by hypothesising that load induced strain is the signalling mechanism by which bone adapts to changes in mechanical environment (Thompson, 1942). In 1964 Harold Frost went further, asserting that not only was mechanical strain the principle regulator of bone adaptation, but that a threshold of minimum effective strain must be exceeded before adaptation would occur (Frost, 1964). Experimental techniques developed in the 1970s and 1980s included the application of strain gauges to animals before skeletal loading, to measure bone strains and strain rates, and empirically demonstrated that strain is a driving mechanism in bone's mechanical adaptation. Continued experiments have begun to resolve the aspects of bone's strain environment that are relevant for this adaptation.

### 2.2.1 Dynamic Loading Drives Bone Adaptation

Liskova and Hert in 1971 externally loaded the tibiae of rabbits in both static and dynamic configurations. They showed empirically that bone adapts to dynamic (cyclical) loading, but not static loading. Cyclically-loaded tibiae were found to have new cortical bone deposits on both periosteal and endocortical surfaces, while tibiae statically loaded to the same magnitude were found to have suppressed cortical bone formation (Liskova & Hert, 1971). Later studies confirmed static loads that were sufficient for producing strains within the functional dynamic strain range, produced endocortical and intracortical bone loss, while loads applied intermittently with equivalent peak strain increased net bone formation on periosteal surfaces, and were protective against endocortical bone loss (Lanyon & Rubin, 1984) (Figure 2.8). Furthermore, increasing the magnitude of static loads does not elicit a greater adaptive response (Robling et al., 2001).

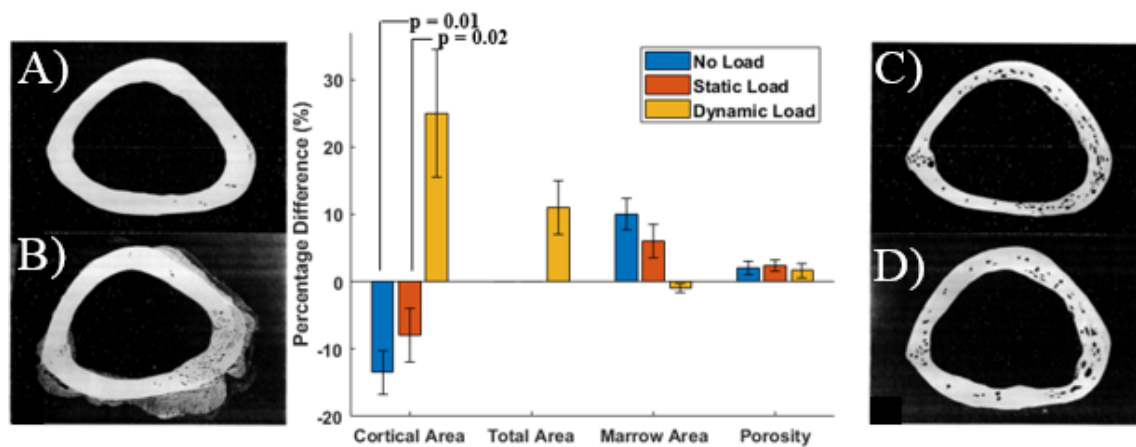


**Figure 2.8.** The results of Lanyon and Rubin's 1984 static versus dynamic loading experiments on the isolated turkey ulna (Lanyon and Rubin, 1984). Graph created from data presented in Lanyon and Rubin (1984). Cross-sections from ulna midshaft from A) contralateral intact, B) functionally isolated, dynamically loaded (100 cycles/day), C) unloaded/immobilised and D) continuously/statically loaded.

### 2.2.2 Dose-response Relationship

In further studies on functionally isolated and externally loaded turkey ulnae, Rubin and Lanyon empirically showed a linear, dose-response relationship between peak dynamic strain magnitude and change in bone mass (cortical bone area), across a strain range from zero (complete disuse) to 4000  $\mu\epsilon$  (Figure 2.9). Peak strains below 1000  $\mu\epsilon$  were associated with bone loss via increased endocortical and intracortical resorption, strains above 1000  $\mu\epsilon$  were associated with bone formation on the periosteal and endocortical surface (Rubin & Lanyon, 1985).

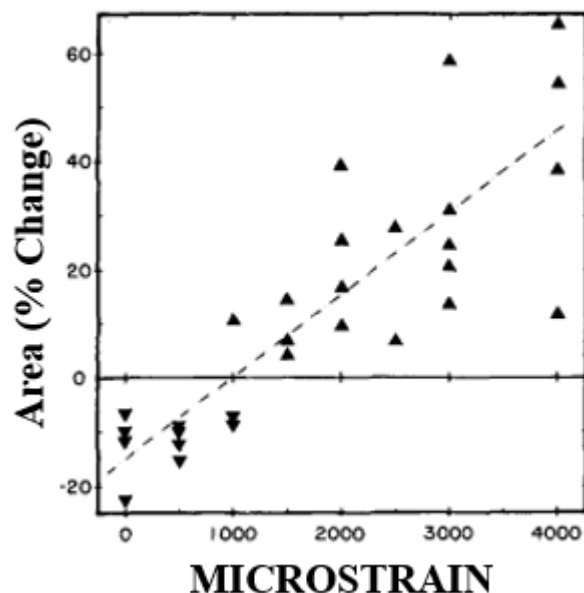


**Figure 2.9.** Results of Rubin and Lanyon's 1985 experiments into strain magnitudes effects on bone mass regulation on the functionally isolated turkey ulna, demonstrating that newly formed cortical bone at the midshaft is proportional to applied strain magnitude. Adapted from Rubin & Lanyon (1985).

### 2.2.3 Strain Environment

The adaptability of bone to dynamic, but not static loads, implies that the strain rate and the loading rate are important aspects of the strain environment. O'Connor et al. through dynamic loading of the sheep ulna and radius at various peak strains and strain rates were the first to show empirically the importance of strain rate to bone adaptability (O'Connor

et al., 1982). Later studies on the rat tibia in four-point bending and rat ulnar loading models verified this relationship and highlighted the fact that increased strain rate causes further increases in bone formation (Mosley & Lanyon, 1998; Turner et al., 1995). Turner loaded tibiae to the same strain magnitude, but cycled to that specific strain at different rates, thus changing the strain rate. A dose-response relationship was observed, i.e. increased bone formation rate was observed with increased strain rate (Figure 2.10A) (Turner et al., 1995).

As well as strain rate, the effect of frequency (number of loading cycles per second) on the adaptability of bone has been demonstrated experimentally (Rubin and McLeod, 1994; Turner et al., 1994). Rubin and McLeod using the isolated turkey ulna showed that brief exposure to low magnitude mechanical strains promoted bony ingrowth around a porous-coated titanium implant. Increasing the frequency of loading from 1 to 20 Hz increased the amount of bony ingrowth significantly (Rubin & McLeod, 1994). Turner confirmed the importance of loading frequency using the rat tibia four-point bending model and a range of loading frequencies (0.1, 0.2, 0.5, 1.0 and 2.0 Hz), while keeping the strain rate constant. Increased bone formation rate was only observed at the higher loading frequencies (0.5 – 2.0 Hz) (Figure 2.10B) (Turner et al., 1994). Higher frequencies (5-10 Hz) have been shown to be even more effective at promoting cortical bone formation (Hsieh & Turner, 2001; Warden & Turner, 2004).

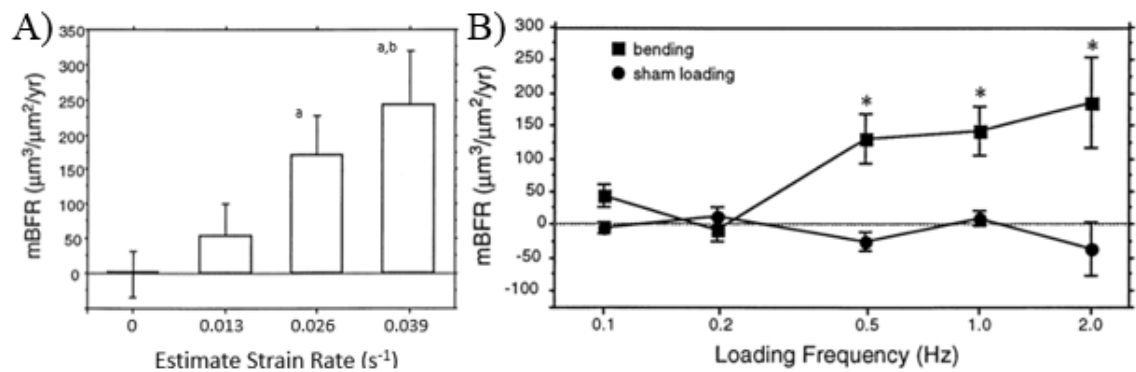


**Figure 2.10.** Strain rate and frequency of loading are important factors for bone adaptability to mechanical stimuli. A) Relative volumetric bone formation rate on the endocortical surface of rat tibia is proportional to strain rate. <sup>a</sup>Significant difference compared with 0.013 s<sup>-1</sup> group. Adapted from Turner et al. (1995). B) Relative volumetric bone formation rate on the endocortical surface of rat tibia increases significantly with loading frequency. \* indicates  $p < 0.05$ . Adapted from Turner et al. (1998).

Increased duration of dynamic loading does not yield proportional increases in bone formation. The mechanical adaptability of bone saturates with time. This was demonstrated in the isolated avian ulna model and in rats that were trained to jump a certain number of times per day (Rubin & Lanyon, 1984; Umemura et al., 1997). Furthermore, the biological mechanisms responsible for the mechanical adaptability of bone become accommodated to routine loading patterns. In other words, this adaptation is error driven, so abnormal strains drive the adaptation, until they become routine strains. Thus, a new biological and structural steady-state is eventually reached for the new loading environment (Turner, 1998).

### ***2.3 Theory: The Mechanical Adaptation of Bone***

During the 1960s, Harold Frost fleshed out a theoretical model of bone's response to mechanical usage which incorporates the empirically derived concepts of the mechanical environment just described; it is termed the mechanostat hypothesis (Frost, 1987). Subsequently in the 1990s and early 2000s with Webster Jee, Harold Frost fleshed out a distinct set of still-evolving concepts, encapsulated in the Utah Paradigm of Skeletal



Physiology, which concern load bearing bones such as femurs, and incorporates the mechanostat into the neuromuscular system. (Frost, 2004; Jee, 2004).

### 2.3.1 The Mechanostat

The mechanostat theory concerns postnatal load bearing bones and how they adapt their structural integrity to the mechanical loads imposed on them (Frost, 1987). It is a hypothesis and conceptual tool, that stands up to a certain amount of scrutiny and suggests some fundamental truths (Frost, 2003). The mechanostat is a negative feedback regulatory system within bone that is responsible for removing and/or adding bone in response to deviations in its mechanical loading environment, thus over time altering the overall mass, conformation, and architecture of the bone, so that it is optimised to meet its new mechanical demands (Figure 2.11).

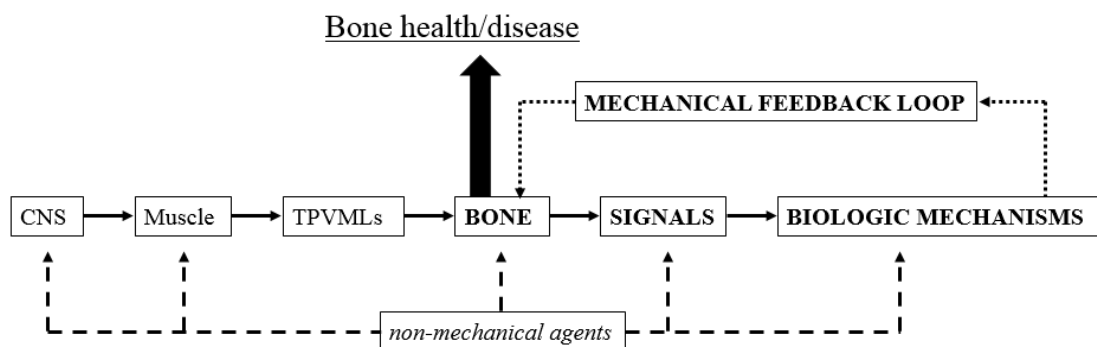


**Figure 2.11.** A simplified representation of the negative feedback within Frost’s mechanostat. Bold font highlights the mechanical feedback loop. Redrawn from (Frost, 2003). CNS: central nervous system; TPVML: typical peak voluntary mechanical loads.

Trauma excepted, the largest loads on bones come from muscle action, not from body weight (static load) (Schoenau & Frost, 2002). Thus proposition #1 of the Utah Paradigm is: “the design of healthy load bearing bones would provide only enough strength/stiffness to keep postnatal voluntary loads from causing spontaneous fracture” (Frost, 2000). The central nervous system (CNS) controls voluntary muscle movement, which generates the peak voluntary mechanical loads (TPVMLs) on load bearing bones, which produces a

strain stimulus within the bone. The strain stimulus generates signals (e.g. zeta potentials or fluid flow), which the underlying biological cells (osteoblasts, osteoclasts, osteocytes) detect, interpret and respond to (Frost, 2004).

### 2.3.2 Mechanical Usage Windows

This adaptational response occurs in opposite directions at extremes of loading (disuse or overuse) (Figure 2.12). An adaptive response is only produced when the strain stimulus is above or below a certain genetically-determined threshold termed a minimum effective strain/stimuli (MES). Thus, the regulation of bone mass in time and anatomical space is a function of the error signal between the strain stimulus and MES. This response has different control mechanisms depending on the loading scenario for bone loss or bone gain.

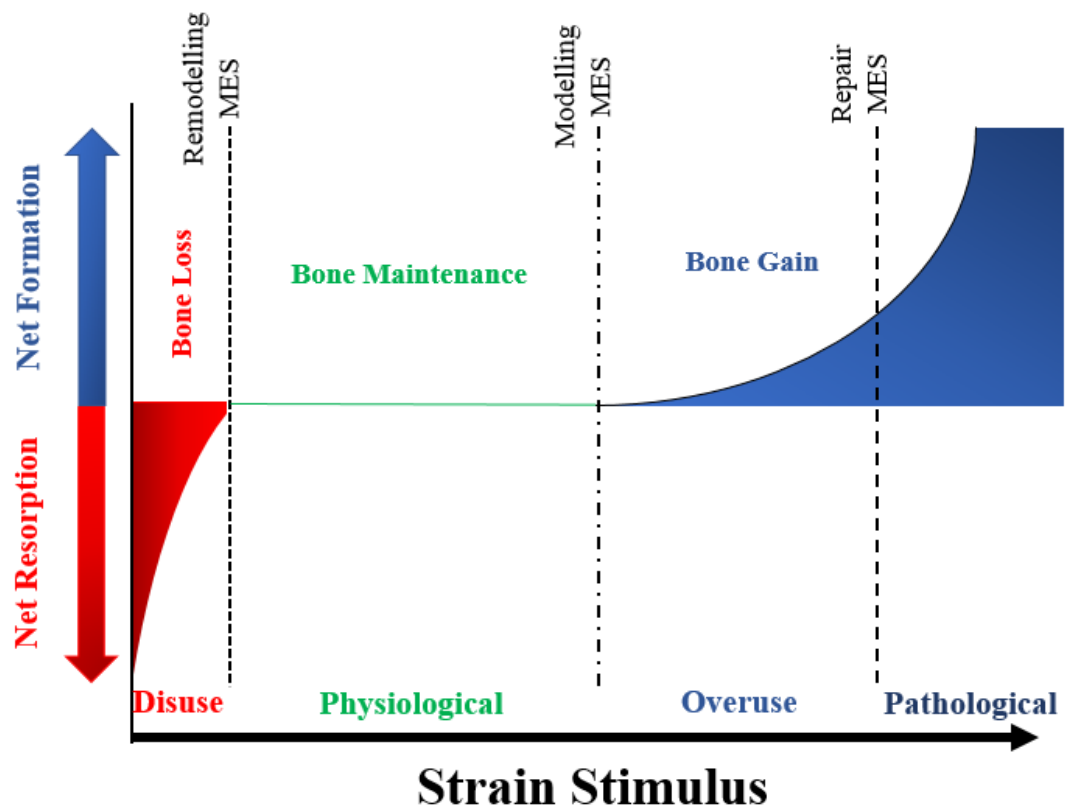


**Figure 2.12.** Representation of the relation between peak strain stimulus and bone’s adaptational response, according to Frost’s mechanostat. Illustrating the four mechanical usage windows (disuse, physiological, overuse, pathological). MES: effective strain.

At normal physiological levels of loading, the strain stimulus exists between the remodelling and modelling MES, there is no net bone resorption or formation and bone is turned over by the process of conservation-mode remodelling. Strain stimuli lower than the remodelling MES (MESr), activate disuse-mode remodelling, resulting in net bone loss. Strain stimuli above the modelling MES (MESm), activate formation modelling drifts resulting in net bone gain (Frost, 1987; 2003). Strain stimuli high enough to cause significant microdamage activate targeted modelling to repair the damage, also rapid woven bone formation can occur. Thus, for a given loading environment, bone is resorbed or formed until the strain stimuli returns to physiological levels. This basal usage window is also termed the lazy zone (Frost, 2004).

Non-mechanical agents (including sex, age, vitamins, hormones and genes) can affect the CNS and the muscles that produce the TPVMLs on bone. They can also affect the strain-stimuli dependant signals that control the activation of the biologic mechanism that bring about bone's adaptive response. Thus, non-mechanical agents can modulate the negative feedback regulatory system but can never replace the mechanical stimulation, i.e. they could never normalise bones in paralysed limbs (Figure 2.11) (Frost, 2003).

### *2.3.3 The Utah Paradigms Predictions for SCI*

According to the paradigm, in the case of complete SCI, where the CNS control of sublesional muscles is completely cut off, TPVMLs and thus muscle-driven bone stimulation are both negligible. Sublesional bones are in a state of mechanical disuse. The strain stimulus on bone is now such that it lies far to the left on Figure 2.12, well into the disuse window. These bones now enter a state of net bone resorption, brought about by increased production of bone multicellular units (BMU) and a biological mechanism mediated by bone marrow, which makes newly formed BMUs form less bone than they resorbed (Martin, 2000), but only on bone envelopes next to or close to the marrow, i.e.

trabecular and endocortical surfaces. This is termed disuse-mode remodelling, and results in a disuse-pattern osteopenia, which weakens the affected bones (Frost, 2004). In adults, this disuse-pattern osteopenia manifests itself for cortical bone by enlarging marrow cavities, thus thinning cortices (via to endocortical thinning), and for trabecular bone struts are thinned and eventually perforated, resulting in reduced number and connectivity, and increased separation of remaining struts (Figure 2.13).

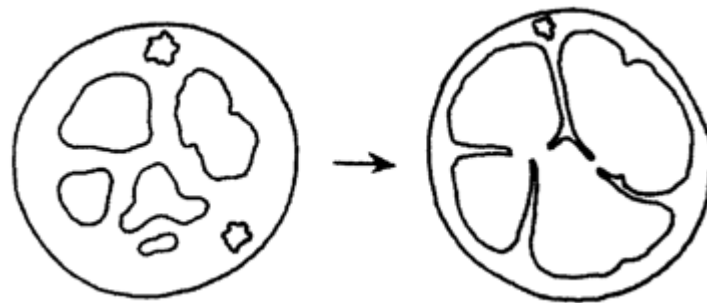


**Figure 2.13.** Schematic of disuse-pattern osteopenia in a skeletally mature load bearing long bone. Redrawn from Frost (2004).

In the case of a SCI that results in paralysed sublesional limbs, the Utah Paradigm informs that there is no intrinsic bone disease. Before the traumatic event these bones were healthy, it was the event and subsequent consequences that triggered a change in the mechanical environment. The load bearing long bones still obey proposition #1 of the Utah Paradigm, and in this sense would be considered healthy, even though they have reduced whole-bone strength. Because of loss of muscle-driven bone stimulation, the bones have more tissue and whole-bone strength than is needed for their reduced mechanical loading environment. Disuse-mode remodelling is the biological mechanism that removes the excess bone. In the chronic state, i.e. when the bone has adapted to its new state of permanent disuse, and has reached a new steady-state, BMU-based remodelling reverts back to its conservation-mode, and the bone resides back in physiological window of Figure 2.12 (Frost, 2004).

## ***2.4 Bone Quantity and Quality***

### ***2.4.1 Osteoporosis***

Osteoporosis is a common progressive metabolic bone disease of multifactorial aetiology and pathophysiology. It is a disease of generalised skeletal fragility, where bone structural integrity is weakened sufficiently so that fracture can occur with minimal trauma. These fractures result from a combination of minor injury (typically a fall) and bone fragility. The bone fragility is a result of altered geometrical, architectural and material properties. It is estimated that approximately 40% of all women and 13% of all men older than 50 years of age will suffer an osteoporotic fracture that will require hospitalisation (Melton et al., 1992). The underlying pathogenesis is a disruption in the biological mechanisms that govern the remodelling and modelling processes. In healthy bone these processes are optimised, maintaining its structural integrity at all the hierarchical levels. In osteoporotic bone these mechanically-adaptive processes are unbalanced, favouring a higher rate osteoclastic activity than osteoblastic activity, which has the progressive effect of resorbing more bone volume than that which is formed. The origins of the disruptions are complex and not completely understood, but are intensively researched, encompassing genetic, epigenetic, mechanical and hormonal factors (Seeman, 2003). These biological mechanisms occur on bone surfaces, trabecular bone with its much larger surface area to volume ratio experiences the deleterious effects more rapidly and extensively.

Osteoporosis is most commonly associated with ageing including post-menopause (driven by hormonal changes and increased disuse). However, many other factors can predispose an individual to osteoporosis, including their genetics and life style. Factors such as smoking, medication and poor diet can also contribute. Mechanical unloading of the musculoskeletal system can also result in a form of the disease termed disuse osteoporosis, which can be induced in prolonged bed rest studies and is seen in astronauts

exposed to microgravity during spaceflight (Alexandre & Vico, 2011). However, the most rapid and extreme manifestation of osteoporosis is observed in the sublesional bones following complete spinal cord injury (SCI).

#### 2.4.1.1 Operational Definition

The World Health Organisation (WHO) has given an operational definition for osteoporosis based on bone mineral density (BMD) measurements (WHO, 1994). The most common technique for acquiring BMD is a Dual-energy X-ray Absorptiometry (DXA) scan acquired from the lumbar spine or hip. The WHO defines osteoporosis as a BMD equal to or more than 2.5 standard deviations below that of the average value of a young healthy adult (WHO, 1994). Table 2.1 describes a more detailed bone status based on hip BMD measurements.

**Table 2.1.** World Health Organisation’s definition of osteoporosis based on bone density measurements (WHO, 1994).

<b>Bone Status</b>	<b>Hip BMD</b>
Normal	T-score of -1 or above
Osteopenia	T-score lower than -1 and greater than -2.5
Osteoporosis	T-score of -2.5 or lower
Severe osteoporosis	T-score of -2.5 or lower, and the presence of at least one fragility fracture

In the clinical setting these definitions are widely accepted, giving diagnostic and intervention thresholds. Fracture risk prediction is also estimated based on BMD measurements, but supplemented with a set of epidemiological parameters, using algorithms such as the fracture risk assessment tool (FRAX) (Kanis et al., 2005). With the currently available clinical tools the disease often does not become apparent until fracture has occurred.

### *2.4.2 Bone Quality*

The common belief that DXA-derived BMD represents a valid predictor of bone strength comes from the large number of controlled laboratory studies that show high correlation between these two variables (Järvinen et al., 2008). However, fracture risk prediction from BMD measurements appears only valid at the population level, whereas at the individual patient level the predictive value of BMD is limited. Given two patients with severe osteoporosis, one will fracture and the other will not, despite having similar BMD values (Siris et al., 2004). Bone quality is a concept used as a solution to this apparent clinical paradox.

To understand this paradox, it helps to define DXA-derived BMD. DXA acquires a single 2D measurement of bone structure, from one angle. It is defined as the integral mass of bone mineral per unit projected area. It represents an integration of everything within the scan path. It is therefore an areal BMD (aBMD) and does not represent true anatomy and is inherently inaccurate. On the patient level the magnitude of error in DXA-derived BMD is between 20% and 50% (Bolotin & Sievänen, 2001; Bolotin et al., 2003).

DXA-derived aBMD reflects the amount of bone mass, which is not an indication of the bone's structure. The definitive measure of bone's mechanical competence is provided by whole-bone strength (Järvinen et al., 2008). Thus, the so called "clinical paradox" stems from the inability to determine bone's actual mechanical integrity. For example, DXA-derived aBMD cannot differentiate persons with low aBMD, but with intact cortical and trabecular microarchitecture, to that of persons with the same aBMD, but with severe cortical porosity and deterioration of trabecular microarchitecture (Boutroy et al., 2005). Bone quality is then a term that extends beyond the clinical measures of bone density and mass, it is the sum of characteristics that give bone its capacity to resist fracture (Bouxsein, 2003; Compston, 2006). Bone quality incorporates geometric, compositional

and mechanical parameters at all length scales and is evolving with technological advancements.

#### *2.4.2.1 Geometric Characterisation*

The geometric characterisation of bone can span many length scales and includes the spatial distribution, organisation and architecture of both cortical and trabecular bone. At the whole-bone scale it is the size, shape and distribution of bone. At the micro-scale it is the geometry, morphometry and topology of the microarchitecture of cortical and trabecular bone. At the nanoscale it is collagen fibre orientation and crystal dimensions. Geometric parameters are sensitive to age, pathological alterations and certain interventions, particularly at sites with high metabolic turnover. In this thesis geometric characterisation of rat femur samples is conducted at the whole-bone scale and micro-scale, using micro-Computed Tomography ( $\mu$ CT).

#### *2.4.2.2 Mechanical Characterisation*

Characterisation of the mechanical properties of bone include measuring its resistance to failure. These measures include stiffness, strength, hardness, toughness and fatigue. These properties can be assessed at different length scales, using techniques that minimise the effects of the higher length scales. At the whole bone scale, destructive tests that fracture the bone can be used to calculate compressive, tensile, bending and torsional properties of the bone. These extrinsic mechanical properties reflect the whole-bone structure and can be normalised with respect to the bone geometry to obtain intrinsic material-level properties. At smaller scales indentation tests can be used to provide geometry independent mechanical measures (Jepsen et al., 2015). In this thesis mechanical characterisation of rat femur samples was conducted at the whole-bone scale on diaphyseal cortical bone using three-point bending and torsion testing and on the femoral neck through a fracture test.



### *2.4.2.3 Density Characterisation*

As described, DXA-derived aBMD is used clinically as a proxy measure for whole-bone strength. Volumetric BMD (vBMD) can be acquired through X-ray-based tomographic techniques, such as Quantitative Computed Tomography (QCT), peripheral-QCT (pQCT) and  $\mu$ CT. When using tomographic techniques BMD refers to the combined density of a volume of interest (VOI) that contains both soft tissue and bone tissue. With high resolution tomographic techniques BMD measurements can be acquired which are restricted to VOIs that exclusively contain bone tissue. These measurements are termed tissue mineral density (TMD) and provide information on just the bone tissue. Both BMD and TMD are defined with respect to known volumetric densities of bone mineral. In this thesis density characterisation of rat femur cortical bone was acquired with  $\mu$ CT-derived cortical TMD.

## ***2.5 Assessment of Bone Mass***

### *2.5.1 Micro-computed Tomography*

Tomography is a non-destructive technique that can use any form of penetrating wave to provide a 3D representation of an object's internal structure. The fundamental principle proved in 1917 by Johann Radon is that "an n-dimensional object can be reconstructed from its (n - 1) projections" (Radon (1917), translated 1986) (Figure 2.14). Computed tomography (CT) is the imaging modality that uses this principle to combine many computer-processed 2D X-ray projection image measurements acquired at incremental rotations over a total of 180 or 360 degrees. Micro-computed tomography ( $\mu$ CT) is CT of small objects (e.g. rat femurs) in specialised scanners that allow 3D imaging of the object at very high spatial resolutions (Feldkamp et al., 1989). Clinical CT scanners

provide reconstructed images with voxel size of the order 1 mm, while  $\mu$ CT provides image resolution in the micrometre range (1 – 50  $\mu$ m) (Kuhn et al., 1990).

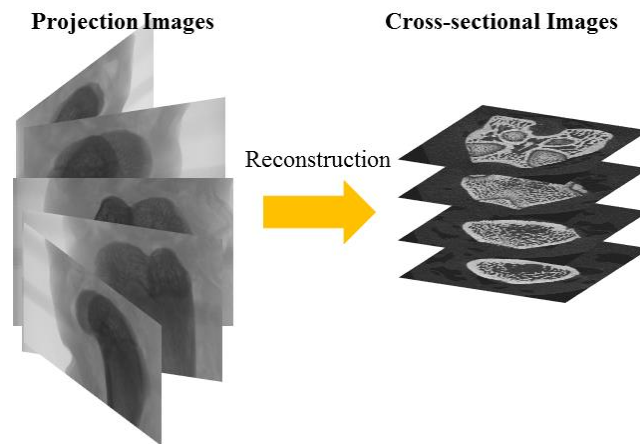


**Figure 2.14.** Through application of a reconstruction algorithm, the 3D object can be reconstructed from its projection images, acquired at incremental rotations over a total of 180 or 360 degrees. The object's internal structure is non-destructively visualised through a series of contiguous cross-sections.

$\mu$ CT quantitative morphometry is the “gold standard” technique for assessment of trabecular and cortical bone micro-architecture and morphology, in the bones of small animal disease models (Bouxsein et al., 2010). Its reproducibility and accuracy has been established through many studies, for example (Müller et al., 1998; Barbier et al., 1999; Chappard et al., 2005). These studies have shown that both 2D and 3D  $\mu$ CT-derived morphology measurements are highly correlated with the previous “gold standard” method, quantitative histomorphometry, where 2D morphometric indices are measured directly from thinly sliced embedded sections of bone (Figure 2.15A). Information regarding the third direction was obtained mathematically using stereological techniques.  $\mu$ CT has many advantages over quantitative histomorphometry for the assessment of bone mass and microarchitecture: i) direct 3D volumetric measuring of these of trabecular morphology e.g. trabecular thickness and separation (Figure 2.15B), ii) significantly larger VOIs can be studied, iii) it is non-destructive, thus other characterisation such as mechanical testing, can be performed, iv) higher throughput and v) estimations of bone

tissue mineralisation can be quantified. Appendices A and B provide in depth overviews of the morphometric parameters utilised in this thesis.

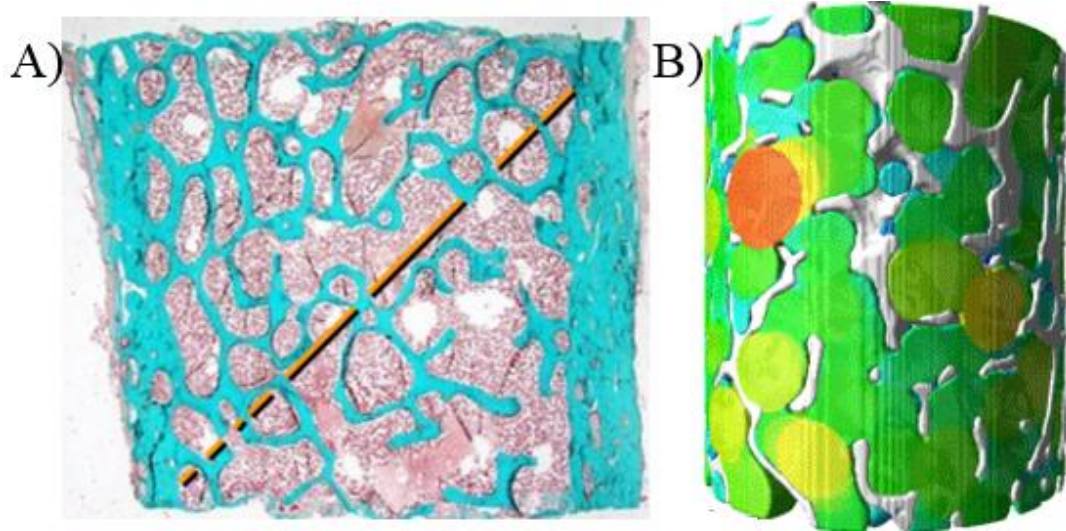


**Figure 2.15.** Comparison between quantitative histomorphology and  $\mu$ CT-derived quantitative morphometry. A) depicts an example sectioned and stained thin slice of bone, the diagonal represents measurements of trabecular separation (Tb.Sp). Adapted from Hodgson et al. (2010). B) depicts an example  $\mu$ CT dataset of a core of trabecular bone, the spheres (diameters) represent measures of Tb.Sp. Adapted from b-cube (2019).

### 2.5.1.1 Theory

The physical principle behind  $\mu$ CT is founded on the interaction of ionising radiation (of which X-rays are utilised here) with matter (of which rat femurs are used here). X-ray photons can interact with matter in several different ways, the three most important interaction modes are the photoelectric effect, Compton Scattering and pair production. Which interaction mode that dominants is dependent on the X-ray energy spectrum ( $E$ ) and the atomic number ( $Z$ ) of the absorbing sample element. For imaging of bone mineral (calcium and phosphorous being high  $Z$  material), X-ray energies between 20 kVp and 100 kVp are typically used (Bouxsein et al., 2010). In this energy range the dominant interaction mechanism is the photoelectric effect (Figure 2.16). In this process photons are completely absorbed by atoms of the sample, this knocks out electrons which are

transmitted in the same direction of travel of the incident photon. This is the preferred mode for  $\mu$ CT since X-rays are cleanly removed from the incident beam. In contrast, Compton scattering results when the photon transfers only part of its energy to an electron, the remaining lower energy photon is emitted (scattered) in a direction different to it to that of the incoming photon. The detection of these scattered photons causes artefacts in images.

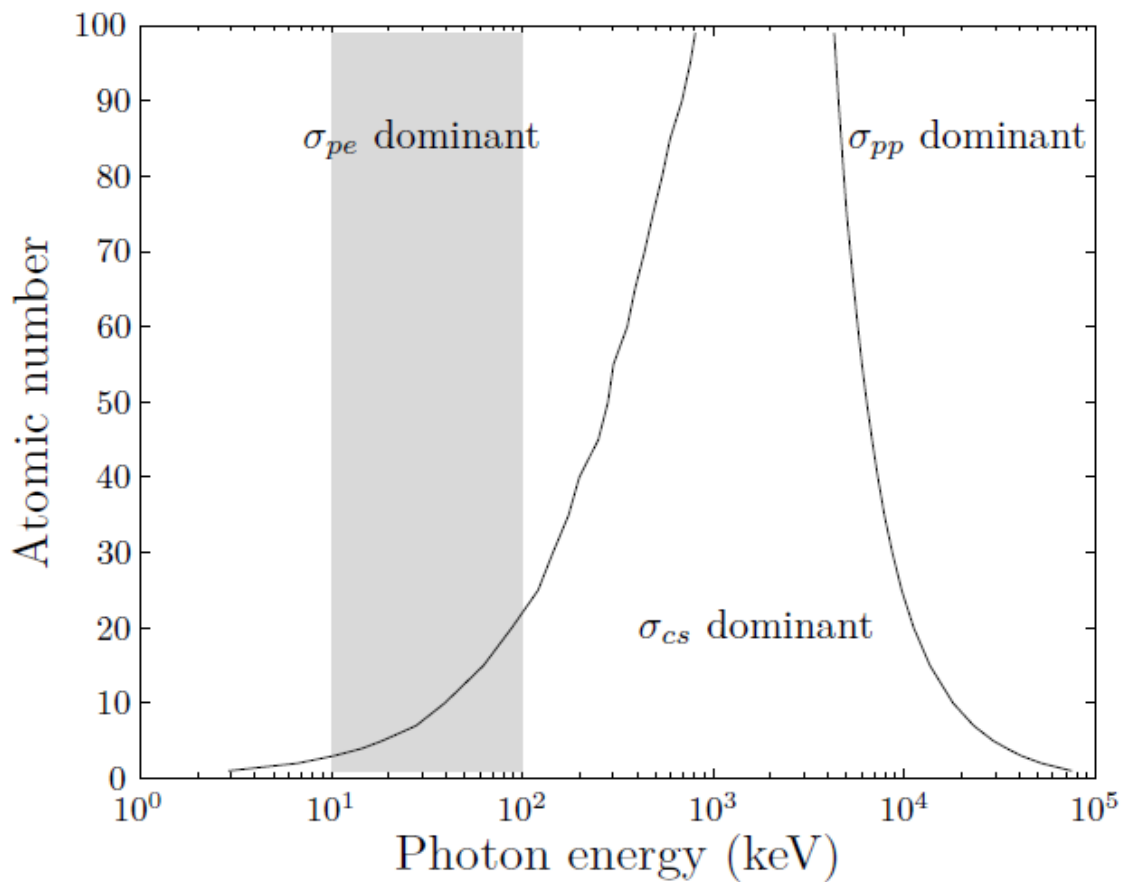


**Figure 2.16.** The relative importance of the three main types of X-ray interaction with matter, with varying atomic number at different photon energies. Lines represent equal strengths of neighbouring interaction modes. Shaded region represents typical energies used for bone imaging. Adapted from Depypere (2013).

As X-rays pass through bone tissue, the incident beam's intensity is attenuated in an exponential manner according to the material along its path. This is described by equation 2.1:

$$I_x = I_o e^{-\mu x} \quad (2.1)$$

Where  $I_o$  is the incident beam intensity,  $I_x$  the intensity of the beam after passing through a distance  $x$  of material with linear attenuation coefficient  $\mu$ . Equation 2.1 assumes X-rays are from a monochromatic source, so all photons undergo the same level of attenuation. The final attenuation is the sum of all local attenuations along the beam. For multiple materials with different attenuation coefficients

$$I_x = I_o e^{-\mu_1 x_1} e^{-\mu_2 x_2} \dots \quad (2.2)$$

Two requirements for  $\mu$ CT imaging are that: i) the energy range of photons used is such that there is partial absorption of X-rays, i.e. some X-rays are absorbed by the sample, while others pass straight through and ii) the sample material is composed of different materials (atomic numbers/attenuation coefficients), i.e. there is differential absorption. This is necessary to provide contrast, otherwise resultant images would be a uniform level of grey

#### 2.5.1.2 $\mu$ CT Scanner

In *ex vivo*  $\mu$ CT the rotation of the sample relative to a fixed X-ray source and detector allows the object's location in 3D to be precisely mapped, and a 3D representation that characterises the spatial distribution of the object's X-ray attenuation properties produced (Figure 2.17) (Cormack, 1963, 1964; Hounsfield, 1973).

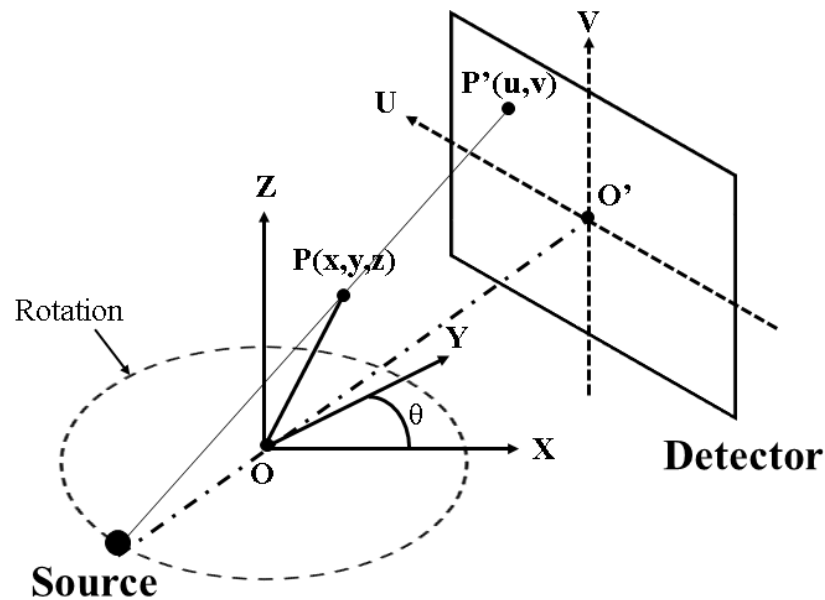


**Figure 2.17.** Schematic of geometry of a  $\mu$ CT scanner. The scanned object rotates around point O, which is the origin of the x, y, z coordinate system. The X-ray source and the detector centred at O' have fixed positions relative to this object. At different angles of rotation ( $\theta$ ), the projection images of the object's points O and P, have different positions O' and P' on the 2D detector. The absolute 3D location of points O and P within the object can be determined through reconstruction at all  $\theta$ .

The X-ray source is a microfocus X-ray tube. In this tube X-rays are generated by accelerating electrons produced at the cathode across a potential difference into a very small spot on the tungsten anode target. In the anode, X-ray photons are produced by Bremsstrahlung (braking radiation). Electrons that penetrate the tungsten target and pass close to atomic nuclei are slowed and deflected, the energy lost by these electrons is in the form of X-ray photons over a range (spectrum) of energies. The range of photon energies is controlled by the applied tube voltage and the number of emitted photons is controlled by the tube current and exposure time.

The detection of unabsorbed X-rays is recorded by a detector. The detector is an array of solid-state elements, each element of which consists of a coupled scintillator and photodiode. The scintillator absorbs the X-ray photons, converting them to lower energy visible light photons. These lower energy photons are absorbed by the photodiode,

producing an electrical charge proportional to the photon's energy. For the given exposure time this charge accumulates in the element. This charge is then read out from each element and an image is built up for that rotation angle.

### 2.5.2 Dual-energy X-ray Absorptiometry

Dual-energy X-ray Absorptiometry (DXA) is the clinical gold standard for densitometric measurements used in the diagnosis of osteoporosis (WHO, 1994), and in the assessment of fracture risk (Kanis et al., 2005). DXA measurements are performed at the lumbar spine and/or hip and/or wrist, for the diagnosis of post-menopausal osteoporosis. DXA uses two X-ray beams with different photon energies, this allows compensation for attenuation through soft tissue, so bone can be differentiated. DXA acquires a projection image of the bone (Figure 2.18), from which a region of interest is selected and a projected aBMD obtained.

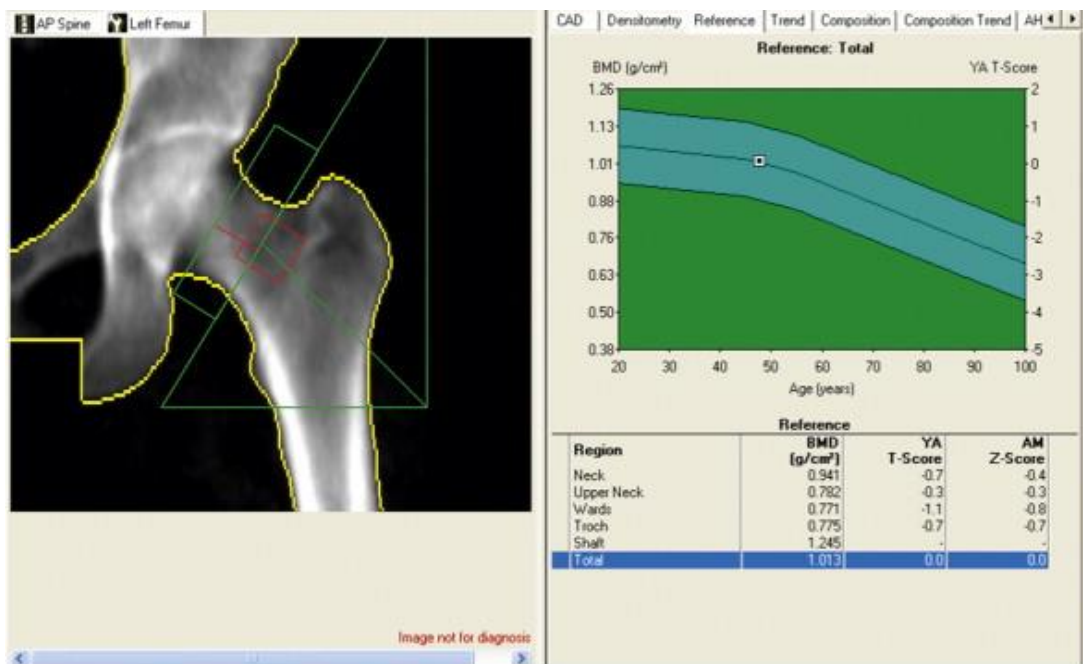


Figure 2.18. Dual-energy X-ray Absorptiometry-based assessment of the femoral neck, with both T and Z score references values. Adapted from Burr & Allen (2013).

### *2.5.3 Peripheral Quantitative Computed Tomography*

Peripheral Quantitative Computed Tomography (pQCT) has been utilised in the research setting to gain a more detailed view of what structurally causes the severe reductions in areal BMD seen in all forms of osteoporosis. It differs from DXA in that it is a tomographic technique, allowing generation of three-dimensional volumes of interest inside the bone. It differs from a full body diagnostic CT scanner in that it has a much smaller gantry, as it is dedicated to imaging of the appendicular skeleton, thus significantly reduces the patient's exposure to radiation. The main advantages of pQCT over DXA are that i) the resolution of the scans produced, typically 100 – 300  $\mu\text{m}$ , and 1mm slice thickness is enough to differentiate both cortical and trabecular bone and quantify their respective volumetric BMD (vBMD), ii) cortical bone geometry can be assessed, iii) superimposition of objects within the scan path does not occur.

### *2.6 Spinal Cord Injury*

The spinal cord is a long bundle of nervous tissue and associated cells, encased in a bony vertebral column, that runs from the brainstem down the vertebral canal. It is a conduit responsible for integrating, processing and coordinating sensory information and motor commands. In humans there are 31 pairs of spinal nerves that branch off from the cord. The spinal cord can be divided into segments according to which parts of the body these branching nerves supply, these are the cervical (C1 – C8), thoracic (T1 – T12), lumbar (L1 – L5), sacral (S1 – S5) and singular coccygeal segments (Figure 2.19).



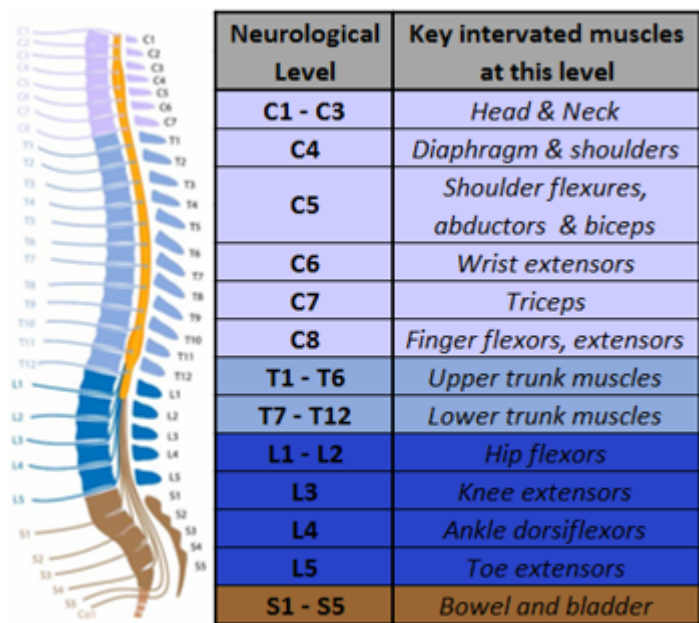


**Figure 2.19.** Schematic lateral view of human adult spinal cord and vertebra, with examples of the muscles innervated at different levels, in real life S1-S5 are level with T12-L1.

Traumatic injury to the spinal cord at any of these segments can result in complete or partial paralysis below the level of injury. The extent of this paralysis is dependent on the level and completeness of the injury. The higher the level of the SCI, i.e. the nearer to the brainstem, the greater the number of muscle groups and organs affected. The more complete the SCI, i.e. the extent of damage to the spinal cord, the more severe the effects on motor and sensory function.

### 2.6.1 The Phases of SCI

The time-point post-injury is an important pathophysiological parameter. It is currently divided into 5 key stages (Rowland et al., 2008). The immediate phase (0 – 2 hours) starts at the time of injury and is dominated by the immediate results of the injury (traumatic severing of axons, death of neurons). The acute phase is the period where secondary injury processes dominate, it is split into i) early acute phase (2 – 48 hours), where continued haemorrhage and inflammation occur, and ii) subacute phase (2 days – 2 weeks), when repair mechanism start to “resolve” the injury. The intermediate phase (2

weeks – 6 months), is when the spinal cord lesion continues to mature. The chronic phase is > 6 months and continues throughout the rest of the patient's lifetime, and is characterised by the stabilisation of the lesion (Rowland et al., 2008). The phases of the injury are of importance since they involve many distinct processes, thus different therapeutic interventions are needed at different stages.

### *2.6.2 Secondary Complications*

Secondary complications resulting from SCI can include cardiovascular and respiratory complications, endocrine and metabolic disorders, chronic pain and spasticity (Sezer, 2015). These complications are generally more severe in tetraplegia than in paraplegia. Muscular paralysis below the level of injury leads to rapid muscle atrophy and the removal of muscle-driven dynamic stimulation, and reduced levels of physical activity also reduces mechanical loading of bone, these both lead to rapid osteoporosis in the sublesional bones (Alexandre & Vico, 2011). For paraplegics it is generally the pelvis and lower limbs where bone loss is observed, while for tetraplegics the upper limbs are also affected (Garland et al., 1992).

### *2.6.3 Fracture Risk*

This SCI-induced osteoporosis results in rapid and severe deterioration of both bone quantity and quality (Garland et al., 1992). SCI patients are at a significantly higher risk of bone fractures than the able-bodied population. An overall fracture incidence of 2.2% per year has been reported, with an average time to first fracture post-SCI of 8.9 years (Zehnder et al., 2004). It is the sublesional lower extremities that are most susceptible to fracture, particularly the trabecular-rich knee region (distal femur and proximal tibia) (Figure 2.20) (Cirnigliaro et al., 2017). In a retrospective study documenting the fracture characteristics of 107 traumatic SCI patients, Frotzler et al., (2015) reported 156 long

bone fractures, 61% of the fractures occurred in the femur, 45% of which occurred within the distal femur. Out of the remaining 39% of tibia fractures, 42% occurred within the proximal tibia. The fractures are typically a result of low impact (energy) events, resulting for example from everyday activities such as transferring from bed to wheelchair. They are therefore termed fragility fractures (fractures that occur in the absence of major trauma) and have a much longer recovery time associated with them, if indeed they do heal at all (Frotzler et al., 2015). Complications from these fractures lead to increased morbidity, mortality and increased healthcare costs. The overall sublesional long bone fracture rate is twice that of the able-bodied population (Vestergaard et al., 1998). Fragility fracture occurrence increases with time post-SCI, that combined with an increasing standard of care and life expectancy of SCI patients, means that likelihood of a fracture will only increase.



**Figure 2.20.** Radiographs of a distal femur fragility fracture. Adapted from (OrthoBullets, 2018).

#### *2.6.4 Non-mechanical Agents*

SCI-induced osteoporosis is often considered simply as a type of disuse osteoporosis. It is disuse-related, although there are host of non-mechanical agents that contribute to the pathogenesis of osteoporosis after SCI. SCI-induced hormonal changes are among these non-mechanical agents that contribute to osteoporosis through many different

mechanisms, including; i) decreased intestinal absorption and increased renal elimination of calcium; ii) vitamin D deficiency (Bauman et al., 2009), iii) antagonised gonadal function, iv) inhibition of osteoanabolic action of sex steroids (Jiang et al., 2006), v) hyperleptinaemia, that is increased levels of leptin, a hormone associated with adipose tissue (Battaglino, et al., 2013) and vi) low parathyroid hormone levels (Drake et al., 2010). Other non-mechanical factors include sympathetic denervation, and changes to vasculature (Tan et al., 2013). Non-mechanical agents contribute to the osteoporosis by oversupplying osteoclasts and/or undersupplying osteoblasts relative to the requirements of bone resorption and/or formation.

#### *2.6.5 Clinical Studies of SCI-induced Osteoporosis*

Initial studies into the effects of bone loss in patients with SCI, carried out histomorphometric analysis on biopsies of sublesional bone (particularly the iliac crest). More recently, Both DXA and pQCT have been adopted for research purposes in the SCI population, where scans are performed at the fracture-prone distal femur and/or proximal tibia (Figure 2.21) (Biering-Sorensen et al., 1988; Morse et al., 2012).

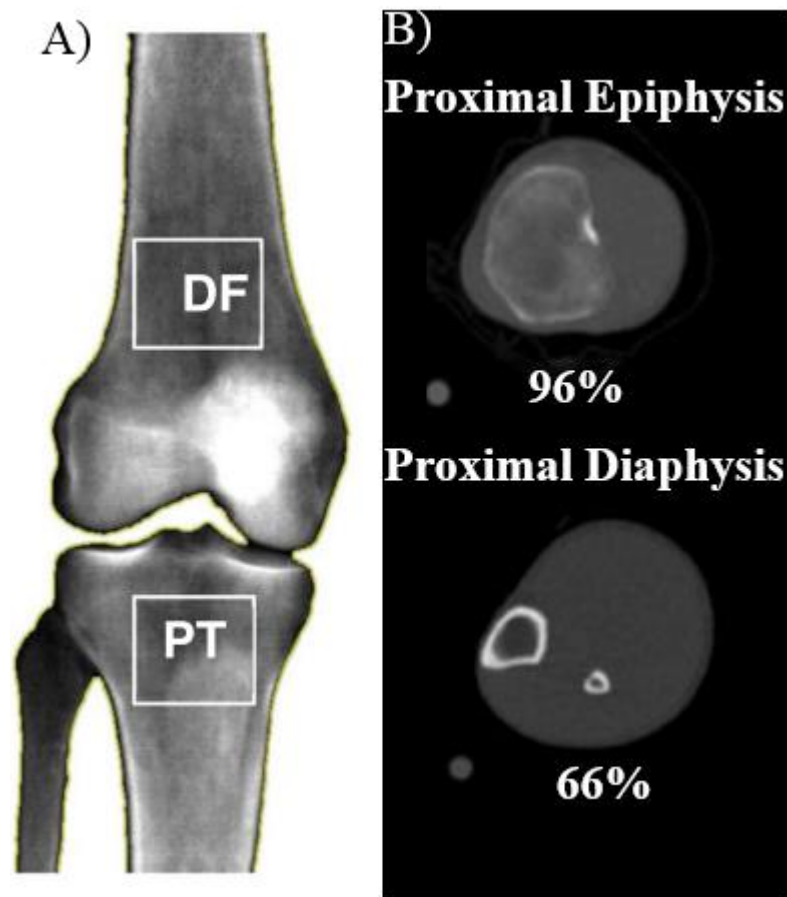


**Figure 2.21.** Examples of A) a DXA scan of the distal femur and proximal tibia with regions of interest. Adapted from Cirnigliaro et al. (2017), B) two pQCT scans at 96% (proximal epiphyseal) and 66% (proximal diaphysis) bone length of the tibia. Adapted from Coupaud et al. (2017). DF: distal femur; PT: proximal tibia.

#### 2.6.5.1 Histomorphometric Analysis

Histomorphometric analysis performed on the sublesional iliac crest in paraplegic patients within the first few weeks post-SCI have revealed increases in remodelling rate (i.e. increased osteoclastic and osteoblastic activity within the BMU) (Chantraine et al., 1986). Rather rapidly over the course of less than five months an uncoupling of this osteoclast/osteoblast relation ensues, with marked depression in osteoblast bone formation, and a marked increase in osteoclast trabecular bone resorption (Minaire et al., 1974). This uncoupling is reinforced by the finding of significantly increased levels of biochemical bone resorption markers, peaking between 10 and 16 weeks post-SCI

(Roberts et al., 1998). These underlying biologic mechanisms lead to the bone loss observed in patients with SCI.

#### *2.6.5.2 Cross-sectional DXA Study Findings*

Cross-sectional DXA studies have been carried out to quantify aBMD in the sublesional bones in patients with SCI. The first such study to be conducted around the fracture-prone knee was conducted on the proximal tibia by Biering-Sorensen et al. (1988). A comparison was made of the bone mineral content (BMC) in the trabecular-rich proximal tibia between 21 SCI subjects (2 – 25 years post-SCI), to that of the able-bodied population. It was found that on average the proximal tibia BMC in the SCI participants was over 50 % lower than that of the able-bodied population, while for the tibial shaft, the average reduction was 25% (Biering-Sorensen et al., 1988). More recent studies are in agreement with these findings (Dauty et al., 2000; Garland et al., 2001; Shields et al., 2005). Dauty et al. (2000) measured aBMD from both the distal femur and proximal tibia for 31 chronic SCI subjects (6 months – 19 years post-SCI) and compared these to 31 healthy control participants. The aBMD was 52 % lower in the distal femur and 70% lower in the proximal tibia for the SCI subjects.

#### *2.6.5.3 Prospective DXA Study Findings*

Prospective DXA studies that obtain a baseline scan and at least one follow-up scan have been carried out to quantify the progression of aBMD loss with time in both acute and chronic phases post-injury. Warden et al. (2002) evaluated bone loss in the proximal tibia in the acute phase of injury in 15 SCI subjects (1 – 6 months post-SCI). Six weeks later a follow up DXA scan was performed, a rapid 5.3 % decrease was observed in aBMD. Wilmet et al. (1995) performed BMC measurements at both trabecular-rich and cortical sites in the sublesional long bones of 31 paraplegic patients within eight weeks of traumatic SCI. The first measurement was obtained at five weeks post-injury, and

subsequent measurements every 10 weeks up to 50 weeks. During the first year, losses of ~ 4% BMC/month and ~ 2% BMC/month were observed in trabecular-rich and cortical sites respectively. Several 2 year follow-up studies have also been performed, Biering-Sorensen performed 2 year follow up-scans on 8 SCI participants (baseline scans 9-167 days post-SCI) at the proximal tibia, aBMD was 40-50% lower than at baseline (Biering-Sørensen et al., 1990), whilst Garland's 2 year follow up at the distal femur and proximal tibia followed 5 SCI participants from very soon after injury ( $33.5 \pm 10$  days), distal femur and proximal tibia aBMD were 27 % and 32% lower respectively.

Long-term DXA studies into the chronic phases of SCI are sparse, currently only one study exists in the literature, where 31 male and 4 female SCI patients took part in a 5 year follow up study (Garland et al., 2008). The study contained 13 paraplegics and 14 tetraplegics and average duration of injury was  $19.8 \pm 8.7$  years. Inter-subject variability was demonstrated, and participants were separated into two groups, based on whether there was an increase or decrease in aBMD. At the 5-year follow-up scan, distal femur aBMD decreased in just more than 50% of patients, while proximal tibia aBMD decreased in approximately 67% of patients.

#### *2.6.5.4 Summary of DXA Findings*

DXA studies have managed to uncover several factors that appear to influence bone loss post-SCI. Firstly, the level of injury, thus extent of impairment has a role. Tetraplegics experience more bone loss throughout the skeleton than paraplegics, but similar aBMD losses in sublesional limbs have been shown (Dauty et al., 2000; Frey-Rindova et al., 2000). Secondly, bone mass loss is greater in more complete SCIs (Garland et al., 2004; Garland et al., 1992; Sabo et al., 2001). Thirdly, the longer the duration of injury (DOI), the more bone loss observed in proximal tibia and distal femur (Dauty et al., 2000). Fourthly, age at time of injury contributes to bone loss in complete SCI, with younger

patients having less reductions in aBMD at the knee and hip (Garland et al., 2001; Kiratli et al., 2000). Finally, DXA studies in SCI patients have shown rapid decreases in BMC and aBMD in the trabecular-rich knee within the acute stage, but also observed is the potential of a new steady-state during the chronic stage of injury, but this remains to be firmly established. (Garland et al., 2008). Cortical bone losses appear less rapid and extensive. Whilst informative, reduced aBMD and BMC do not give a clear picture of the structural changes occurring post-SCI in paralysed limbs.

#### *2.6.5.5 Cross-sectional pQCT Study Findings*

Eser et al. (2004) in a cross-sectional study described the relationship between duration of paralysis post-SCI and bone structure, quantifying the vBMD and geometry within the trabecular-rich distal epiphyses and diaphysis of the femur. 89 motor-complete spinal cord injured men (65 paraplegic, 24 tetraplegic) with SCI duration between 2 months and 50 years (predominantly chronic) participated in the study. It was found that trabecular vBMD of the epiphyses and cortical bone cross-sectional area of the diaphysis decreased exponentially with time since injury, but at different rates depending on the parameter. Rapid trabecular vBMD reductions were observed, while cortical geometry and vBMD loss occurred more slowly. These parameters reached a new steady state between 3 and 8-years post-SCI. At the steady state, bone loss of 50% was observed at the epiphyses, while only 35% bone loss was observed in the femoral shaft, compared to able-bodied controls. The epiphyseal bone loss was accounted for by reductions in trabecular vBMD, while shaft loss was accounted for by reductions in cortical bone thickness via endocortical resorption. Later cross-sectional studies have confirmed this picture (Coupaud et al., 2009), with several studies also examining the proximal tibia epiphyses, observing more extensive bone loss in this compartment compared to distal femur epiphyses (Dudley-Javoroski & Shields, 2012; McCarthy et al., 2012). Despite these



general trends, all these studies have shown that there is high inter-subject variability in vBMD variability. (Figure 2.22). Table 2.2 provides a summary of all current cross-sectional pQCT studies that evaluate vBMD and cortical geometry around the knee in adults with SCI.

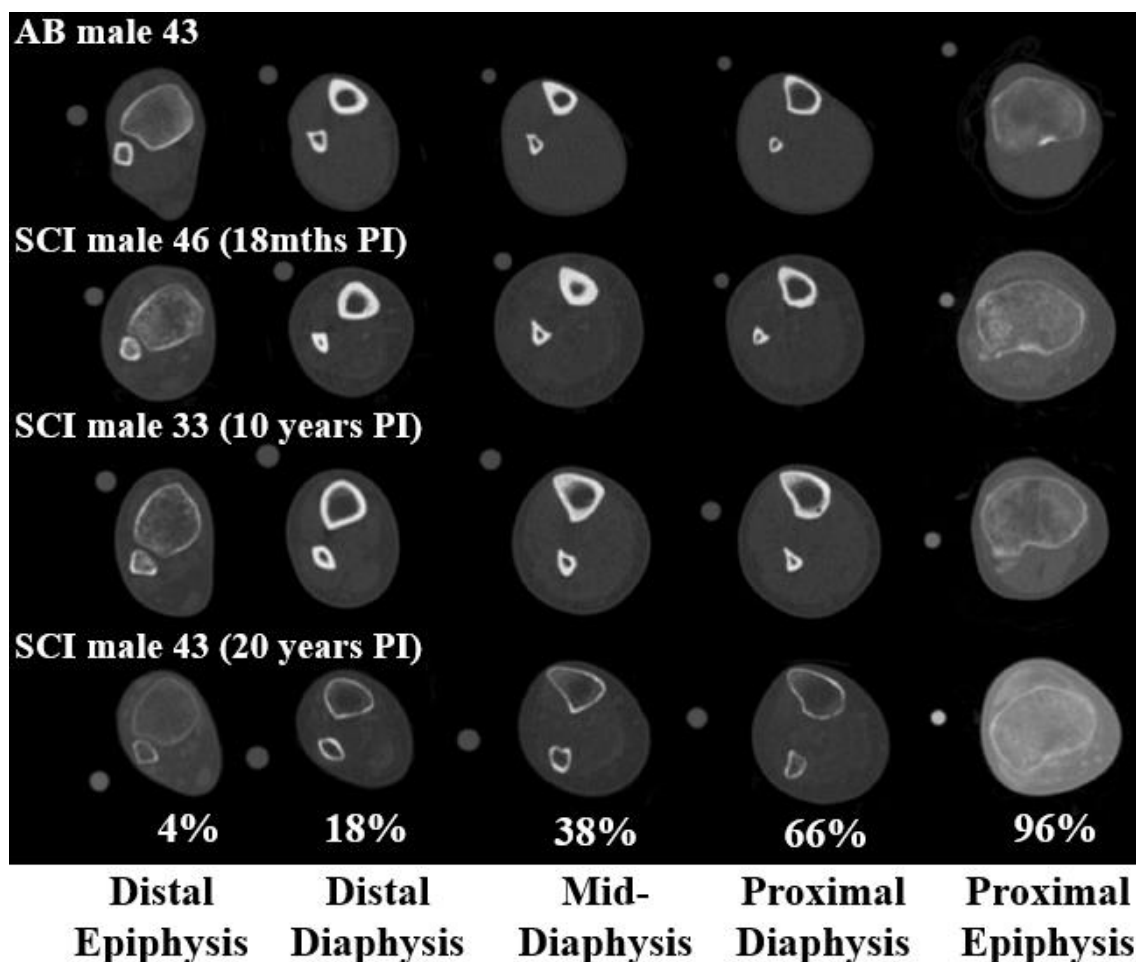


**Figure 2.22.** Example pQCT images at select locations along the length of the tibia, in 1 able-bodied (AB) and 3 SCI male subjects. 43: 43 years old; 46 (18mths PI): 46 years old, 18 months post-injury; 33 (10 years PI): 33 years old, 10 years post-injury; 43 (20 years PI): 43 years old, 20 years post-injury. Adapted from Coupaud et al. (2017).

#### 2.6.5.6 Prospective pQCT Study Findings

The first longitudinal pQCT study in the SCI population was a continuation of the cross-sectional study just described (Eser et al., 2004). Frotzler et al. (2008), followed up with 39 of the chronic SCI patients, making two further pQCT measurements at 15 and 30

months after the initial measurement, again at the femoral distal epiphyses and diaphysis. No significant differences between the three time-points for epiphyseal or diaphyseal parameters were found, thus confirming the stabilisation of BMD and cortical bone geometric properties at reduced bone strength levels in the chronic stages of SCI. A more recent longitudinal study has looked at the acute phase of injury (< 12 months). Coupaud et al. (2015) analysed trabecular bone loss at the distal femur and proximal tibia metaphysis, and cortical bone loss in the femoral and tibial shaft in 26 motor-complete acute SCI patients (Table 2.3). Baseline pQCT measurements were obtained within 5-weeks of SCI, with repeat scans at 4, 8 and 12-months post-baseline. This study is the only one to describe early changes in trabecular and cortical bone post-SCI, in a homogeneous group of motor-complete participants. At the 12-month time-point, 15% and 20% reductions were observed in epiphyseal trabecular vBMD in the femur and tibia respectively, while 3% and 2.5% reductions were observed in diaphyseal vBMD of the femur and tibia, with no detectable differences in cortical thickness. The absolute diaphyseal vBMD losses were comparable with trabecular vBMD losses and occurred at approximately the same rate. This finding is counter to the previously described finding that diaphyseal vBMD loss occurs more slowly, and that cortical thinning via endocortical resorption accounts for the reduction in BMC of the shaft. Further investigations need to be conducted to see if these acute bone loss observations are transient, i.e. by extending the observations in the SCI population to chronic stages. Table 2.3 provides a summary of all current longitudinal pQCT studies that evaluate vBMD and cortical geometry around the knee in adults with SCI.

pQCT has provided answers for several questions regarding the structural changes occurring post-SCI in paralysed limbs, but it has poised more questions, such as: **How is the trabecular architecture affected?** As pQCT resolution is not suitable for quantification of the trabecular microstructure. **Are there site-specific effects?** With

pQCT, VOIs are limited to single slices of thickness approximately 300  $\mu\text{m}$ . **How is the bone material density affected?** To try to answer these questions, higher resolution datasets with more scan coverage are needed. To acquire this data an animal model of SCI is needed.

**Table 2.2.** Summary of cross-sectional pQCT studies evaluating volumetric bone mineral density and geometry of sublesional bones (femur and tibia) in adults with SCI.

<b>Study</b>	<b>Population</b>	<b>Control</b>	<b>Outcome Measures</b>	<b>Region of Interest</b>	<b>Principle Findings</b>
Eser et al. (2004)	89 Males Motor complete 24 tetraplegics 65 paraplegics DOI 2 months – 50 years Age: 42 ± 14	21 Males Able-bodied Age 44 ± 16	vBMD <sub>Tb</sub> vBMD <sub>Ct</sub> Cortical Area CtTh	Femur: 4% (epiphysis) 25% (diaphysis)	All Outcome measures (except vBMD <sub>Ct</sub> ) displayed followed exponential decay equations post-SCI, before reaching new steady states 3–8 years post-SCI. DF vBMD <sub>Tb</sub> ↓ 54% (at steady-state) Diaphysis CtTh ↓ 35% (at steady-state) No significant different in vBMD <sub>Ct</sub> Summary: Epiphyseal bone loss via reduction in vBMD <sub>Tb</sub> , diaphyseal bone loss via endocortical resorption.
Coupaud et al. (2009)	47 (38 Males, 9 Females) ASIA: A-C (All Paraplegic) Age: 37 ± 13	N/A	vBMD <sub>Tb</sub> vBMD <sub>Ct</sub> Cortical Area	Femur: 4% (epiphysis), 25% (diaphysis)	vBMD <sub>Tb</sub> decreased exponentially with time post-SCI. Confirmation of findings by Eser et al. (2004)
Rittweger et al. (2010)	9 Males Age: 39 ± 6 DOI: 32 – 9 years (mean 21.4)	9 Males Age: 39 ± 8	vBMD <sub>Tot</sub> vBMD <sub>Ct</sub>	Tibia: every 5% bone length (5% to 95%)	PT vBMD <sub>Tb</sub> ↓ 47% compared to control.
McCarthy et al. (2012)	9 Males Age: 33 ± 9 DOI: 6.5 ± 2.8 years ASIA: A (Chronic)	14 Males Able-bodied	vBMD <sub>Tb</sub> Cortical Area CSMI	Tibia: 96% (epiphysis),	PT vBMD <sub>Tb</sub> ↓ 62% compared to control. PT cortical area ↓ 56% compared to control

**Table 2.3.** Summary of longitudinal pQCT studies evaluating volumetric bone mineral density and geometry of sublesional bones (femur and tibia) in adults with SCI.

Study	Population	Control	Outcome Measures	Region of Interest	Principle Findings
Frotzler et al. (2008)	39 Males from Eser et al. (2004) Age: $42 \pm 12$ DOI: 0.9 – 32 years	15 & 30 month follow up from baseline	vBMD <sub>Tb</sub> vBMD <sub>Ct</sub> Total Area Cortical Area CtTh	Femur: 4%, 25%,	No significant difference all 3 time-points. Confirmation of stabilisation of: vBMD <sub>Tb</sub> at DF vBMD <sub>Ct</sub> , Total Area, Cortical Area & CtTh at femur diaphysis (at > t <sub>steady-state</sub> )
Dudley-Javoroski & Shields (2012)	12 Males 1 Female DOI < 6 months	21 Males Able-bodied	vBMD <sub>Tb</sub> vBMD <sub>Ct</sub> Cortical Area	Tibia: 86% (metaphysis) Femur: 12% (metaphysis)	vBMD <sub>Tb</sub> ↓ by 15 – 35% (1 – 2 years post-SCI) in DF and PT Steady-state vBMD <sub>Tb</sub> achieved 4 years (at 50% non-SCI value) Continued decline of Cortical area > 4 years post-SCI (no cortical steady-state) Note: insufficient data to effects <1-year post-SCI
Coupaud et al. (2015)	26 (21 Males, 5 Females) 14 tetraplegics 12 paraplegics ASIA: A or B DOI ( $1.0 \pm 0.2$ months) Age: $39 \pm 20$	4, 8, 12 months post-baseline time points	vBMD <sub>Tot</sub> vBMD <sub>Tb</sub> vBMD <sub>Ct</sub> Cortical Area	Femur: 4% (epiphysis), 25% (diaphysis) Tibia: 66% (diaphysis), 96% (epiphysis)	By the end of the first year: vBMD <sub>Tb</sub> ↓ by 20% in PT & 15% in DF vBMD <sub>Ct</sub> ↓ by 2.5% in tibia diaphysis & 3% in femur diaphysis

### 2.6.6 Animal Models of SCI-induced Osteoporosis

Animal models have been used to increase our understanding of the structural effects of SCI on paralysed bones. Most studies have used the rat with tools such as  $\mu$ CT (both *in vivo* and *ex vivo*), histomorphometry and mechanical testing. There are several studies that have used the mouse, but in these bone structure has only been studied through DXA and/or histomorphometry (McManus & Grill, 2011; Picard et al., 2008).

#### 2.6.6.1 The Rat as a Model of SCI-induced Bone Loss

Rat models have been critical for developing our current understanding of osteoporosis, fracture repair and bone diseases, to name but a few (Jee & Yao, 2001). These models are valuable in that they have reliably reproduced given interventions and have a relatively low cost of acquisition, thus are studied in large numbers, compared to other animal models (Lelovas et al., 2008). The rationale for selecting a rat model for studying the deterioration of bone quantity and quality in the sublesional long bones post-SCI is that, compared to the human SCI population, rats have a much faster bone turnover rate, and confounding factors can be controlled for, to achieve low genetic and environmental variability and reproducibility of the SCI. Caution still must be taken when comparing these species for our purposes. The vast majority of patients who present with SCI are adults, where long bones have fused growth plates, thus longitudinal bone growth has ceased (Lee et al., 2013). Rat long bones on the other hand continually grow longitudinally throughout life, their growth plates do not close even at 2.5 years of age (Dawson, 1925). Also, rats lack well-developed Haversian systems, which is the main cause of cortical porosity in humans (Turner, 2001). However, taking the physiological differences into account, rodent models of SCI used in conjunction with high resolution imaging modalities and destructive mechanical tests, can provide extremely useful information regarding bone loss and structural changes post-SCI, that is currently not

possible to acquire with current *in vivo* tests on the SCI population. Figure 2.23 gives a comparison of the detail possible with *ex vivo*  $\mu$ CT in rats and *in vivo* pQCT in humans.

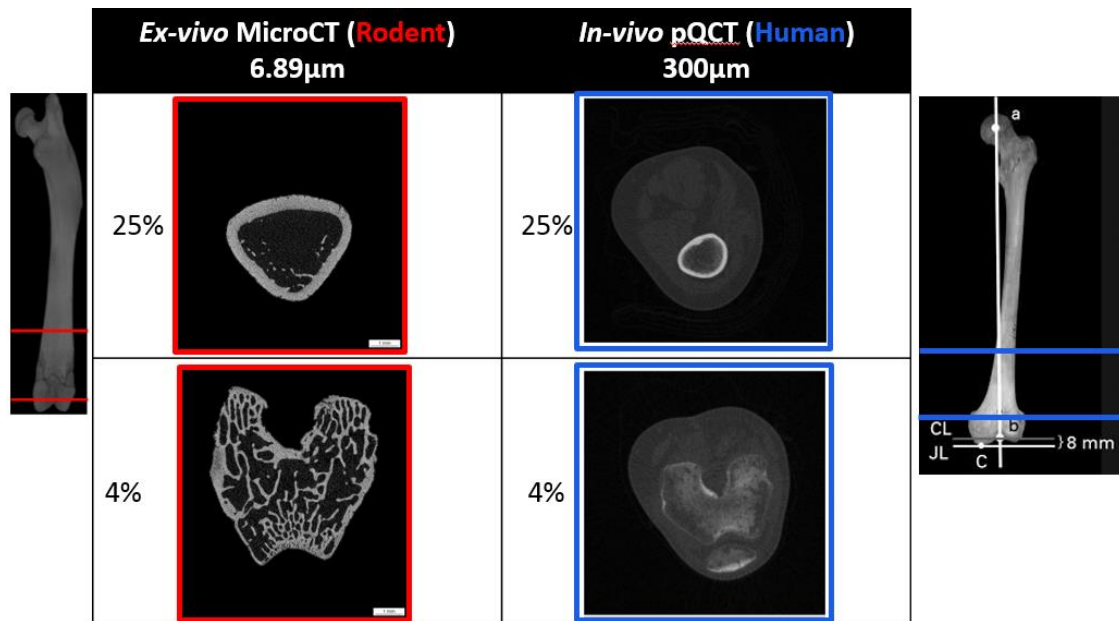


**Figure 2.23.** Comparison between image quality that can be obtained with *ex vivo*  $\mu$ CT in rats and *in vivo* pQCT in humans, at a 4% distal epiphyseal site, and 25% diaphyseal site of the femur.

#### 2.6.6.2 Cross-sectional Rat Study Findings

To date there are a limited number of cross-sectional rat studies that use  $\mu$ CT to assess the effects SCI has on the morphology of cortical and/or trabecular bone in the sublesional paralysed limbs (Table 2.4). Most of these studies look at less than 2-month old, skeletally immature male rats, there are only two studies that look at more mature rats, 4 and 5 months of age. The injury time in most of these studies is less than a month (between 7 days and 28 days), only one study has extended to 16 weeks. Two types of SCI are used i) transection, where the spinal cord is completely severed resulting in a complete and permanent loss of function below the level of injury, and ii) contusion, where the spinal cord is impacted using a controlled weight-drop device, producing an incomplete lesion on the spinal cord, where partial or even complete recovery is possible (Choi, 2005; Lu et al., 2014). The main advantage of contusion injuries is that they closely recreate the

histopathologic appearance of injuries seen in most human SCI cases (Basso et al., 1996), but in rodent models of SCI there are a significant number of spontaneous recoveries (Hooshmand et al., 2014), which are rare in the human SCI population. With transection there is minimal chance of any functional recovery, thus providing more consistency in results but a less realistic model of human SCI.

#### *2.6.6.3 Cortical Bone*

Two cortical bone sites have been assessed with  $\mu$ CT and destructive mechanical tests, the fracture-prone metaphysis of the proximal tibia and distal femur and diaphyseal bone at the mid-shaft of both bones.

##### Metaphyseal Cortical Bone

Jiang et al. (2006) carried out the first study that quantified the effects SCI has on sublesional long bone 3D geometry. They employed DXA and  $\mu$ CT on metaphyseal cortical bone in the proximal tibia of 6-week old male Sprague-Dawley rats with motor complete T11 transection SCIs. DOI was 21 days and age-matched control rats were used for comparison. The BMD of the trabecular-rich proximal tibia was significantly decreased compared to control ( $p < 0.001$ ), no trabecular morphometric parameters were acquired, but proximal metaphyseal cortical bone thickness was 41% lower, characterised by a 24% lower total area (Jiang et al., 2006). Decrease in proximal tibia metaphyseal BMD was confirmed by Morse et al. (2008) in 7-week old male Sprague-Dawley rats with T10 contusion SCI, who observed a rapid 34% lowering at 10 days post-SCI. Their study was more comprehensive because both periosteal and endosteal geometric parameters were measured, but different geometric outcomes were observed. The metaphyseal cortical bone thickness was 31% lower, characterised by a 6% and 25% raising of the total and marrow area respectively. A third study on metaphyseal cortical



bone was conducted by Yarrow et al. (2014) this time on the femur in 4-month old contusion injured rats, with a of DOI 3 weeks. An average 12% lowering of cortical thickness was observed, characterised by non-significant reductions to both the total and marrow areas (Figure 2.24). No definitive picture is currently available for changes that occur in metaphyseal cortical bone post-SCI, the variation in reported results may be due to confounding variables that exist between studies, such as VOI selection, age, strain and sex of rat, type of SCI and DOI.

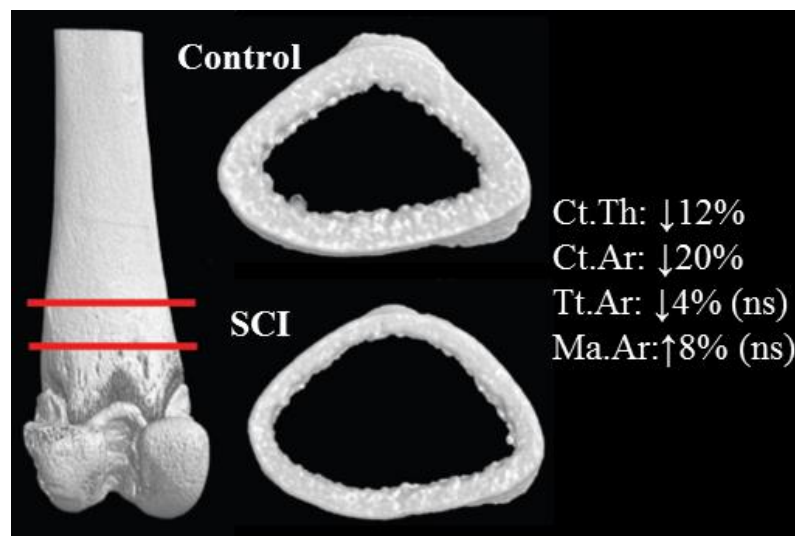


**Figure 2.24.** Representative distal femur metaphyseal cortical bone VOIs for a contusion-SCI and age-matched control rat, highlighting the effects of the SCI on cortical bone spatial distribution. Red lines indicate the start and end of the VOI. Adapted from Yarrow et al. (2014).

### Diaphyseal Cortical Bone

The second commonly assessed cortical bone site in rat  $\mu$ CT studies of SCI is the mid-diaphysis, it contains no trabecular bone, so is favourable since no segmentation is required, but it is a less clinically relevant site, since fracture is less common here (Frotzler et al., 2015). Jiang et al. (2007) were the first to study this site in 3D with  $\mu$ CT, but with female rats. Liu et al. (2008) characterised the aBMD, vBMD and geometry of the tibia midshaft in 6-week old male Sprague-Dawley rats, with motor complete T11

transection SCI, DOI 28 days (Liu et al., 2008). aBMD and cortical vBMD were significantly lower compared to age-matched controls ( $p < 0.05$ ), with 36% and 27% lowering of cortical area and thickness respectively, characterised by a 24% reduction in marrow area (no periosteal parameters) (Liu et al., 2008). The midshaft was also subjected to three-point bend testing, the BMD and geometric changes contributed to significant reduction in the ultimate load and work-to-fracture ( $p < 0.05$ ). Similar geometric changes were observed in more skeletally mature (4-month old) rats with T13 contusions SCIs, with an extended DOI of 16 weeks. Here a 16% reduction in cortical thickness was observed ( $p < 0.04$ ), characterised by a 14% reduction in periosteal perimeter ( $p < 0.001$ ) and an 8% reduction in endocortical perimeter ( $p < 0.001$ ). These shifts in spatial distribution of bone in the mid-shaft resulted in a lower polar moment of area ( $p < 0.001$ ), thus a decreased resistance to deformation, compared to age-matched control. The cortical bone results generally contrast with the disuse-pattern osteopenia expected in the adult SCI population (Figure 2.13).

#### *2.6.6.4 Trabecular Bone*

In human SCI patients the trabecular-rich proximal tibia and distal femur are the most fracture-prone regions of the sublesional long bones (Frotzler et al., 2015). The structural, material and mechanical changes to the trabecular bone within these regions has been considered in many rat SCI studies. There are two trabecular bone sites that have been assessed with  $\mu$ CT; these are metaphyseal trabecular bone in the proximal tibia and distal femur, and epiphyseal trabecular bone in the distal femur.

## Metaphyseal Trabecular Bone

The first study to quantify the effects of trabecular bone changes post-SCI in male rats was conducted on 7-week old growing Sprague-Dawley rats with T10 contusion SCIs, DOI 10 days. In this acute time-frame significant deterioration was evident in the trabecular bone. The bone loss was quantified by a significant 62% reduction in trabecular bone volume fraction in the distal femur metaphysis. This loss of trabecular bone was characterised by statistically significant 24%, 25% and 83% decreases in trabecular number, thickness and connectivity density respectively, with a 35% increase in average trabecular separation, compared to control (Morse et al., 2008). This picture of rapid and severe trabecular deterioration in the early (acute) phase of SCI has subsequently been confirmed for the distal femur (Liu et al., 2008; Yarrow et al., 2014; Beggs et al., 2015), and also verified in the proximal tibia (Figure 2.25).

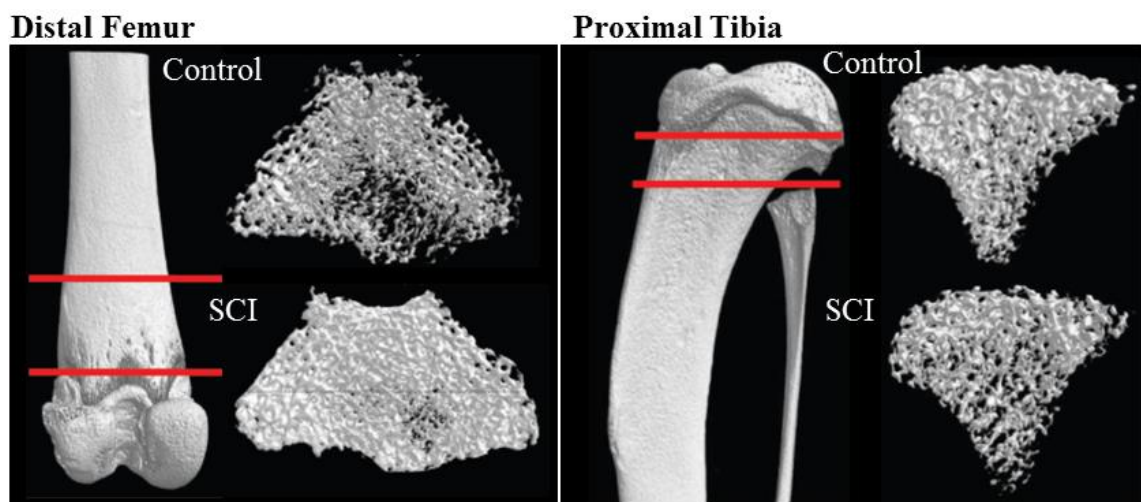


**Figure 2.25.** Representative distal femur and proximal tibia metaphyseal trabecular bone VOIs for a contusion-SCI and age-matched control rat, highlighting the effects of the SCI on trabecular bone microarchitecture. Red lines indicate the start and end of the VOI. Adapted from Yarrow et al. (2014).

Only one cross-sectional rat  $\mu$ CT study has looked at what would be considered the chronic stage of injury (DOI 4 months), in this study a significant 56% lowering of trabecular bone volume fraction in the distal femur metaphysis, characterised by

significant 34% and 30% reduction in trabecular number and thickness, with a 70% increase in average trabecular separation (Lin et al., 2015). No conclusions can be drawn as to whether a steady-state of bone loss was reached due to measurements being made at only one time point. The significant deterioration of trabecular bone of sublesional limbs observed in these aforementioned rat studies is in line with the disuse-pattern osteopenia observed in the adult SCI population.

#### Epiphyseal Trabecular Bone

Only one paper also looked at epiphyseal (or subchondral) trabecular bone (Lin et al., 2015). Much less deterioration of epiphyseal trabecular bone microarchitecture was observed, compared to the metaphyseal trabecular bone (Figure 2.26). This was the first evidence that trabecular bone loss induced by SCI is site-specific within a bone.

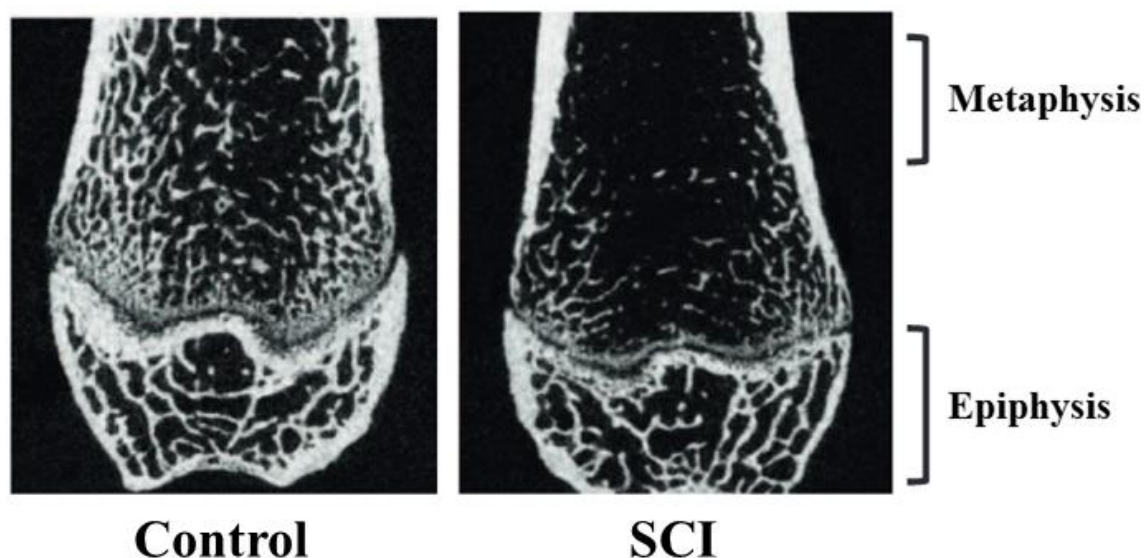


**Figure 2.26.** Representative  $\mu$ CT image sagittal slices, highlight the site-specific effects SCI in metaphyseal and epiphyseal VOIs. Adapted from Lin et al. (2015).

#### 2.6.6.5 Time-course Rat Study Findings

To date there are only two rat  $\mu$ CT studies that have described the time course changes in the bone structure of sublesional paralysed limbs post-SCI. Both studies looked at the

time course changes in the trabecular microstructure of the proximal tibia metaphysis, at acute periods post-SCI, in young growing male rats. In the first study, 8-week old male Wistar rats underwent low thoracic transection SCI (n = 16) and sham-operated controls (n = 14). Trabecular microarchitecture was assessed over a 5-week period post-injury, with rats being sacrificed at 1, 3 and 5 weeks. At one-week post-injury there was a significant decrease in all trabecular morphometric parameters ( $p < 0.05$ ) in SCI the group compared to control group. These differences were maintained at 3 and 5 weeks with only the thickness of remaining trabecular increasing to control levels at 5 weeks post-SCI.

Current rat  $\mu$ CT studies of SCI-induced osteoporosis have investigated several questions regarding the structural changes occurring post-SCI in paralysed limbs, such as how the microstructure (bone quality) of trabecular and cortical bone been affected in singular VOIs at several different time points post-SCI. The study presented in this thesis is the first  $\mu$ CT rat study of SCI-induced osteoporosis that investigates the time-course and site-specific changes to the structural, mechanical and material-level properties of bone.

**Table 2.4.** Summary of cross-sectional  $\mu$ CT studies that evaluate morphometric changes in trabecular and/or cortical bone in rats with SCI.

<b>Study</b>	<b>Population</b>	<b>Region of Interest</b>	<b>Principle Findings</b>
Jiang et al. (2006)	10 Male Sprague-Dawley Age: 6 Weeks (adolescent) SCI: T10-T12 transection DOI: 3 weeks (acute) Control: 10 age-matched	Cortical: PT Metaphysis Trabecular: N/A	PT Metaphysis $\downarrow$ 35% Ct.Th, characterised by $\downarrow$ 24% Tt.Ar. $\downarrow$ DXA-BMD ( $p < 0.001$ )
Jiang, et al. (2007)	10 Female Sprague-Dawley Age: 6 Weeks (adolescent) SCI: T10-T12 transection DOI: 3 weeks (acute) Control: 10 age-matched	Cortical: Tibia Mid-Shaft Trabecular: PT Metaphysis	Tibia Mid-Shaft $\downarrow$ 32% Ct.Th & $\downarrow$ 72% J, characterised by $\downarrow$ 40% in both Ps.Pm & Ec.Pm PT Metaphyseal Trabecular Bone $\downarrow$ 73% BV/TV, characterised by $\downarrow$ 52%, $\downarrow$ 65% & $\downarrow$ 50% in Tb.Th, Tb.N & Conn.D, & $\uparrow$ 82% Tb.Sp.
L. Morse et al. (2008)	5 Male Sprague-Dawley Age: 7 Weeks (adolescent) SCI: T10 contusion DOI: 10 days (acute) Control: 5 age-matched	Cortical: Femur Mid-shaft Trabecular: DF Metaphysis	Femur Mid-Shaft $\downarrow$ 31% Ct.Th, characterised by $\uparrow$ 24% & $\uparrow$ 6% in Ma.Ar & Tt.Ar. DF Metaphyseal Trabecular Bone $\downarrow$ 62% BV/TV, characterised by $\downarrow$ 25%, $\downarrow$ 24% & $\downarrow$ 83% in Tb.Th, Tb.N & Conn.D, & $\uparrow$ 35% Tb.Sp.
Liu et al. (2008)	10 Male Sprague-Dawley Age: 6 Weeks (adolescent) SCI: T10-T12 transection DOI: 4 Weeks (acute) Control: 10 age-matched	Cortical: Tibia Mid-Shaft Trabecular: PT Metaphysis	Tibia Mid-Shaft $\downarrow$ 27% Ct.Th, characterised by $\downarrow$ 24% Ma.Ar. PT Metaphyseal Trabecular Bone $\downarrow$ 57% BV/TV, characterised by $\downarrow$ 33%, $\downarrow$ 65% & $\downarrow$ 58% in Tb.Th, Tb.N & Conn.D, & $\uparrow$ 73% Tb.Sp.

Yarrow et al. (2014)	8 Female Sprague-Dawley Age: 16 Weeks (skeletally mature) SCI: T8 contusion DOI: 3 Weeks (acute) Control: 16age-matched	Cortical: DF Metaphysis Trabecular: PT & DF Metaphysis	DF Metaphysis ↓12% Ct.Th, characterised by ↑8% Ma.Ar & ↓4% Tt.Ar (ns) PT Trabecular Bone ↓38% BV/TV, characterised by ↓18%, ↓30% in Tb.Th, Tb.N & ↑16% in Tb.Sp. DF Trabecular Bone ↓40% BV/TV, characterised by ↓27%, ↓23% in Tb.Th, Tb.N & ↑27% in Tb.Sp.
Beggs et al. (2015)	n ≥ 11 Male Sprague-Dawley Age: 5 months (skeletally mature) SCI: T8 contusion DOI: 3 Weeks (acute) Control: n ≥ 11 age-matched	Cortical: N/A Trabecular: PT & DF metaphysis	PT Trabecular Bone ↓48% BV/TV, characterised by ↓ 7%, ↓ 36% in Tb.Th, Tb.N & ↑ 20% (ns) in Tb.Sp. DF Trabecular Bone ↓37% BV/TV, characterised by ↓ 5% (ns), ↓ 27% in Tb.Th, Tb.N & ↑7% (ns) in Tb.Sp.
Lin et al. (2015)	10 Male Fischer 344 Age: 16 Weeks (skeletally mature) SCI: T13 contusion DOI: 16 Weeks (chronic) Control: 10 age-matched	Cortical: Femur Mid-Shaft Trabecular: DF Metaphysis and Epiphysis	Femur Mid-Shaft ↓16% Ct.Th, characterised by ↓14% & ↓8% in Ps.Pm & Ec.Pm DF Metaphysis Trabecular Bone ↓65% BV/TV, characterised by ↓26%, ↓36% in Tb.Th, Tb.N & ↑ 73% in Tb.Sp. DF Epiphysis Trabecular Bone ↓19% BV/TV, characterised by ↓13%, ↓6% in Tb.Th, Tb.N & ↑7% in Tb.Sp.

SCI: Spinal Cord Injury; T: Thoracic; DOI: Duration of Injury; DXA-BMD: Areal Bone Mineral Density; Ct.Th: Cortical Thickness; Tt.Ar: Total Area; Ma.Ar: Marrow Area; Ec.Pm: Endocortical Perimeter; Ps.Pm: Periosteal Perimeter; J: Polar Moment of Area; BV/TV: Trabecular Bone Volume Fraction; Tb: Trabecular; Th: Thickness; N: Number; Sp: Separation; Conn.D: Connectivity Density; ns: Not Significant; PT: Proximal Tibia; DF: Distal Femur.

## Chapter 3 Materials and Methods

This chapter introduces the animal model of SCI and experimental design, the imaging modality used to assess bone loss ( $\mu$ CT) and the mechanical tests performed to assess the structural and material properties of the femur. The chapter begins with an overview of the animal model, post-operative care and bone sample preparation. Followed by a detailed overview of the  $\mu$ CT image analysis pipeline. Two types of morphometric are described in-depth (direct-3D and 2D (slice-by-slice) approaches). The protocols for mechanical characterisation of the femur are given, finally the statistical techniques used are described.

### 3.1 Animal Model

Femurs were obtained from rats prepared for an ongoing study of the effects of SCI on the cardiovascular system, to be reported elsewhere (Dr John Riddell, University of Glasgow, UK). The SCI model used was a complete transection of the spinal cord at a low thoracic level (T9). The advantage of this model for studies of disuse osteoporosis is that it results in a complete and permanent paralysis of the hind limbs and thus avoids the complication of functional recovery seen in incomplete SCI models. 64 male Wistar rats were acquired from Harlan Laboratories, Loughborough, UK and left to acclimatise for 2 weeks before surgery. The rats were 200–250 g in weight (approximately 10–12 weeks old), equivalent to human adolescence (Sengupta, 2011). Rats were housed in pairs under a 12-hour light/dark cycle with *ad libitum* access to food and water. All experimental procedures were approved by the Ethical Review Panel of the University of Glasgow and carried out in accordance with the Animals (Scientific Procedures) Act 1986. Rats belonged to eight different ( $n = 8$ ) experimental groups (Table 3.1). Four groups sustained the SCI transection and were sacrificed at 2, 6, 10 and 16-weeks post-SCI. Each SCI group had an age-matched sham-operated control group.



Table 3.1. Experimental design. (n = 8) animals for all groups.

Group	Day 0	Week 2	Week 6	Week 10	Week 16
Control – 2	▲	×			
SCI – 2	▼	×			
Control – 6	▲		×		
SCI – 6	▼		×		
Control – 10	▲			×	
SCI – 10	▼			×	
Control – 16	▲				×
SCI – 16	▼				×

▲ Sham surgery, ▼ T9-transection SCI, × Animals are sacrificed.

### 3.1.1 Surgery and Post-operative Care

For both types of surgical preparation (SCI and Sham), rats were anaesthetised with isoflurane and laminectomy was performed to expose the spinal cord at the T9 segmental level (Figure 3.1). Spinal cord transections were performed by a method similar to that described by Lu et al. (2014). A small opening was made in the dura and the spinal cord cut transversely, at two locations, separated by approximately 1mm, using iridectomy scissors (FST, No. 15002-08). A blunt 23G needle, connected to an aspirator, was used to remove a small amount of spinal cord tissue and any accumulating fluid. The completeness of the transection was confirmed visually by observing complete separation of the proximal and distal stumps through an operating microscope. The wound was closed, and rats allowed to recover in warmed cabinets (28°C) for up to 3 days, until thermoregulation was restored. Rats received analgesia (buprenorphine, 0.05 mg/kg and carprofen, 5 mg/kg subcutaneously at induction of anaesthesia and the morning after surgery). Saline (3–5 ml) and enrofloxacin (5 mg/kg) were given subcutaneously for 3 and 7 days after injury, respectively. Bladders were manually expressed as necessary three times daily until reflexive emptying returned (typically 12–14 days after SCI). Rats were humanely killed by anaesthetic overdose (Euthatal, Merial Animal Health Ltd,

Harlow, UK) at 2, 6, 10 or 16 weeks after surgery depending on group. These age ranges are equivalent to human adolescence to early adulthood (Sengupta, 2011).

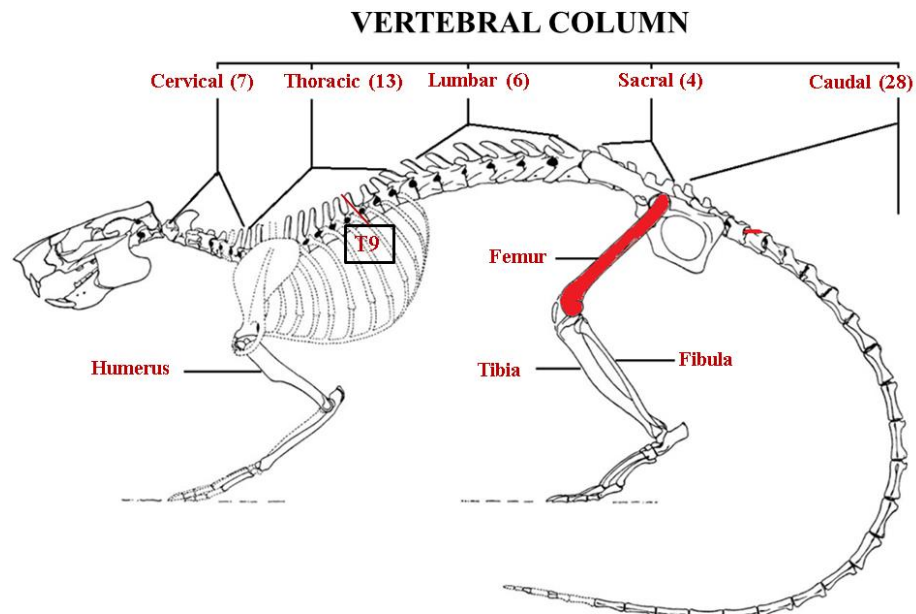


FIG. 8. *Paramys delicatus*, restoration of the skeleton, based largely on A.M.N.H. No. 12506, approximately  $\times 0.36$ .

**Figure 3.1.** Schematic of a rat skeleton, highlighting the location of transection SCI (thoracic level T9), and the femur, the bone of interest for this thesis.

### 3.1.2 Preparation of Bones

After sacrifice, femurs were dissected, and soft tissue (muscle, cartilage and ligament) removed. Wet weight and femoral length (measured parallel to the femoral shaft, between the femoral head and femoral condyle using digital callipers) were obtained. Femurs were then wrapped in phosphate buffered saline (PBS)-soaked gauze and placed individually in low X-ray attenuating plastic Bijou tubes. Bones were then stored at  $-20^{\circ}\text{C}$  to preserve microstructure and mechanical properties (Pelker et al., 1984) for subsequent analysis (*ex vivo*  $\mu\text{CT}$  and mechanical testing).

### 3.2 *Micro-Computed Tomography*

The *ex vivo*  $\mu$ CT analysis performed here can be divided into six main processes:

- i) Image Acquisition
- ii) Reconstruction
- iii) Co-registration
- iv) Segmentation
- v) VOI Selection
- vi) Morphometric and Densiometric Analysis

#### 3.2.1 *Image Acquisition*

Prior to  $\mu$ CT scanning the whole femurs were thawed to room temperature.  $\mu$ CT scanning is non-destructive, but there is potential for the bones to dry out during scanning, therefore femurs were left wrapped in PBS-soaked gauze (Figure 3.2). It is a requirement that there is no movement of the bone sample, and that it sits as close as possible to the scanner's isocentre during scanning (to avoid unnecessary imaging artefacts). Femurs were therefore scanned in Bijou tubes, securely attached to a sturdy platform, rigidly fitted to the stage, at the scanner's isocentre (Figure 3.2).

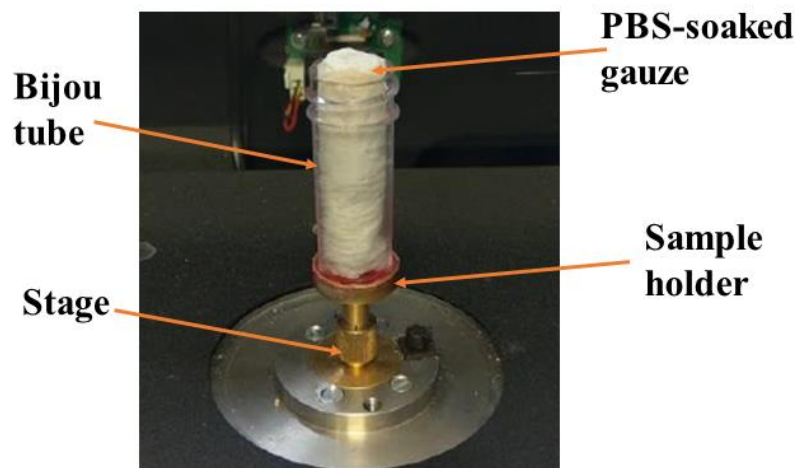


**Figure 3.2.** Set-up for *ex vivo*  $\mu$ CT scanning of the rat femur, wrapped in PBS-soaked gauze, attached to the sample holder with Bijou tube and fitted to the stage at the isocentre.

The most distal 60% bone length (from the proximal end) of the distal femur was scanned with a Bruker SkyScan 1172  $\mu$ CT scanner (Kontich, Belgium), proceeding from the medial and lateral condyles past the epiphysis and growth plate into the metaphysis and cortical shaft (Figure 3.3). All scans used the following optimised settings: 70 kVp X-ray tube voltage, 100  $\mu$ A X-ray tube current, 470 ms exposure time, 6.89  $\mu$ m isotropic voxel size with 2 k camera resolution, 0.4° rotation step for a total of 180°, frame averaging of 2 and a 0.5 mm aluminium filter in place to reduce beam hardening artefacts.

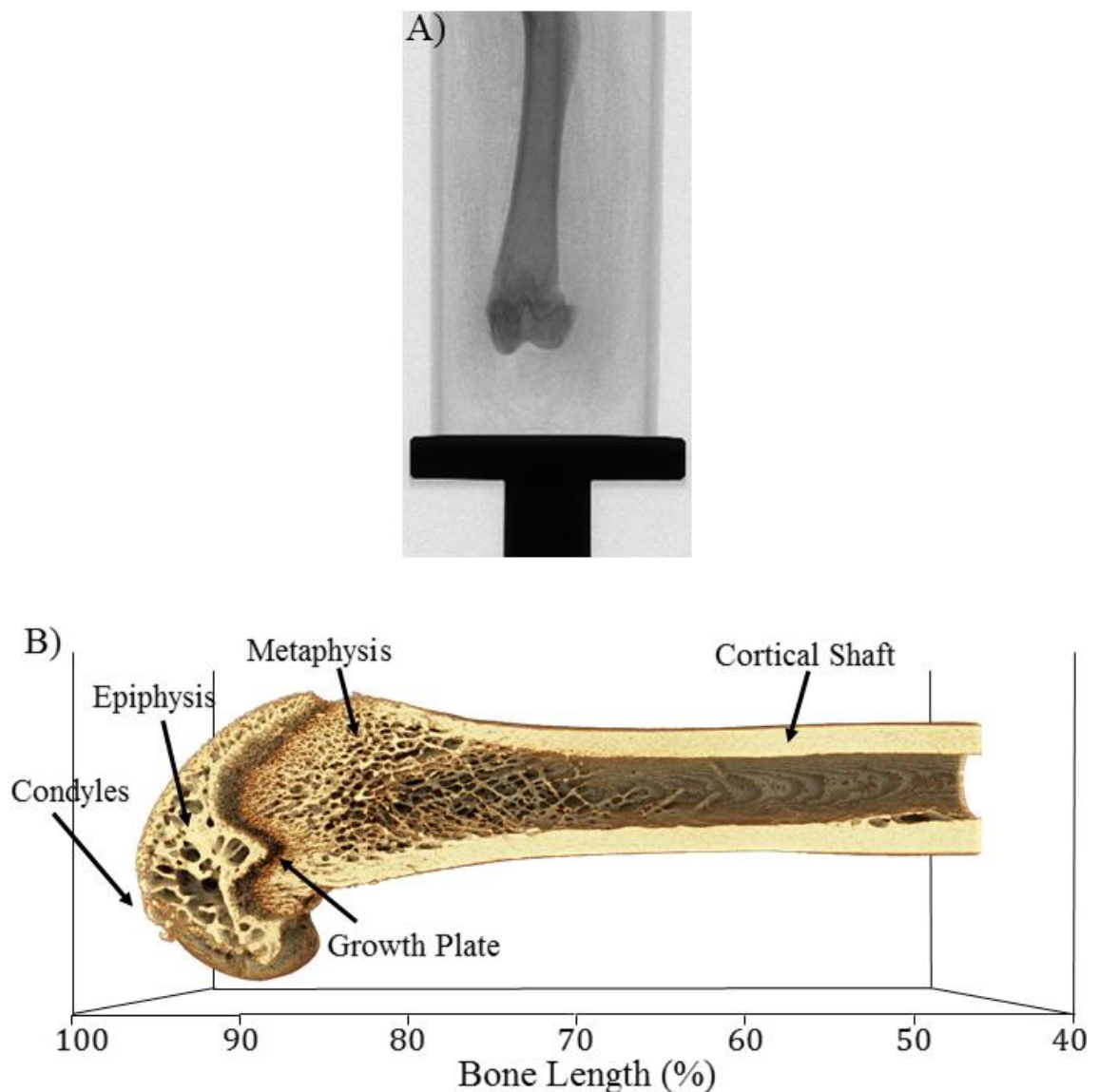


**Figure 3.3.** Scanned VOI (most distal 60% bone length). A) Representative projection image of distal femur. B) Labelled representative reconstructed distal femur.

### *3.2.2 Reconstruction*

Reconstruction of the raw projection images into 8-bit grey level cross-sectional images was performed using the Feldkamp-Davis-Kress (FDK) filtered back projection-convolution reconstruction algorithm modified for cone-beam using a Hamming window-filter, in SkyScan NRecon software (Version 1.6.9.18, Kontich, Belgium) (Feldkamp et al., 1984). Ideally, with large photon numbers, monochromatic X-rays, perfect detectors, zero motion, no Compton scattering or pair-production, this algorithm would reconstruct a femur that perfectly reflects reality. This is not the case here, as when any of these conditions are not met, image artefacts are introduced, which lower the fidelity of images and their subsequent analysis. Techniques used for image artefact reduction were all implemented in NRecon software and are described below.

#### *3.2.2.1 Beam Hardening*

The X-ray beam produced by the micro-focus X-ray tube is polychromatic, i.e. it covers a broad spectrum of energies. A polychromatic X-ray beam is more easily attenuated in its first interactions with the sample, since materials absorb lower energy X-rays more easily than higher energy X-rays. The average photon energy of the beam therefore increases as it traverses through the sample, i.e. the beam “hardens”, thus later interactions with the sample are less easily attenuated. However, the FDK algorithm assumes that there is equal attenuation along the X-ray path throughout the sample. This hardening leads to a non-linear relationship between grey level values and sample thickness in projection images. The reconstructed image then contains cupping and streak artefacts which respectively appear as falsely bright (high grey level) values around the periphery of the sample, and dark streaks between dense parts of the sample (Figure 3.4A).

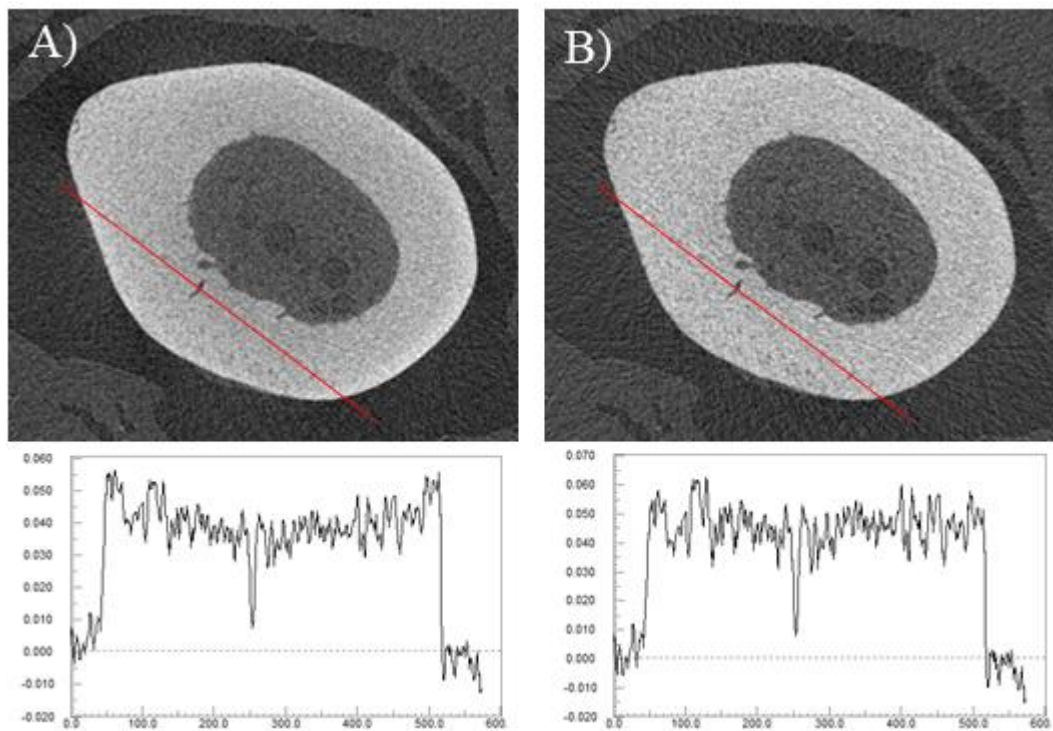


**Figure 3.4.** Beam hardening. A) With no software correction applied, beam hardening makes the bone appear artificially denser at the outer surfaces. The red line depicts the region over which an X-ray attenuation profile line is taken. In this profile cupping artefacts can be seen at the outer surfaces, observed as artificially elevated density peaks. B) 40% beam hardening correction applied, gives a flatter profile and more uniform apparent mineral density through the cortical bone.

Two methods are used to reduce the effect of beam hardening, hardware and software approaches. The hardware approach is to pre-filter the beam by placing a 0.5 mm aluminium foil between the X-ray source and sample, this pre-hardens the X-ray spectrum minimising the amount of low energy X-rays, producing a harder and more monochromatic beam. Remaining beam hardening effects were compensated for by a software correction using the NRecon beam hardening correction, which applies a variable 2nd order polynomial transformation to the attenuation, with the aim of restoring linearity (Herman, 1979). The value of this variable was set to 40% for all datasets. This value defines the percent weighting of the quadratic term (Salmon & Liu, 2014) (Figure

3.4B). This type of correction is only possible because we assume that bone has approximately uniform absorption.

### 3.2.2.2 Ring Artefacts

Imperfections in, failure or mis-calibration of one or more charged coupled device (CCD) detector elements, or small particles in the beam path can result in continual under- or over-estimation of grey level pixel values in projection images. The incremental rotation results in reconstructed images containing concentric-ring artefacts (Figure 3.5A). Two methods are used to reduce ring artefacts. Before scanning, dark and flat-field corrections were performed without samples present at the aforementioned scan parameters, this obtained a background image which is subtracted to minimise ring artefacts. Remaining ring artefacts were suppressed using the NRecon Fourier transform-based ring artefact correction set to 13 (Wolkowski et al., 2015) (Figure 3.5B). This artefact correction number refers to the kernel size of the operation.

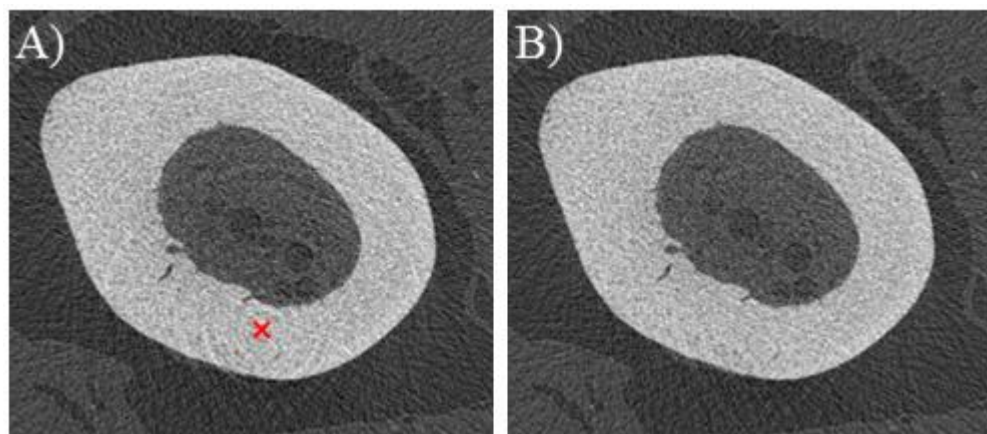


**Figure 3.5.** Ring artefacts. A) No software-based ring artefact reduction applied. Concentric rings are seen spanning out from the scanner's isocentre, indicated by a red  $\times$ . B) ring artefacts reduced with software correction.



### 3.2.2.3 Mis-alignment

It is extremely difficult to align the centre of rotation of the bone specimen with that of the scanner's isocentre. Thus, projection images need this misalignment corrected before reconstruction, to avoid introducing streaking artefacts. (Figure 3.6A). The mis-alignment correction was estimated by aligning the overall attenuation profiles of the first ( $0^\circ$ ) and last ( $180^\circ$ ) projection images as closely as possible (Figure 3.6B).

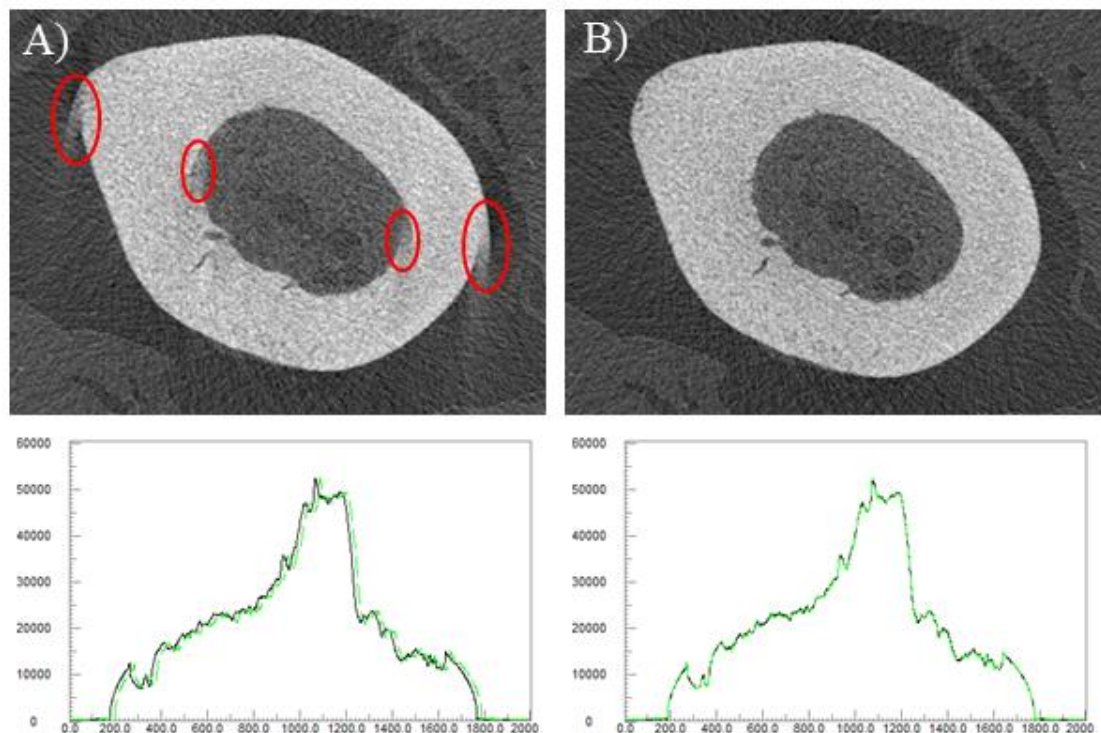


**Figure 3.6.** Mis-alignment. A) No misalignment correction applied, as seen by the non-overlapping attenuation profiles, indicated by the red circles. B) correction of misalignment with overlap of attenuation profiles. The black and green distributions represent the attenuation profiles of the first ( $0^\circ$ ) and last ( $180^\circ$ ) projection images respectively.

### 3.2.2.4 Mottle

Mottle is a result of the stochastic nature of the interaction of X-ray photons with the discrete detector elements of the scanner (Barnes, 1982). On zoomed in images it gives a mottled appearance (Figure 3.7A). It can be reduced by increasing the image signal



strength (increasing frame averaging, reducing rotation step size). These are very time-consuming processes, so post-scan mottling was suppressed by application a smoothing operation, directly to the projection images. However, too much smoothing blurs fine detail (Figure 3.7C).

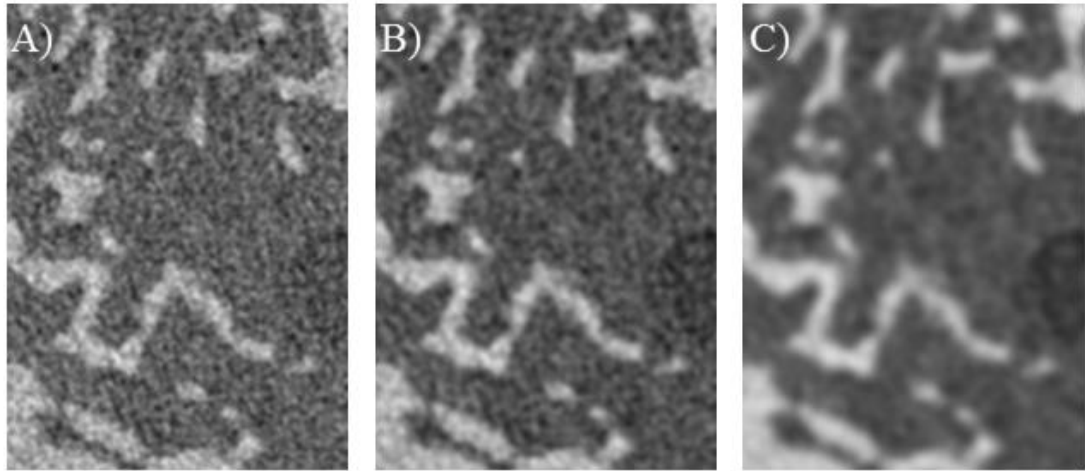


**Figure 3.7.** Magnified part of reconstructed  $\mu$ CT image. A) un-smoothed image, mottle is evident. B) same image with Gaussian smoothing kernel of standard deviation (SD) of 0.75 applied, mottle is less evident. C) same image with Gaussian smoothing kernel of SD of 2.75 applied, too much smoothing resulting in loss of detail (image blur).

#### 3.2.2.5 Contrast Limits

The same attenuation coefficient range was used for all sample datasets. The lower limit was set to zero and the upper limit was set to just above the high density tail. This range was defined after assessing many different datasets, to ensure no saturation. The optimised threshold range used was 0 to 0.081884.

#### 3.2.2.6 Oversize Scan

The scan parameters used meant that bone samples were too long for the scanner's axial field of view. To image the most distal 60% of the distal femur an oversize scan was performed, consisting of 3 sub-scans. Between sub-scans the sample stage was moved

upwards to fit the new VOI into the field of view. To ensure matching between sub-scans, z and x-y shift and rotation corrections were applied and overlapping regions between the sub-scans were averaged.

### 3.2.2.7 Summary of Reconstruction Parameters

Only mis-alignment correction differed for each scan (and sub-scans). All other reconstruction parameters depend on the  $\mu$ CT instrumentation; they were standardised for all bones within the study. Table 3.2 summarises the values used.

Table 3.2. Optimised parameters used to reconstruct projection images in NRecon (Version 1.6.9.18).

<b>Reconstruction Parameter</b>	<b>NRecon Value</b>
Beam Hardening Correction	40%
Ring Artefact Reduction	13
Mis-alignment Correction	Scan specific
Smoothing	Gaussian kernel, SD = 0.75
Minimum Threshold	0
Maximum Threshold	0.081884

### 3.2.3 Image Co-registration

Co-registration was used to ensure that the distal femur datasets were spatially aligned. It was required because femurs are not perfect cylinders, thus when  $\mu$ CT scanned they do not sit perfectly within the scanner's isocentre. This results in the raw reconstructed datasets having different coordinate systems. The image co-registration implemented here is defined as the use of affine transformations (translations and rotations, no scaling) to standardise the alignment of all distal femurs as best as possible to a reference distal femur. The co-registration procedure performed on all reconstructed greyscale  $\mu$ CT datasets of the rat distal femur consisted of 4 steps and was carried out in Dataviewer (Version 1.5.1.9, Kontich, Belgium).

### *Step 1: Definition of Reference Dataset*

A representative  $\mu$ CT dataset was selected from both control and SCI groups at each time-point. These 8 reference datasets were manually aligned to achieve a vertical femoral shaft centreline (Figure 3.8B). All remaining  $\mu$ CT scans in each group ( $n = 7$ ) were rigidly registered i.e. transformed into the coordinate system of the reference dataset.

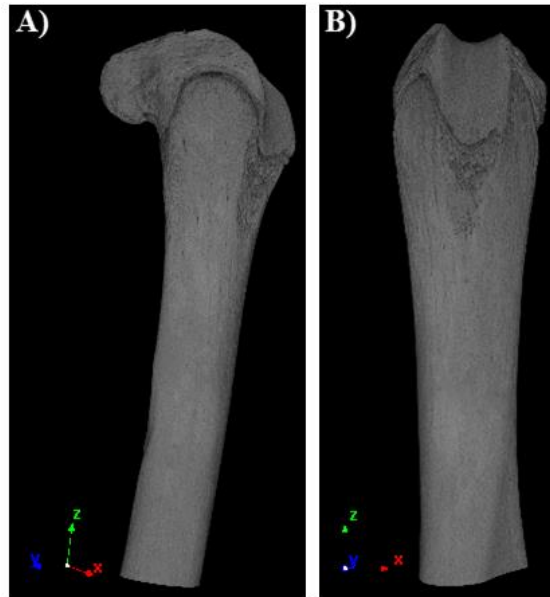


**Figure 3.8.** Manual alignment of a representative reference distal femur. A) unaligned distal femur. B) Manually aligned so that the femoral shaft is orientated parallel to the image z-axis (in green).

### *Step 2: Acquire Global Shape*

Large changes in the morphology of the internal (trabecular) architecture can occur not just between treatment and control groups, but also within groups. These differences can obstruct the ability to co-register the bones. The global shape of the femur is much better preserved within groups, so co-registration was applied to the overall bone shape (without internal structure). This global shape was acquired by applying a global threshold at 35% of the maximum grey value to the reconstructed greyscale dataset, followed by a flood-fill operation that limited the region of interest (ROI) to the bone's endocortical perimeter. This resulted in a binarised femur, without any internal architecture (Figure 3.9).



**Figure 3.9.** Schematic in 2D showing the image processing steps needed to acquire the overall shape of the femur.

*Step 3: Co-registration of Global Shape.*

Once all reference and target binarised global shape datasets were acquired, all target datasets ( $n = 7$  for each group) could be transformed into the coordinate system of the reference dataset. To speed up the registration process, initially the target dataset was manually translated and/or rotated close to that of the reference's orientation. Automatic matching then could take over. The matching between datasets was carried out over a small VOI that contains structures, within the datasets. The VOI chosen here was the femoral condyles, due to its characteristic shape. 3D registration was decomposed in to separate 2D tasks, matching (two translations and one rotation) was done iteratively on each of the orthogonal views (Figure 3.10), once the difference between the two datasets becomes small in each view the matching stopped. The resulting rigid transformation matrix was then applied to the binarised reference dataset (Figure 3.10).

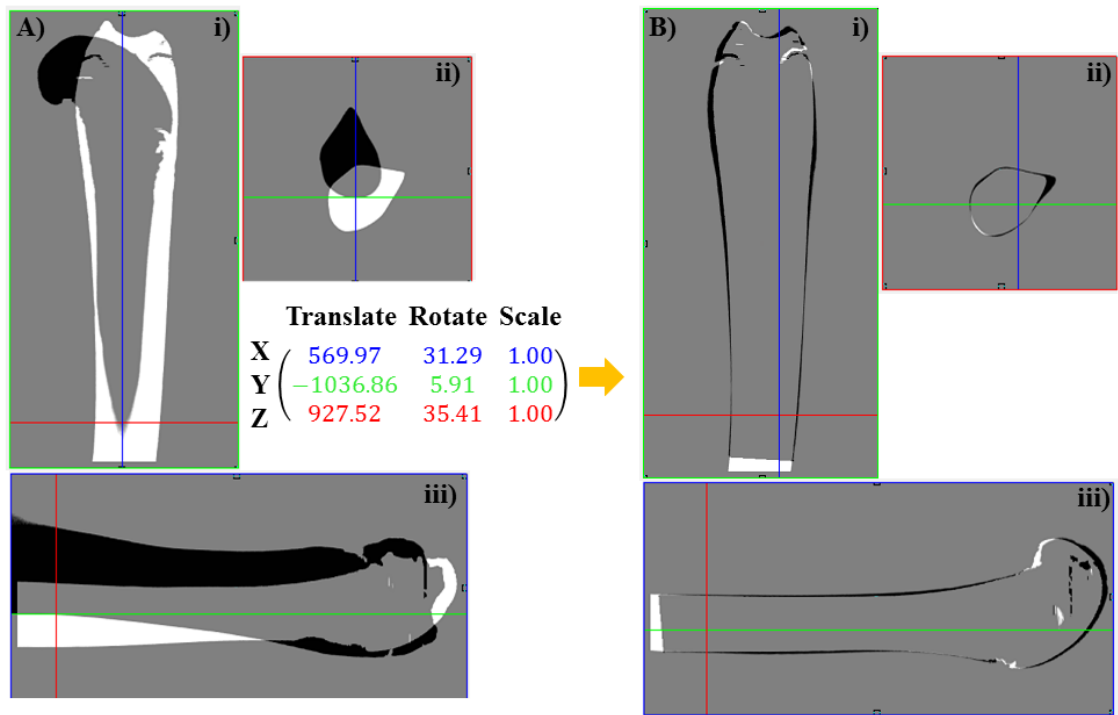


**Figure 3.10.** Overview of co-registration, shown in i) coronal (X-Z), ii) transverse (X-Y) and iii) sagittal (Z-Y) views. A) Un-aligned datasets, the reference dataset is in white and the target dataset is in black. B) The rigid transformation matrix is applied to transform the target dataset into the reference's coordinate system.

*Step 4: Application of Transform to Original*

The final step was to apply the rigid transformation matrix to the original target greyscale dataset (Figure 3.11.)

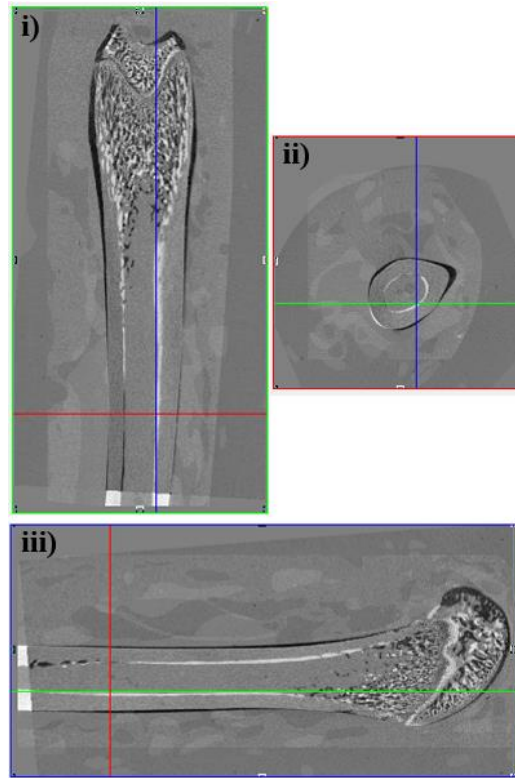


**Figure 3.11.** Co-registered greyscale distal femurs achieved with the transformation matrix. Shown in i) coronal (X-Z), ii) transverse (X-Y) and iii) sagittal (Z-Y) views.

### 3.2.4 Segmentation

The use of *ex vivo*  $\mu$ CT to study the effects of an intervention (e.g. SCI) on bone lead to the generation of large quantities of data. Each bone dataset was made up of between 3000 and 3500 8-bit greyscale images. Separate analysis was performed on both trabecular and cortical bone, which required the segmentation of both bone compartments. The current gold standard protocols for segmentation are all semi-automated (Buie et al., 2007). These procedures require initial input free-hand drawings of the contour between the two compartments in a slice-by-slice manner (Laib et al., 1998). An interpolation function then minimises the number of contours that must be drawn by hand (Buie et al., 2007). Due to the large number of datasets ( $n = 64$ ), scanned at high resolution (6.89 microns), semi-automated segmentation procedures were thought

to be impractical. Instead a procedure was implemented to automatically segment the trabecular and cortical bone VOIs.

An overview of the steps involved in the automated segmentation algorithm implemented in this thesis is presented below. All thresholds and kernel sizes used were chosen through optimisation for the datasets in question. This algorithm was applied to all reconstructed co-registered greyscale  $\mu$ CT datasets of the rat distal femur and was implemented in CTA<sub>n</sub> (Version 1.16.10.0, Kontich, Belgium). This method does not introduce operator bias, is faster, more accurate and more reproducible than semi-automated methods.

#### *3.2.4.1 Trabecular Bone Segmentation*

The purpose of this algorithm is to delineate the marrow cavity, while including trabecular bone, but excluding the cortical bone. The algorithm is here presented in two parts, each with a specific purpose. Each part is subsequently divided into essential steps.

##### *Part 1 – Defining the Bone Cross-sectional Area*

Defining the bone was achieved by segmenting the bone tissue from surrounding soft tissue, removing remaining noise, and defining a region of interest (ROI) that encapsulates the bone.

##### *Step 1: Global Thresholding*

The  $\mu$ CT datasets acquired are high resolution, and with high contrast between the bone and the surrounding softer tissues (PBS-soaked gauze exterior, marrow fat interior). The partial volume effect is minimal, and a simple global threshold was suitable for segmenting the bone tissue from surrounding softer tissues (Figure 3.12). The two limits of the threshold range used throughout this study to distinguish bone from non-bone material were 90 – 255 grey levels, corresponding to 35% - 100% of the maximum grey value.

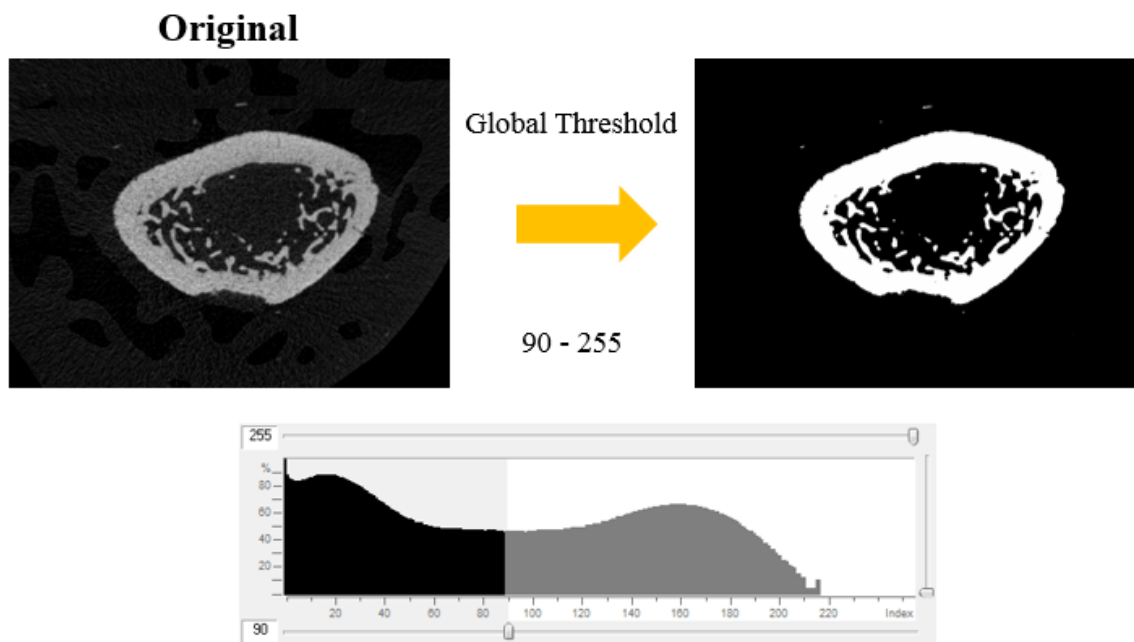


**Figure 3.12.** Global threshold for segmentation of bone tissue from softer tissues.

### Step 2: Noise Removal

Any remaining noise in the binarised dataset was removed with a sweep function which was applied in 3D (to the entire dataset) (Figure 3.13). This function first found all the connected components (objects) in the binarised dataset, all objects that were not connected to the largest object, i.e. the bone were removed. This binarised segmented bone was the starting point for the “image view” and “internal ROI view” in part 2.

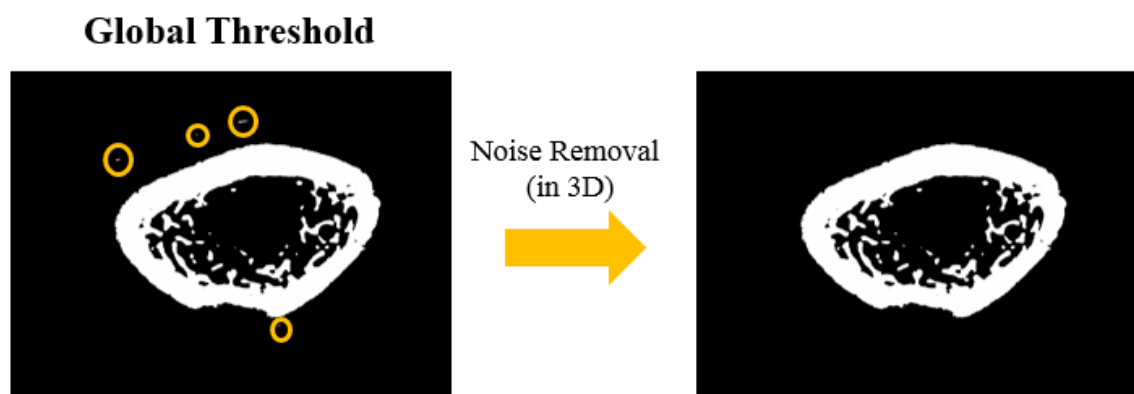


**Figure 3.13.** Removal of white speckles, by removal of all except the largest object (in 3D).



### Step 3: Cortical Bone ROI Selection

A flood-fill function was applied in 2D (slice-by-slice), this functioned to completely fill the marrow cavity and closed pores within the cortical bone. In slices where a pore runs completely through the cortical bone, meaning the marrow cavity is connected to the space outside, e.g. at nutrient foramina, a morphological closing operation with structuring element (kernel) size of 70 pixels was applied. This had the effect of stretching over holes and filling in open pores. Thus, this step limits the ROI to the bone's periosteal surface (Figure 3.14) and defines the starting ROI view for part 2 (Figure 3.15).

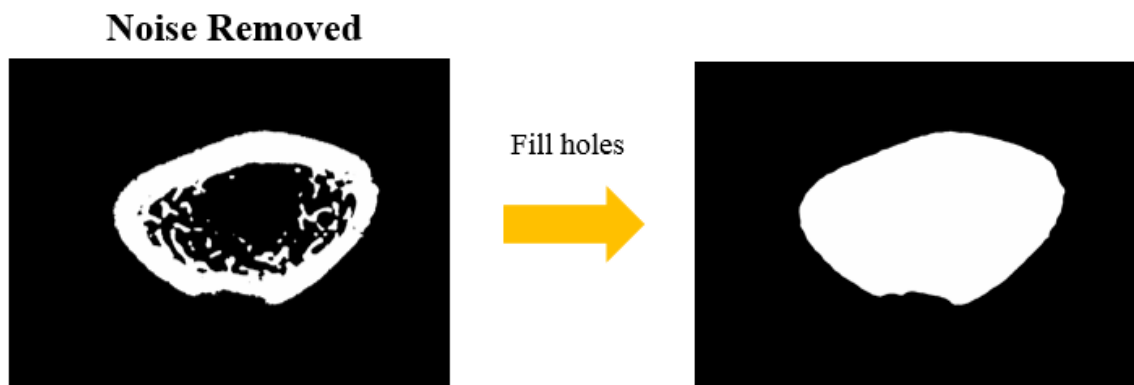


**Figure 3.14.** Defining the bone's total cross-sectional area with flood-fill and morphological closing operations.

To help describe the next steps, the three views are now defined. These are the image view, the ROI view and the internal ROI view (Figure 3.15). The effects each of the following operations have on each of the views will be visualised.

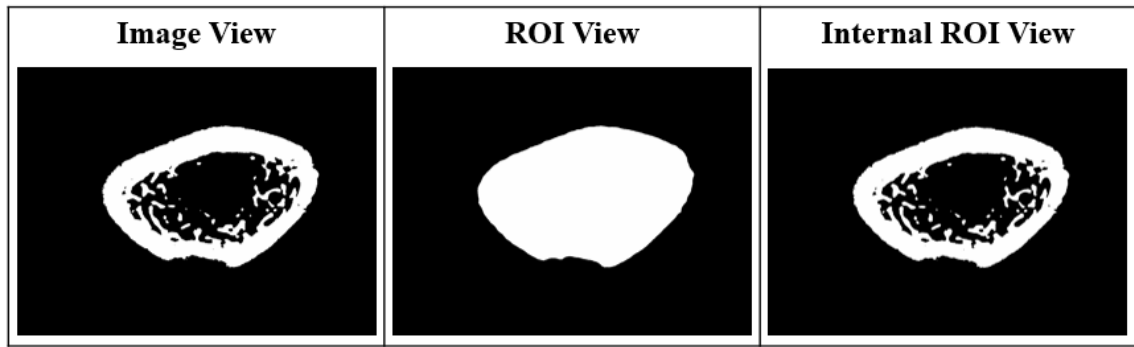


**Figure 3.15.** The input image view, ROI view and internal ROI view, for part 2 of the segmentation algorithm, the purpose of which is to select the marrow cavity.

### *Part 2 – Selection of Marrow Cavity*

Now that the bone cross-sectional area had been defined, the second part of the algorithm selected the marrow cavity.

#### Step 4: Bitwise NOT Operator

Firstly, the image was inverted with a bitwise operation (Image = **NOT** Image) (Figure 3.16). White become black and black becomes white.

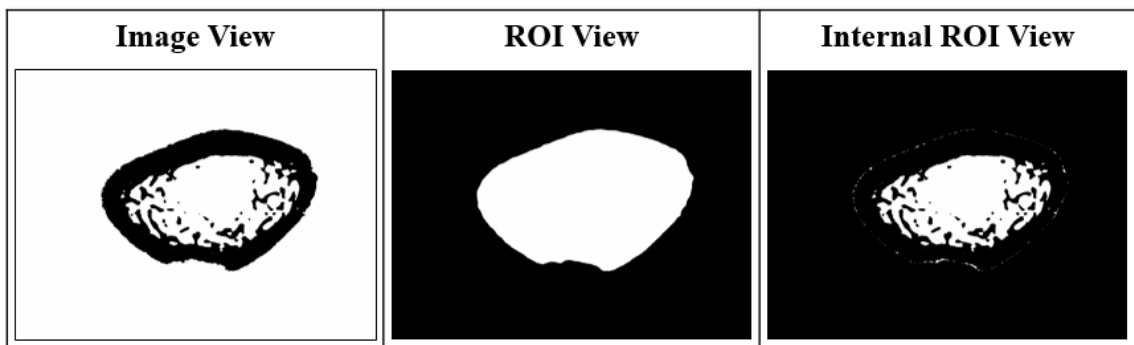


**Figure 3.16.** Effects of applying an inversion (bitwise NOT operator) to the image.

#### Step 5: Bitwise AND Operator

The image view shows that the inversion led to the selection of both the marrow cavity and the space exterior to the bone (Figure 3.16). To limit the marrow cavity selection to

just the interior space of the bone a second bitwise operation was applied to the image (Image = Image **AND** ROI) (Figure 3.17).

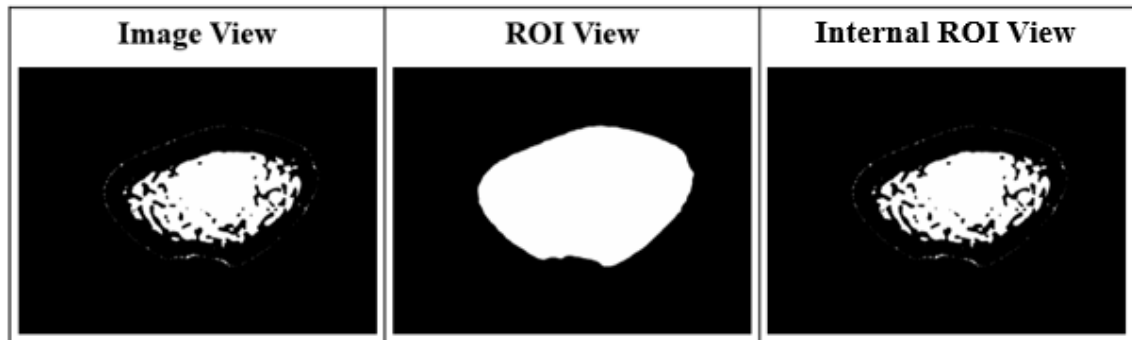


**Figure 3.17.** Application of the bitwise AND operator to the image view. It compares each pixel in the first operand to that of the corresponding pixel in the second operand. If both pixels are white, then the resultant pixel is white, otherwise it is black.

#### Step 6: White Speckle Removal

White speckles exist at the periosteal perimeter of the bone in both the image and internal ROI views (Figure 3.17). This was due to the morphological closing operation that was used in step 3, which stretched over holes and filled in open pores (Figure 3.14). To remove these speckles, which are smaller than all marrow cavity objects selected, a morphological opening was applied with a disk-shaped kernel of radius 5 pixels (Figure 3.18). Opening is defined as an erosion followed by a dilation using the same kernel. This has the effect of removing all objects that cannot be entirely contained by the kernel and forming new boundaries that conform with the disk-like shape of the kernel.

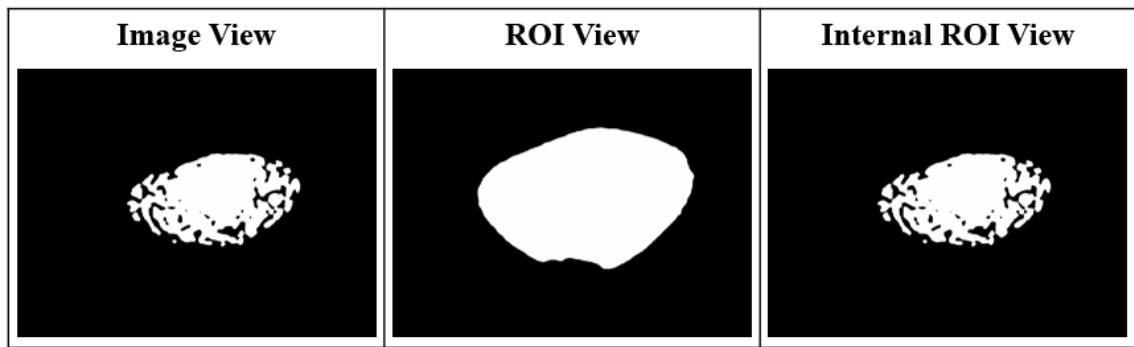


**Figure 3.18.** Effect of the removal of white speckle with disk-shaped kernel of radius 5 pixels.

#### Step 7: Inclusion of Trabecular Bone

The empty regions of the marrow cavity have been selected, but the trabecular bone has not (it appears as black gaps within the marrow cavity) (Figure 3.18). These gaps were filled with a morphological closing operation, with disk-shaped kernel of radius equal to at least half that of the largest gap (Figure 3.19). A radius of 50 pixels was used here. Closing is defined as a dilation followed by an erosion using the same kernel. Here it had the effect of turning background (black) pixels in to foreground (white) pixels, if the kernel could not completely fit within the background gap.

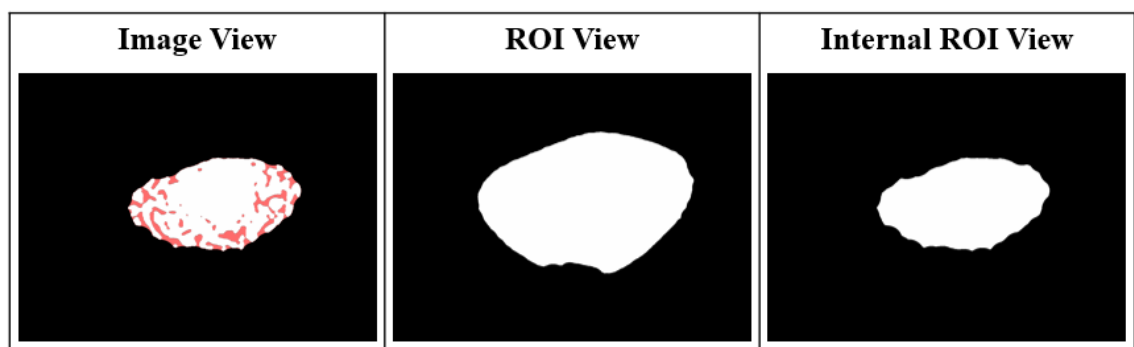


**Figure 3.19.** Effect of morphological closing with disk-shaped kernel of radius 50 pixels in red, indicating that the gaps have now been filled in.

### Step 8: Erosion to Ensure No Cortical Bone Selected

To ensure that the marrow cavity did not contain any cortical bone an erosion with disk-shaped kernel of size 3 pixels was used. This resulted in the bone marrow cavity ROI starting just several pixels from the endocortical perimeter (Figure 3.20).

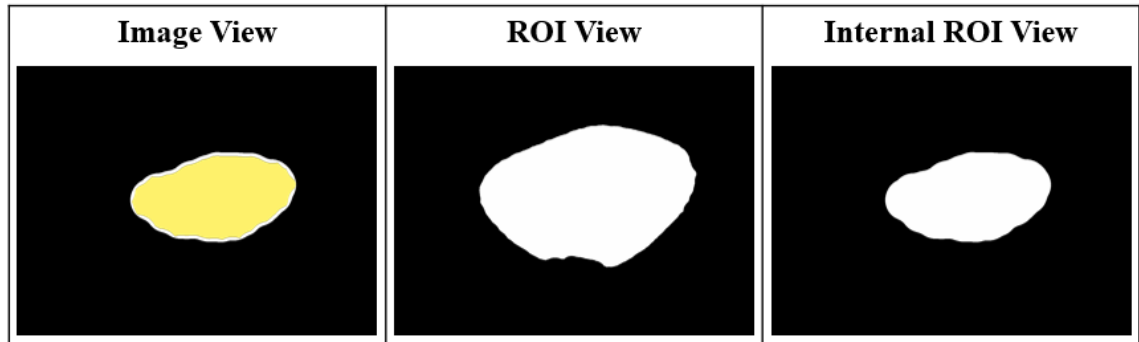


**Figure 3.20.** Effect of morphological erosion with disk-shaped kernel of radius 3 pixels. Yellow indicates the new image view of the marrow cavity after erosion (not to scale).

### Step 9: Reload Original Image into Marrow Cavity ROI

The ROI view was then made a copy of the image view in Figure 3.20. The original image was then loaded back into this ROI of the marrow cavity thus the trabecular bone had been segmented from the cortical bone (Figure 3.21).

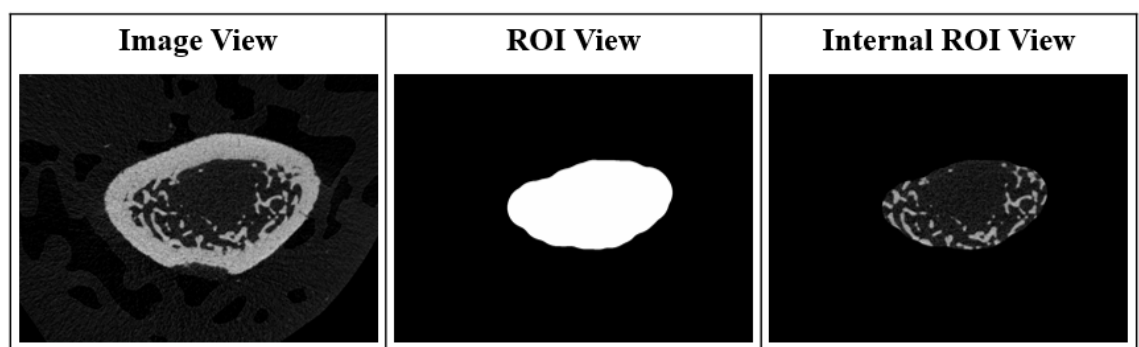


**Figure 3.21.** Effect of reloading original image into marrow cavity ROI.

### 3.2.4.2 Cortical Bone Segmentation

The segmentation of the cortical bone follows on directly from that of the approach used to segment the trabecular bone, since an ROI has already been defined for the marrow cavity. The procedure is identical up to step 8, thereafter it diverges.

Step 10: Dilation to ensure all cortical bone included

Following on from step 8, a dilation with disk-shaped kernel of size 3 pixels was applied to the ROI (not the image), ensuring all cortical bone was encapsulated within the ROI (Figure 3.22).

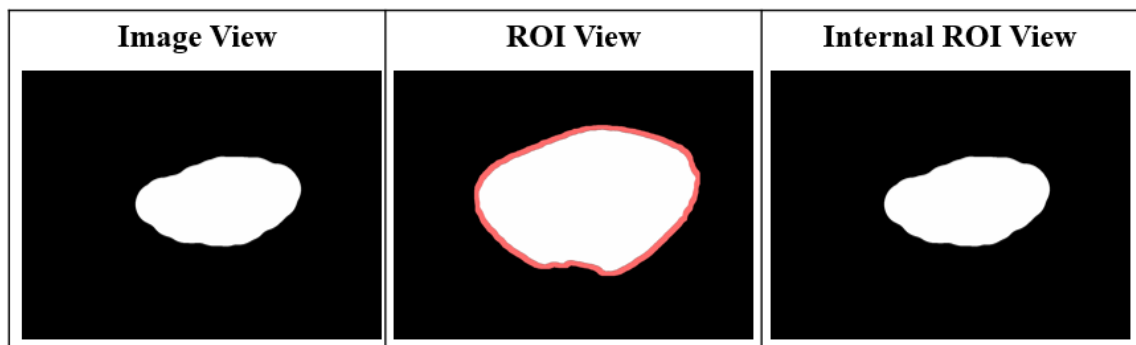


**Figure 3.22.** Effect of morphological erosion with disk-shaped kernel (not to scale). Red outline representation the increased area.

Step 11: Removal of Marrow Cavity From ROI

The marrow cavity ROI was then subtracted from the dilated ROI, via the bitwise operation  $ROI = ROI \text{ SUB Image}$  (Figure 3.23).

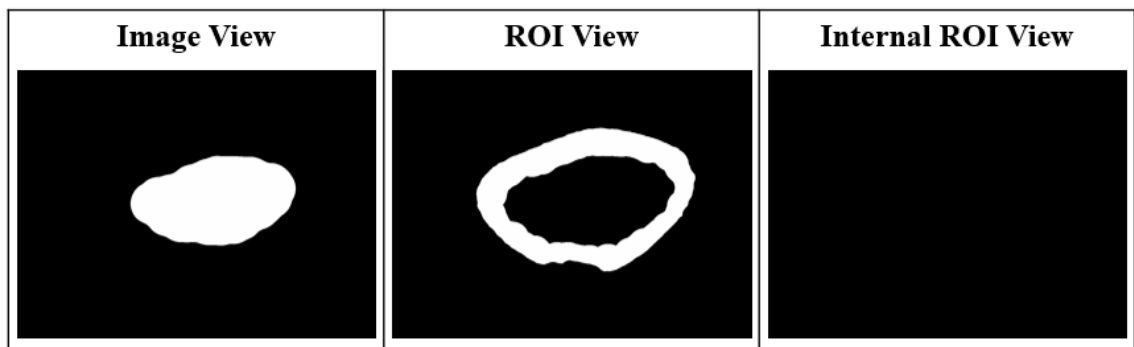


**Figure 3.23.** Effect of the subtraction of the marrow cavity on the ROI.

#### Step 12. Reload Original Image into Cortical Bone ROI

The original image was then loaded back into the ROI, as done in Step 9, thus the cortical bone was now segmented from the trabecular bone (Figure 3.24).

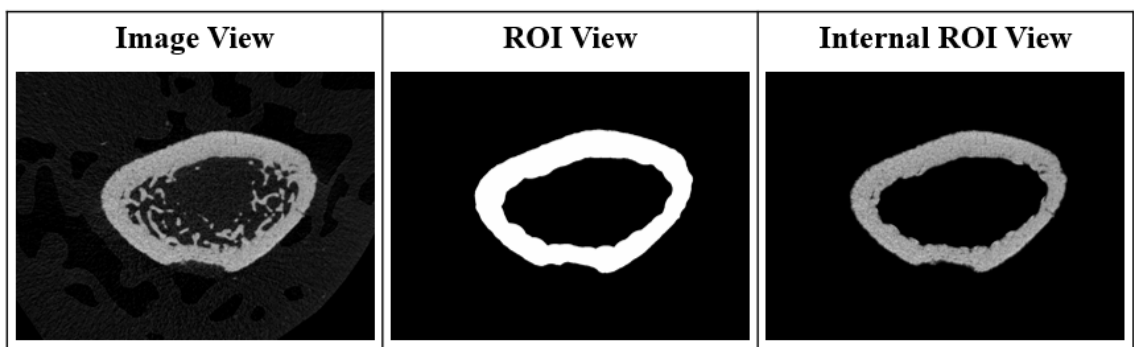


**Figure 3.24.** Effect of reloading the original image into the ROI.

### 3.2.5 Volume of Interest Section

For reliable and reproducible quantification of trabecular bone architecture two important factors need to be considered when selecting the VOI. These are the location and size of the VOI.

#### 3.2.5.1 Location of VOI

The architecture of trabecular bone, particularly in the appendicular skeleton can vary considerably over short distances in humans (Whitehouse & Dyson, 1974., Whitehouse,

1975) and in rats, therefore it is imperative that every effort is made to identify anatomically and biomechanically similar VOIs.

There are two accepted protocols for determining the VOI location, they are the commonly-used set distance (number of slices) from an anatomical landmark or use of a scaled VOI that is based on a percentage of longitudinal bone length. In situations where bone length differs between groups, an approach that uses a set number of slices would oversample for shorter femurs and under sample for longer femurs. This bias should be avoided more than the bias introduced when using a scaled VOI, i.e. that more trabeculae would be present in the VOI for longer than shorter femurs. That is because the goal is to compare anatomically and biomechanically similar regions.

An added complication when comparing the bones of growing animals at different stages of development, is that the longitudinal growth of bone results in a decrease in both the thickness of the growth plate and extent of primary spongiosa (where newly formed trabeculae are actively modelling) with age (Figure 3.25). To ensure that anatomically and biomechanically homologous regions of bone are being compared, we must ensure that any new bone growth as well as trabeculae that are actively undergoing modelling are excluded from the analysis, therefore for the analysis comparing trabecular bone at different time points post-injury, the metaphyseal secondary spongiosa (MSS) VOI was restricted to relatively mature trabecular i.e. secondary spongiosa, whose prevailing activity is remodelling (Erben, 1996; Jee & Yao, 2001).



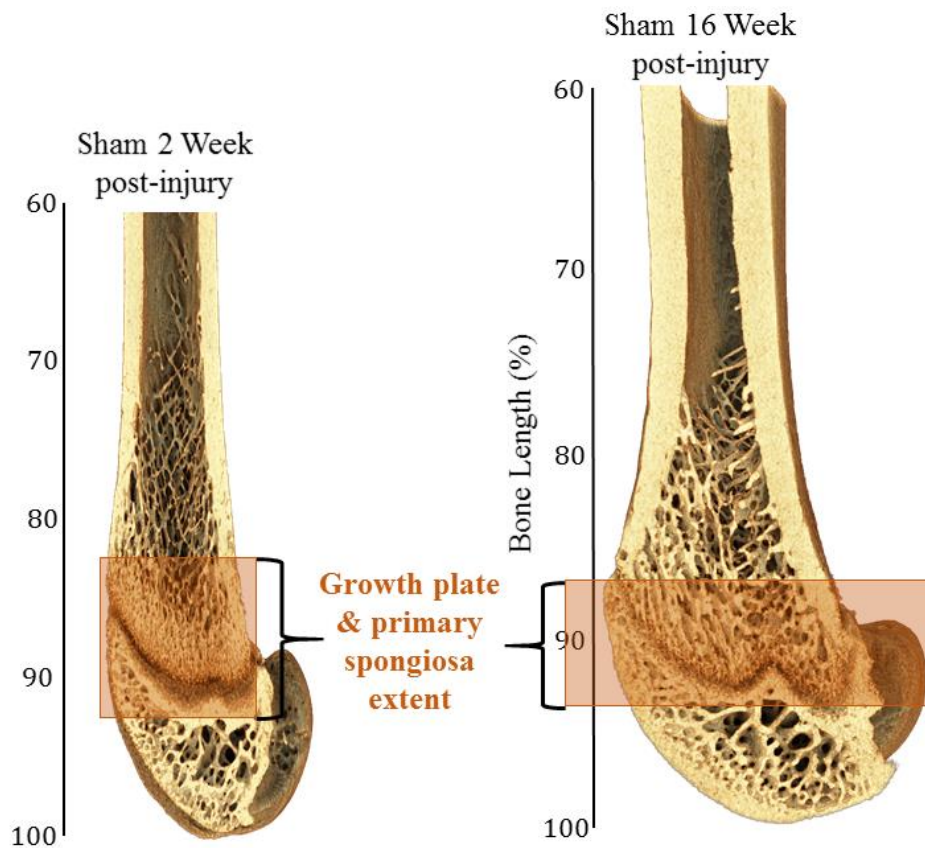


**Figure 3.25.** Comparison of the extent of the growth plate and primary spongiosa between representative control-2 and control-16 distal femurs, both for the distal 40% of femur length.

### 3.2.5.2 Size of VOI

The second important factor is the length of the VOI. If the VOI chosen is very long, i.e. it extends far into the diaphysis, then the average trabecular BV/TV relative to the VOI will be lower than a shorter VOI, so the VOI must be carefully chosen based on the structure of interest. Conversely, problems also occur when the VOI chosen is too small. The morphometric analysis run on the VOI reports parameters that represent averages of certain properties within the VOI. To acquire meaningful values for a 3D morphometric parameter, the variation of the parameter must be small enough such that substantial changes to it do not occur over dimensions which are of the same order of magnitude as the VOI (Harrigan et al. 1988). So, to acquire an accurate measure of trabecular separation

the VOI must be longer than the length of trabeculae separation. Good practice is to ensure that the VOI contains at least 3 – 5 intertrabecular lengths (Bouxsein et al., 2010).

### *3.2.5.3 Trabecular VOIs*

Three VOIs were used to characterise the 3D morphometric properties of trabecular bone in the distal femur. For each femur, all three VOIs were scaled in the longitudinal (z) axis to the length of the bone. Each VOI had a z-axis extent of 4% bone length.

#### Metaphyseal Secondary Spongiosa VOI

A metaphyseal secondary spongiosa (MSS) VOI was selected that spanned from 81 to 85% bone length (from the proximal end). This VOI in all time-point post-surgery groups was far away enough from the growth plate such that it was well within the mature, predominately remodelling trabecular bone (Figure 3.26).

#### Metaphyseal Primary Spongiosa VOI

Within the SCI population there is poor localisation of the exact position within the distal femur that fragility fractures occur. To ensure coverage of the most affected areas, a second metaphyseal trabecular VOI was also selected. This VOI, here termed metaphyseal primary spongiosa (MPS) extended from 85 to 89% bone length (from the proximal end). Unlike the MSS VOI, it contained the two main types of trabecular bone (primary and secondary spongiosa) in different quantities. For 2-week post-surgery femurs this VOI predominantly contained primary spongiosa actively undergoing modelling, while by 16-week post-surgery femurs this VOI predominantly contained secondary spongiosa actively undergoing remodelling (Figure 3.26).

## Epiphyseal Secondary Spongiosa VOI

The trabecular bone located within the epiphysis is entirely enclosed by the outer shell of cortical bone. The epiphyseal secondary spongiosa (ESS) VOI was selected such that it contained predominantly mature trabecular bone. It extended from 93 to 97% bone length (from the proximal end) (Figure 3.26).

### *3.2.5.4 Cortical VOI*

Two VOIs were used to characterise the 3D morphometric properties of cortical bone in the distal femur. These VOI also had a z-axis extent of 4% bone length.

#### Mid-diaphyseal Cortical Bone

The mid-diaphyseal cortical bone VOI extended between 58 and 62% bone length (Figure 3.26). It was selected to reduce effects of the third trochanter, a bony projection which is of minor importance in humans but has a noticeable size in rats. This VOI was also used to acquire tissue-level derived properties for three-point bend tests.

#### Distal-metaphyseal Cortical Bone

The mid-diaphyseal cortical bone VOI extended between 81 and 85% bone length (Figure 3.26). This cortical bone VOI is therefore acquired from a trabecular-rich region.

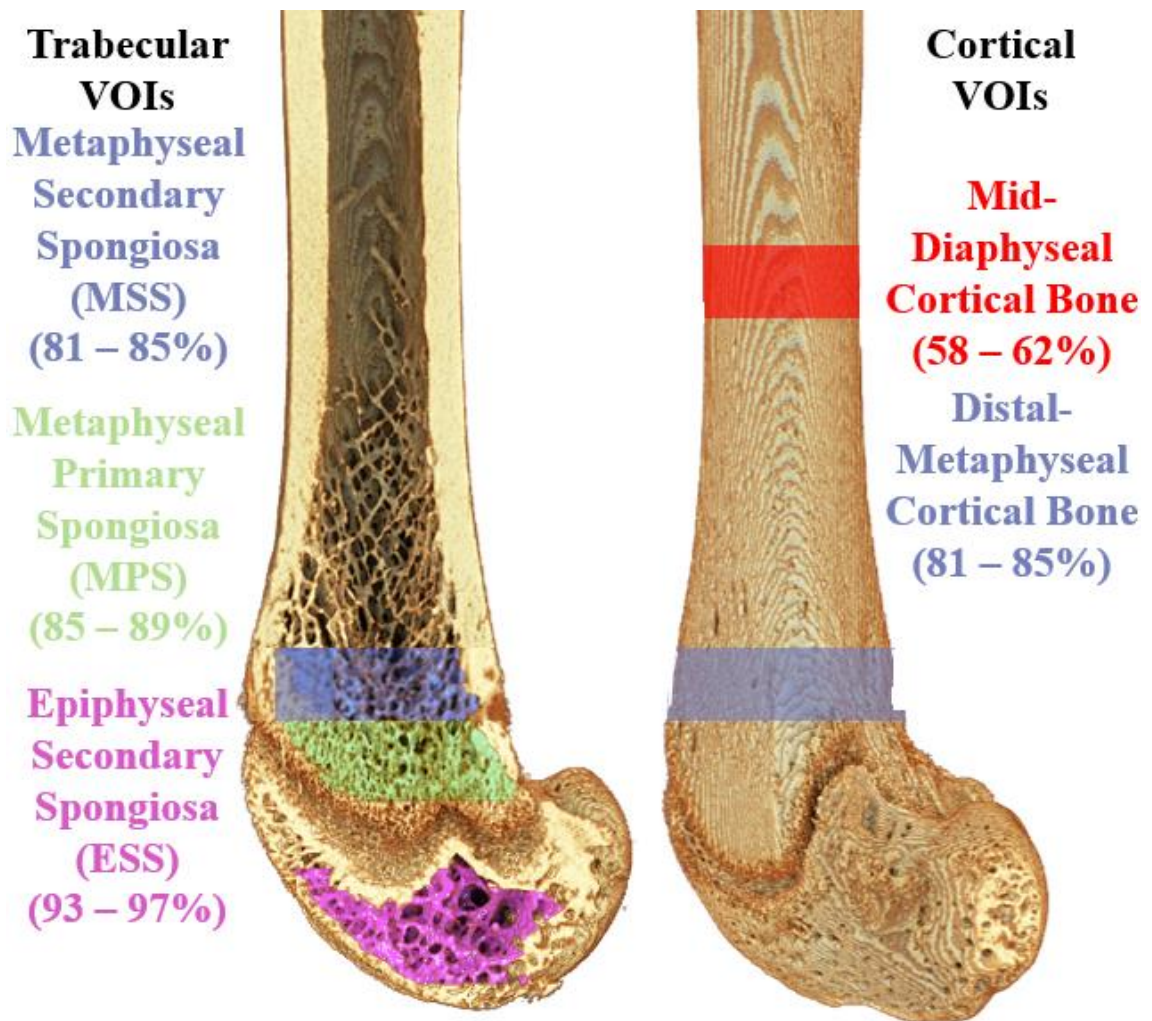


**Figure 3.26.** Schematic of the three trabecular and two cortical VOIs selected for 3D morphometric analysis. The three trabecular VOIs are; Metaphyseal Secondary Spongiosa (MSS) (81 – 85% bone length); Metaphyseal Primary Spongiosa (MPS) (85 – 89% bone length) and Epiphyseal Secondary Spongiosa (ESS) (93 – 97% bone length). The two cortical VOIs are; Mid-diaphyseal (58 – 62% bone length) and Distal-metaphyseal (81 – 85% bone length). All percentage bone lengths are from the proximal end.

### 3.2.6 Morphometric Analysis

With VOIs acquired, the morphology of the trabecular architecture and the geometry of cortical bone could now be quantified. Two types of morphometric analysis were performed i) 3D analysis, where 3D representations of the morphometry were calculated directly from a 3D surface-rendered model of the VOI (Figure 3.27A) (Lorensen & Cline, 1987; Müller et al., 1994), ii) 2D analysis, where morphometric parameters were

calculated on individual cross-sections in a slice-by-slice manner (Figure 3.27B). Both types of morphometric analyses were performed on co-registered segmented binarised datasets.

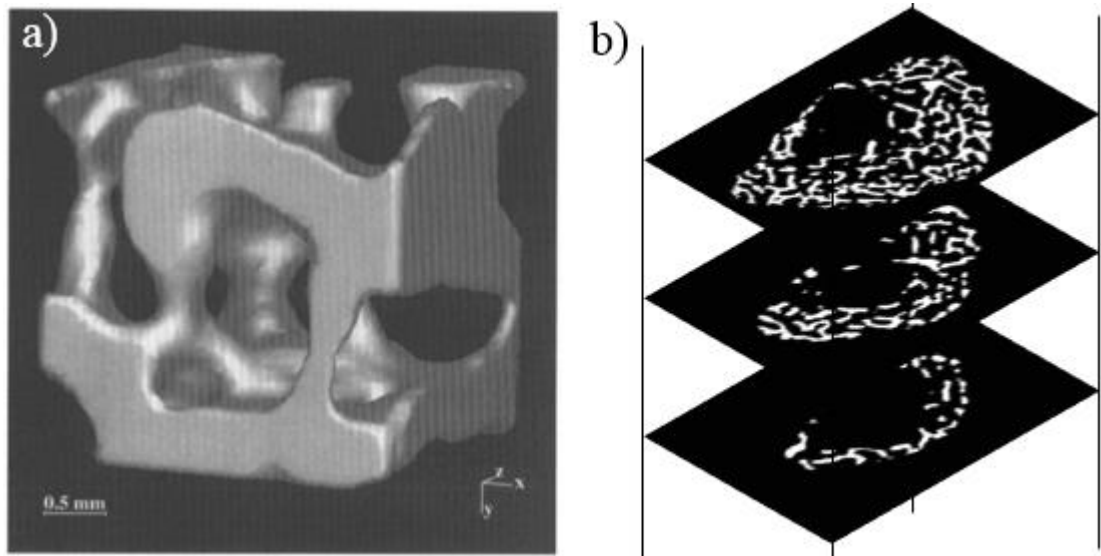


**Figure 3.27.** Comparison of 3D and 2D approaches to morphometric analysis of  $\mu$ CT scanned trabecular bone. A) depicts a surface-rendered trabecular bone model. Adapted from Müller & Rüeegsegger (1995). B) depicts individual binarised slices of trabecular bone.

### 3.2.6.1 3D Analysis

For 3D analysis to produce meaningful results, appropriate VOIs must be defined, because each 3D morphometric parameter is reported as a mean  $\pm$  standard error.

#### Software Considerations

The 3D morphometric analysis described above is the gold standard technique for assessment of trabecular and cortical micro-architecture of long bones in small animal models. There are several software packages available to help with this analysis, the ones utilised in this thesis were CTAn (Version 1.16.10.0, Kontich, Belgium) and BoneJ (Version 1.4.2) (Doube et al., 2010). CTAn is the scanner manufacturer provided software for measuring quantitative parameters from  $\mu$ CT datasets. It is the most popular software

used for morphometric analysis, used by all recent rodent  $\mu$ CT studies of SCI-induced osteoporosis (Lin et al., 2015; Yarrow et al., 2014), but it is a black box, meaning the codes that perform the quantitative analysis cannot be examined. BoneJ on the other hand is an open source plugin for bone image analysis in ImageJ, meaning the codes can be viewed and optimised for use.

Throughout the project comparisons between the two software packages were performed for all morphometric parameters used in this thesis. No differences were seen in the 2 primary or 3 metric morphometric parameters, therefore CTAn was used to determined them. The remaining 5 non-metric parameters require a degree of control to acquire unbiased results, BoneJ was therefore used for these. Table 3.3 lists all morphometric parameters used to characterise trabecular architecture with the corresponding software package used. Appendix A provides an in-depth summary of each of the trabecular morphometric parameters, which is of vital importance for interpretation of the results.

Table 3.3. Parameters used to quantify the 3D morphometry and architecture of trabecular bone VOIs, with abbreviation, unit and software package used.

<b>Parameter</b>	<b>Abbreviation</b>	<b>Unit</b>	<b>Software</b>
Trabecular Bone Volume Fraction	BV/TV	%	CTAn
Trabecular Bone Surface to Volume Ratio	BS/BV	$\text{mm}^{-1}$	CTAn
Trabecular Thickness	Tb.Th	mm	CTAn
Trabecular Separation	Tb.Sp	mm	CTAn
Trabecular Number	Tb.N	$\text{mm}^{-1}$	CTAn
Trabecular Pattern Factor	Tb.Pf	$\text{mm}^{-1}$	BoneJ
Structure Model Index	SMI		BoneJ
Fractal Dimension	FD		BoneJ
Degree of Anisotropy	DA		BoneJ
Connectivity Density	Conn.D	$\text{mm}^{-1}$	BoneJ

All cortical morphometric parameters except cortical bone surface to volume ratio and fractal dimension were determined for the mid-diaphyseal and distal-metaphyseal VOIs in CTAn, for the same reason. Table 3.4 lists all morphometric parameters used to

characterise cortical bone. Appendix B provides an in-depth summary of each of the cortical morphometric parameters

Table 3.4. Parameters used to quantify the morphometry and architecture of cortical bone VOIs, with abbreviation, unit and software package used.

<b>Parameter</b>	<b>Abbreviation</b>	<b>Unit</b>	<b>Software</b>
Cortical Thickness	Ct.Th	mm	CTAn
Cortical Area	Ct.Ar	mm <sup>2</sup>	CTAn
Area Enclosed by Periosteum	Tt.Ar	mm <sup>2</sup>	CTAn
Marrow (Medullary) Area	Ma.Ar	mm <sup>2</sup>	CTAn
Relative Cortical Area	Ct.Ar/Tt.Ar		CTAn
Robustness	Tt.Ar/L	mm	CTAn
Periosteal Perimeter	Ps.Pm	mm	CTAn
Endocortical Perimeter	Ec.Pm	mm	CTAn
Polar Moment of Area	J <sub>2D</sub>	mm <sup>4</sup>	CTAn
Eccentricity	Ecc		CTAn
Fractal Dimension	FD		BoneJ
Cortical Bone surface to volume ratio	BS/BV	mm <sup>-1</sup>	BoneJ

### 3.2.6.2 2D Analysis

CTAn and BoneJ are both capable of performing 2D analysis, meaning all morphometric parameters were calculated for each individual cross-section, but the final reported result is integrated over the entire VOI, so again it is reported as a mean  $\pm$  standard error.

Custom MATLAB scripts were developed to perform 2D analysis both of trabecular and cortical morphometry, except they the final integration step was not performed. This allowed for the morphometric parameter to be reported as a function of percentage bone length (i.e. a distribution), thus maintaining the underlying spatial variability and directionality and allowing site-specific effects to be quantified. A second novel attribute of this technique is that it allows the whole bone to be quantified, that is no VOI needs to be selected. This is important because as demonstrated in this thesis, conclusions based from single sites do not generalise well to the whole bone, and do not allow for quantification of site-specific effects.

## Trabecular Morphometry

The trabecular morphometric parameters used to characterise trabecular architecture in 2D as a function of bone length are shown in Table 3.5.

Table 3.5. Parameters used to quantify the morphometry and architecture of trabecular bone as a function of bone length, with abbreviation, unit and software package used to implement.

<b>Parameter</b>	<b>Abbreviation</b>	<b>Unit</b>	<b>Software</b>
Trabecular Bone Area Fraction	BA/TA	%	MATLAB
Trabecular Thickness	Tb.Th <sub>2D</sub>	mm	MATLAB
Trabecular Separation	Tb.Sp <sub>2D</sub>	mm	MATLAB
Trabecular Number	Tb.N <sub>2D</sub>	mm <sup>-1</sup>	MATLAB

Charting the distribution of trabecular morphometry as a function of bone length allows the quantification of another parameter, the trabecular extent (Tb.E), which is novel to this thesis. Tb.E quantifies how far trabecular bone extends into the medullary cavity from the distal growth plate. It is the distance at which the trabecular bone area fraction distribution last touches the abscissa. Here it is quantified as a function of trabecular bone area fraction, where BA/TA was set at 30%, 20%, 10%, the first occurrence of no trabecular bone (0) and the absolute 0 (last) occurrence.

## Cortical Morphometry

The cortical morphometric parameters used to characterise cortical bone geometry in 2D as a function of bone length are shown in Table 3.6.



Table 3.6. Parameters used to quantify the morphometry and geometry of cortical bone as a function of bone length, with abbreviation, unit and software package used to implement.

<b>Parameter</b>	<b>Abbreviation</b>	<b>Unit</b>	<b>Software</b>
Cortical Thickness	Ct.Th <sub>2D</sub>	mm	MATLAB
Cortical Area	Ct.Ar <sub>2D</sub>	mm <sup>2</sup>	MATLAB
Area Enclosed by Periosteum	Tt.Ar <sub>2D</sub>	mm <sup>2</sup>	MATLAB
Marrow/Medullary Area	Ma.Ar <sub>2D</sub>	mm <sup>2</sup>	MATLAB
Periosteal Perimeter	Ps.Pm <sub>2D</sub>	mm	MATLAB
Endocortical Perimeter	Ec.Pm <sub>2D</sub>	mm	MATLAB
Polar Moment of Area	J <sub>2D</sub>	mm <sup>4</sup>	MATLAB

All parameters described followed the standard nomenclature recommended by the American Society of Bone and Mineral Research (Bouxsein et al., 2010), with a subscript 2D to indicate the nature of calculation. Appendices A and B summarise how each of the 2D trabecular and cortical morphometric parameters were determined.

#### Morphometric Distributions

All femurs were of different geometry and length, but the slice thickness was identical, so each 2D morphometric distribution was made up of a different number of  $\mu$ CT slices. To compare fixed points along the bone length (e.g. at 80% total bone length) a cubic interpolation was performed on each distribution.

All 2D trabecular morphometric distributions were plotted over segmented trabecular bone VOIs, 100 – 60% bone length in size, while all 2D cortical morphometric distributions were plotted over segmented cortical bone VOIs, 85 - 40% bone length in size (Figure 3.28).

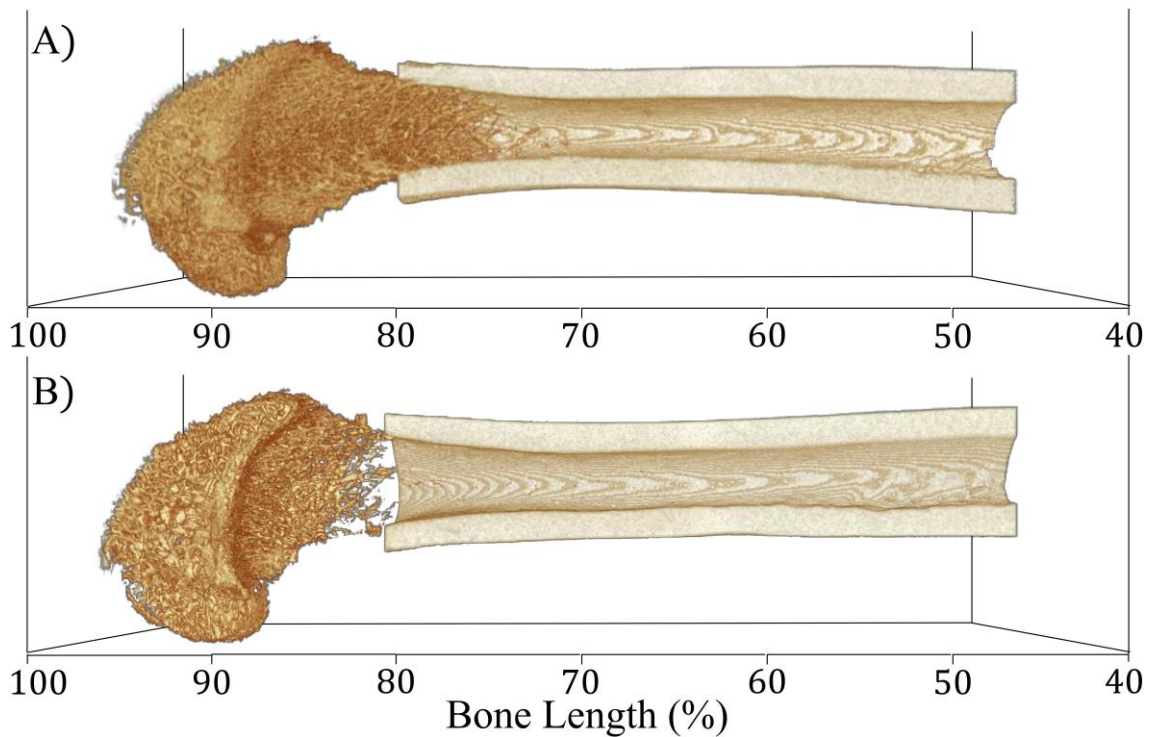


**Figure 3.28.** Representative 3D visualisation of  $\mu$ CT distal femur datasets for A) sham-operated control and B) T9-SCI, both at 10-weeks post-SCI. Segmented trabecular VOI ranging from 100% - 60% bone length and segmented cortical VOI ranging from 80% - 40% bone length.

The 2D morphometric distributions determined with custom-written MATLAB scripts were validated against 2D analysis performed in CTAn, with details given in Appendix C.

### 3.2.7 Densiometric Analysis

Densiometric analysis was only performed on cortical bone. With the  $6.89 \mu\text{m}$  voxel size used here it was not appropriate to assess TMD of individual trabeculae. A thickness of at least 5 voxels is needed for a meaningful densiometric measure (Bouxsein et al., 2010).

#### 3.2.7.1 Mineral Density Calibration

Two mineral density calibration phantoms, both 4 mm in diameter, one composed of 0.25 and the other  $0.75 \text{ g cm}^{-3}$  calcium hydroxyapatite (CaHA) (Bruker  $\mu$ CT, Kontich, Belgium), were scanned at the start of each scanning session with the same scanner

settings and reconstruction parameters used for the femur samples (Figure 3.29A). A Circular VOI 200 slices thick was acquired from within each phantom to exclude edges, minimising partial volume effects in CTAn (Version 1.16.10.0, Kontich, Belgium) (Figure 3.29B).

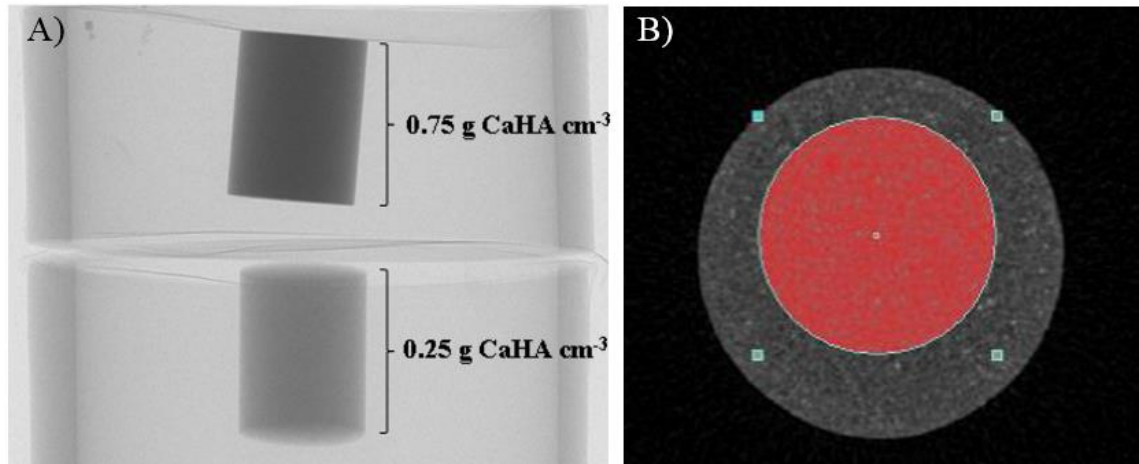


**Figure 3.29.** Mineral density calibration phantoms. A) X-ray image of both calibration rods 0.25 (bottom) and 0.75 (top) g cm<sup>-3</sup> calcium hydroxyapatite. B) Example reconstructed cross-section of 0.75 g cm<sup>-3</sup> phantom with circular ROI selected.

The average attenuation coefficient (AC) for each VOI was then calculated using MATLAB (2015b). The two values were then used to create a linear relationship between mineral density and AC (Figure 3.30).

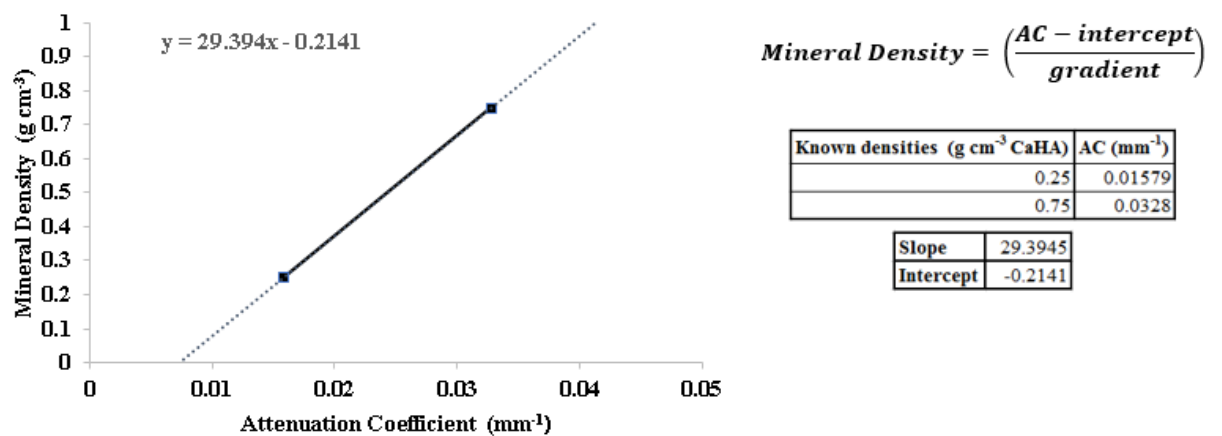


**Figure 3.30.** Mineral density calibration.

Cortical TMD was then determined for segmented cortical bone (40 – 85% bone length). For all TMD measurements, a one-pixel erosion was applied to both periosteal and endosteal surfaces to minimise partial volume effects.

### ***3.3 Mechanical Testing***

Femurs were thawed at room temperature and kept wrapped in PBS-soaked gauze to remain moist until mechanical tests were performed. Right femurs underwent three-point bending until fracture, and subsequently the remaining proximal end of the femur underwent femoral neck fracture. Left femurs underwent torsion until fracture.

#### ***3.3.1 Three-point Bending***

Right femurs were loaded to failure in a three-point bend test configuration at  $1 \text{ mm s}^{-1}$  using a servohydraulic testing machine with a 2kN load cell (Zwick/Roell z2.0, August-Nagel-Strasse 11, Ulm, Germany) (Figure 3.31). Load and actuator displacement were digitally recorded at a sampling rate of 100 Hz, with testXpert II (Version 3.61) software. The span length was 15 mm for all femurs in the 6, 10 and 16-weeks post-SCI groups, for 2-week post-SCI femurs the span length was reduced to 13 mm, to avoid the distal growth plate resting on one of the supports. Femurs were oriented in the posterior-anterior (P-A) direction on the bottom supports, so the anterior quadrant was subjected to tensile loads. The bone was positioned such that the top support point of contact with the diaphysis occurred at approximately 60% of bone length (from proximal end) (Figure 3.31). This allowed testing of the cortical diaphysis and to reduce effects of the third trochanter, a bony projection which is of minor importance in humans, but has a noticeable size in rats (Bolanowski et al, 2005). A MATLAB script was written to extract i) the whole-bone mechanical properties; stiffness ( $\text{N mm}^{-1}$ ), maximum load (N), post-yield displacement (mm) and work-to-fracture (mJ) from the load-displacement graphs; ii) the tissue-level

mechanical properties; elastic modulus (GPa) and maximum stress (MPa) from the geometry of diaphyseal bone cross-sections, acquired from 6.89  $\mu\text{m}$  resolution  $\mu\text{CT}$  scans of the 58 – 62% bone length VOI.

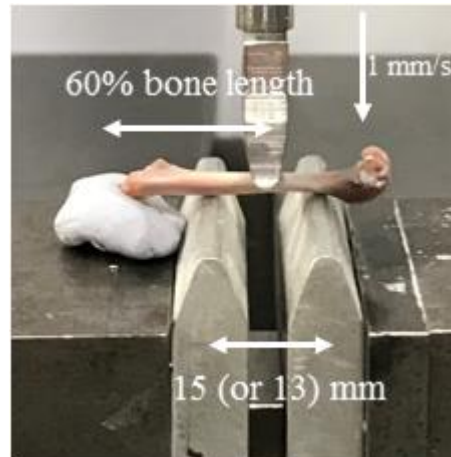


**Figure 3.31.** Three-point bend experimental set-up.

### 3.3.2 Torsion

In the torsion tests, the proximal-end of the bone was fixed, and the-distal end was rigidly rotated.

#### 3.3.2.1 Preparation/Embedding

The embedding material used to rigidly constrain both ends of the bone was Low Melting Temperature Alloy (LMTA) (Alloy 47°, Grad FA16; Alpha-Fry Technologies B.V., Cookson Electronics Assembly Materials, Naarden, The Netherlands). When liquid the LMTA was poured into M6 nuts, before the ends of the bone were embedded. The proximal-end was embedded at the location where the third trochanter's outer eccentricity and diameter are at their maximum, for the same reason that the three-point bend test was conducted at 60% bone length. The distal-end was embedded up to 2 mm above the distal growth plate to ensure testing of cortical bone, as opposed to the metaphysis-growth plate junction (Figure 3.32).

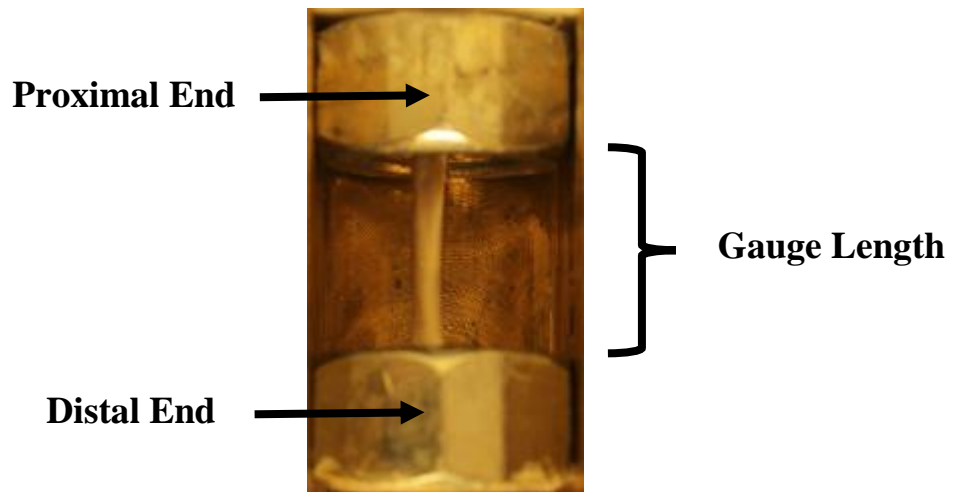


**Figure 3.32.** Representative rodent left femur in the proximal to distal orientation, with proximal and distal ends embedded inside M6 nuts with LMTA.

### 3.3.2.2 Torsion/Twist Testing

The rigidly attached M6 nuts fitted into custom-built Perspex holders attached to a servohydraulic testing system (Instron 8511 load frame, High Wycombe, UK) with an MTS Series 793 controller (Figure 3.33). Torque and angular displacement acquired from the fixed distal-end were digitally recorded at a sampling rate of 100 Hz using a 20 Nm torque load, with MTS TestSuite Multipurpose Elite (Version 3.6.6.2020) software. Left femurs were initially ramped to 10N axial load over 10 seconds, followed by a 10 second dwell time to allow for adaptation, before they were subjected to torsion. The rigidly fixed proximal-end was held stationary and the distal-end was subjected to rotation at an angular displacement of  $6^\circ/\text{second}$  until failure. A MATLAB script was written to extract i) the whole-bone mechanical properties; rotational stiffness (Nmm/ $\theta$ ), maximum torque (N mm) and work-to-fracture (mJ) from the torque-angular displacement graphs (post-yield rotation was not quantified since long bones tend to fail in a brittle manner in torsion tests (Silva et al., 2006); ii) the tissue-level mechanical properties; shear (rigidity) modulus (GPa) and ultimate shear stress (MPa) from the geometry of the entire diaphyseal

bone contained within the gauge length acquired from 6.89  $\mu\text{m}$  resolution  $\mu\text{CT}$  scans.

Further details are available in Appendix A.

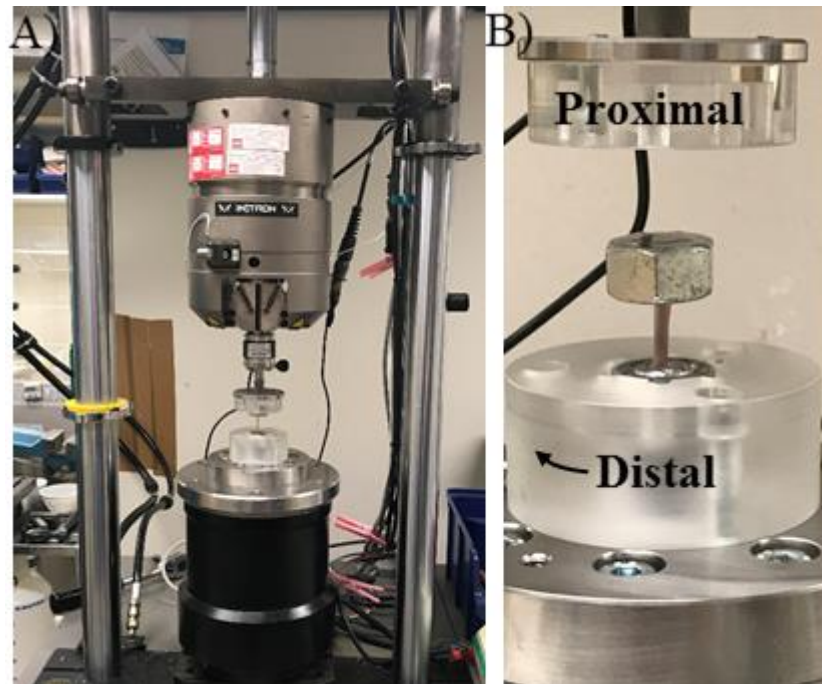


Figure 3.33. Torsion test experimental set-up. A) servohydraulic testing machine. B) zoomed in on embedded femur, proximal-end is fixed, while distal-end rotated  $6^\circ/\text{second}$  until failure.

### 3.3.3 Femoral Neck Fracture

After three-point bend testing, the proximal part of the femur was positioned using a cylindrical holding device, mounted on an adjustable platform, so that the femur could be fixed at a shaft angle of  $9^\circ$  to the vertical plane, similar to the position of the femur *in vivo*, as described by Hessle et al. (2013). However, Hessle et al. held the femur at  $9^\circ$  of adduction and this test was performed at  $9^\circ$  of abduction. Using a servohydraulic testing machine with a 2kN load cell (Zwick/Roell z2.0, August-Nagel-Strasse 11, Ulm, Germany) with testXpert II (Version 3.61) testing software, displacement was applied to the femoral head using a flat-ended indenter at 0.1 mm/second (avoiding the greater trochanter) until fracture (Figure 3.34). Load and actuator displacement were digitally recorded at a sampling rate of 100 Hz. Femurs were subsequently examined visually to

ensure fracture occurred across the femoral neck. maximum load (N) was extracted from the resulted load-displacement graph.



**Figure 3.34.** Femoral neck fracture experimental set-up, showing 9° of abduction applied.

### ***3.4 Statistical Analysis***

#### ***3.4.1 2D Morphometric Distributions***

The Anderson-Darling and Kolmogorov-Smirnov tests were used to test for normality between control and SCI group at each time point (2, 6, 10 and 16-week post-injury groups) for all 2D morphometric parameters. No significant deviations from normal distribution ( $p < 0.05$ ) occurred for any parameter reported. Student's t-test for independent samples was therefore performed for all parameters at every 1% bone length, using a custom-written code (MATLAB 2015b).



### *3.4.2 3D Morphometric Parameters*

For 3D trabecular and cortical morphometric parameters, the following statistical analysis was performed:

Three-way analysis of variance (ANOVA) was used to determine if there were significant interactions between surgery type (SCI or Sham), time post-surgery (2, 6, 10 and 16 weeks) and VOI (MSS, MPS and ESS for trabecular bone, mid-diaphyseal and distal metaphyseal for cortical bone). Significance is here defined as  $p < 0.05$ .

Initially the Anderson-Darling, Kolmogorov-Smirnov and the Shapiro-Wilk tests were used to test for approximate normality between the dependent variable (morphometric parameter) and each combination of the groups of the three independent variables. Levene's test was used to test for homogeneity of variance. No assumptions of the three-way ANOVA were broken.

If three-way ANOVA indicated a significant (surgery type – time post-surgery – VOI) interaction, which it did for all trabecular and cortical morphometric and mechanical properties, then two-way ANOVA was performed to determine the effects of each of the pair (surgery type – time post-surgery), (surgery type – VOI) or (time post-surgery – VOI) of interactions. Then post-hoc analysis was performed (Tukey's HSD) on the pair to determine differences between the pair. When the two-way ANOVA indicated a significant surgery type effect and either a time-post surgery effect or (surgery type – time post-surgery) interaction, then one-way ANOVAs were used to assess i) the effect of surgery-type on each time post-surgery separately, followed by post-hoc testing if the surgery-type effect was significant; and ii) to assess the effect of time-post surgery at both surgery types. Tests performed with a custom-written code (MATLAB 2015b). This

statistical analysis is similar to that performed on a study on the age-related changes in bone structure in male and female mice (Willinghamm et al., 2010).

### *3.4.3 Correlations*

Linear regression analysis was used to examine relationships between cortical and mechanical parameters and trabecular parameters. All Results are presented as mean  $\pm$  standard error (SE).

## Chapter 4 Results

In this chapter the major findings are presented, including the overall macroscopic changes to the femur, overall and site-specific changes to trabecular and cortical bone morphometry and densitometry, and changes to the mechanical properties of cortical bone as a result of growth and SCI-induced osteoporosis.

### *4.1 Overall Macroscopic Changes to the Femur*

To determine any gross abnormalities in the sublesional appendicular musculoskeletal system (the hindlimb) post-SCI, the gastrocnemius muscle, femoral and tibial wet masses, and femoral length were measured (Figure 4.1).

#### *4.1.1 Muscle and Bone Mass*

SCI disuse led to significant decreases in the gastrocnemius muscle (Figure 4.1A) and femur mass (Figure 4.1B) at all time points post injury ( $p < 0.001$ ) compared to control. The reduction in muscle mass occurred rapidly, by two weeks post-injury a 36% ( $p < 0.0001$ ) difference existed between control and SCI group, which was maintained at all later time-matched groups. Due to growth in this rat model, between 2 and 16-weeks post-surgery 45% and 43% increases in muscle mass (both  $p < 0.0001$ ) were observed between 2 and 16-week control and SCI groups respectively. Femoral mass changes lagged behind gastrocnemius muscle mass changes at 2 weeks post-injury, an 8% ( $p < 0.001$ ) decrease in mass was observed compared to control, by 6 weeks the difference increased to 20% ( $p < 0.0001$ ) and was maintained for all later time points. 48% and 31% increases in bone mass (both  $p < 0.001$ ) were observed 2 and 16-week control and SCI groups respectively. A similar trend was seen for tibial mass (Figure 4.1C).

### 4.1.2 Femur Length

The significant reduction in femoral mass observed due to SCI-induced osteoporosis was not primarily caused by changes in femoral length, as no significant differences were observed between any SCI group and time-matched control group (Figure 4.1D). SCI also did not cause any temporal longitudinal growth effects, as no significant injury - time post-injury interactions were observed. Between 2 and 16-weeks post-surgery a 16% and 15% increase in femur length (both  $p < 0.0001$ ) was observed for control and SCI femurs respectively. A similar trend was seen for tibial length (data not shown).

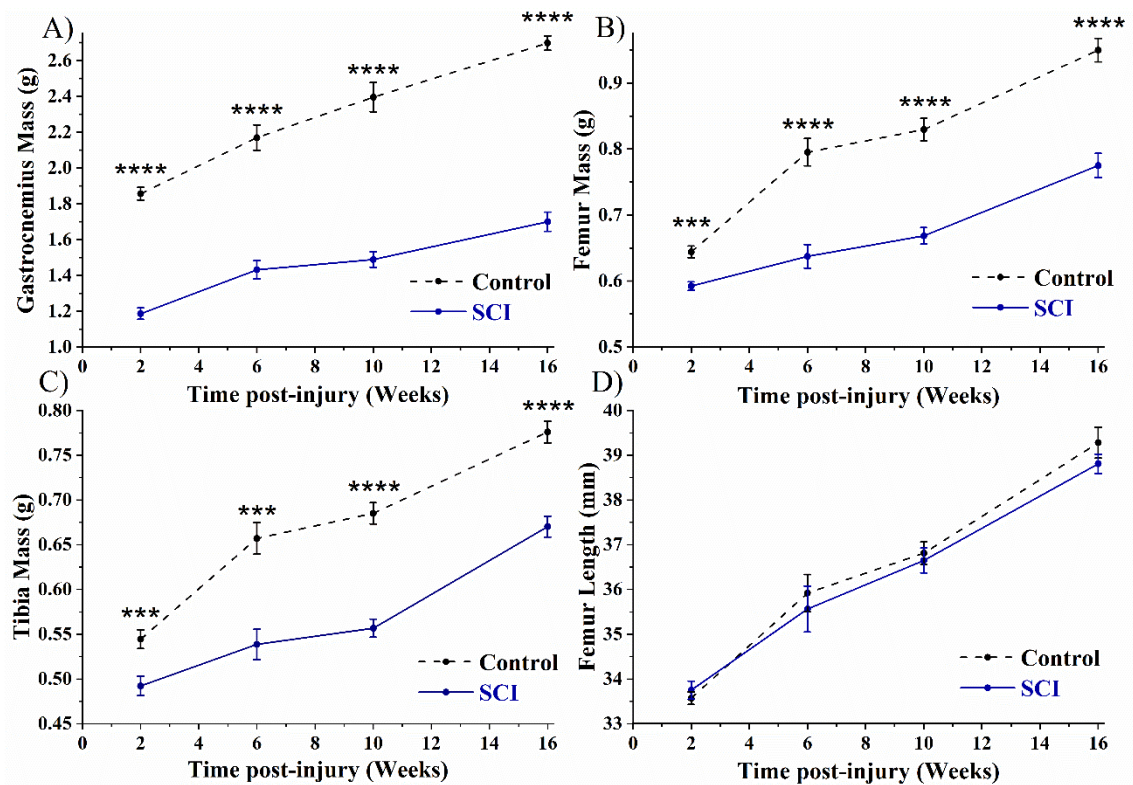


**Figure 4.1.** Gross anatomical measurements of A) gastrocnemius mass, B) femur wet mass, C) tibia wet mass and D) femur longitudinal length for control and SCI rat groups at all time-points post-surgery. Data shown as mean  $\pm$  SE. \*\*\* and \*\*\*\* indicate  $p < 0.001$  and  $p < 0.0001$  respectively.

## 4.2 Trabecular Bone Morphometry

The trabecular bone structure enclosed within the distal femoral cortex of a 10-week control rat is shown in Figure 4.2. It is an example of a healthy femur (2, 6 and 16-week control group femurs display similar overall trends in trabecular bone as a function of bone length). Two main trabecular bone compartments are inside the structure:

- i) Epiphyseal trabecular bone between 98 and 91% bone length,
- ii) Metaphyseal trabecular bone between 88 and 60% bone length,

which are separated by the growth plate complex (91 – 88% bone length).

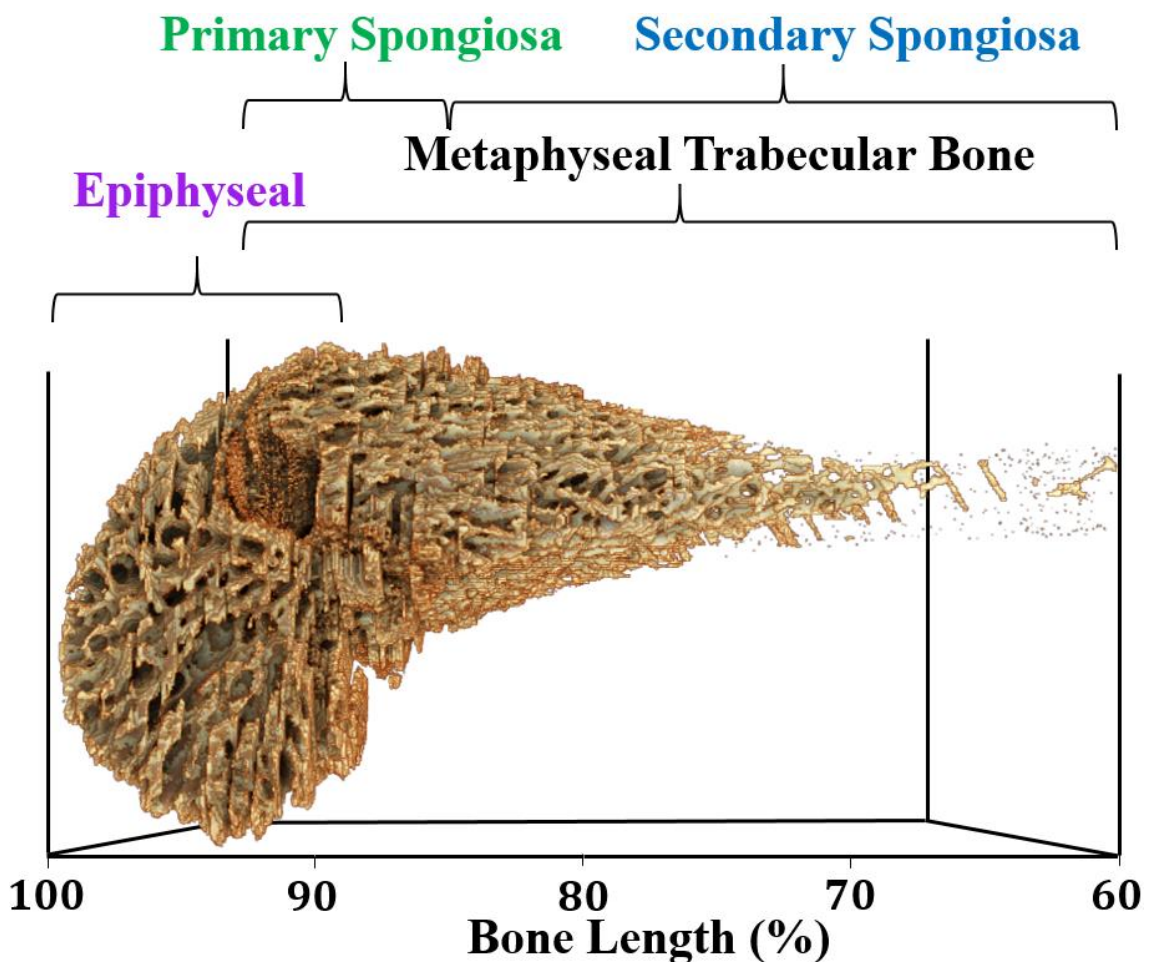


**Figure 4.2.** The entire trabecular bone structure of the distal femur of a representative 10-week post-surgery control rat.

#### 4.2.1 Variation in Trabecular Bone as a Function of Length

Figure 4.3A indicates that throughout the epiphyseal region of the distal femur there is limited variation in the area fraction (BA/TA) of trabecular bone. In contrast, throughout the metaphyseal region there is rarefaction of trabecular bone, indicated by the monotonically decreasing BA/TA gradient that runs proximally from the growth plate where trabecular BA/TA is highest, extending throughout the metaphysis and into the cortical shaft until there is no more trabecular bone.

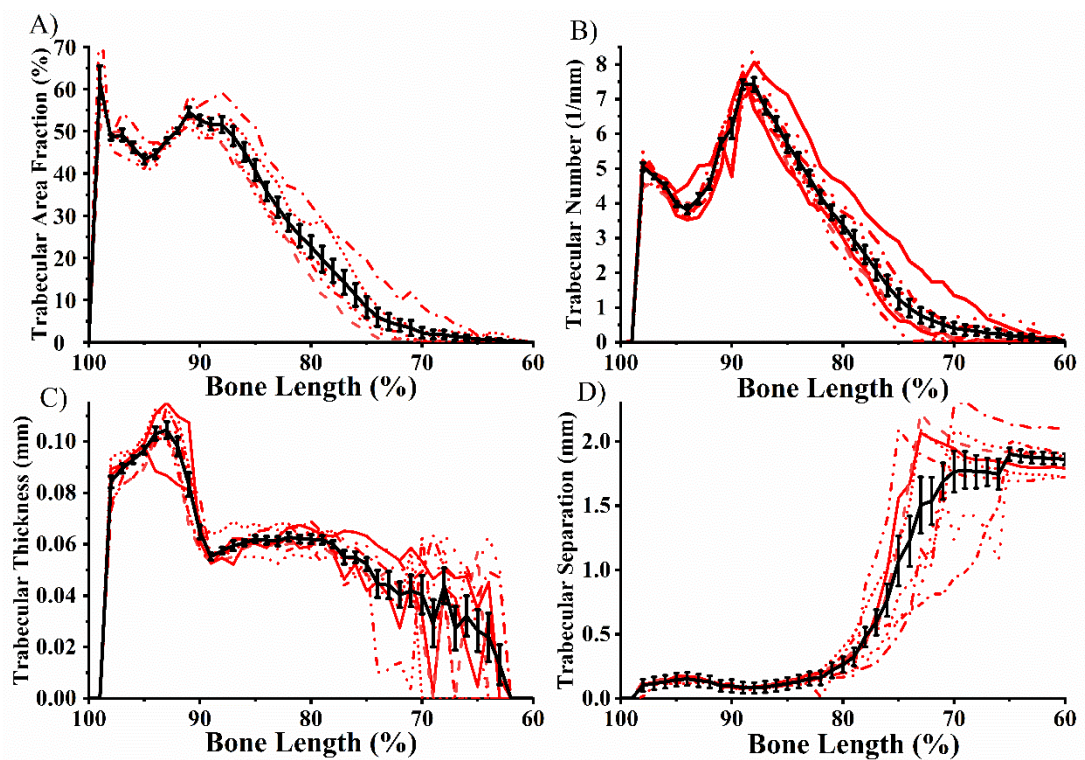


**Figure 4.3.** 2D  $\mu$ CT morphometric plots highlighting the variation of trabecular bone properties along the length of the bone for 10-week control distal femurs. Trabecular VOIs span 60 – 100% bone length. A) Trabecular bone area fraction (BA/TA), B) Trabecular number (Tb.N<sub>2D</sub>), C) Trabecular thickness (Tb.Th<sub>2D</sub>) and D) Trabecular separation (Tb.Sp<sub>2D</sub>). Individual animals are represented by red lines and mean  $\pm$  SE error bars are in black.

Although BA/TA is fairly uniform within the epiphyseal compartment, Tb.N<sub>2D</sub> and Tb.Th<sub>2D</sub> vary substantially throughout this region (Figures 4.3B & 4.3C). These two morphometric parameters have an inverse relationship, such that in the more distal

regions the trabeculae are fewer, but thicker than more proximally. The maximum differences of  $Tb.N_{2D}$  and  $Tb.Th_{2D}$  within this compartment are 33% and 31% respectively. Despite these microstructural changes  $Tb.Sp_{2D}$  remains approximately constant throughout (Figure 4.3D). For metaphyseal trabecular bone, the  $Tb.N_{2D}$  distributions decrease monotonically with distance from the growth plate in a similar manner to BA/TA. In contrast, between 88 and 80% bone length  $Tb.Th_{2D}$  statistically does not change, such that the rarefication of trabecular BA/TA here is associated with a reduction in number of trabeculae, but not their thickness, which results in a steady increase in separation. More proximally (80 – 60% bone length), the decline in BA/TA is a combination of decreasing number and thickness, which over a very short distance results in a rapid increase in separation, to the point where  $Tb.Sp_{2D}$  represents the average diameter of the marrow cavity.

Representative 10-week control cross-sectional trabecular bone slices with  $Tb.Th_{2D}$  mapped are shown in Figure 4.4 at 5% bone length intervals from 95% to 75% bone length from the proximal end. These cross-sections depict the spatial variation in trabecular bone in the radial directions, information lost in the 2D distributions which describe only the average longitudinal component of each morphological parameter. For epiphyseal regions (95% and 90% slices), despite only moderate changes in BA/TA (Figure 4.3A), the cross-sectional area (TA) varies considerably. Trabeculae within the condyles are on average thicker than in the more anterior regions of the epiphysis. For metaphyseal regions (85%, 80% and 75% slices) trabecular bone is not homogenously spaced within the marrow cavity, thicker trabeculae are primarily located in regions contiguous with the cortex, while thinner trabeculae extend into the central regions of the marrow cavity. More proximally, the extent of trabeculae into the central marrow cavity progressively decreases. The monotonically decreasing metaphyseal BA/TA and  $Tb.N_{2D}$  longitudinal gradients (Figure 4.3A & 4.3B) can then be explained by the presence of the

cone-like void of the marrow cavity, with its vertex positioned centrally within the primary spongiosa, which expands proximally. This explains the rapid increase in Tb.Sp<sub>2D</sub> between 80 and 70% bone length (Figure 4.3D), remaining trabeculae are primarily found in regions close to the cortex.

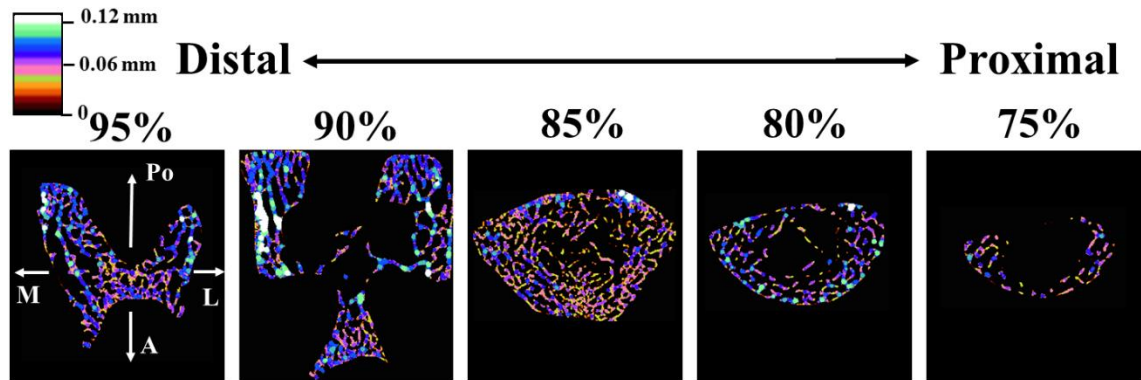


**Figure 4.4.** Cross-sectional segmented trabecular bone slices with Tb.Th<sub>2D</sub> mapped by colour, for a representative 10-week control femur at 5% bone length intervals from 95% - 75% bone length from the proximal-end. Po: posterior, A: anterior, M: medial and L: lateral.

#### 4.2.2 The Effects of Growth Throughout the Distal Femur

While similar overall trends in the distal femur trabecular bone morphometric distributions are seen between different timepoint post-surgery groups, growth does invoke important site-specific changes. Figure 4.5 provides a comparison of the trabecular bone morphometric distributions for 2 and 16-week post-surgery (14 and 28 weeks of age) control groups. For epiphyseal trabecular bone and growth plate regions there is a significant increase in BA/TA for 16-week compared to 2-week groups, which fluctuates between 7 and 11% ( $p < 0.01$ ) throughout (Figure 4.5A). Throughout the metaphyseal regions there were no growth-related changes in trabecular BA/TA.



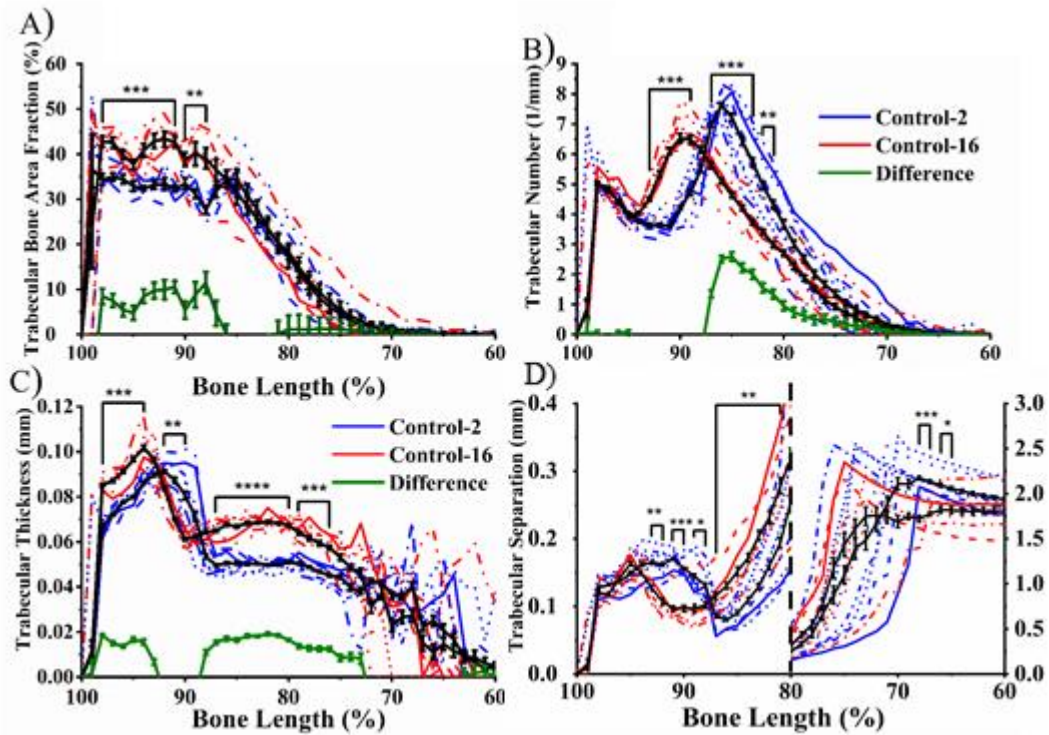


**Figure 4.5.** 2D  $\mu$ CT morphometric plots indicating the effects of growth on trabecular bone properties of the distal femur in anatomical time and space. 2-week and 16-week post sham-surgery control groups in blue ( $n = 8$ ) and red ( $n = 8$ ) respectively. The trabecular VOIs span 60 – 100% bone length. A) Trabecular bone area fraction ( $BA/TA_{2D}$ ), B) Trabecular number ( $Tb.N_{2D}$ ), C) Trabecular thickness ( $Tb.Th_{2D}$ ) and D) Trabecular Separation ( $Tb.Sp_{2D}$ ). Solid black lines represent the average for 2 week and 16-week control groups respectively, while the green line represents the difference in their average. Data shown as mean  $\pm$  SE. \*, \*\*, \*\*\* and \*\*\*\* indicate  $p < 0.05$ ,  $p < 0.01$ ,  $p < 0.001$  and  $p < 0.0001$  respectively.

The increase in epiphyseal trabecular BA/TA between the 2 and 16-week post-surgery control groups resulted from different growth-related structural changes in different regions of the epiphysis. In the most distal regions (98 - 94%), it resulted from increased  $Tb.Th_{2D}$  ( $p < 0.001$ ), but not  $Tb.N_{2D}$  (Figures 4.5B & 4.5C). This increase in thickness occurred quite uniformly throughout each cross-section. While in the more proximal epiphyseal regions (94 – 91%), it resulted from a combination of increased  $Tb.N_{2D}$  and decreased average  $Tb.Th_{2D}$  ( $p < 0.01$  for both). There was only a decrease in average  $Tb.Th_{2D}$ , due to the increased number of smaller trabeculae particularly in peripheral regions, thicker trabeculae remained within the condyles. The only significant changes in

Tb.Sp<sub>2D</sub> occurred in the proximal region where a significant reduction was observed ( $p < 0.01$ ). The maintenance of metaphyseal BA/TA with growth, was not due to constant trabecular thickness and number, in the older group, trabeculae were on average thicker, but there were fewer, particularly between 88 and 80% bone length ( $p < 0.01$ ), which led to an increase in average separation compared to the 2-week group. More proximal than 75% bone length, there were only transient differences in Tb.Sp<sub>2D</sub> and no difference in the normalised extent of the trabecular structure into the cortical shaft.

The metaphyseal slices (85%, 80% and 75%) highlight that despite relatively constant BA/TA between 2 and 16-week groups, the overall spatial distribution of trabecular bone had changed and that total area (TA) has increased; to maintain this ratio the amount of trabecular bone (BA) also increased in the older group (Figure 4.6). The growth-related microstructural changes described above are observed spatially by the formation of a more distinct cone-like central void, whose vertex occurs nearer to the distal growth plate in the older compared to younger group. The void is surrounded by fewer but thicker trabeculae.

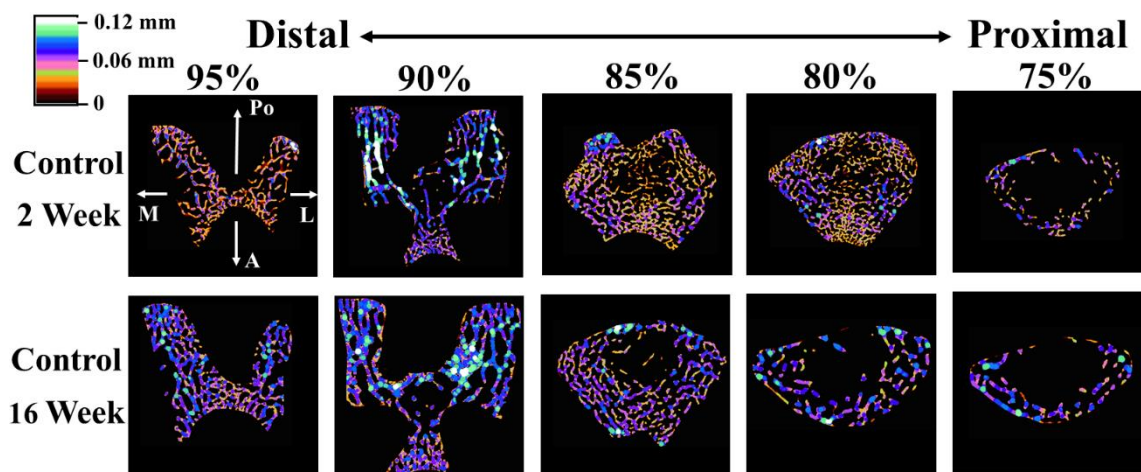


**Figure 4.6.** Cross-sectional segmented trabecular bone slices with Tb.Th<sub>2D</sub> mapped by colour, for representative 2 and 16-week post-surgery control group femurs at 5% bone length intervals from 95% - 75% bone length from the proximal-end. Po: posterior, A: anterior, M: medial and L: lateral.

### *4.2.3 The Effects of Spinal Cord Injury Throughout the Distal Femur*

SCI animals exhibited rapid site-specific patterns of trabecular bone loss in the distal femur. At 2 weeks, comparison of control and SCI group showed that the structural effects of SCI on BA/TA were not wide-spread, a significant reduction was seen only in the most distal regions (98 - 80% bone length) (Figure 4.7A). Metaphyseal regions proximal to the growth plate containing both primary and secondary spongiosa (88% - 80% bone length) experienced the most severe decreases in BA/TA. A peak difference in BA/TA between 2-week Control and SCI groups of 18% ( $p < 0.001$ ) was observed at 85% bone length. These metaphyseal changes were characterised by decreased Tb.N<sub>2D</sub> ( $p < 0.01$ ) and average Tb.Th<sub>2D</sub> ( $p < 0.01$ ) throughout, which resulted in increased Tb.Sp<sub>2D</sub> ( $p < 0.05$ ) throughout (Figures 4.7C, 4.7E & 4.7G). Further transient thinning of trabeculae was observed more proximally. In the 2-week SCI group nowhere within the metaphysis contained trabecular bone with a BA/TA greater than 26%, while in the 2-week Control group BA/TA of up 36% was observed. The distal femoral trabecular bone extent (Tb.E) quantifies how far metaphyseal trabecular bone extends into the medullary cavity. The Tb.E at BA/TA equal to 20% (Tb.E<sub>BA/TA = 20%</sub>) was 8.5% bone length for SCI-2, while for Control-2 Tb.E<sub>BA/TA = 20%</sub> was 2.5% bone length, despite this difference there was no statistically significant difference in the overall extent of metaphyseal bone at 2 weeks post-surgery (Figure 4.9A). Compared to metaphyseal trabecular bone within the proximity of the growth plate, less severe reductions in BA/TA ( $p < 0.01$ ) were observed for epiphyseal trabecular bone, characterised by decreased Tb.Th<sub>2D</sub> ( $p < 0.01$ ) but not Tb.N<sub>2D</sub>.



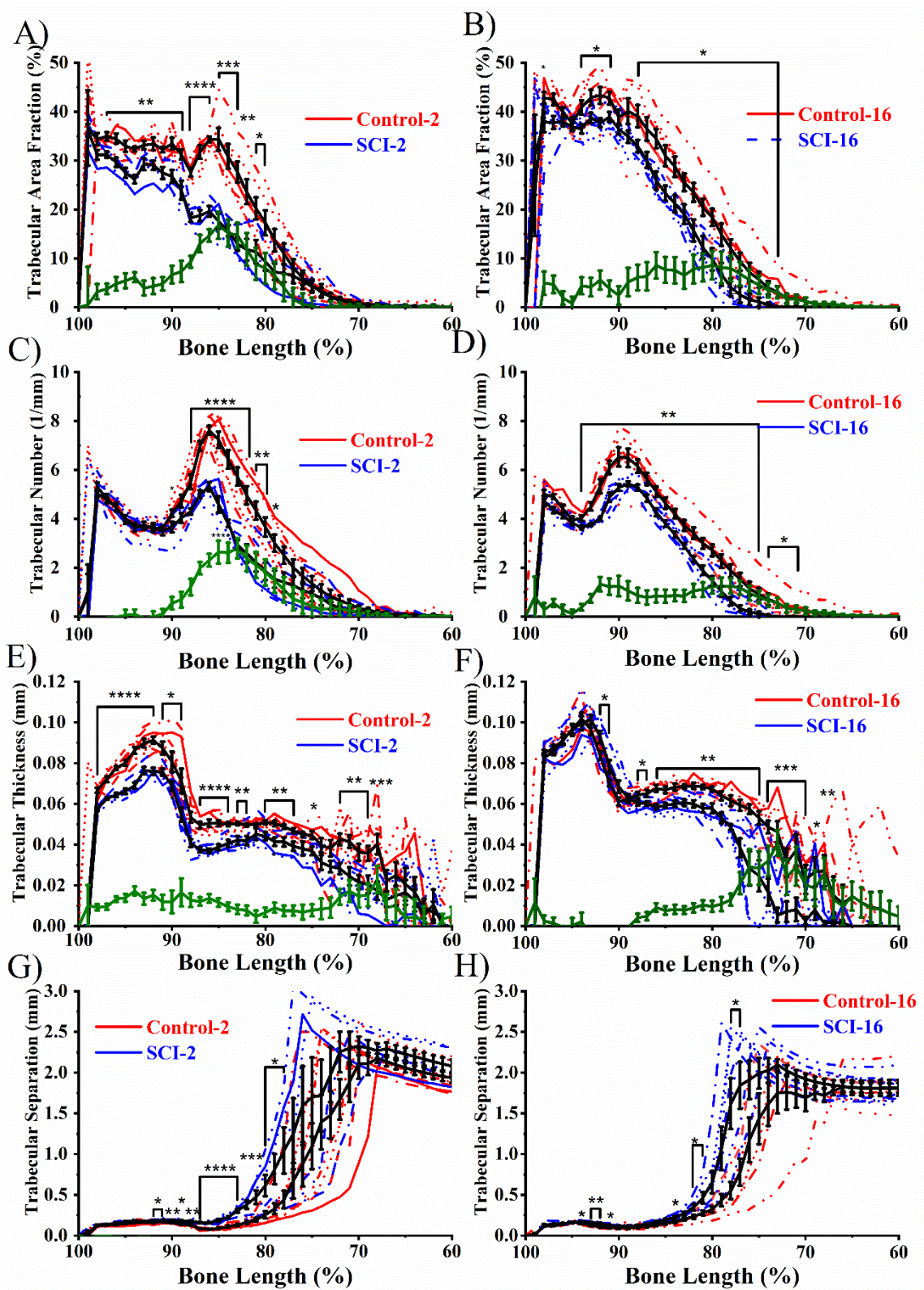


**Figure 4.7.** Trabecular bone morphometric distributions of the distal femoral trabecular structure. A) and B) Trabecular bone area fraction (BA/TA), C) and D) Trabecular thickness (Tb.Th<sub>2D</sub>), E) and F) Trabecular number (Tb.N<sub>2D</sub>) and G) and H) Trabecular separation (Tb.Sp<sub>2D</sub>) for 2-week control and SCI groups and 16-week control and SCI groups respectively (n = 8 for all groups). Control groups in red and

SCI groups in blue. The trabecular VOIs span 60 – 100% bone length. Solid black lines represent the average for control and SCI groups, while the green line represents the difference in the average between the control and SCI group. Data shown as mean  $\pm$  SE. \*, \*\*, \*\*\* and \*\*\*\* indicate  $p < 0.05$ ,  $p < 0.01$ ,  $p < 0.001$  and  $p < 0.0001$  respectively.

By 16 weeks post-surgery, there were more wide-spread decreases in metaphyseal BA/TA than at 2 weeks, covering 88 to 73% bone length, although this was less site-specific with a peak difference in BA/TA at 16 weeks between control and SCI of 9% ( $p < 0.05$ ), which occurred at 80% of bone length (Figure 4.7B). Over the entire region both Tb.N<sub>2D</sub> ( $p < 0.01$ ) and Tb.Th<sub>2D</sub> ( $p < 0.05$ ) were significantly reduced, with only regional significant increases in Tb.Sp<sub>2D</sub> (Figures 4.7D, 4.7F & 4.7H). Nowhere within the metaphysis contained trabecular bone with a BA/TA greater than 38% in 16-week SCI femurs, while in 16-week control femurs BA/TA of up 45% was observed. There were significant decreases in the extent of trabecular bone at all four measurement sites (BA/TA = 30%, 20%, 10% and 0) compared to control (Figure 4.9B). This indicated that the extent of the trabecular structure had significantly decreased, as shown in Figure 4.8 and qualitatively in Figure 4.30. Epiphyseal BA/TA was only significantly decreased in the most proximal regions (91 – 94%) bone length, characterised by decreased Tb.N<sub>2D</sub> ( $p < 0.01$ ).

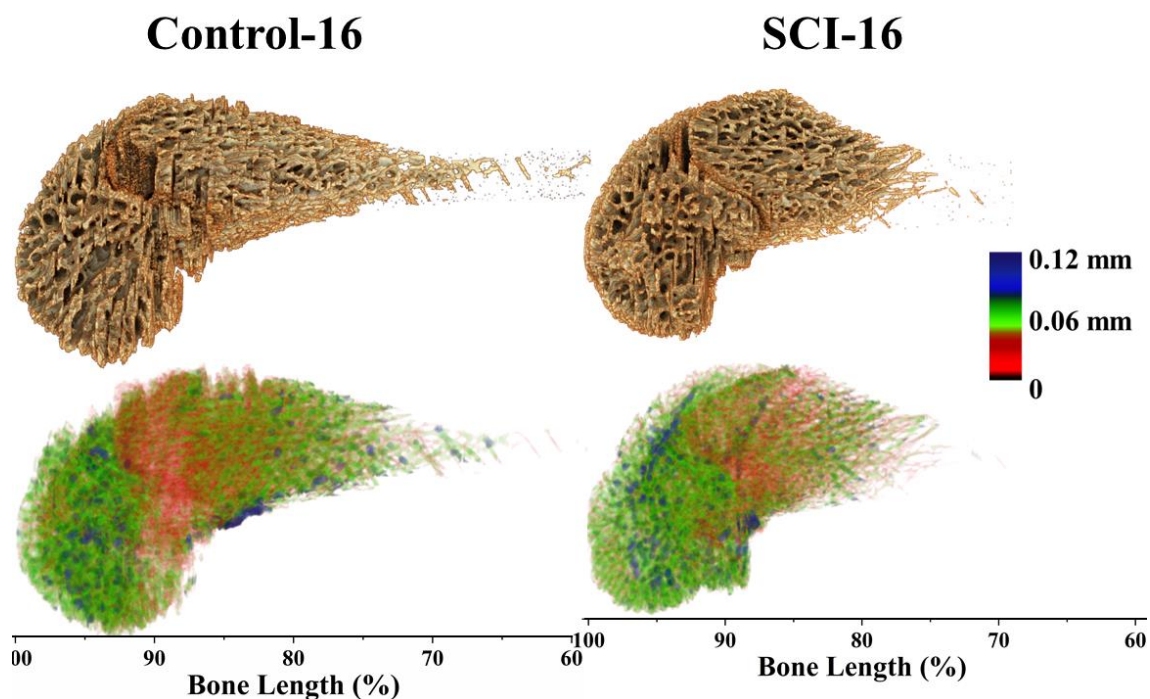


**Figure 4.8.** Representative 16-week control and SCI complete distal femoral trabecular bone structures with 3D trabecular thickness mapped.

The metaphyseal slices (85%, 80% and 75%) in Figure 4.10 highlight that the severe decrease in BA/TA in 2 week-post SCI rats was due to uniform thinning of trabeculae across each cross-section, such that the originally thinner more centrally-located trabeculae were removed. In contrast, the more moderate decrease in BA/TA of the thicker epiphyseal trabecular bone was characterised by only a uniform thinning of trabeculae throughout each cross-section, without removal of trabeculae. At 16 weeks post-SCI, the remaining trabeculae thickened as the rat grew.

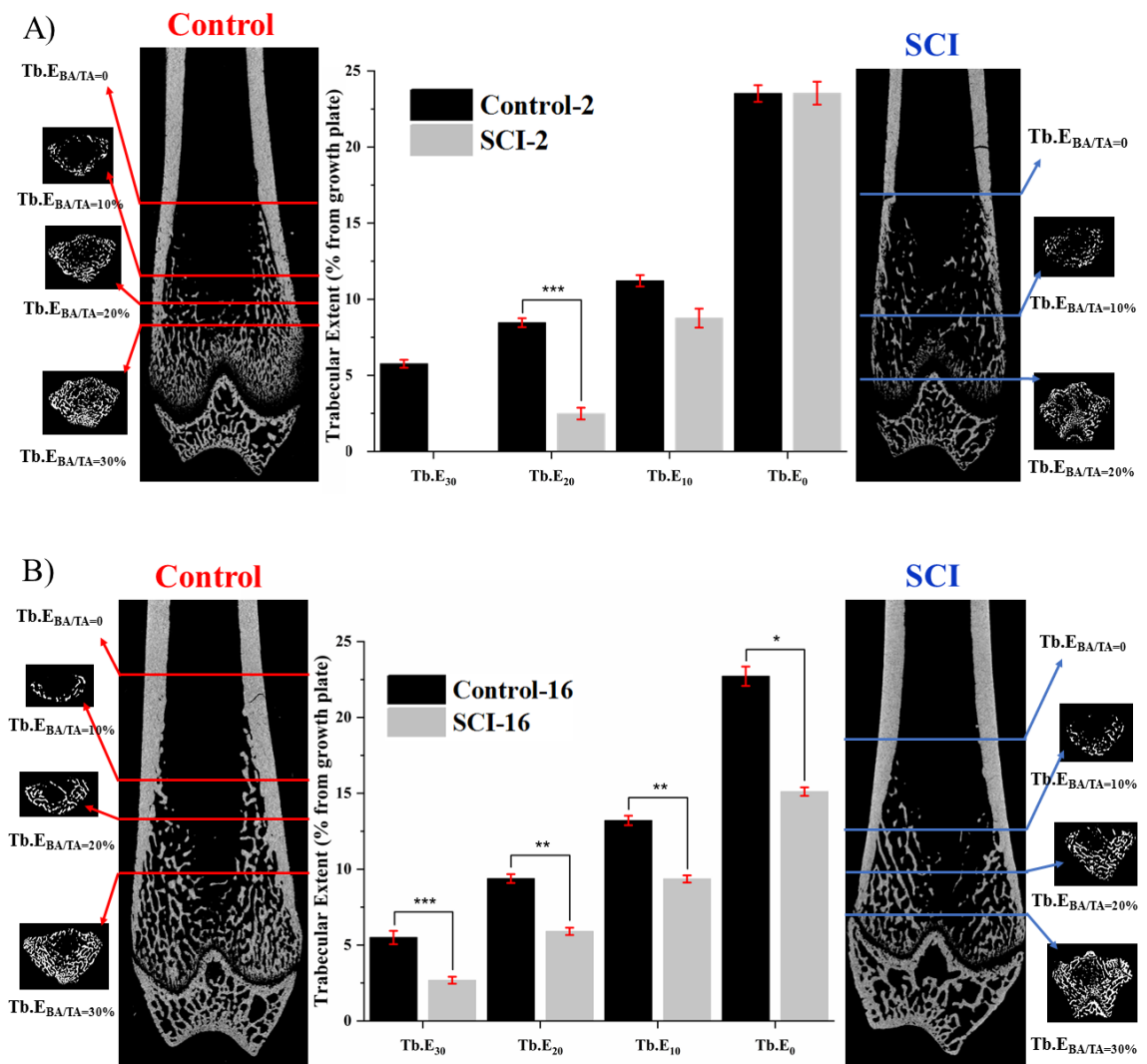


**Figure 4.9.** Trabecular extent (Tb.E) measured from the distal growth plate, proximal through to the diaphysis, as a function of trabecular area fraction (BA/TA), at BA/TA = 30%, 20%, 10% and 0 (first occurrence) for A) 2-week control and SCI groups and B) 16-week control and SCI groups. Data shown as mean  $\pm$  SE. \*, \*\* and \*\*\* indicate  $p < 0.05$ ,  $p < 0.01$  and  $p < 0.001$  respectively. Coronal  $\mu$ CT slices of representative control and SCI distal femur for both timepoints are depicted with binarised cross-sectional slices at each Tb.E value quantified, depicting the BA/TA present at that slice.



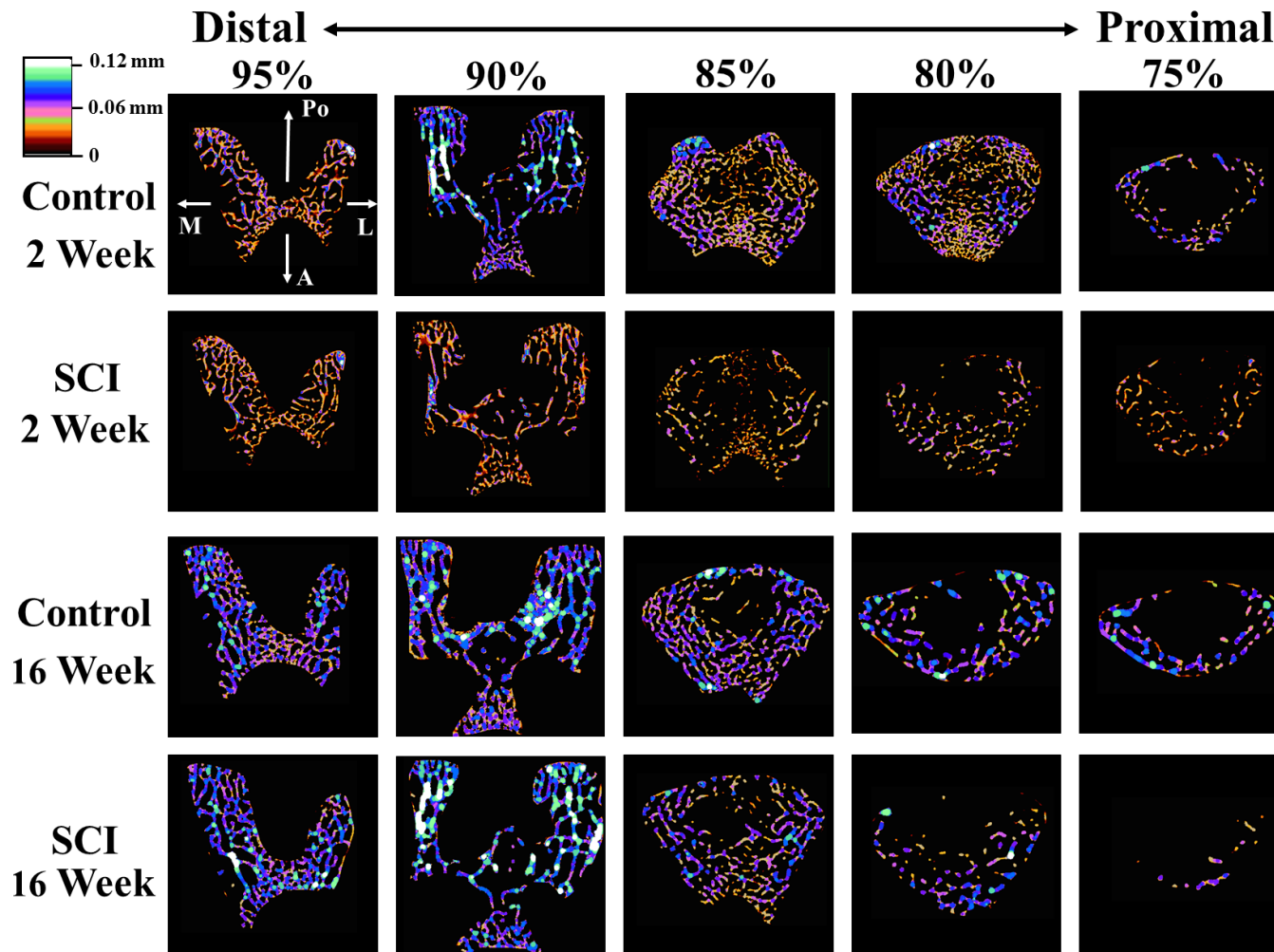


**Figure 4.10.** Cross-sectional segmented trabecular bone slices with Tb.Th<sub>2D</sub> mapped by colour, for representative 2 and 16-week post-surgery control and SCI groups at 5% bone length intervals from 95% - 75% bone length from the proximal end of the rat femur. Po: posterior, A: anterior, M: medial and L: lateral.



#### *4.2.4 Direct 3D Trabecular Morphometry*

To further examine the trabecular bone microstructure 3D morphometry was performed on three distinct VOIs. The metaphyseal compartment was further subdivided and enabled the distinction of primary spongiosa from more mature secondary spongiosa. The three trabecular VOI used were:

- i) Metaphyseal secondary spongiosa (MSS) (81 – 85% bone length),
- ii) Metaphyseal primary spongiosa (MPS) (85 - 89% bone length),
- iii) Epiphyseal secondary spongiosa (ESS) (93 – 97% bone length).

Further to this, results for all four post-surgery time point groups (2, 6, 10 and 16 weeks) are calculated for both surgery types:

- i) Sham-operated (control),
- ii) T9 transection spinal cord injury (SCI).

There were significant interactions between (3-way ANOVA):

- i) Surgery type – Time post-surgery,
- ii) Surgery type – VOI,
- iii) Time post-surgery – VOI.

Most morphometric parameters indicated that all three anatomically distinct trabecular VOIs, were affected by “normal” growth and SCI in different time-dependent ways post-surgery.

#### 4.2.4.1 Metaphyseal Secondary Spongiosa

The SCI animals rapidly lost mature metaphyseal trabecular bone after complete transection of the spinal cord at T9. After just 2 weeks, compared to control, there was a 59% ( $p < 0.01$ ) decrease in trabecular bone volume fraction (BV/TV) (Figure 4.11). For all later time point groups trabecular BV/TV remained approximately constant, i.e. there was no further significant growth-related changes in either SCI or control groups. A peak difference in MSS trabecular BV/TV occurred at 6 weeks post-SCI of 75% ( $p < 0.0001$ ).

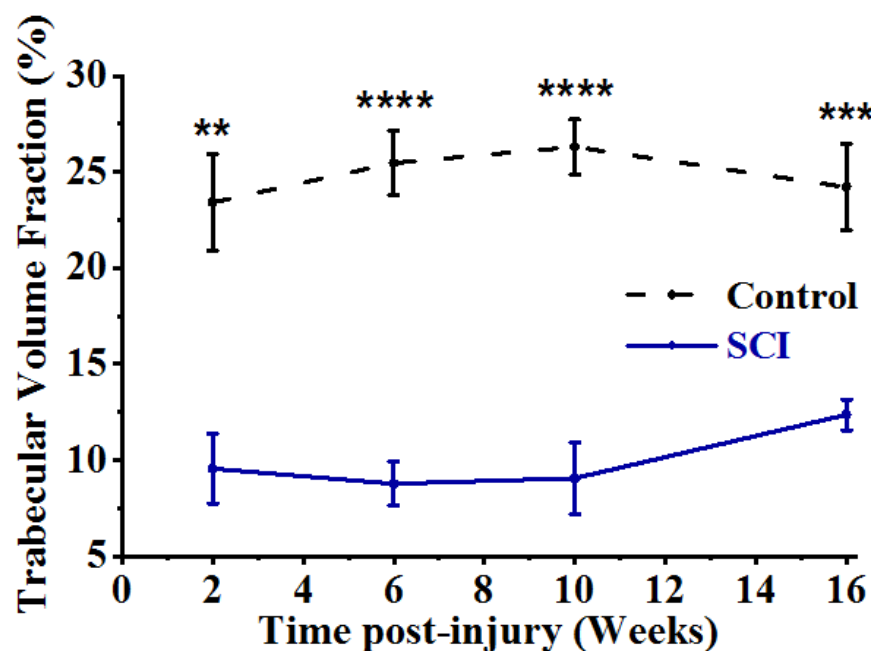


**Figure 4.11.** Trabecular bone volume fraction (BV/TV) for metaphyseal secondary spongiosa VOIs as a function of time for control (black dashed line) and SCI (blue line) groups. Data shown as mean  $\pm$  SE. \*\*, \*\*\* and \*\*\*\* indicate  $p < 0.01$ ,  $p < 0.001$  and  $p < 0.0001$  respectively.

At 2 weeks post-SCI compared to control, the decrease in MSS trabecular BV/TV was characterised by a 53% ( $p < 0.001$ ) and 15% ( $p < 0.01$ ) decrease respectively in average trabecular number (Tb.N) and thickness (Tb.Th) (Figure 4.12A & 4.12B). This resulted in a 65% ( $p < 0.05$ ) increase in average trabecular separation (Tb.Sp), which particularly affected proximal regions of the VOI (Figure 4.12C and 4.13). Despite no significant changes in the BV/TV of MSS at later time points post-SCI, significant changes to its

microarchitecture did occur. In longer term SCI groups, Tb.N stayed relatively constant, but the remaining trabeculae monotonically increased in thickness, by 16 weeks post-SCI Tb.Th was on average 39% ( $p < 0.0001$ ) higher than at 2 weeks. Tb.Sp monotonically increased between 2 and 10-weeks post-SCI. Control groups behaved similarly.

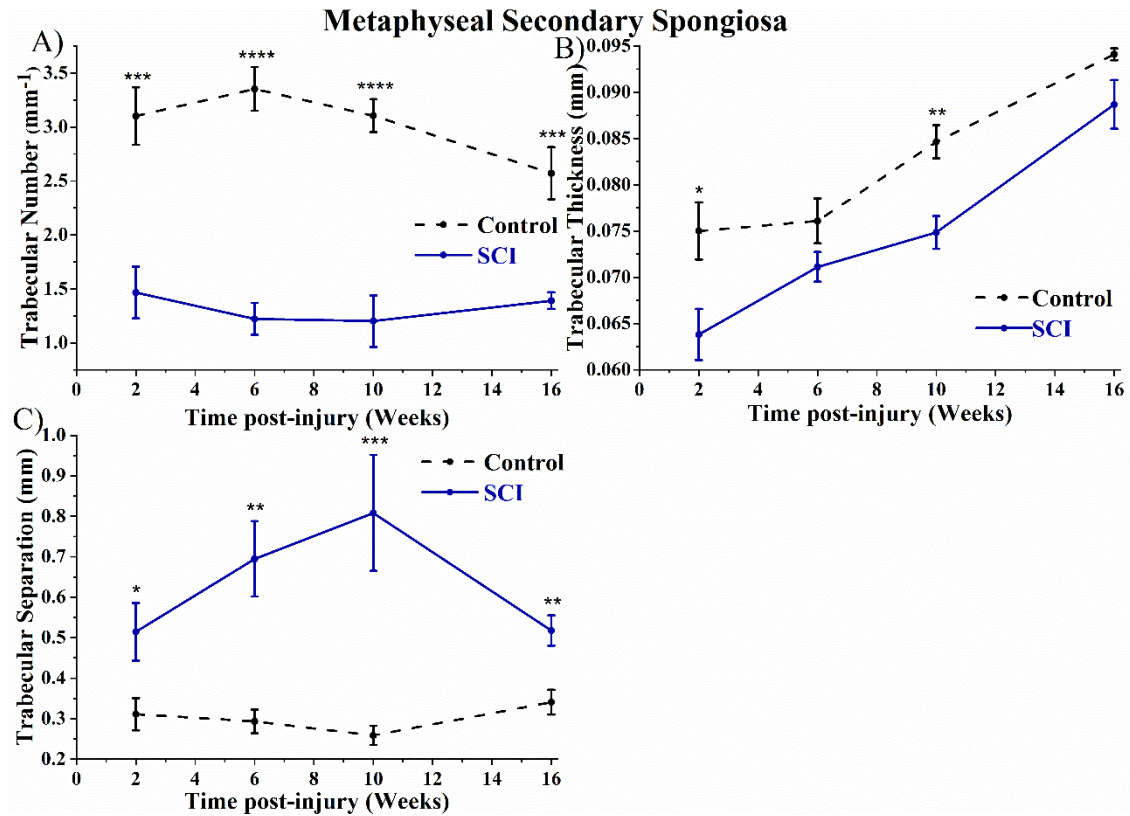


**Figure 4.12.** Directly-assessed morphometric indices for metaphyseal secondary spongiosa VOIs for 2, 6, 10 and 16-week control (black dashed line) and SCI (blue line) groups. A) Trabecular Number (Tb.N), B) Trabecular Thickness (Tb.Th) and C) Trabecular Separation (Tb.Sp). Data shown as mean  $\pm$  SE. \*, \*\*, \*\*\* and \*\*\*\* indicate  $p < 0.05$ ,  $p < 0.01$ ,  $p < 0.001$  and  $p < 0.0001$  respectively.

## Metaphyseal Secondary Spongiosa

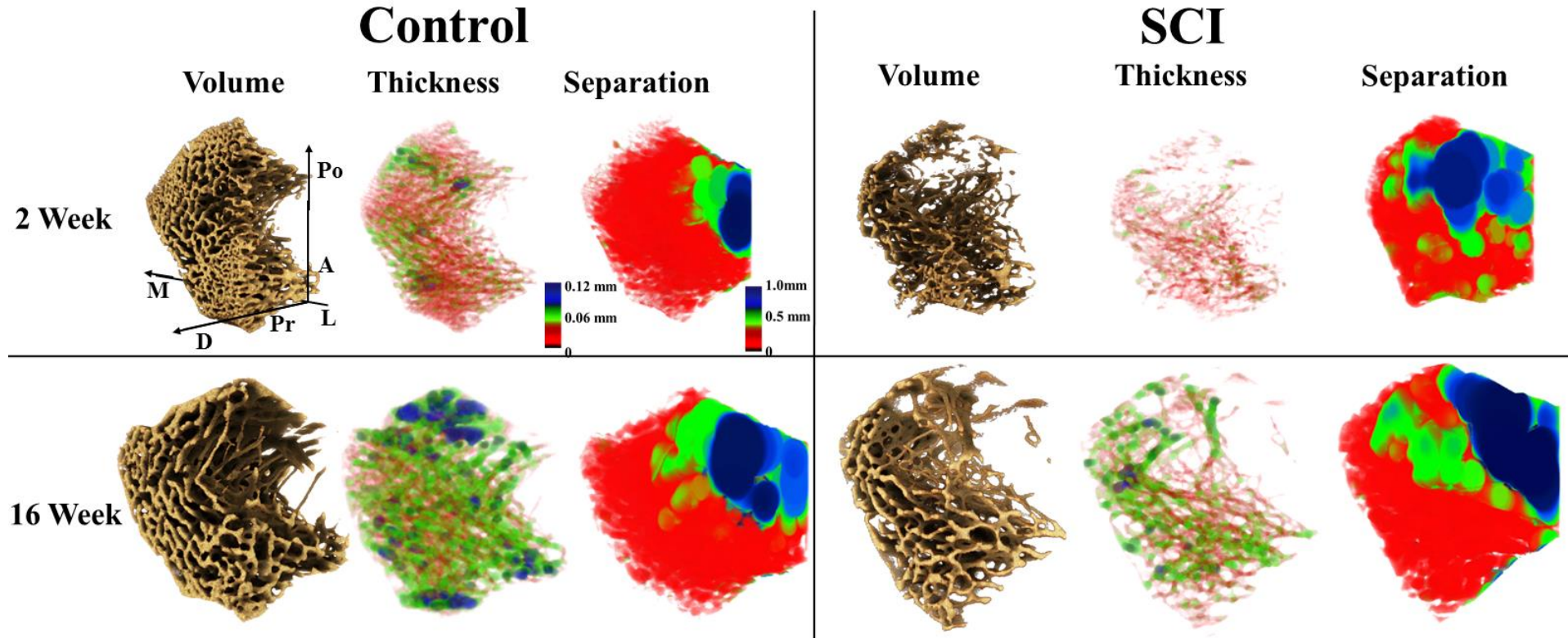


**Figure 4.13.** Representative metaphyseal secondary spongiosa VOIs (81 – 85% bone length) clipped in the L to M direction to show interior, for 2 and 16-week control and SCI distal femurs. Trabecular thickness (Tb.Th) and trabecular separation (Tb.Sp) mapped separately to the structure. Pr: proximal, D: distal, Po: posterior, A: anterior, M: medial, L: lateral.

At 2 weeks post-SCI, the fewer remaining thinner trabeculae in the MSS compartment had on average 30% ( $p < 0.01$ ) higher specific bone surface to volume ratios (BS/BV) compared to their control group (Figure 4.14B). With time the change in BS/BV in both groups reflected inversely the change in Tb.Th, i.e. as trabeculae thickness increased, the surface area to volume ratio decreased. The breaking of a single trabecular connection leaves the entire trabecular network less well connected, this is evident as early as 2 weeks post-injury, where the connectivity density (Conn.D) of the trabecular structure was on average 32% ( $p < 0.01$ ) decreased compared to control (Figure 4.14A). There was a further monotonic decline in the Conn.D in later groups post-SCI, which appeared to plateau by 10 weeks post-SCI. Control Conn.D also declined in later groups, but not monotonically. The peak difference in Conn.D between a time-matched control and SCI group was 59% ( $p < 0.01$ ) and occurred at 10 weeks post-injury.

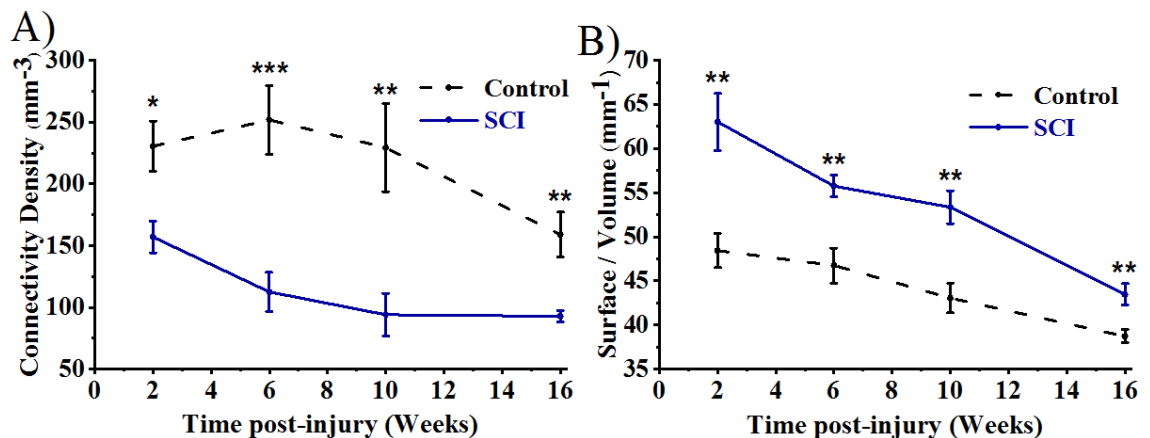


**Figure 4.14.** Directly-assessed non-metric morphometric indices for metaphyseal secondary spongiosa VOIs for 2, 6, 10 and 16-week control (black dashed line) and SCI (blue line) groups. A) connectivity density (Conn.D) and B) specific bone surface to volume (BS/BV). Data shown as mean  $\pm$  SE. \*, \*\* and \*\*\* indicate  $p < 0.05$ ,  $p < 0.01$  and  $p < 0.001$  respectively.

The structure model index (SMI) characterises the surface curvature of trabeculae in terms of the ratio of convex to concave surfaces. At 2 weeks post-SCI, there is a 59% ( $p < 0.001$ ) increase in SMI, such that the remaining trabecular post-SCI are significantly

more convex (Figure 4.15A), as confirmed by Tb.Pf (Table 4.1). SMI was maintained at later time point post-SCI groups. There was no significant variation in SMI between control groups. Degree of anisotropy (DA) is a measure of how highly orientated are the trabeculae. An overall significant trend of decreasing in DA with time post-surgery for both SCI and control groups was found indicating that both groups become more isotropic with time (Figure 4.15B). The fractal dimension (FD) is a measure of a structure's overall complexity, its self-similarity and space filling capacity. At 2 weeks post-SCI, FD was significantly decreased compared to control, with no significant time-post injury recovery (Table 4.1).

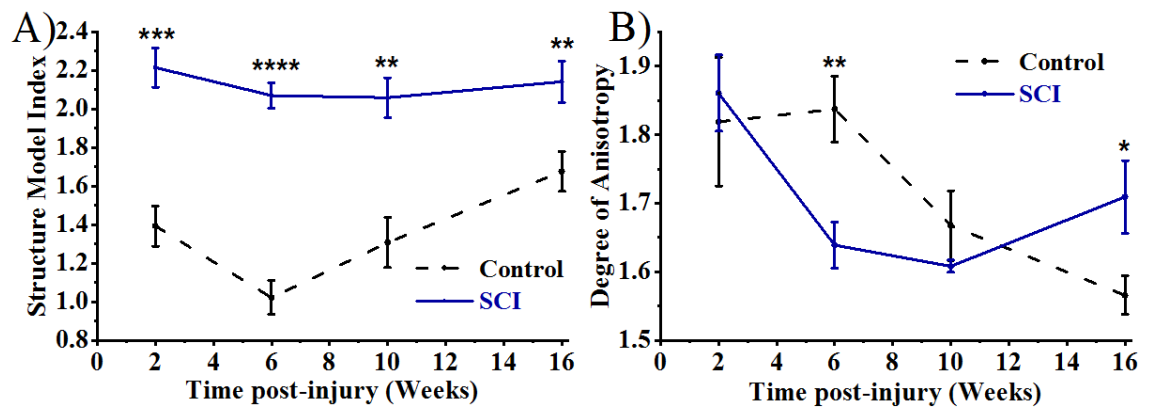


**Figure 4.15.** Directly-assessed non-metric morphometric indices for metaphyseal secondary spongiosa VOIs for 2, 6, 10 and 16-week control (black dashed line) and SCI (blue line) groups. A) Structure model index (SMI) and B) Degree of Anisotropy (DA). Data shown as mean  $\pm$  SE. \*, \*\*, \*\*\* and \*\*\*\* indicate  $p < 0.05$ ,  $p < 0.01$ ,  $p < 0.001$  and  $p < 0.0001$  respectively.

#### *4.2.4.2 Metaphyseal Primary Spongiosa*

The metaphyseal primary spongiosa (MPS) VOIs (Figure 4.17), are adjacent to the distal growth plate and as such, depending on the age of the animal, contain varying quantities of the two main types of trabecular bone (primary and secondary spongiosa). 2-week post-surgery VOIs contain predominantly primary spongiosa, while 16-week post-surgery VOIs contain predominantly secondary spongiosa. Compared to the more distal MSS, this VOI in a young healthy rat would contain a significant higher density of trabeculae, characterised by more but much thinner trabeculae (Table 4.1). For example, in the 2 weeks post-surgery control group, these VOIs had on average 148% ( $p < 0.001$ ) higher Tb.N, but 15% ( $p < 0.001$ ) lower average Tb.Th compared to the MSS VOIs. As with the MSS VOI, SCI animals rapidly underwent significant losses of this thinner-structured, but more spatially dense trabecular bone compared to control. At 2 weeks post-SCI compared to control, there was a 54% ( $p < 0.0001$ ) decrease in MPS BV/TV (Figure 4.16A). This was the peak difference between age-matched control and SCI groups, with no further reduction in BV/TV at later times. Control animals underwent a non-significant growth-related decline.



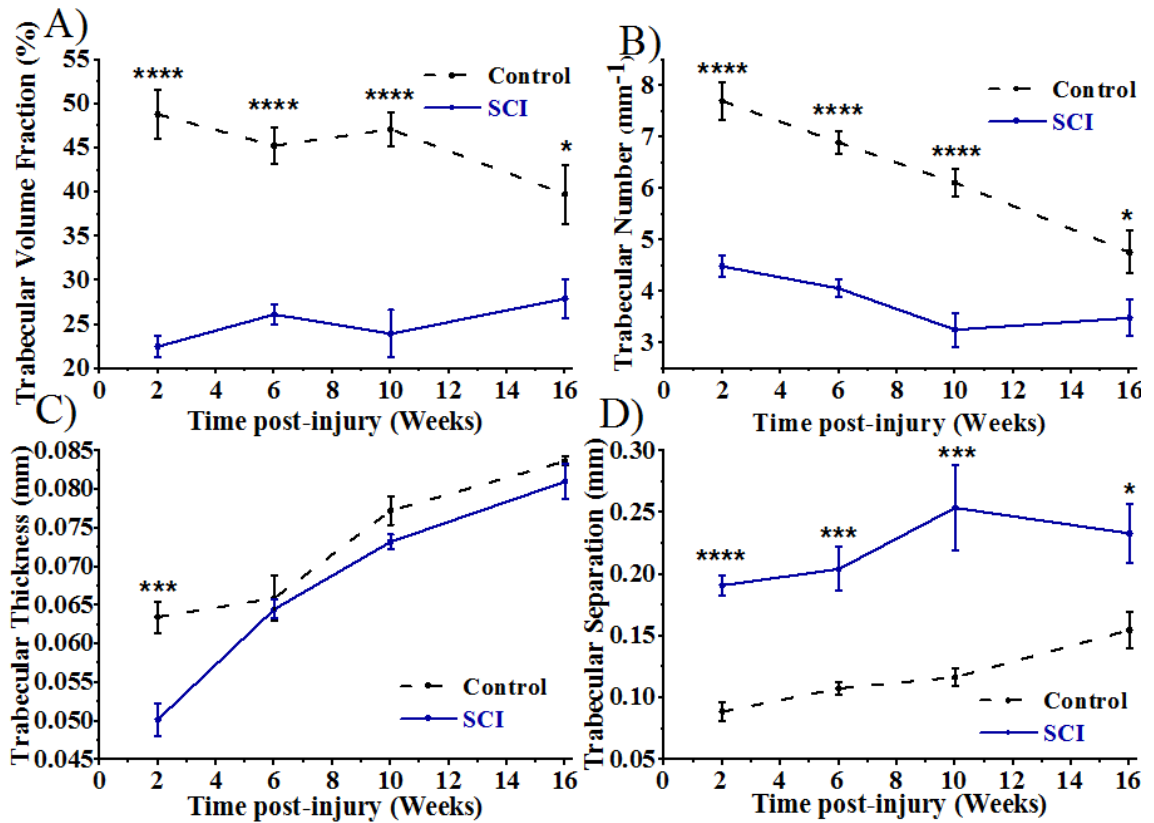


**Figure 4.16.** Directly-assessed morphometric indices for metaphyseal primary spongiosa VOIs as a function of time for control (black dashed line) and SCI (blue line) groups. A) Trabecular Bone Volume Fraction (BV/TV), B) Trabecular Number (Tb.N), C) Trabecular Thickness (Tb.Th) and D) Trabecular Separation (Tb.Sp). Data shown as mean  $\pm$  SE. \*, \*\*\*, \*\*\*\* indicate  $p < 0.05$ ,  $p < 0.001$  and  $p < 0.0001$  respectively.

At 2 weeks post-SCI compared to control, the decrease in MPS trabecular BV/TV was characterised by 54% ( $p < 0.0001$ ) and 31% ( $p < 0.001$ ) decreases in average Tb.N and Tb.Th respectively (Figure 4.16B & 4.16C). This resulted in a 115% ( $p < 0.0001$ ) increase in average Tb.Sp (Figure 4.16D). The spatial changes these percentages represent are shown in Figure 4.17. Despite no further significant changes in the trabecular BV/TV in either group, significant changes in the microarchitecture of both SCI and control were seen at later time points. The remaining primary spongiosa transitioned to more fully-modelled mature secondary spongiosa, as observed in the control groups, where an almost linear lowering of Tb.N and monotonic increases in Tb.Th and Tb.Sp with time post-



surgery was seen. For SCI groups, no further significant reductions in Tb.N were seen, but the fewer remaining trabeculae on average thickened with time, so much so that by 6 weeks post-injury Tb.Th was comparable with control.

## Metaphyseal Primary Spongiosa

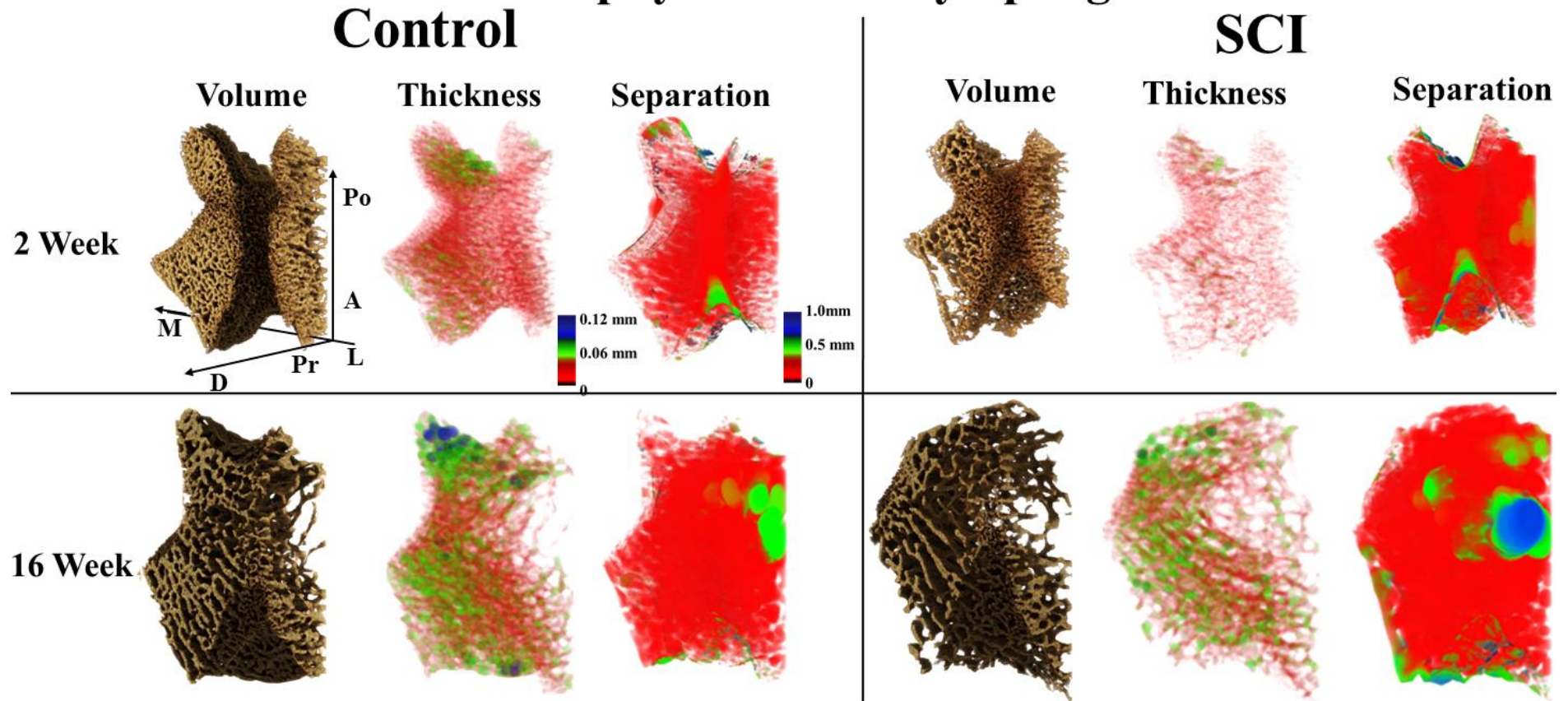


**Figure 4.17.** Representative metaphyseal primary spongiosa VOIs (85 – 89% bone length) clipped in the L to M direction to show interior, for 2 and 16-week control and SCI distal femurs. Trabecular thickness (Tb.Th) and trabecular separation (Tb.Sp) mapped separately to the structure. Pr: proximal, D: distal, Po: posterior, A: anterior, M: medial, L: lateral.

At 2 weeks post-SCI, the compromised MPS VOIs exhibited on average 27% ( $p < 0.05$ ) decrease in Conn.D compared to control (Figure 4.18A). There were further monotonic but slower decreases at later time points. In control rats this decrease in Conn.D was almost linear, such that by 16 weeks, both structures were comparable, even though the SCI group had significantly fewer trabeculae. BS/BV was significantly elevated compared to 2-week control, but the effects of growth significantly decreased this ratio in a similar manner to that seen within the MSS VOI (Figure 4.18B). At 2 weeks post-SCI, the trabecular structure became more rod-like compared to control as measured by SMI, with trabecular surfaces becoming more convex (Figure 4.18C). Later time point groups showed no further significant transformations in to a more plate-like architecture. Both SCI and control trabecular structures became progressively less preferentially aligned in later time point groups (Figure 4.18D).

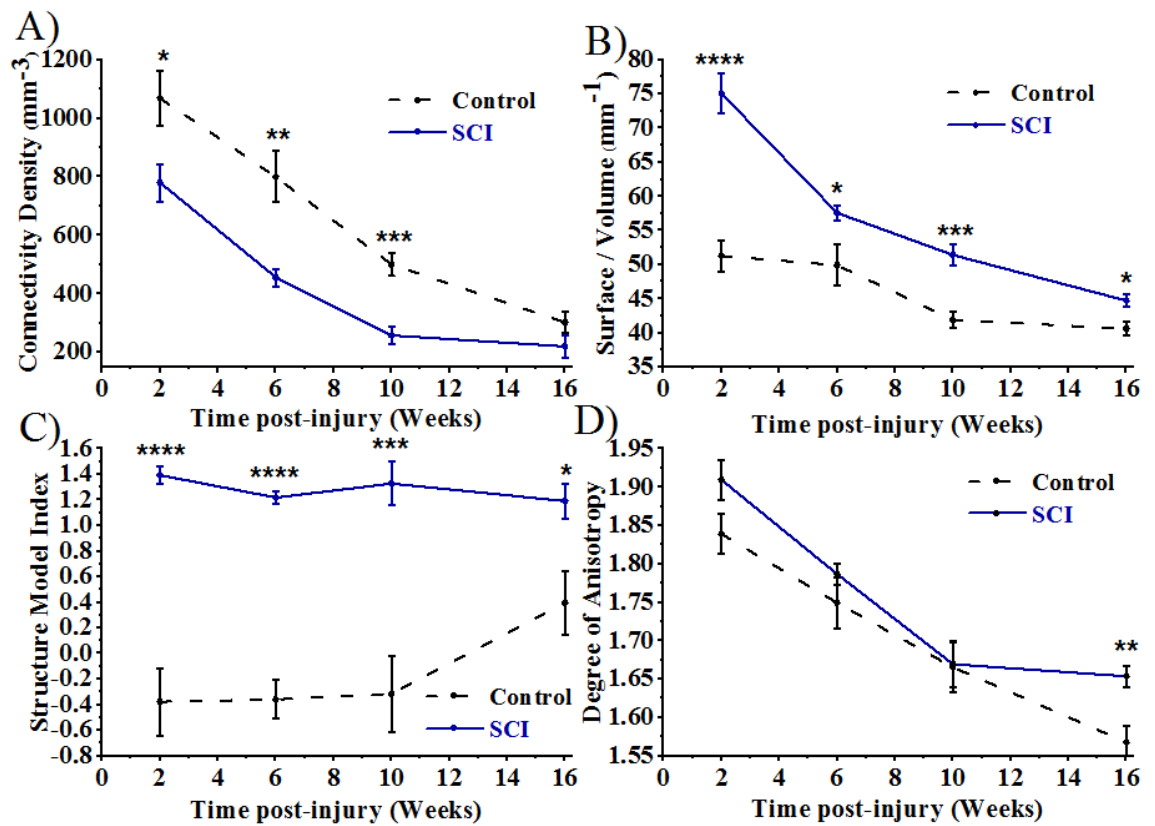


**Figure 4.18.** Directly-assessed non-metric morphometric indices for metaphyseal primary spongiosa VOIs for 2, 6, 10 and 16-week control groups (black dashed line) and SCI (blue line) groups. A) connectivity

density (Conn.D), B) specific bone surface to volume (BS/BV), C) structure model index (SMI) and D) degree of anisotropy (DA). Data shown as mean  $\pm$  SE. \*, \*\*, \*\*\* and \*\*\*\* indicate  $p < 0.05$ ,  $p < 0.01$ ,  $p < 0.001$  and  $p < 0.0001$  respectively.

#### 4.2.4.3 Epiphyseal Trabecular Bone

The EES compartment is composed of an approximately uniform volume fraction of trabecular bone that is on average thicker than metaphyseal trabecular bone. After 2 weeks, there was a 23% ( $p < 0.001$ ) decrease of BV/TV compared to control. This was the maximum difference between SCI and control (Figure 4.19A). Unlike the metaphyseal trabecular VOIs, the epiphyseal VOI for both SCI and control groups displayed growth-related increases in BV/TV, with a 25 % increase ( $p < 0.0001$ ) between 2 and 10-week control groups and a 42 % increase ( $p < 0.0001$ ) between 2 and 16-week SCI groups.

At 2 weeks post-SCI, the decrease in BV/TV compared to control was characterised by a 15% ( $p < 0.001$ ) decrease in average Tb.Th compared to control (Figure 4.19C). The growth-related increase in BV/TV between 2 and 10-week control groups was primarily characterised by a 22% ( $p < 0.01$ ) increase in Tb.N (Figure 4.19B). While for SCI groups, the BV/TV between 2 and 16 weeks was primarily characterised by a 26% ( $p < 0.001$ ) increase in Tb.Th, with a modest 13% ( $p < 0.05$ ) increase in Tb.N. The spatial patterns of these epiphyseal trabecular bone changes due to growth and SCI are shown in Figure 4.20 for representative 2 and 16-week post-surgery control and SCI VOIs.

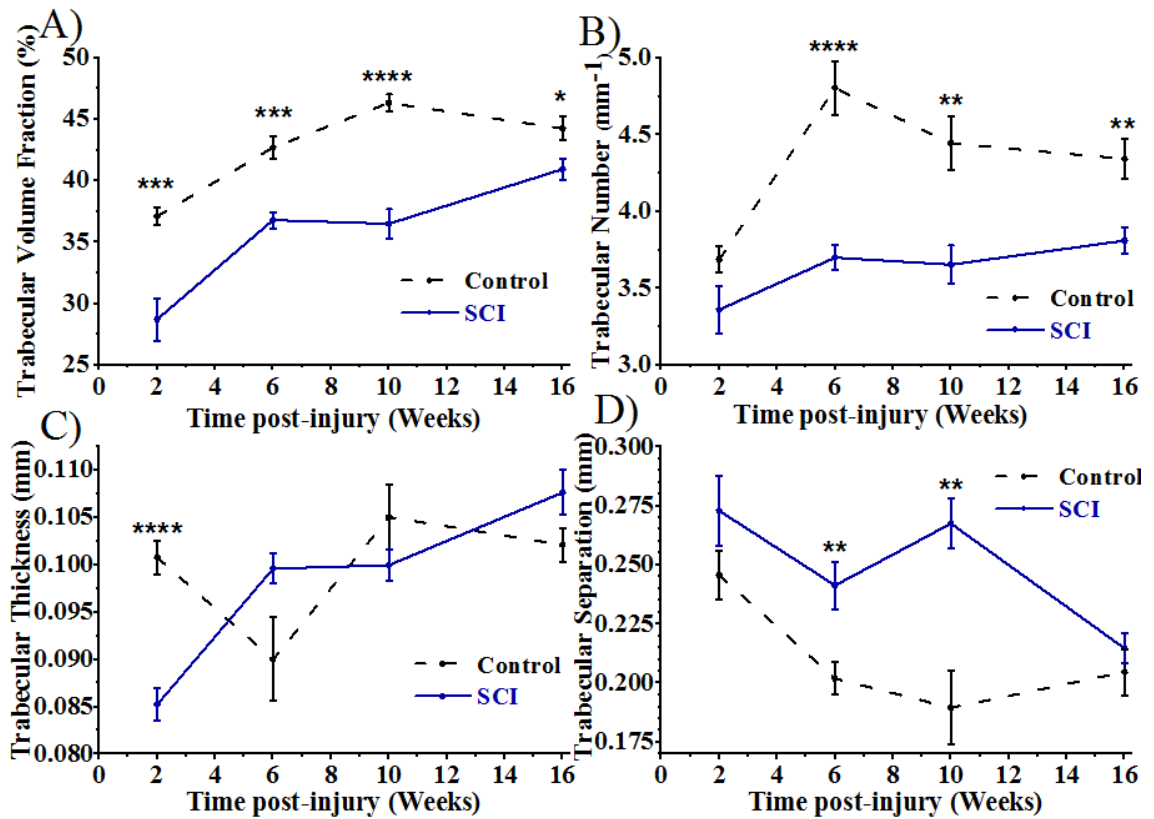


**Figure 4.19.** Directly-assessed morphometric indices for epiphyseal secondary spongiosa VOIs for 2, 6, 10 and 16-week control and SCI (blue line) groups. A) Trabecular volume fraction (BV/TV), B) Trabecular Number (Tb.N), C) Trabecular Thickness (Tb.Th) and D) Trabecular Separation (Tb.Sp). Data shown as mean  $\pm$  SE. \*, \*\*, \*\*\*, \*\*\*\* indicate  $p < 0.05$ ,  $p < 0.01$ ,  $p < 0.001$  and  $p < 0.0001$  respectively.

The Conn.D of the ESS network was not found to be significantly affected by SCI, but there were comparable growth-related decreases for both control and SCI groups, with total overall decreases of 53% ( $p < 0.05$ ) and 55% ( $p < 0.001$ ) between 2 and 16 weeks for control and SCI groups respectively (Figure 4.21A). The initial decrease in Tb.Th led to a significant increase in BS/BV for 2-week SCI compared to control, with further growth-related monotonic decline on par with age-match controls (Figure 4.21B). 6-week post-surgery and later SCI groups were more anisotropic with age compared to control groups ( $p < 0.01$ ) (Figure 4.21D).



## Epiphyseal Trabecular Bone

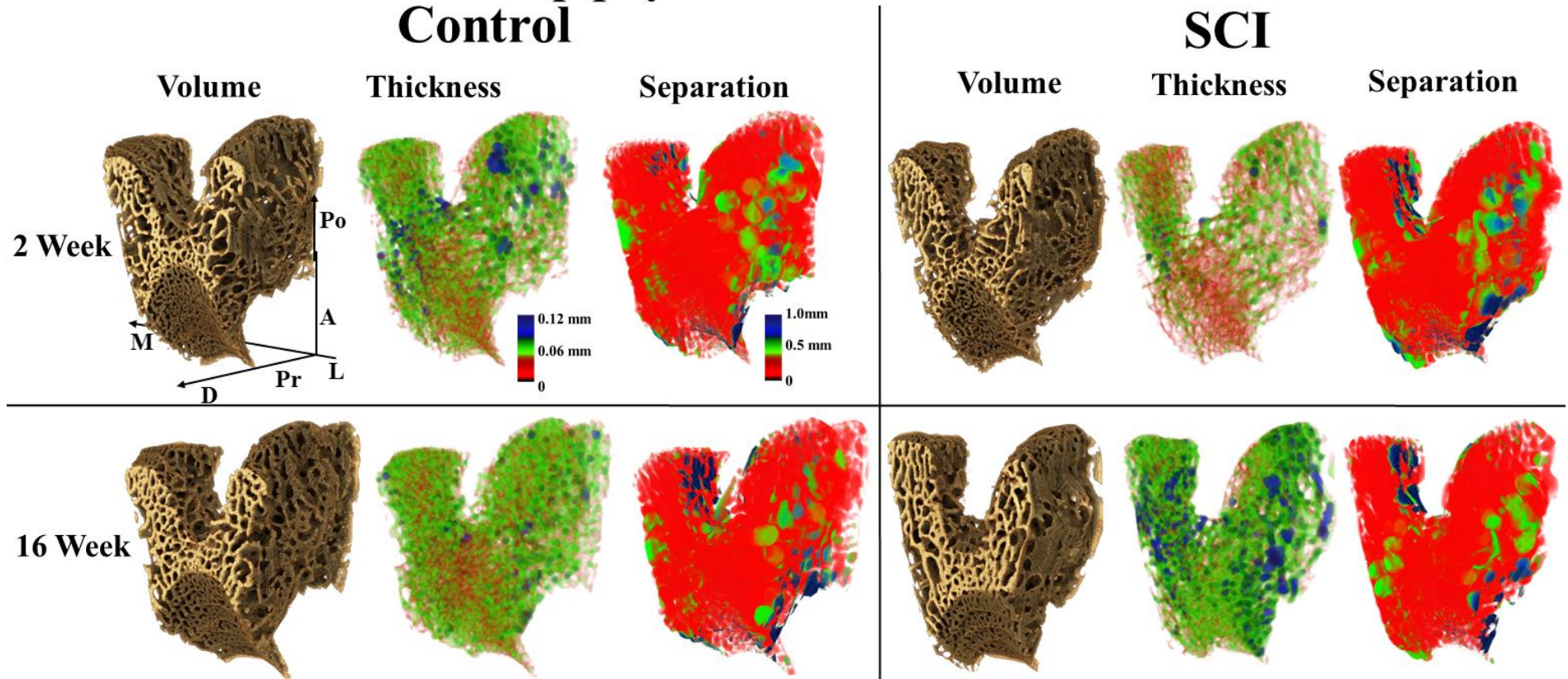


**Figure 4.20.** Representative epiphyseal trabecular bone VOIs (97 – 93% bone length), for 2 and 16-week control and SCI distal femurs. Trabecular thickness (Tb.Th) and trabecular separation (Tb.Sp) mapped separately to the structure. Pr: proximal, D: distal, Po: posterior, A: anterior, M: medial, L: lateral.

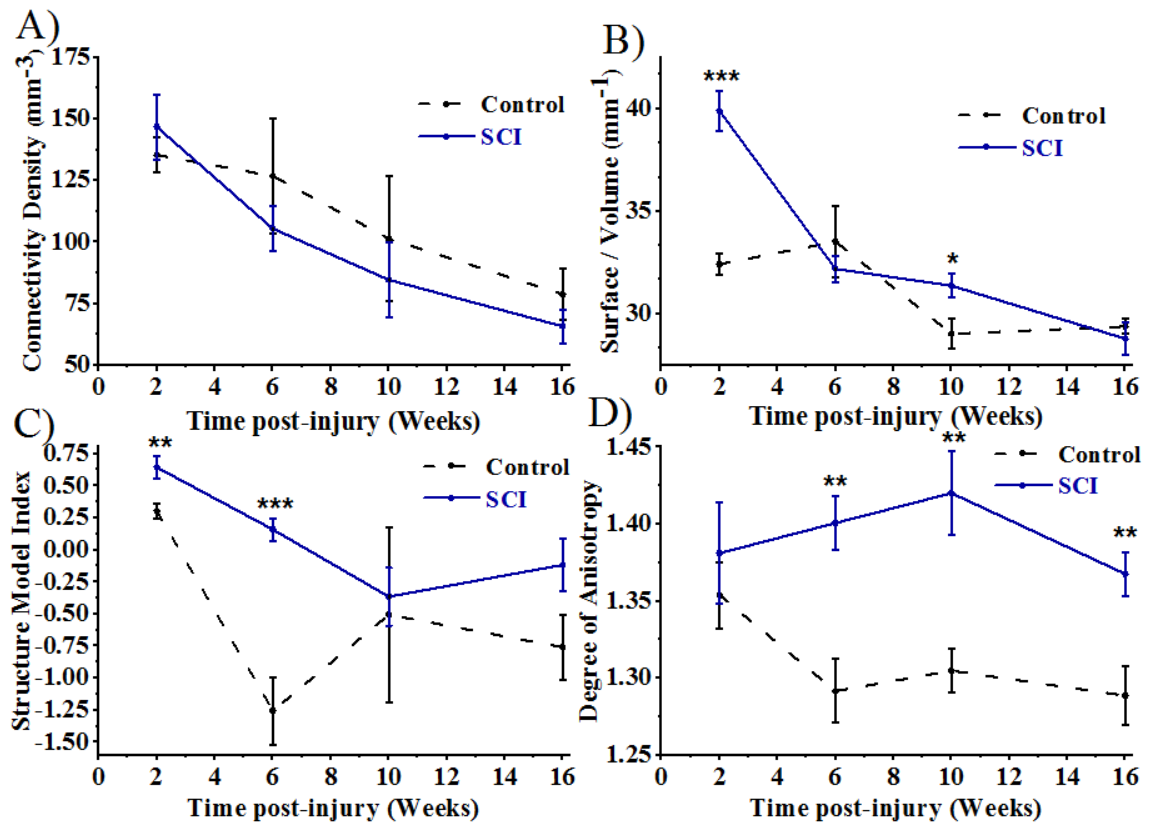


**Figure 4.21.** Directly-assessed non-metric morphometric indices for metaphyseal primary spongiosa VOIs for 2, 6, 10 and 16-week control (black dashed line) and SCI (blue line) groups. A) connectivity density (Conn.D), B) specific bone surface to volume (BS/BV), C) structure model index (SMI) and D) degree of anisotropy (DA). Data shown as mean  $\pm$  SE. \*, \*\*, \*\*\* and \*\*\*\* indicate  $p < 0.05$ ,  $p < 0.01$ ,  $p < 0.001$  and  $p < 0.0001$  respectively.

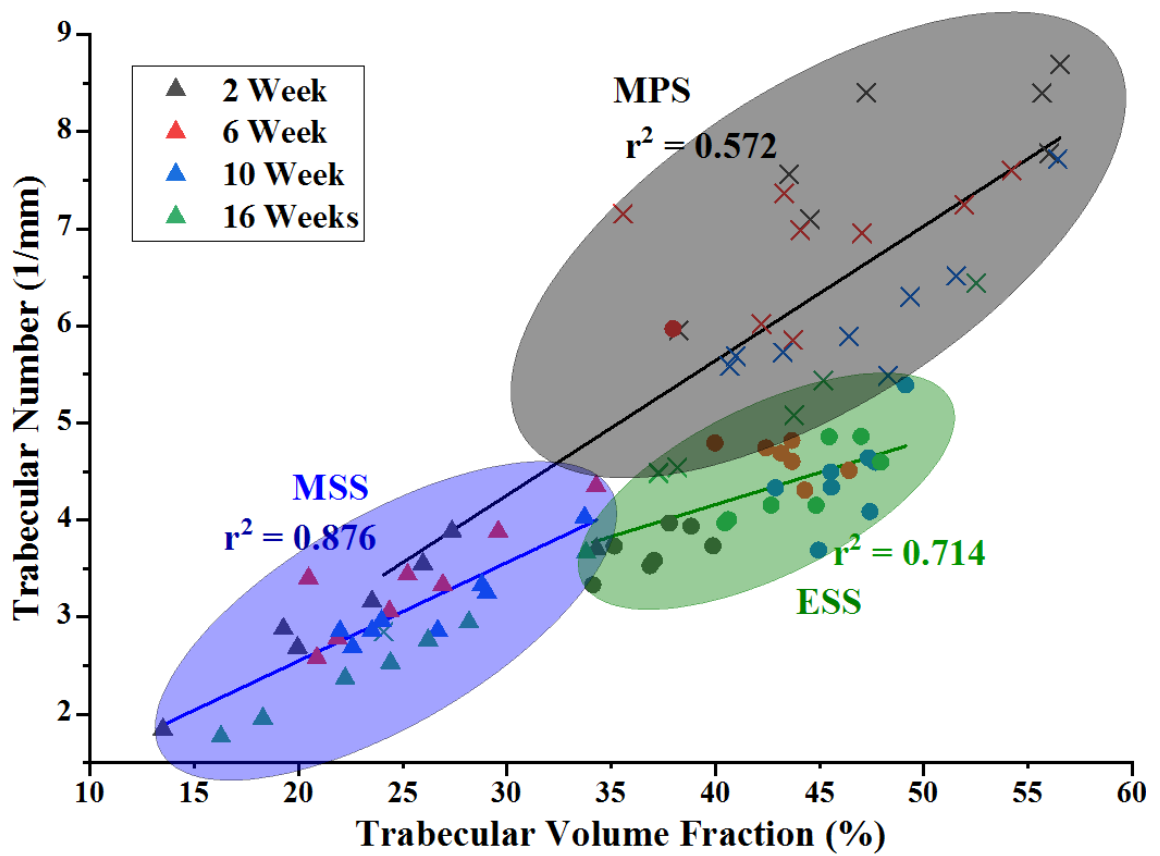


**Figure 4.22.** Graph of trabecular number against trabecular volume fraction for all three trabecular VOIs of interest for control. Black, red, blue, and green markers represent 2, 6, 10 and 16-week groups. Triangles, crosses and circles represent metaphyseal secondary spongiosa (MSS), metaphyseal primary spongiosa (MPS) and epiphyseal secondary spongiosa (ESS) respectively. The grey, green and blue ellipses show the MPS, MSS and ESS locations.



**Table 4.1.** 3D morphology of three trabecular VOIs within the distal femur; metaphyseal secondary spongiosa (81 – 85% bone length), metaphyseal primary spongiosa (85 – 89% bone length) and epiphyseal secondary spongiosa (93 – 97% bone length).

	Control				SCI			
	2 Weeks (n = 8)	6 Weeks (n = 8)	10 Weeks (n = 8)	16 Weeks (n = 9)	2 Weeks (n = 8)	6 Weeks (n = 8)	10 Weeks (n = 8)	16 Weeks (n = 9)
<b>Secondary Spongiosa</b>								
BV (mm <sup>3</sup> )	4.86 ± 0.63	6.67 ± 0.52 <sup>a</sup>	6.24 ± 0.42	6.28 ± 0.68	2.20 ± 0.45*	1.70 <sup>a</sup> ± 0.21*	1.91 ± 0.49*	2.86 ± 0.24 <sup>*,b</sup>
BV/TV <sup>S,S-T</sup> (%)	23.41 ± 2.53	25.45 ± 1.67	26.29 ± 1.43	24.20 ± 2.26	9.55 ± 1.81*	8.76 ± 1.16*	9.04 ± 1.88*	12.35 ± 0.80*
BS/BV (mm <sup>-1</sup> )	51.29 ± 2.32	49.92 ± 3.00	41.88 ± 1.22 <sup>a,b</sup>	40.62 ± 0.94 <sup>a,b</sup>	75.09 ± 2.91*	57.56 ± 1.17 <sup>*,a</sup>	51.43 ± 1.60 <sup>*,a</sup>	44.71 ± 0.97 <sup>*,a,b</sup>
Tb.Th <sup>S,T,S-T</sup> (mm)	0.08 ± 0.00	0.08 ± 0.00	0.08 ± 0.00 <sup>a,b</sup>	0.09 ± 0.00 <sup>a,b,c</sup>	0.06 ± 0.00*	0.07 ± 0.00	0.07 ± 0.00 <sup>*,a</sup>	0.09 ± 0.00 <sup>a,b,c</sup>
Tb.Sp <sup>S,S-T</sup> (mm)	0.31 ± 0.04	0.29 ± 0.03	0.26 ± 0.02	0.34 ± 0.03	0.51 ± 0.07*	0.69 ± 0.09*	0.81 ± 0.14*	0.52 ± 0.04*
Tb.N <sup>S,S-T</sup> (mm <sup>-1</sup> )	3.10 ± 0.27	3.35 ± 0.20	3.10 ± 0.15	2.57 ± 0.24	1.47 ± 0.24*	1.22 ± 0.15*	1.20 ± 0.24*	1.39 ± 0.08*
Tb.Pf <sup>S,T,S-T</sup> (mm <sup>-1</sup> )	8.54 ± 1.22	4.15 ± 0.95 <sup>a</sup>	10.23 ± 4.03	9.19 ± 1.04 <sup>b</sup>	20.95 ± 2.03*	17.28 ± 1.28*	16.48 ± 1.44*	15.11 ± 1.39*
SMI <sup>S,T,S-T</sup>	1.39 ± 0.10	1.02 ± 0.09	1.63 ± 0.39	1.67 ± 0.10 <sup>b</sup>	2.21 ± 0.10*	2.07 ± 0.07*	2.06 ± 0.10*	2.14 ± 0.11*
Conn.D <sup>S,T,S-T</sup> (mm <sup>-3</sup> )	230.55 ± 20.17	251 ± 28.09	229.34 ± 35.72	158.82 ± 18.23	156.99 ± 12.75*	112.44 ± 15.91*	94.02 ± 17.29 <sup>*,a</sup>	92.83 ± 4.73 <sup>*,a</sup>
DA <sup>S,T,S-T</sup>	1.82 ± 0.09	1.84 ± 0.05	1.67 ± 0.05	1.57 <sup>a,b</sup> ± 0.03	1.86 <sup>*</sup> ± 0.06	1.64 <sup>*,a</sup> ± 0.03	1.61 <sup>a</sup> ± 0.01	1.71 <sup>*</sup> ± 0.05
FD <sup>S,S-T</sup>	2.54 ± 0.03	2.59 ± 0.02	2.59 ± 0.02	2.53 ± 0.03	2.32 ± 0.06*	2.24 ± 0.05*	2.25 ± 0.07*	2.34 ± 0.02*

	Control				SCI			
	2 Weeks (n = 8)	6 Weeks (n = 8)	10 Weeks (n = 8)	16 Weeks (n = 9)	2 Weeks (n = 8)	6 Weeks (n = 8)	10 Weeks (n = 8)	16 Weeks (n = 9)
<b>Primary Spongiosa</b>								
BV (mm <sup>3</sup> )	6.79 ± 0.38	7.81 ± 0.34	8.08 ± 0.32 <sup>a</sup>	7.47 ± 0.74	2.88 ± 0.20*	3.52 ± 0.12*	3.54 ± 0.41*	4.84 ± 0.57* <sup>a,b</sup>
BV/TV <sup>T,T-S</sup> (%)	48.84 ± 2.76	45.27 ± 2.07	47.13 ± 1.92	39.76 ± 3.34	22.50 ± 1.23*	26.14 ± 1.10*	23.96 ± 2.69*	27.93 ± 2.25*
BS/BV (mm <sup>-1</sup> )	48.43 ± 19.4	46.75 ± 1.98	43.07 ± 1.68	38.73 ± 0.74 <sup>a,b</sup>	63.02 ± 3.24*	55.75 ± 1.23*	53.35 ± 1.85* <sup>a</sup>	43.46 ± 1.23* <sup>a,b,c1</sup>
Tb.Th <sup>S,T,T-S</sup> (mm)	0.06 ± 0.00	0.07 ± 0.00	0.08 ± 0.00 <sup>a,b</sup>	0.08 ± 0.00 <sup>a,b,c</sup>	0.05 ± 0.00*	0.06 ± 0.00 <sup>a</sup>	0.07 ± 0.00 <sup>a,b</sup>	0.08 ± 0.00 <sup>a,b,c</sup>
Tb.Sp <sup>S,T,T-S</sup> (mm)	0.09 ± 0.01	0.11 ± 0.01	0.12 ± 0.01	0.15 ± 0.01	0.19 ± 0.01*	0.20 ± 0.05*	0.25 ± 0.03*	0.23 ± 0.02* <sup>a,b,c</sup>
Tb.N <sup>S,T,S-T</sup> (mm <sup>-1</sup> )	7.70 ± 0.36	6.90 ± 0.22	6.11 ± 0.26 <sup>a</sup>	4.76 ± 0.42 <sup>a,b,c</sup>	4.49 ± 0.20*	4.06 ± 0.18*	3.26 ± 0.33* <sup>a</sup>	3.49 ± 0.36*
Tb.Pf <sup>S,T,S-T</sup> (mm <sup>-1</sup> )	-15.78 ± 2.86	-13.84 ± 1.38	-11.02 ± 2.59	-3.63 ± 2.65 <sup>a,b</sup>	8.95 ± 1.69*	5.78 ± 2.19*	7.28 ± 1.96*	4.79 ± 1.51*
SMI <sup>S,S-T</sup>	-0.38 ± 0.26	-0.36 ± 0.15	-0.32 ± 0.30	0.40 ± 0.25	1.39 ± 0.07*	1.22 ± 0.05*	1.33 ± 0.17*	1.19 ± 0.14*
Conn.D <sup>S,T,S-T</sup> (mm <sup>-3</sup> )	1068.77 ± 94.56	800.25 ± 87.97	500.02 ± 38.49 <sup>a,b</sup>	302.55 ± 36.71 <sup>a,b</sup>	780.63 ± 63.75*	455.99 ± 29.60* <sup>a</sup>	257.67 ± 28.93* <sup>a,b</sup>	220.10 ± 38.34 <sup>a,b</sup>
DA <sup>S,T,S-T</sup>	1.84 ± 0.03	1.75 ± 0.03	1.67 ± 0.03 <sup>a</sup>	1.57 ± 0.02 <sup>a,c</sup>	1.91 ± 0.03	1.79 ± 0.01 <sup>a</sup>	1.67 ± 0.03 <sup>a,b</sup>	1.65 ± 0.01* <sup>a,b</sup>
FD <sup>S,S-T</sup>	2.67 ± 0.01	2.67 ± 0.00	3.67 ± 0.01	2.65 ± 0.02	2.55 ± 0.03*	2.56 ± 0.01*	2.53 ± 0.03*	2.57 ± 0.02*

	Control				SCI			
	2 Weeks (n = 8)	6 Weeks (n = 8)	10 Weeks (n = 8)	16 Weeks (n = 9)	2 Weeks (n = 8)	6 Weeks (n = 8)	10 Weeks (n = 8)	16 Weeks (n = 9)
<b>Epiphysis</b>								
BV (mm <sup>3</sup> )	11.69 ± 0.69	12.92 ± 0.50	12.96 ± 0.35	11.30 ± 0.69	9.15 ± 0.55*	11.84 ± 0.36 <sup>a</sup>	11.72 ± 0.30* <sup>a</sup>	12.16 ± 0.44 <sup>a</sup>
BV/TV <sup>S,T,S-T</sup> (%)	37.11 ± 0.76	42.71 <sup>a</sup> ± 0.93	46.33 ± 0.69 <sup>a,b</sup>	44.24 ± 0.97 <sup>a</sup>	28.72 ± 1.73*	36.79 ± 0.66* <sup>a</sup>	36.49 ± 1.19* <sup>a</sup>	40.93 ± 0.82* <sup>a,b,c</sup>
BS/BV (mm <sup>-1</sup> )	32.42 ± 0.51	33.53 ± 1.74	29.04 ± 0.72 <sup>b</sup>	29.39 ± 0.35 <sup>b</sup>	39.90 ± 1.00*	32.20 ± 0.64 <sup>a</sup>	31.3 <sup>a</sup> ± 0.60* <sup>a</sup>	29.39 ± 0.80 <sup>a,b</sup>
Tb.Th <sup>S,T,S-T</sup> (mm)	0.10 ± 0.00	0.09 ± 0.00	0.11 ± 0.00 <sup>b</sup>	0.10 ± 0.00 <sup>b</sup>	0.09 ± 0.00*	0.10 ± 0.00 <sup>a</sup>	0.10 ± 0.00 <sup>a</sup>	0.11 ± 0.00 <sup>a,b,c</sup>
Tb.Sp <sup>S,T,S-T</sup> (mm)	0.25 ± 0.01	0.20 ± 0.01	0.19 ± 0.02 <sup>a</sup>	0.20 ± 0.01	0.27 ± 0.01	0.24 ± 0.01*	0.27 ± 0.01*	0.21 ± 0.01 <sup>a,c</sup>
Tb.N <sup>S,T,S-T</sup> (mm <sup>-1</sup> )	3.69 ± 0.09	4.80 ± 0.18 <sup>a</sup>	4.44 ± 0.17 <sup>a</sup>	4.34 ± 0.13 <sup>a</sup>	3.36 ± 0.16	3.70 ± 0.08*	3.65 ± 0.12*	3.81 ± 0.08* <sup>a</sup>
Tb.Pf <sup>S,T,S-T</sup> (mm <sup>-1</sup> )	-2.29 ± 0.41	-14.79 ± 3.17 <sup>a</sup>	-7.35 ± 4.05	-8.95 ± 1.67	0.93 ± 0.86*	-3.01 ± 0.55*	-6.62 ± 1.81 <sup>a</sup>	-4.28 ± 1.21* <sup>a,b</sup>
SMI <sup>S,T,S-T</sup>	0.30 ± 0.06	-1.26 ± 0.26	-0.51 ± 0.68	-0.76 ± 0.25	0.64 ± 0.09*	0.16 ± 0.09*	-0.37 ± 0.22 <sup>a</sup>	-0.12 ± 0.21 <sup>a</sup>
Conn.D <sup>T,S-T</sup> (mm <sup>-3</sup> )	135.4 ± 7.17	126.82 ± 23.16	101.41 ± 25.31	78.83 ± 10.22 <sup>a</sup>	146.77 ± 13.19	105.48 ± 9.15	84.67 ± 15.23 <sup>a</sup>	65.77 ± 6.76 <sup>a</sup>
DA <sup>S,S-T</sup>	1.35 ± 0.02	1.29 ± 0.02	1.30 ± 0.01	1.29 ± 0.02	1.38 ± 0.03	1.40 ± 0.02*	1.42 ± 0.03*	1.37 ± 0.01*
FD <sup>S,T,S-T</sup>	2.57 ± 0.01	2.61 ± 0.00 <sup>a</sup>	2.61 ± 0.01 <sup>a</sup>	2.59 ± 0.01	2.54 ± 0.01	2.57 ± 0.01*	2.56 ± 0.01*	2.59 ± 0.01 <sup>a,c</sup>

<sup>S</sup> Significant effect of SCI, <sup>T</sup> significant effect of time post-injury, <sup>S-T</sup> significant injury-time post injury interaction; ANOVA p < 0.05.

\* SCI different from Control at same timepoint post-injury; p < 0.05.

<sup>a</sup> Different from 2 weeks, <sup>b</sup> different from 6 weeks, <sup>c</sup> different from 10 weeks post-injury; p < 0.05.

### 4.3 Cortical Bone Morphometry

The cortical bone between 85 and 40% bone length from the proximal end for a representative 10-week control group femur is depicted in Figure 4.23. The structure can be split into three main regions:

- i) Distal metaphyseal cortical bone between 75 – 85% bone length,
- ii) Mid-diaphyseal cortical bone between 55 – 75% bone length,
- iii) Diaphyseal bone with third trochanter between 40 – 55% bone length.

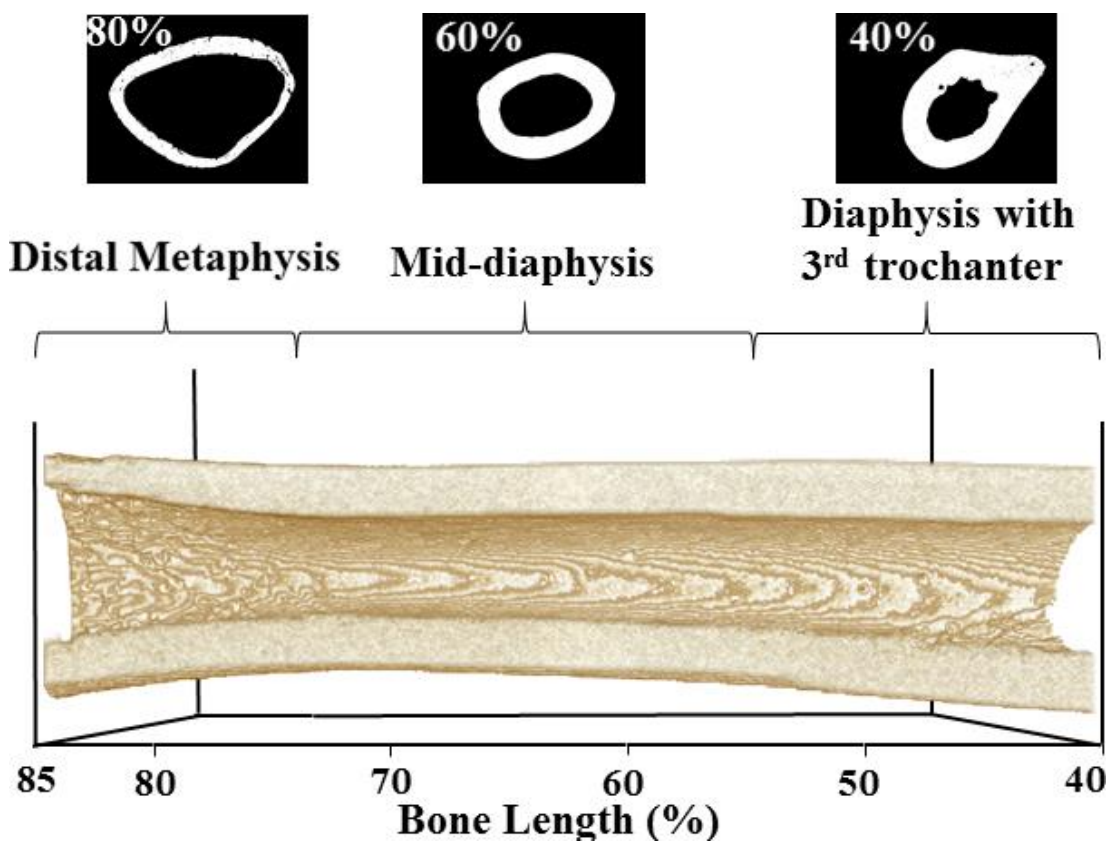


**Figure 4.23.** A representative 10-week control cortical bone (85 – 40% bone length) VOI. Example 80% (distal metaphyseal), 60% (mid-diaphyseal) and 40% (diaphysis with third trochanter) bone length from the proximal end cross-sectional segmented cortical bone slices.

### *4.3.1 2D Morphometric Distributions*

2D (slice-by-slice) morphometric distributions were used to investigate:

- i) The variation of cortical bone as a function of bone length,
- ii) The effects of growth,
- iii) The combined effects of spinal cord injury.

#### *4.3.1.1 Variation of Cortical Bone as a Function of Bone Length*

Cortical bone morphometric distributions for the 10-week control group are shown in Figure 4.24. These distributions indicate the variation of cortical bone as a function of bone length, over the cortical regions (40 - 80% bone length). The trend is for increasing total area enclosed by the periosteum (Tt.Ar) and marrow area (Ma.Ar) moving distally from the mid-shaft towards the distal metaphysis. At 80% bone length Tt.Ar<sub>2D</sub> and Ma.Ar<sub>2D</sub> are 49% and 221% greater than at the mid-shaft (50 % bone length) (both  $p < 0.0001$ ) (Figure 4.24B). Ps.Pm<sub>2D</sub> and Ec.Pm<sub>2D</sub> distributions confirm this finding (data not shown). In contrast, at 80% bone length Ct.Ar<sub>2D</sub> is 23% lower ( $p < 0.001$ ) than at the mid-shaft (Figure 4.24A). Regardless of the decreasing cortical area observed moving distally from the midshaft, the changes in the spatial distribution of bone around its centre of gravity (i.e. increasing Tt.Ar and Ma.Ar) leads to higher polar moment of area in the more distal regions compared to the midshaft. At 80% bone length the polar moment of area is 54% higher than at 60% bone length (Figure 4.24C).

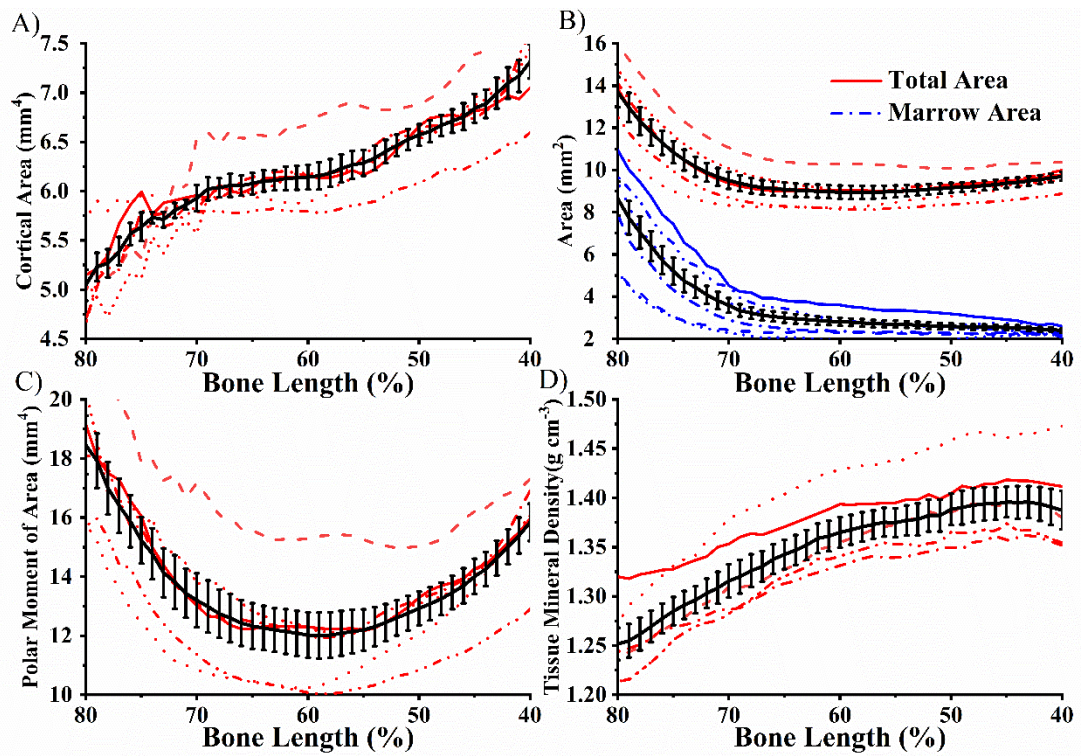


**Figure 4.24.** 2D  $\mu$ CT morphometric plots highlighting the variation of cortical bone properties along the length of the bone for all 10-week control femurs. The cortical VOIs span 40 – 80% bone length. A) Cortical area ( $Ct.Ar_{2D}$ ), B) Total area ( $Tt.Ar_{2D}$ ) and Marrow area ( $Ma.Ar_{2D}$ ), C) Polar moment of area ( $J_{2D}$ ) and D) Cortical tissue mineral density (TMD). Solid black line represents the average distribution with SE error bars.

#### 4.3.1.2 The Effects of Growth on Cortical Bone

Figure 4.25 provides a comparison of the cortical bone morphometric distributions for both 2 and 16-week control groups for 40 to 85% bone length. There was a universal increase in the amount of cortical bone between the 2 and 16-week groups, as evidenced by the significant increase in  $Ct.Ar_{2D}$  throughout ( $p < 0.05$ ) (Figure 4.24A). There were regional effects; the distal metaphyseal region displayed the smallest increase in  $Ct.Ar$  between 2 and 16-week groups. It was only in the 40 to 67% and 81 to – 85% bone length regions where  $Tt.Ar$  significantly increased ( $p < 0.05$ ) in the 16-week control compared to 2-week group (Figure 4.25B). Despite these regional

morphometric changes, polar moment of area significantly increased throughout the bone length (Figure 4.25D).

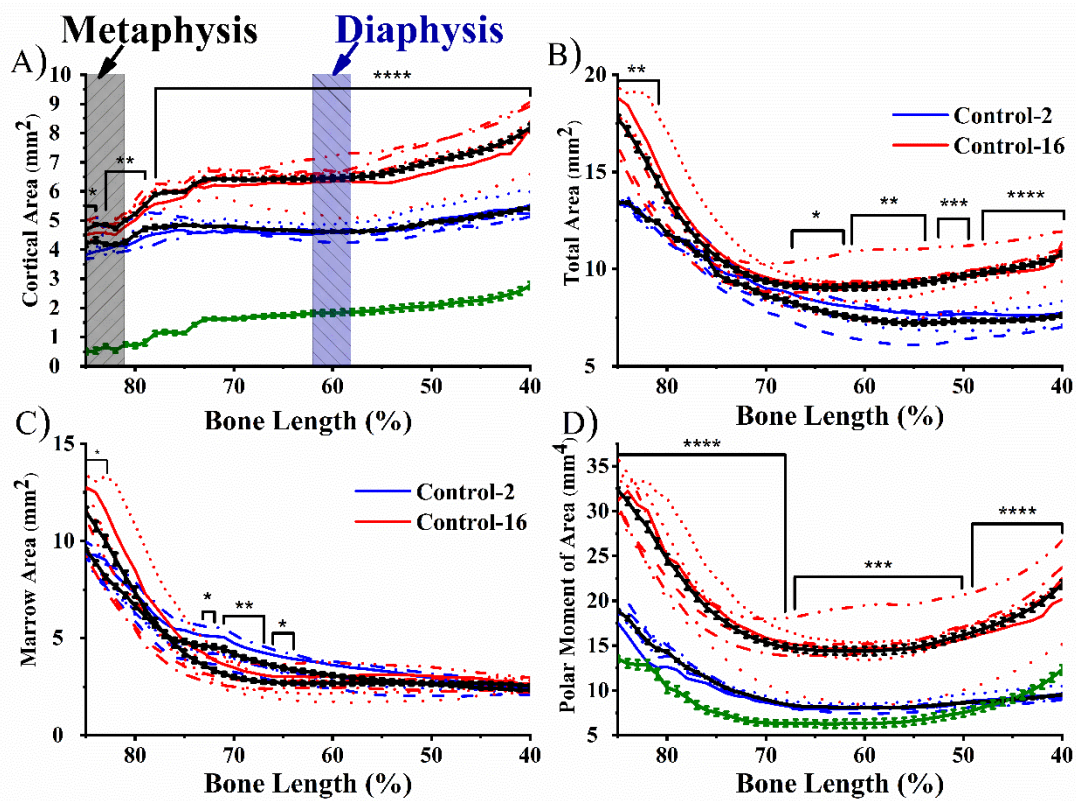


**Figure 4.25.** 2D  $\mu$ CT morphometric plots highlighting the effects of ageing on cortical bone properties of the femur in anatomical time and space. 2 and 16-week control groups in blue ( $n = 8$ ) and red ( $n = 8$ ) respectively. Solid black lines represent the average, with average difference in green. The cortical VOI spans 85– 40%. A) Cortical area ( $Ct.Ar_{2D}$ ), B) Total area ( $Tt.Ar_{2D}$ ), C) Marrow area ( $Ma.Ar_{2D}$ ) and D) Polar moment of area ( $J_{2D}$ ). Data shown as mean  $\pm$  SE. \*, \*\*, \*\*\* and \*\*\*\* indicate  $p < 0.05$ ,  $p < 0.01$ ,  $p < 0.001$  and  $p < 0.0001$  respectively. Black and blue boxes at 81 – 85% and 58 – 62% bone length indicate the distal-metaphyseal and mid-diaphyseal VOIs over which further direct 3D morphometry was performed at all time points.

#### *4.3.1.3 The Effects of Spinal Cord Injury on Cortical Bone*

At 2 weeks post-SCI the distal-metaphyseal and mid-diaphyseal (56 – 85% bone length) Ct.Ar<sub>2D</sub> had significantly decreased compared to control ( $p < 0.05$ ) (Figure 2.26A). This was characterised by decreased Tt.Ar<sub>2D</sub> and Ma.Ar<sub>2D</sub> in distal-metaphyseal regions ( $p < 0.05$ ) (Figures 2.26C & 2.26E), resulting in decreased distal metaphyseal polar moment of area ( $p < 0.05$ ) (Figure 2.26G). By 6, 10 (data not shown) and 16 weeks post-SCI, the entire cortical region (40 – 85% bone length) had significantly reduced Ct.Ar<sub>2D</sub> compared to control ( $p < 0.05$ ) (Figure 2.26B), characterised by decreased Tt.Ar<sub>2D</sub> and Ma.Ar<sub>2D</sub> in the distal-metaphysis (both  $p < 0.05$ ) and decreased Tt.Ar<sub>2D</sub> ( $p < 0.05$ ) in the diaphysis with third trochanter region (Figure 2.26D & 2.26F). Polar moment of area had significantly decreased throughout ( $p < 0.001$ ) (Figure 2.26H).



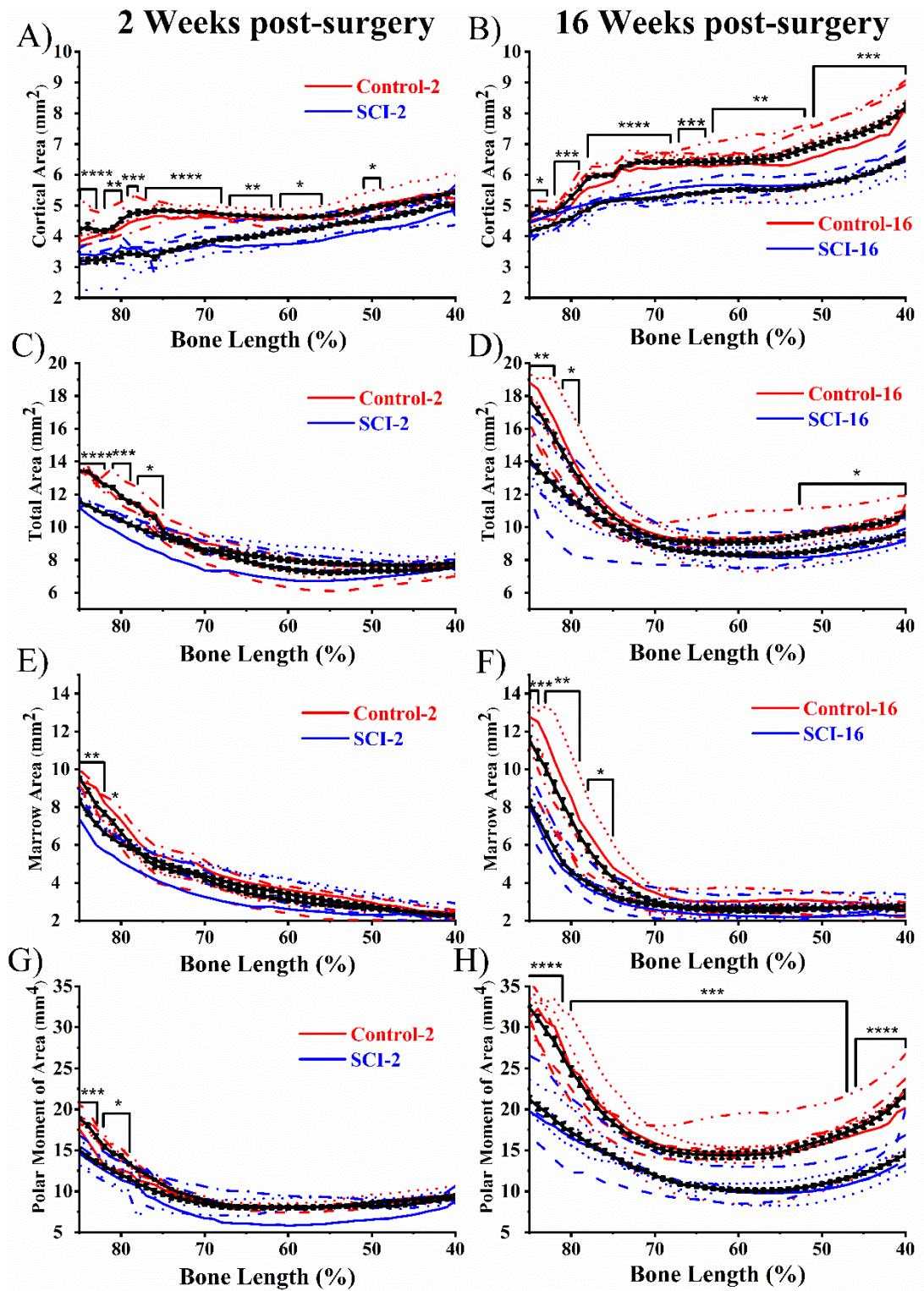


**Figure 4.26.** 2D cortical bone morphometric plots highlighting the effects of SCI-induced osteoporosis on the femur (40 – 85% bone length) in 2 and 16-week control (red) and SCI (blue) groups.  $n = 8$  for both 2-week and  $n = 9$  for both 16-week groups. Solid black lines represent the average of each group. A) and B) Cortical area ( $Ct.Ar_{2D}$ ), C) and D) Total area ( $Tt.Ar_{2D}$ ), E) and F) Marrow area ( $Ma.Ar_{2D}$ ) and G) and H) Polar moment of area ( $J_{2D}$ ). Data shown as mean  $\pm$  SE. \*, \*\*, \*\*\* and \*\*\*\* indicate  $p < 0.05$ ,  $p < 0.01$ ,  $p < 0.001$  and  $p < 0.0001$  respectively.

### 4.3.2 Direct 3D Morphometry

To further examine the cortical bone in depth, 3D morphometry was performed on two distinct VOIs, for all four post-surgery time points (2, 6, 10 and 16 weeks):

- i) Distal metaphyseal cortical bone (85 – 81% bone length),
- ii) Mid-diaphyseal cortical bone (62 – 58% bone length).

There were significant interactions between:

- i) Surgery type – Time post-surgery,
- ii) Surgery type – VOI,
- iii) Time post-surgery – VOI,

for most morphometric parameters (3-way ANOVA). This indicated that both metaphyseal and mid-diaphyseal cortical bone VOIs, were affected by “normal” growth and SCI in different time-dependent ways post-surgery.

#### 4.3.2.1 Comparison of Distal-metaphysis and Mid-diaphysis

Compared to mid-diaphyseal bone the distal-metaphyseal cortical bone was on average thinner and contained less bone, but the surface area and spatial distribution over which it extends were significantly greater. Comparing 2-week control group VOIs, metaphyseal cortical bone was on average 32% thinner ( $p < 0.0001$ ), occupying 11% less bone area ( $p < 0.05$ ), but the total area enclosed by the periosteum (Tt.Ar) and marrow area (Ma.Ar) were on average 68% and 191% larger (both  $p < 0.0001$ ), with 59% higher bone surface/volume ratio (BS/BV), 155% higher polar moment of area (J) (both  $p < 0.001$ ) and 68% ( $p < 0.001$ ) more robust, but 20% ( $p < 0.05$ ) less

eccentric compared to the mid-diaphyseal bone (Table 4.2). These differences are shown in Figure 4.29.

#### 4.3.2.2 Acute Cortical Bone Changes

By 2 weeks post-SCI compared to control group significant changes were observed in both distal distal-metaphyseal and mid-diaphyseal cortical bone VOIs. Distal-metaphyseal Ct.Ar decreased by 17% ( $p < 0.01$ ), while mid-diaphyseal Ct.Ar decreased by 10% ( $p < 0.05$ ) (Figures 4.27B & 4.28B). These changes equated to absolute average reductions in Ct.Ar of  $0.70 \pm 0.12 \text{ mm}^2$  and  $0.45 \pm 0.14 \text{ mm}^2$  respectively compared to control.

The decrease in distal-metaphyseal Ct.Ar at 2 weeks post-SCI was characterised by a 12% ( $p < 0.01$ ) and 10% ( $p < 0.05$ ) decrease in Tt.Ar and Ma.Ar respectively compared to control group. These structural changes contributed to a 12% decrease in Ct.Th, robustness (Tt.Ar/L) (i.e. increased slenderness) (both  $p < 0.01$ ) and BS/BV ( $p < 0.05$ ) and a 26% ( $p < 0.01$ ) decrease in average polar moment of area. No significant changes in eccentricity were observed at 2 weeks (Figure 4.27) (Table 4.2).

In contrast, the decrease in mid-diaphyseal Ct.Ar at 2 weeks post-SCI led to a 12% ( $p < 0.01$ ) average decrease in Ct.Th and 13% ( $p < 0.01$ ) increase in BS/BV compared to control, although Tt.Ar and Ma.Ar changes were non-significant. No significant changes in slenderness, polar moment of area or eccentricity were observed at 2 weeks (Figure 4.28) (Table 4.2).

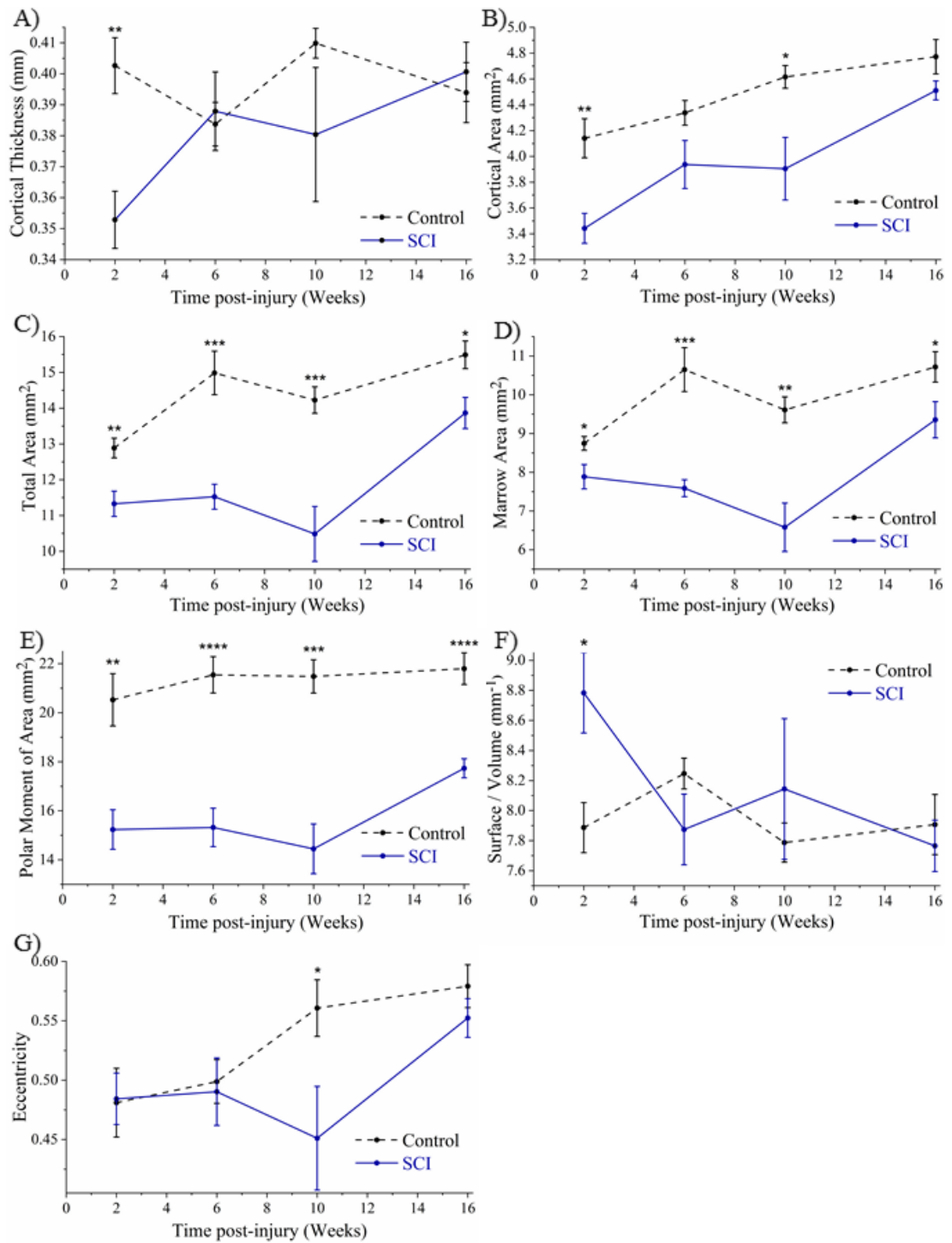


**Figure 4.27.** The variation of 3D cortical bone morphometric properties for distal-metaphyseal cortical bone VOIs (81- 85% bone length) for 2, 6, 10 and 16-week control (black dashed line) and SCI (blue line) groups.  $n = 8$  for all groups. A) Cortical thickness (Ct.Th), B) Cortical area (Ct.Ar), C) Total area (Tt.Ar), D) Marrow area (Ma.Ar), E) Polar moment of area (J), F) Cortical bone surface to volume ratio (BS/BV) and G) eccentricity (Ecc). Data shown as mean  $\pm$  SE. \*, \*\*, \*\*\*, \*\*\*\* indicate  $p < 0.05$ ,  $p < 0.01$ ,  $p < 0.001$  and  $p < 0.0001$  respectively

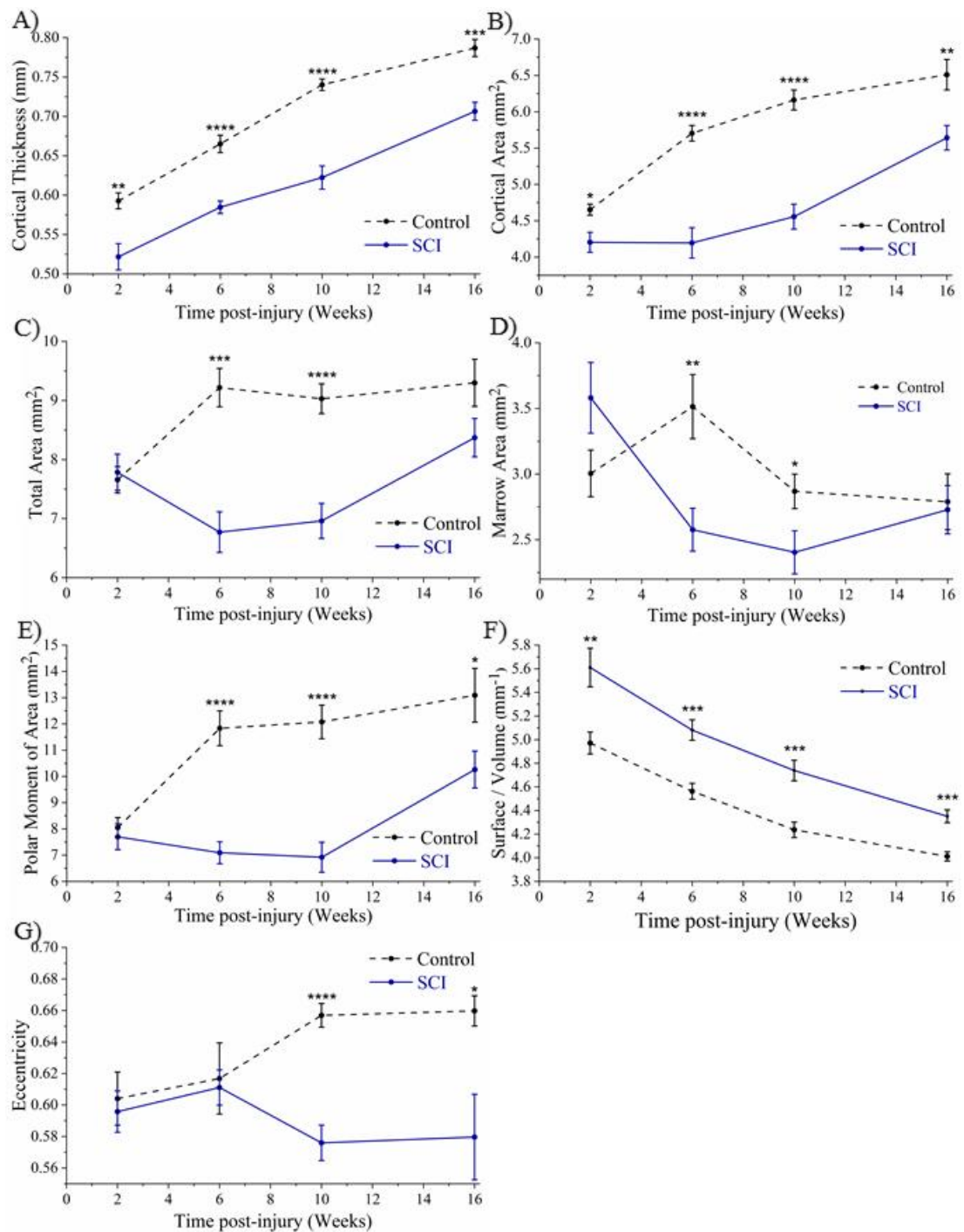


**Figure 4.28.** The variation of 3D cortical bone morphometric properties for mid-diaphyseal cortical bone VOIs (58 - 62% bone length) for 2, 6, 10 and 16-week control (black dashed line) and SCI (blue line) groups.  $n = 8$  for all groups. A) Cortical thickness (Ct.Th), B) Cortical area (Ct.Ar), C) Total area (Tt.Ar), D) Marrow area (Ma.Ar), E) Polar moment of area (J), F) Cortical bone surface to volume ratio (BS/BV) and G) eccentricity (Ecc). Data shown as mean  $\pm$  SE. \*, \*\*, \*\*\* and \*\*\*\* indicate  $p < 0.05$ ,  $p < 0.01$ ,  $p < 0.001$  and  $p < 0.0001$  respectively.



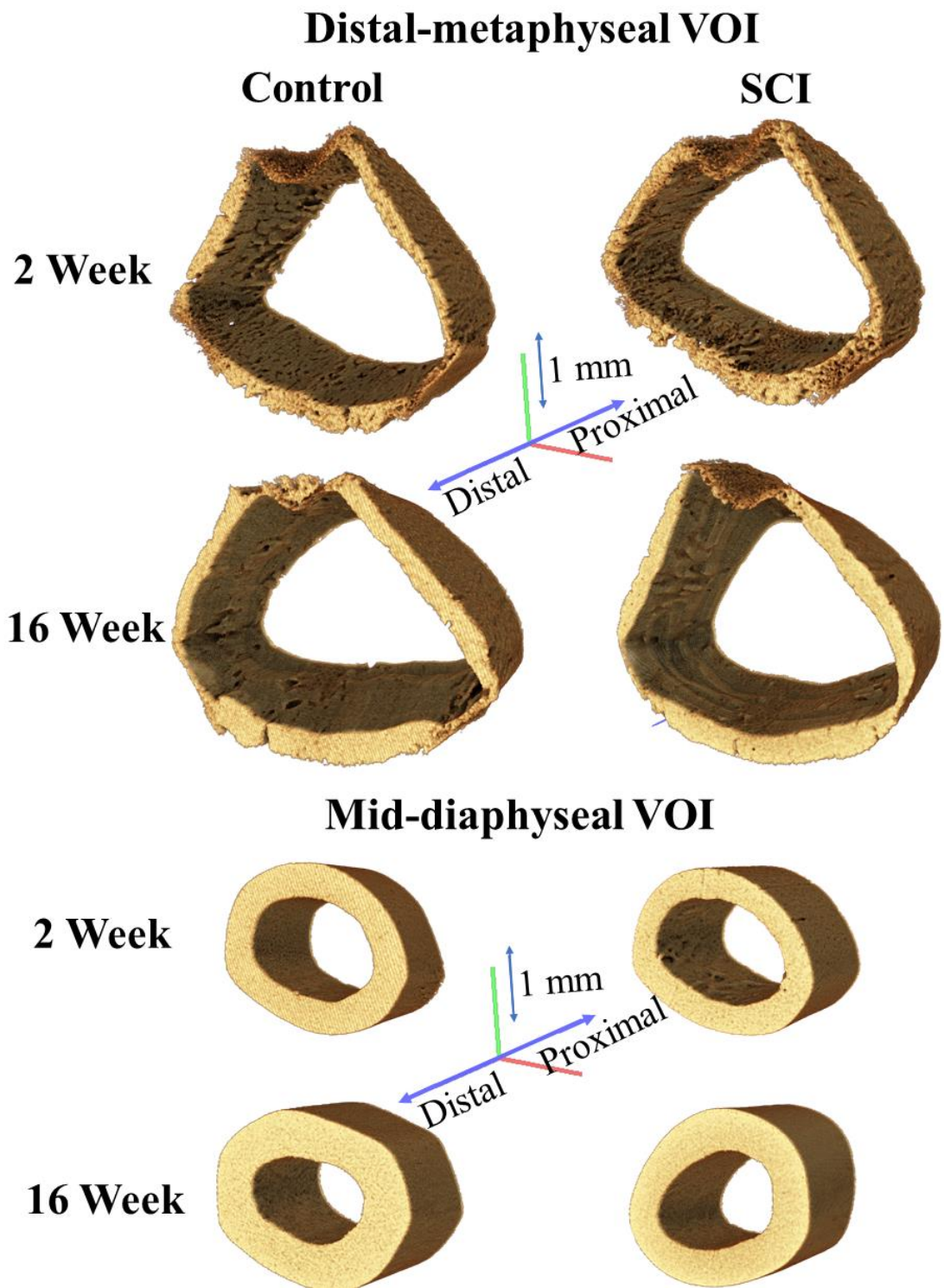


**Figure 4.29.** Representative distal-metaphyseal (81 - 85% bone length) and mid-diaphyseal (58 - 62% bone length) VOIs for both 2 and 16-week control and SCI groups.

#### *4.3.2.3 More Chronic Cortical Bone Changes*

With time post-surgery, there was a general trend of increasing amounts of cortical bone in both distal-metaphyseal and mid-diaphyseal VOIs. This was evident in both control and SCI groups but occurred at different rates.

#### **Distal-metaphyseal Cortical Bone Changes**

For SCI, between 2 and 10-week groups, there was a non-significant change in distal-metaphyseal Ct.Ar (Figure 4.27) (Table 4.2). Significant changes in relation to previous time points were seen only in the 16-week post-SCI group. Between 10 and 16-week groups Ct.Ar increased by 16% ( $p < 0.05$ ). The non-significant change in Ct.Ar between 2 and 10-week groups was characterised by a non-significant change in both Tt.Ar and Ma.Ar. This did not significantly alter the average cortical thickness, polar moment of area, surface to volume ratio or eccentricity of the metaphysis. The significant increase in Ct.Ar between 10 and 16-week groups was characterised by an increase in both Tt.Ar and Ma.Ar of 32% and 42% (both  $p < 0.001$ ) respectively. These changes significantly increased the average polar moment of area of the metaphysis by 23% ( $p < 0.05$ ) and decreased the slenderness, but did not alter the average Ct.Th, BS/BV or eccentricity.

In contrast for control groups, distal-metaphyseal Ct.Ar displayed a growth-related monotonic increase between groups (Figure 4.27) (Table 4.2). This was characterised by a combination of increasing Tt.Ar and Ma.Ar. Both peaked in the 6-week group, with no further growth-related changes. Between 2 and 6-week groups Tt.Ar and Ma.Ar increased by 16% and 22% ( $p < 0.05$  for both) respectively. Ct.Th, slenderness, polar moment of area and BS/BV did not vary with time post sham-surgery, but the

eccentricity of metaphyseal cortical bone increased monotonically between 2 and 16 weeks, overall eccentricity increased by 20% ( $p < 0.05$ ).

At 16 weeks post-SCI compared to control, SCI group distal metaphyseal VOIs did not on average have significant differences in Ct.Ar or Ct.Th, but Tt.Ar and Ma.Ar were 10% and 13% (both  $p < 0.05$ ) lower. These changes resulted in a 19% decrease in polar moment of area ( $p < 0.001$ ).

### **Mid-diaphyseal Cortical Bone Changes**

As with distal-metaphyseal cortical bone, there was no significant change in mid-diaphyseal Ct.Ar between 2 and 10-week groups (Figure 4.28) (Table 4.2). It was only in the 16-week post-SCI group that a significant change in relation to the previous time points was seen. Between 10 and 16-week groups Ct.Ar increased by 24% ( $p < 0.01$ ). Despite the non-significant change in Ct.Ar between 2 and 10-week groups, there was a 33% ( $p < 0.01$ ) decrease in Ma.Ar, and only fractional non-significant decrease in Tt.Ar. This change did not alter the polar moment of area or eccentricity of the diaphysis. The significant increase in Ct.Ar between 10 and 16-week groups was characterised by a 20% ( $p < 0.05$ ) increase in Tt.Ar, and only fractional increase in Ma.Ar. This change significantly increased the average polar moment of area of the diaphysis by 48% ( $p < 0.05$ ) but did not change the eccentricity. Overall, despite the temporal changes in Ct.Ar, Ct.Th monotonically increased by 35% and BS/BV monotonically decreased by 22% between 2 and 16-week groups (both  $p < 0.0001$ ).

In comparison for control groups, mid-diaphyseal Ct.Ar displayed a growth-related monotonic increase between groups that slowed with time post-surgery (Figure 4.28) (Table 4.2). There was an overall 39% ( $p < 0.01$ ) increase between 2 and 16-week



groups. This was characterised by increased Tt.Ar which peaked in the 6-week group and was maintained with no further changes, while no significant temporal changes in Ma.Ar were observed. The polar moment of area closely followed Tt.Ar. As with the SCI groups, in the control groups Ct.Th monotonically increased, and BS/BV monotonically decreased between 2- and 16-week groups. The difference between SCI and control groups for both parameters was the significant offset that existed at 2 weeks post-injury. Eccentricity did not change significantly between 2 and 16 weeks.

At 16 weeks post-SCI compared to control, the SCI group mid-diaphyseal VOIs had 13% ( $p < 0.01$ ) and 10% ( $p < 0.001$ ) reduced Ct.Ar and Ct.Th respectively. These changes resulted in 22% and 12% (both  $p < 0.05$ ) decreases in polar moment of area and eccentricity, and an 8% ( $p < 0.01$ ) increase in BS/BV ratio.

All the trabecular and cortical bone morphometric changes described in this chapter as a result of growth and SCI-induced osteoporosis are qualitatively visualised in the Figure 4.30.

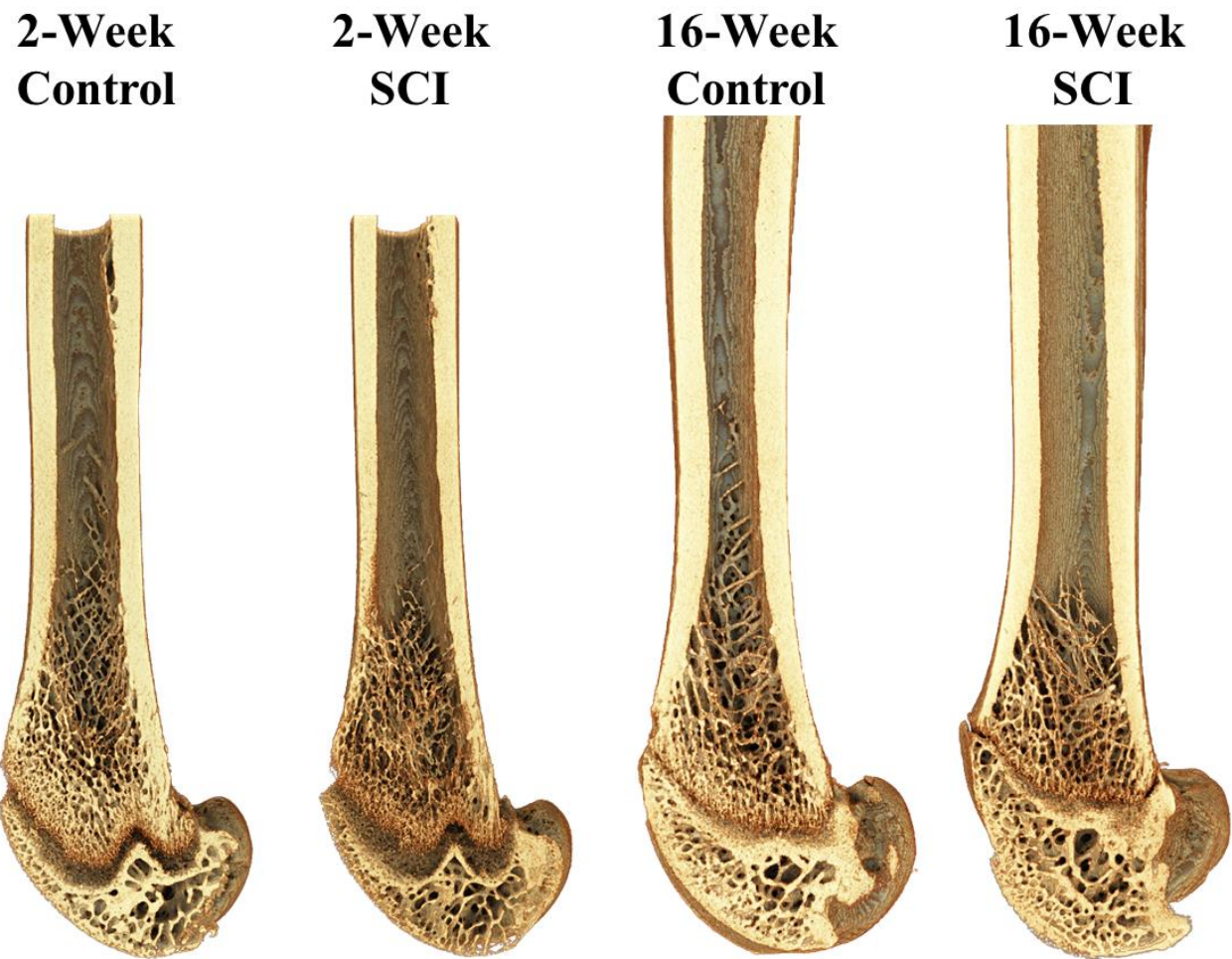


**Figure 4.30.** 2 and 16-week control and SCI distal femurs. Each VOI extends from 40 – 100% bone length from the proximal end, but are at the same scale

**Table 4.2.** 3D cortical morphometric parameters for distal-metaphyseal (85 - 81% bone length) and mid-diaphyseal (62 – 58% bone length) VOIs. Data shown as mean  $\pm$  SE.

Distal-metaphysis	Control				SCI			
	2 Weeks (n = 8)	6 Weeks (n = 8)	10 Weeks (n = 8)	16 Weeks (n = 9)	2 Weeks (n = 8)	6 Weeks (n = 8)	10 Weeks (n = 8)	16 Weeks (n = 9)
Ct.Th <sup>S,S-T</sup> (mm)	0.40 $\pm$ 0.01	0.38 $\pm$ 0.01	0.41 $\pm$ 0.00	0.39 $\pm$ 0.01	0.35 $\pm$ 0.01*	0.39 $\pm$ 0.01	0.38 $\pm$ 0.02	0.40 $\pm$ 0.01
Tt.Ar <sup>S,T,S-T</sup> (mm <sup>2</sup> )	12.89 $\pm$ 0.28	14.98 $\pm$ 0.61 <sup>a</sup>	14.23 $\pm$ 0.37	15.49 $\pm$ 0.39 <sup>a</sup>	11.33 $\pm$ 0.35*	11.52 $\pm$ 0.35*	10.49 $\pm$ 0.77*	13.86 $\pm$ 0.44 <sup>*,a,b,c</sup>
Ct.Ar <sup>S,T,S-T</sup> (mm <sup>2</sup> )	4.14 $\pm$ 0.15	4.34 $\pm$ 0.10	4.62 $\pm$ 0.09	4.77 $\pm$ 0.13 <sup>a</sup>	3.44 $\pm$ 0.12*	3.94 $\pm$ 0.19	3.90 $\pm$ 0.24*	4.51 $\pm$ 0.07 <sup>a</sup>
Ma.Ar <sup>S,T,S-T</sup> (mm <sup>2</sup> )	8.75 $\pm$ 0.18	10.65 $\pm$ 0.57 <sup>a</sup>	9.61 $\pm$ 0.34	10.72 $\pm$ 0.39 <sup>a</sup>	7.88 $\pm$ 0.31*	7.59 $\pm$ 0.22*	6.58 $\pm$ 0.63*	9.35 $\pm$ 0.04 <sup>b,c</sup>
Ct.Ar/Tt.Ar <sup>S,T,S-T</sup>	0.32 $\pm$ 0.01	0.29 $\pm$ 0.01	0.33 $\pm$ 0.01	0.31 $\pm$ 0.01	0.30 $\pm$ 0.01	0.34 $\pm$ 0.01*	0.38 $\pm$ 0.02 <sup>*,a</sup>	0.33 $\pm$ 0.01
Tt.Ar/L <sup>S,T,S-T</sup> (mm)	0.38 $\pm$ 0.01	0.41 $\pm$ 0.01	0.39 $\pm$ 0.01	0.40 $\pm$ 0.01	0.34 $\pm$ 0.01*	0.32 $\pm$ 0.01*	0.28 $\pm$ 0.02*	0.36 $\pm$ 0.01 <sup>*,c</sup>
Ec.Pm <sup>S</sup> (mm)	16.16 $\pm$ 0.27	16.69 $\pm$ 0.27	16.96 $\pm$ 0.63	16.76 $\pm$ 0.31	15.07 $\pm$ 0.52	14.76 $\pm$ 0.27	16.14 $\pm$ 1.05	15.32 $\pm$ 0.30*
Ps.Pm <sup>S,T,S-T</sup> (mm)	29.05 $\pm$ 0.38	30.29 $\pm$ 0.40	29.77 $\pm$ 0.45	29.93 $\pm$ 0.40	27.28 $\pm$ 0.69*	26.22 $\pm$ 0.27*	25.83 $\pm$ 0.54*	27.63 $\pm$ 0.40 <sup>*,c</sup>
J <sup>S,T,S-T</sup> (mm <sup>4</sup> )	20.53 $\pm$ 1.07	21.54 $\pm$ 0.74	21.48 $\pm$ 0.68	21.80 $\pm$ 0.65	15.23 $\pm$ 0.81*	15.32 $\pm$ 0.78*	14.44 $\pm$ 1.01*	17.73 $\pm$ 0.39 <sup>*,c</sup>
Ecc <sup>S,T,S-T</sup>	0.48 $\pm$ 0.03	0.50 $\pm$ 0.02	0.56 $\pm$ 0.02	0.58 $\pm$ 0.02 <sup>a</sup>	0.48 $\pm$ 0.02	0.49 $\pm$ 0.03	0.45 $\pm$ 1.05 0.04*	0.55 $\pm$ 0.02
BS/BV <sup>S,S-T</sup> (mm <sup>-1</sup> )	7.89 $\pm$ 0.17	8.25 $\pm$ 0.10	7.79 $\pm$ 0.013	7.91 $\pm$ 0.20	8.78 $\pm$ 0.27*	7.87 $\pm$ 0.24	8.14 $\pm$ 0.47	7.76 $\pm$ 0.17
FD <sup>S,S-T</sup>	2.19 $\pm$ 0.00	2.19 $\pm$ 0.00	2.19 $\pm$ 0.00	2.19 $\pm$ 0.00	2.20 $\pm$ 0.00*	2.19 $\pm$ 0.00	2.19 $\pm$ 0.00	2.19 $\pm$ 0.00

	Control				SCI			
Mid-diaphysis	2 Weeks (n = 8)	6 Weeks (n = 8)	10 Weeks (n = 8)	16 Weeks (n = 9)	2 Weeks (n = 8)	6 Weeks (n = 8)	10 Weeks (n = 8)	16 Weeks (n = 9)
Ct.Th <sup>S,T,S-T</sup> (mm)	0.59 ± 0.01	0.67 ± 0.01 <sup>a</sup>	0.74 ± 0.01 <sup>a,b</sup>	0.79 ± 0.01 <sup>a,b,c</sup>	0.52 ± 0.02*	0.58 ± 0.01 <sup>*a</sup>	0.62 ± 0.01 <sup>*a</sup>	0.71 ± 0.01 <sup>*a,b,c</sup>
Tt.Ar <sup>S,T,S-T</sup> (mm <sup>2</sup> )	7.66 ± 0.22	9.22 ± 0.32 <sup>a</sup>	9.03 ± 0.25 <sup>a</sup>	9.30 ± 0.40 <sup>a</sup>	7.78 ± 0.31	6.77 ± 0.34*	6.96 ± 0.30*	8.37 ± 0.33 <sup>b,c</sup>
Ct.Ar <sup>S,T,S-T</sup> (mm <sup>2</sup> )	4.65 ± 0.08	5.70 ± 0.11 <sup>a</sup>	6.16 ± 0.14 <sup>a</sup>	6.51 ± 0.21 <sup>a,b</sup>	4.20 ± 0.14*	4.20 ± 0.21*	4.56 ± 0.17*	5.64 ± 0.17 <sup>*a,b,c</sup>
Ma.Ar <sup>S,T,S-T</sup> (mm <sup>2</sup> )	3.00 ± 0.18	3.51 ± 0.24	2.87 ± 0.13	2.79 ± 0.21	3.58 ± 0.27	2.58 ± 0.16 <sup>*a</sup>	2.40 ± 0.16 <sup>*a</sup>	2.73 ± 0.18 <sup>a</sup>
Ct.Ar/Tt.Ar <sup>S,T,S-T</sup>	0.61 ± 0.01	0.62 ± 0.01	0.68 ± 0.01	0.70 ± 0.01	0.54 ± 0.02*	0.62 ± 0.01	0.66 ± 0.01	0.68 ± 0.01
Tt.Ar/L <sup>S,T,S-T</sup> (mm)	0.23 ± 0.01	0.25 ± 0.01	0.25 ± 0.01	0.24 ± 0.01	0.23 ± 0.01	0.19 ± 0.0 <sup>*a</sup>	0.19 ± 0.01 <sup>*a</sup>	0.22 ± 0.01
Ec.Pm <sup>S,T,S-T</sup> (mm)	10.57 ± 0.15	11.63 ± 0.19 <sup>a</sup>	11.56 ± 0.16 <sup>a</sup>	11.72 ± 0.28 <sup>a</sup>	10.66 ± 0.21	10.19 ± 0.18*	10.02 ± 0.22*	11.03 ± 0.19 <sup>b,c</sup>
Ps.Pm <sup>S,T,S-T</sup> (mm)	17.35 ± 0.40	18.97 ± 0.43	18.34 ± 0.32	18.33 ± 0.54	17.99 ± 0.46	16.63 ± 0.35*	16.02 ± 0.42 <sup>*a</sup>	17.54 ± 0.38
J <sup>S,T, S-T</sup> (mm <sup>4</sup> )	8.05 ± 0.38	11.83 ± 0.66 <sup>a</sup>	12.08 ± 0.64 <sup>a</sup>	13.09 ± 1.02 <sup>a</sup>	7.70 ± 0.49	7.09 ± 0.42*	6.92 ± 0.57*	10.26 ± 0.71 <sup>*a,b,c</sup>
Ecc <sup>S,S-T</sup>	0.60 ± 0.02	0.62 ± 0.02	0.66 ± 0.01	0.66 ± 0.01	0.60 ± 0.01	0.61 ± 0.01	0.58 ± 0.01*	0.58 ± 0.03*
BS/BV <sup>S,T</sup> (mm <sup>-1</sup> )	4.97 ± 0.09	4.56 ± 0.07 <sup>a</sup>	4.24 ± 0.07 <sup>a,b</sup>	4.01 ± 0.04 <sup>a,b</sup>	5.61 ± 0.16*	5.08 ± 0.09 <sup>*a</sup>	4.74 ± 0.09 <sup>*a</sup>	4.35 ± 0.05 <sup>*a,b,c</sup>
FD <sup>S,T,S-T</sup>	2.12 ± 0.00	2.11 ± 0.00	2.10 ± 0.00 <sup>a</sup>	2.09 ± 0.00 <sup>a,b</sup>	2.15 ± 0.00*	2.12 ± 0.01 <sup>a</sup>	2.11 ± 0.00 <sup>*a</sup>	2.10 ± 0.00 <sup>*a</sup>

<sup>S</sup> Significant effect of SCI, <sup>T</sup> significant effect of time post-injury, <sup>S-T</sup> significant injury-time post injury interaction; ANOVA p < 0.05.

\* SCI different from Control at same timepoint post-injury; p < 0.05. <sup>a</sup> Different from 2 weeks, <sup>b</sup> different from 6 weeks, <sup>c</sup> different from 10 weeks post-injury; p < 0.05.

### *4.3.3 Tissue Mineral Density*

There was a trend of decreasing cortical tissue mineral density (TMD) moving distally from the midshaft in all control and SCI groups (10-week groups shown) (Figure 4.31A). So much so that in the 2, 6 and 16-week control groups, and 6 and 10-week SCI groups the mid-diaphyseal bone (58 – 62% bone length) had significantly higher TMD than distal-metaphyseal bone ( $p < 0.05$ ) (Figure 4.31B) Table (4.3).

At all-time points assessed there was no significant difference in TMD between control and SCI group (Figure 4.31B) or a difference in the width or height of the density distribution (Figure 4.31C). There was a slight trend of increased TMD with time post-surgery for both control and SCI groups, but this increase did not reach significance.

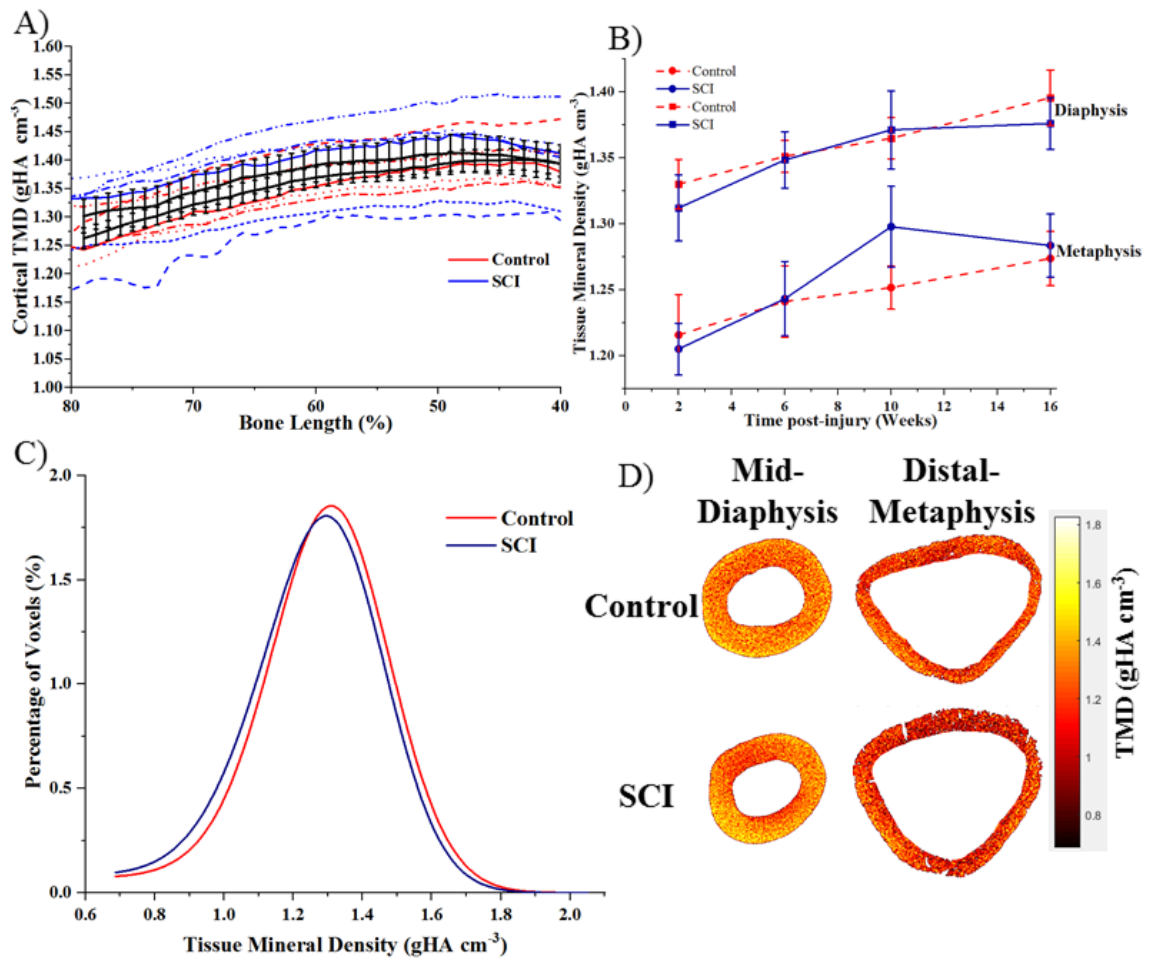


**Figure 4.31.** SCI does not affect cortical tissue mineral density (TMD). A) Cortical TMD distribution for the 40 – 80% bone length VOI for 10-week control (red) and SCI (blue) group. Solid black lines represent the average for control and SCI. B) The variation of TMD for both mid-diaphyseal (58 - 62% bone length) and distal-metaphyseal VOIs (81- 85% bone length) for 2, 6, 10 and 16-week control (dashed red lines) and SCI (blue line) groups. C) TMD distribution for 40 – 80% bone length, for a representative 10-week control and SCI 10-week rat. D) Colour maps of the spatial distribution of TMD within representative 10-week control and SCI mid-diaphyseal (60% bone length) and distal-metaphyseal (83% bone length) slices.

#### *4.3.4 Cortical Porosity*

At the resolution of 6.89  $\mu\text{m}$  it was only possible to conduct porosity measurements on the distal-metaphyseal VOI. At this resolution there was a trend of increasing pore volume fraction and average pore diameter moving distally for both 2 and 6-week control and SCI groups.

At 2 weeks post-SCI compared to control group pore volume fraction of the SCI group had increased by 51% ( $p < 0.05$ ), but by 6 weeks the pore volume fraction of the SCI group was 35% ( $p < 0.05$ ) lower than that of the control group (Figure 4.32). At later time points SCI pore volume fraction was never above that of control. There was a monotonic decrease in pore volume fraction between 2 and 16 weeks for both control and SCI groups. There was no significant difference in average pore diameter between any control and SCI group (Table 4.4).

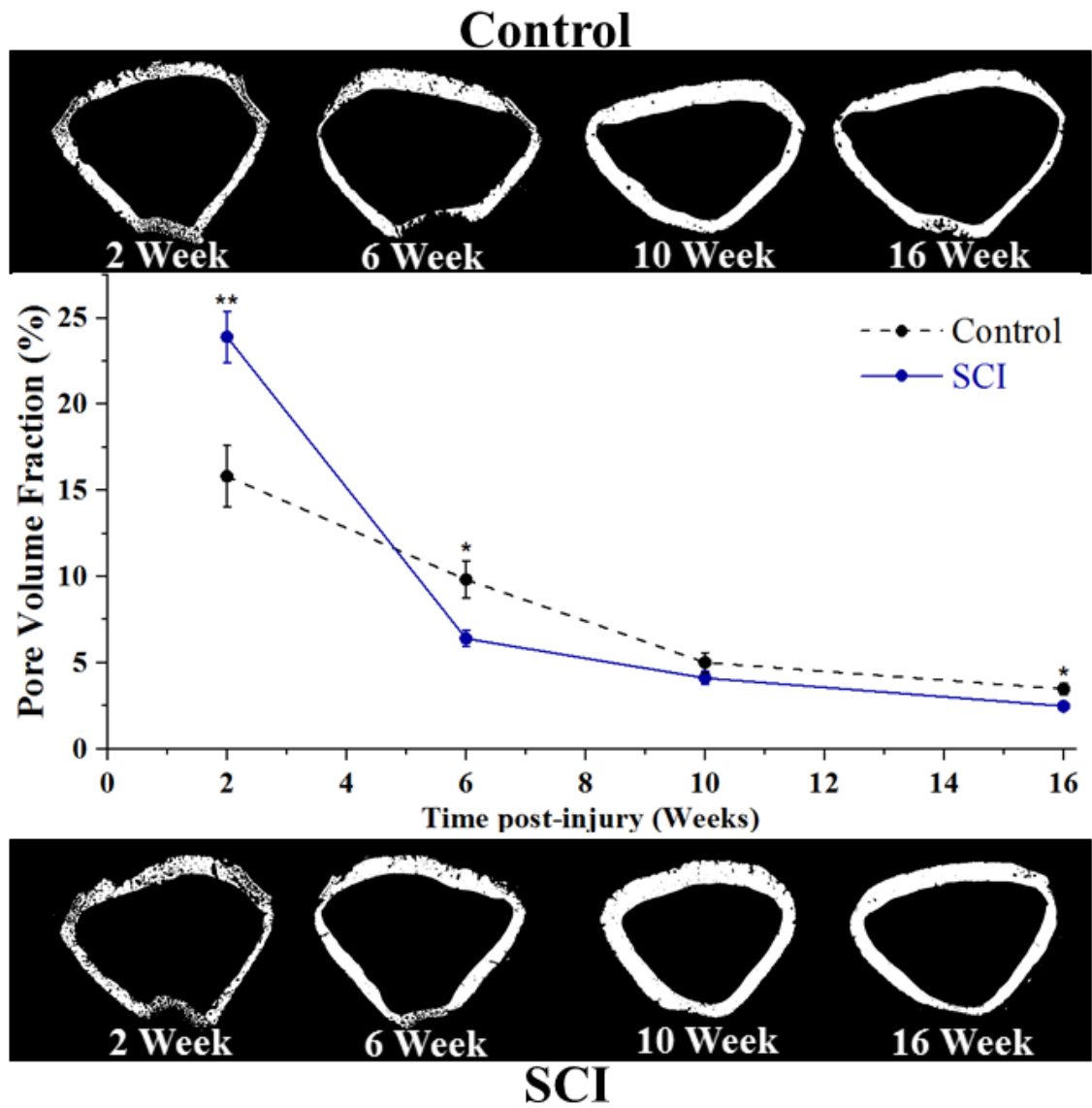


**Figure 4.32.** The variation of pore volume fraction for distal-metaphyseal cortical bone VOIs (81- 85% bone length) for 2, 6, 10 and 16-week control (black dashed line) and SCI (blue line) groups. Determined at a resolution of 6.89  $\mu\text{m}$ . Representative 83% bone length distal-metaphyseal slices highlight the porosity.



**Table 4.3.** 3D cortical tissue mineral density (TMD) for distal-metaphyseal (81 - 85% bone length) and mid-diaphyseal (58 – 62% bone length) VOIs. Data shown as mean ± SE.

	Control				SCI			
	2 Weeks (n = 8)	6 Weeks (n = 8)	10 Weeks (n = 8)	16 Weeks (n = 9)	2 Weeks (n = 8)	6 Weeks (n = 8)	10 Weeks (n = 8)	16 Weeks (n = 9)
<b>Distal-metaphysis</b>								
TMD (gHA cm <sup>-3</sup> )	1.22 ± 0.03	1.24 ± 0.03	1.25 ± 0.02	1.27 ± 0.02	1.21 ± 0.02	1.24 ± 0.03	1.30 ± 0.03	1.28 ± 0.02
<b>Mid-diaphysis</b>								
TMD (gHA cm <sup>-3</sup> )	1.33 ± 0.02	1.35 ± 0.01	1.36 ± 0.02	1.40 ± 0.02	1.31 ± 0.03	1.35 ± 0.02	1.37 ± 0.03	1.38 ± 0.02

**Table 4.4.** 3D cortical morphometric porosity parameters for distal-metaphyseal (81 - 85% bone length) VOI. Data shown as mean ± SE.

	Control				SCI			
	2 Weeks (n = 8)	6 Weeks (n = 8)	10 Weeks (n = 8)	16 Weeks (n = 9)	2 Weeks (n = 8)	6 Weeks (n = 8)	10 Weeks (n = 8)	16 Weeks (n = 9)
Po.V (mm <sup>3</sup> ) <sup>S,T,S-T</sup>	1.31 ± 0.18	0.86 ± 0.11	0.45 ± 0.05 <sup>a</sup>	0.33 ± 0.03 <sup>a,b</sup>	1.63 ± 0.12	0.50 ± 0.05 <sup>*,a</sup>	0.32 ± 0.04 <sup>a</sup>	0.22 ± 0.02 <sup>*,a,b</sup>
Po.V/TV (%) <sup>S,T</sup>	15.82 ± 1.78	9.83 ± 1.06	5.01 ± 0.58 <sup>a</sup>	3.48 ± 0.33 <sup>a</sup>	23.90 ± 1.48 <sup>*</sup>	6.41 ± 0.48 <sup>*,a</sup>	4.12 ± 0.39 <sup>a</sup>	2.48 ± 0.23 <sup>*,a,b</sup>
Po.Dm (mm)	0.050 ± 0.001	0.047 ± 0.001	0.047 ± 0.002	0.054 ± 0.002	0.050 ± 0.002	0.046 ± 0.001	0.045 ± 0.001	0.049 ± 0.002
Po.N <sup>S,T</sup>	1682 ± 122	1870 ± 202	1289 ± 97	1055 <sup>a</sup> ± 94	1217 ± 105 <sup>*</sup>	1768 ± 148	1429 ± 87	800 ± 60 <sup>*,a,b,c</sup>

<sup>S</sup> Significant effect of SCI, <sup>T</sup> significant effect of time post-injury, <sup>S-T</sup> significant injury-time post injury interaction; ANOVA p < 0.05.

\* SCI different from Control at same timepoint post-injury; p < 0.05.

<sup>a</sup> Different from 2 weeks, <sup>b</sup> different from 6 weeks, <sup>c</sup> different from 10 weeks post-injury; p < 0.05.

## 4.4 Mechanical Tests

### 4.4.1 Three-Point Bend Test

Data failed to be collected for one 2-week control femur. 62 out of 65 right femurs undergoing three-point bending fractured at the mid-diaphysis (58 – 62% bone length), at the location where the top support made contact (Figure 4.33A). The remaining 3 femurs (1 each of Control-6, Control-10 and SCI-6) initially fractured at the distal metaphysis (Figure 4.33B), at the location of the bottom support, these 3 results were removed from the final analysis. No difference in type of fracture was observed between control and SCI groups.

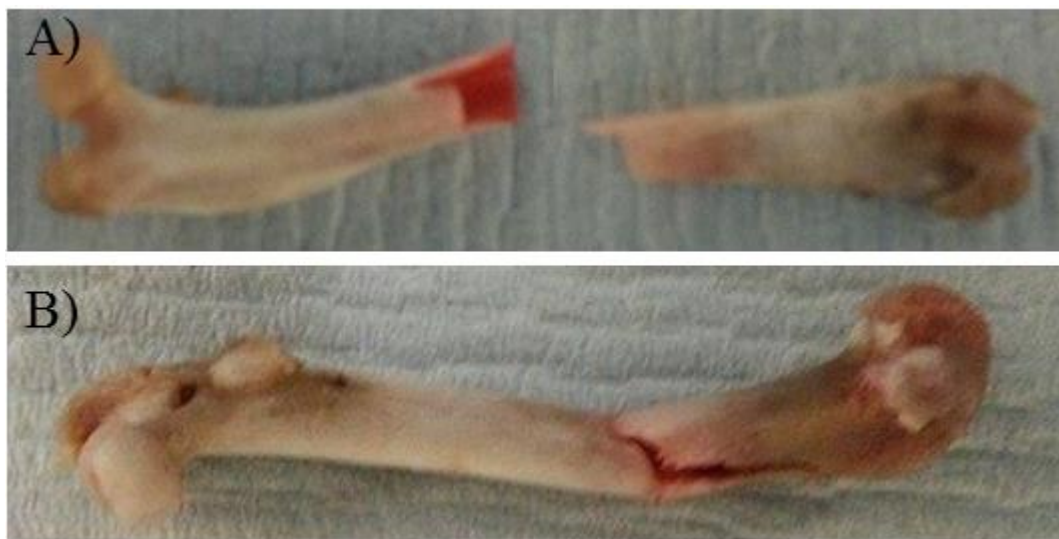


**Figure 4.33.** Three-point bend fractures. A) typical mid-diaphyseal fracture. B) Atypical fracture that propagated from the distal-metaphysis.

#### 4.4.1.1 Whole Bone Mechanical Properties

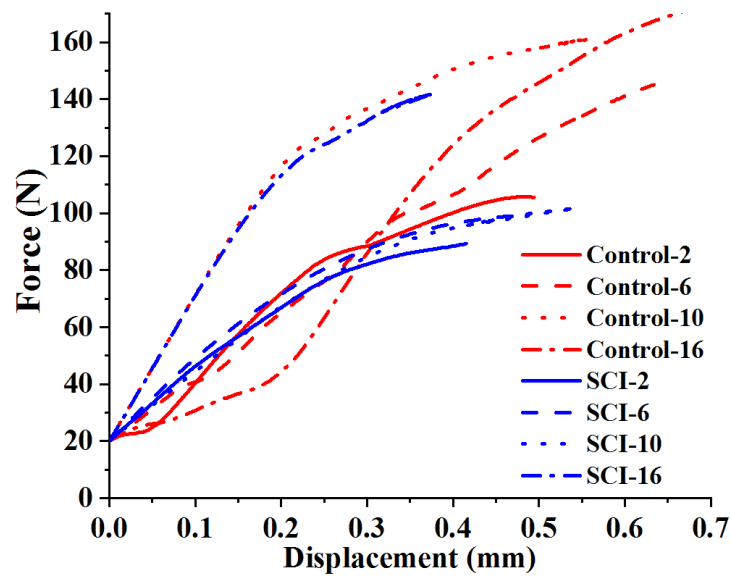


**Figure 4.34.** Three-point bend-derived load-displacement graphs for 2, 6, 10 and 16-week post-surgery control (red) and SCI (blue) groups. Each curve represents the median value with respect to maximum load for each group.

By 2 weeks post-SCI stiffness, maximum load and absorbed energy to fracture of the femur tested through three-point bending had decreased by 25%, 32% and 46% respectively (all  $p < 0.01$ ) compared to control (Figure 4.35) (Table 4.5). A maximum difference of 63% ( $p < 0.001$ ) between SCI and control groups for absorbed energy to fracture occurred at 6 weeks, while maximum differences of 46% and 40% both ( $p < 0.0001$ ) occurred at 10 weeks for stiffness and maximum load respectively. At 16 weeks post-SCI, there was no significant difference between the control and SCI group for all three whole-bone properties.

For SCI, consistent with diaphyseal cortical area results, there was no significant change in stiffness or strength (both yield and maximum load) between 2 and 10-week groups. Significant changes in relation to previous time points were seen only in the

16-week post-SCI group. The maximum load correlated significantly with mid-diaphyseal cortical area ( $r^2 = 0.614$ ,  $p < 0.05$ ) (Figure 4.36). Between 10 and 16-week groups stiffness and maximum load increased by 45% ( $p < 0.001$ ) and 43% ( $p < 0.0001$ ) respectively. Absorbed energy to fracture and post-yield displacement (PYD) did not vary with time post-surgery.

For the control groups, the stiffness and strength (both yield and maximum load) of the diaphysis increased with time post-surgery, levelling off at 10 weeks post-surgery. This is consistent with diaphyseal morphology, with the maximum load correlating significantly with mid-diaphyseal cortical area ( $r^2 = 0.673$ ,  $p < 0.05$ ) (Figure 4.36). Between 2 and 10-weeks diaphyseal stiffness increased by 64% and maximum load by 43% (both  $p < 0.0001$ ). Absorbed energy to fracture and PYD did not vary with time post-surgery.

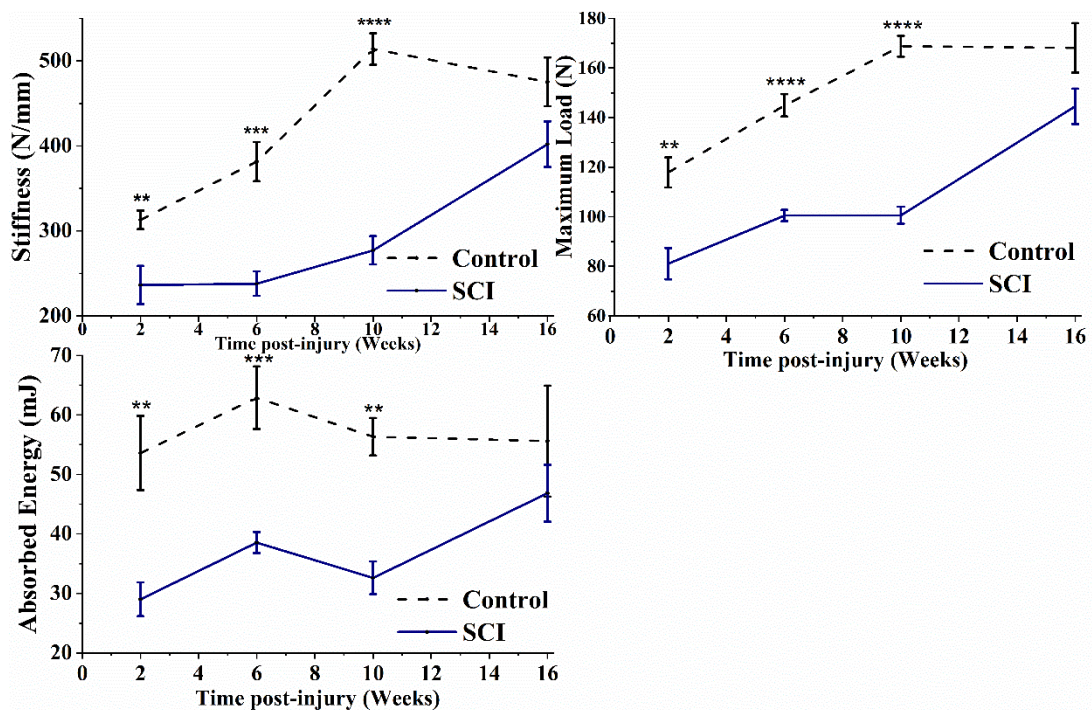


**Figure 4.35.** Three-point bend determined whole-bone mechanical properties for 2, 6, 10 and 16-week control (black dashed line) and SCI (blue line) groups. A) stiffness, B) maximum load, C) absorbed

energy to fracture. Data shown as mean  $\pm$  SE. \*\*, \*\*\* and \*\*\*\* indicate  $p < 0.01$ ,  $p < 0.001$  and  $p < 0.0001$  respectively.

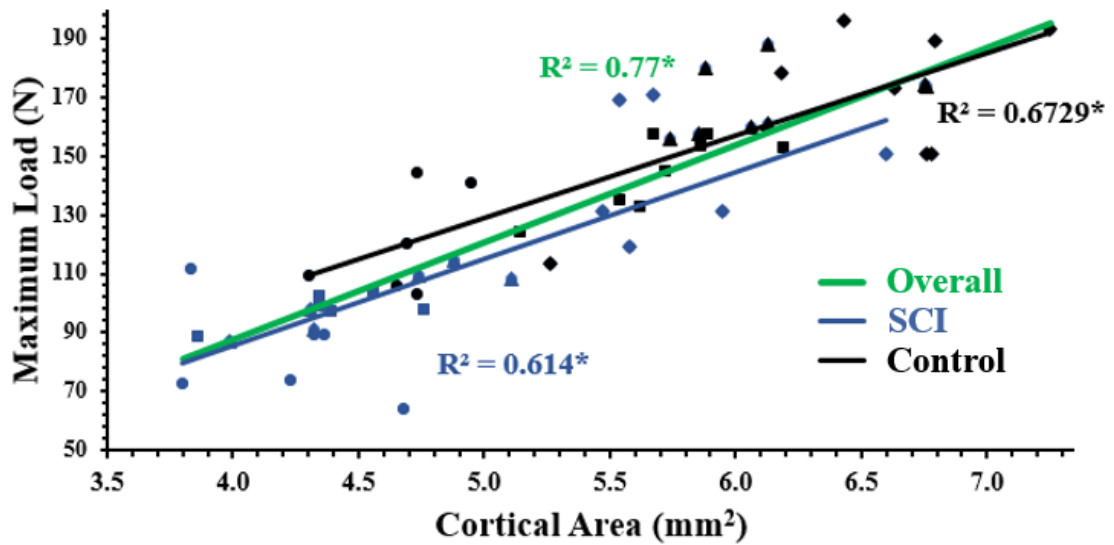


**Figure 4.36.** Linear correlation between three-point bend derived maximum load and mid-diaphyseal cortical area for all control (black) and SCI (blue) femurs. Circles, squares, triangles and diamonds represent 2, 6, 10 and 16-week post-surgery groups respectively. The green line represents the combined linear correlation of control and SCI femurs. Pearson's correlation \* indicates  $p < 0.05$ .

#### 4.4.1.2 Material-level Mechanical Properties

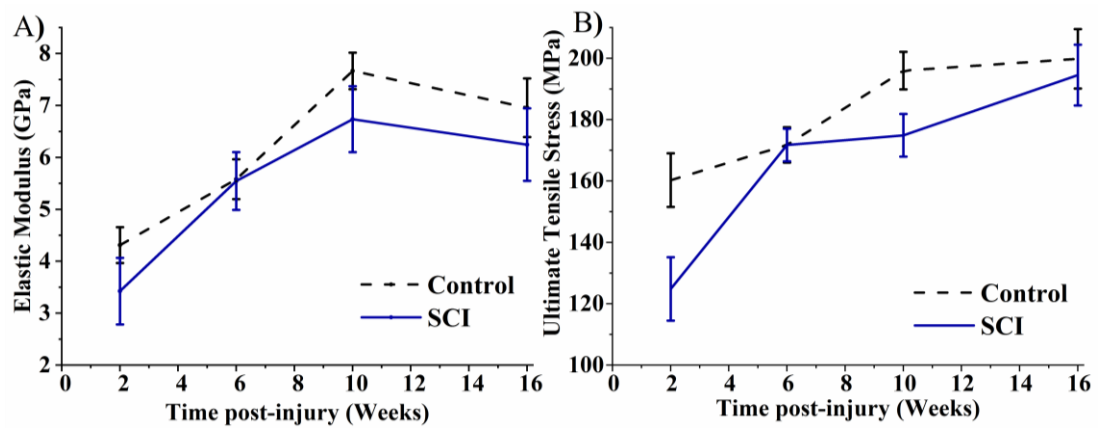


**Figure 4.37.** Three-point bend determined material level mechanical properties for 2, 6, 10 and 16-week control (black dashed line) and SCI (blue line) groups. A) Elastic modulus and B) Ultimate tensile stress. Data shown as mean  $\pm$  SE.

There were no significant differences in elastic modulus or ultimate tensile stress between any age-matched control and SCI group (Figure 4.37) (Table 4.5). The elastic modulus increased with time post-surgery, plateauing at 10 weeks. Between 2 and 10-weeks the elastic modulus increased by 78% ( $p < 0.0001$ ) and 109% ( $p < 0.001$ ) for control and SCI respectively. The ultimate tensile stress increased monotonically with time post-surgery for both control and SCI groups, between 2 and 16 weeks there was a 25% ( $p < 0.01$ ) and 56% ( $p < 0.001$ ) increase respectively.

#### *4.4.2 Torsion Test*

All 66 left femurs that underwent torsion testing failed with a spiral-pattern fracture. These fractures were located in the supracondylar regions, ranging approximately from 60 – 85 % bone length from the proximal end (distal regions without the third trochanter) (Figure 4.38). No differences in fracture pattern or location were observed between control and SCI groups.

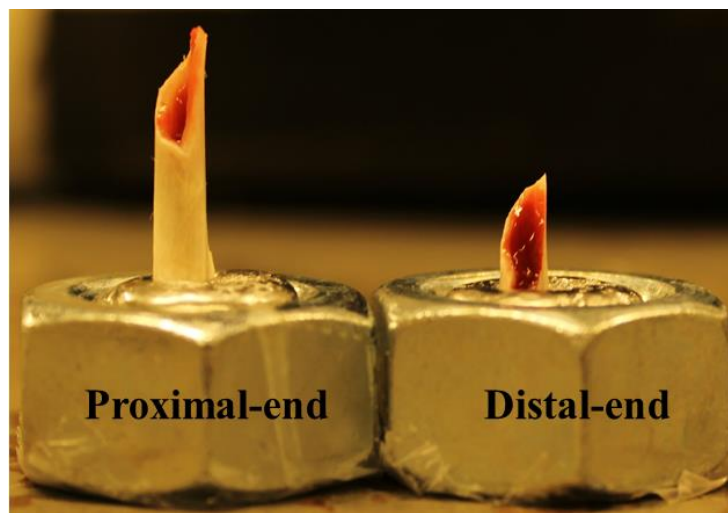


**Figure 4.38.** A representative spiral fracture produced by the torsion test.

#### 4.4.2.1 Whole Bone Mechanical Properties

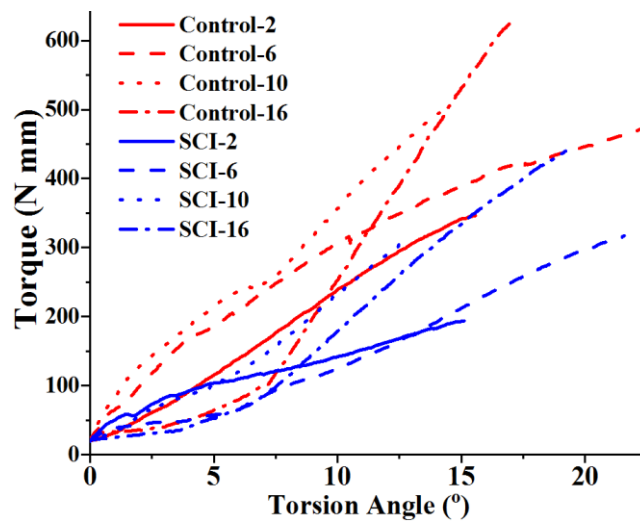


**Figure 4.39.** Torsion test-derived torque-angular displacement graphs for 2, 6, 10 and 16-week post-surgery control (red) and SCI (blue) groups. Each curve represents the median value with respect to maximum torque for each group.

By 2 weeks post-surgery the SCI group, rotational stiffness and maximum torque had decreased by 54% ( $p < 0.0001$ ) and 41% ( $p < 0.001$ ) respectively compared to control (Figure 4.40) (Table 4.5). At all later time points these whole bone properties were significantly decreased in SCI compared to their age-matched control. At 16 weeks rotational stiffness and maximum torque were 36% ( $p < 0.0001$ ) and 27% ( $p < 0.001$ ) lower in SCI than control.

For SCI, rotational stiffness increased monotonically with time post-surgery, between 2 and 16-week groups it increased by 199%, while maximum torque increased by 118% (both  $p < 0.0001$ ). The maximum torque correlated significantly with distal-metaphyseal Ct.Ar ( $r^2 = 0.769$ ,  $p < 0.01$ ) and J. For the control groups, the rotational stiffness and maximum torque increased monotonically with time post-surgery. Between 2 and 16-week groups rotational stiffness increased by 144% and maximum



load by 76% (both  $p < 0.0001$ ). Absorbed energy to fracture and PYD did not vary with time post-surgery.

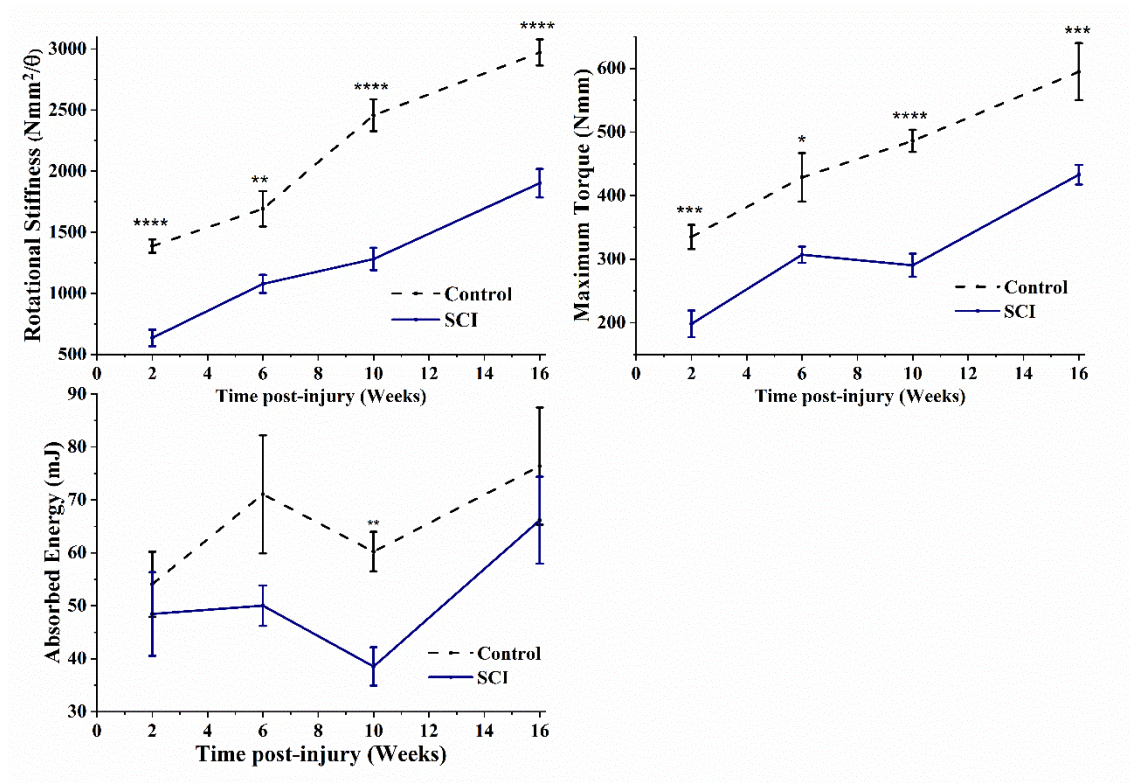


**Figure 4.40.** Torsion test determined whole-bone mechanical properties for 2, 6, 10 and 16-week control (black dashed line) and SCI (blue line) groups. A) rotational stiffness, B) maximum torque, C) rotational absorbed energy to fracture. Data shown as mean  $\pm$  SE. \*, \*\*, \*\*\* and \*\*\*\* indicate  $p < 0.05$ ,  $p < 0.01$ ,  $p < 0.001$  and  $p < 0.0001$  respectively.

#### 4.4.2.2 Material-level Mechanical Properties

At 2 weeks post-SCI compared to control group, rigidity modulus and ultimate shear stress had decreased by 24% ( $p < 0.01$ ) and 20% ( $p < 0.05$ ) respectively (Figure 4.41) (Table 4.5). This was the only timepoint where there was a significant difference in rigidity modulus or ultimate shear stress between age-matched control and SCI groups. Rigidity modulus increased monotonically with time post-surgery for both control and SCI, between 2 and 16 weeks there was a 93% ( $p < 0.001$ ) and 144% ( $p < 0.0001$ )



increase respectively. Ultimate shear stress also increased between 2 and 16 weeks for both control and SCI by 34% ( $p < 0.05$ ) and 48% ( $p < 0.001$ ) respectively.

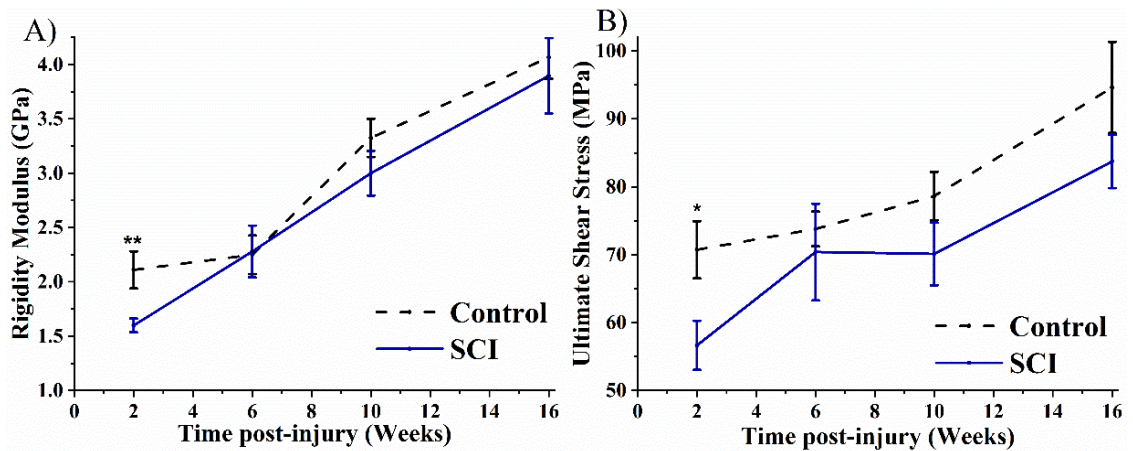


**Figure 4.41.** Torsion test determined material level mechanical properties for 2, 6, 10 and 16-week control (black dashed line) and SCI (blue line) groups. A) Rigidity modulus and B) Ultimate shear stress. Data shown as mean  $\pm$  SE. \* and \*\* indicates  $p < 0.05$  and  $p < 0.01$  respectively.

#### 4.4.3 Femoral Neck Fracture

Data failed to be collected for 2 femurs (one each of SCI-2 and Control-10). All 64 right femurs fractured through the femoral neck. No differences in fracture pattern or location were observed between control and SCI groups.

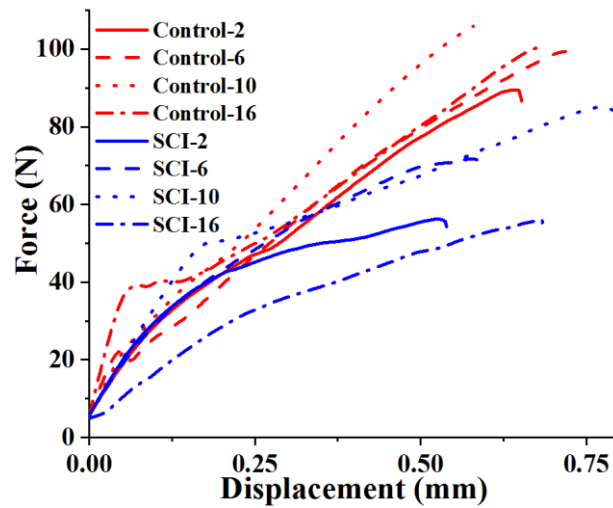


**Figure 4.42.** Femoral neck fracture test-derived median value load-displacement graphs for 2, 6, 10 and 16-week post-surgery control (red) and SCI (blue) groups. Each curve represents the median value with respect to maximum load for each group.

By 2 weeks post-SCI, peak fracture force for the femoral neck had decreased by 35% ( $p < 0.01$ ) compared to control group (Figure 4.43) (Table 4.5). This was the maximum difference between age-matched control and SCI groups. For SCI, between 2 and 10-week groups peak fracture force of the femoral neck increased by 53% ( $p < 0.001$ ). For control groups there was no significant change in peak fracture force of the femoral neck with time post-surgery.

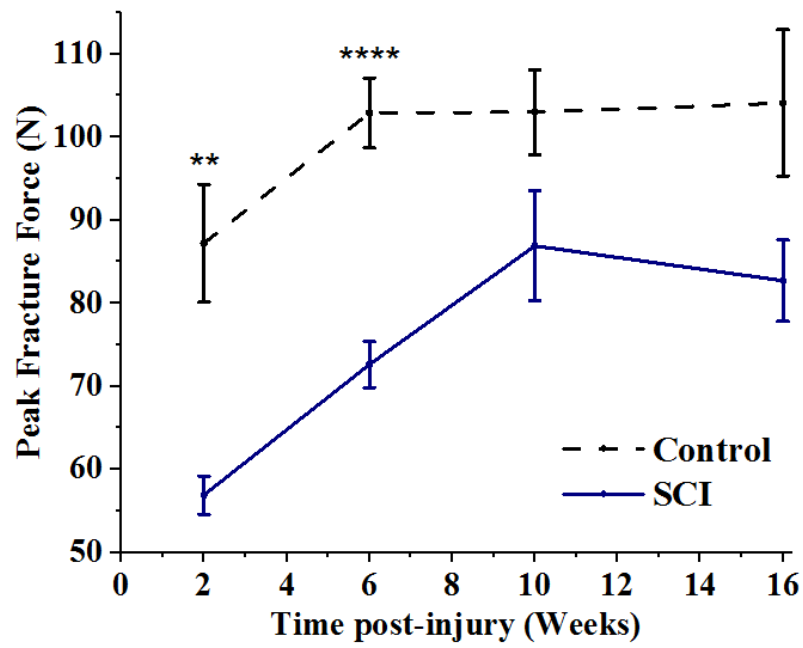


**Figure 4.43.** Peak fracture force of the right femoral neck, for 2, 6, 10 and 16-week control (black dashed line) and SCI (blue line) groups. Data shown as mean  $\pm$  SE. \*, \*\*, \*\*\* and \*\*\*\* indicate  $p < 0.05$ ,  $p < 0.01$ ,  $p < 0.001$  and  $p < 0.0001$  respectively.

**Table 4.5.** Whole-bone and material-level mechanical properties of the femur, from three-point bend, torsion and femoral neck fracture tests.

	<b>Control</b>				<b>SCI</b>			
<b>Three-point Bend</b>	2 Weeks (n = 7)	6 Weeks (n = 7)	10 Weeks (n = 7)	16 Weeks (n = 9)	2 Weeks (n = 8)	6 Weeks (n = 7)	10 Week s (n = 8)	16 Weeks (n = 9)
Stiffness (N/mm) <sup>S,T</sup>	312.9 ± 10.9	381.4 ± 23.0	513.9 ± 18.6 <sup>a,b</sup>	475.3 ± 28.6 <sup>a,b</sup>	236.3 ± 22.4*	237.9 ± 14.4*	277.13 ± 16.7*	402.0 ± 26.8 <sup>a,b,c</sup>
Yield Force (N) <sup>S,T</sup>	63.0 ± 2.5	87.9 ± 3.3 <sup>a</sup>	107.5 ± 2.7 <sup>a,b</sup>	99.6 ± 3.4 <sup>a,b</sup>	45.8 ± 3.6*	67.9 ± 1.4 <sup>*,a</sup>	70.5 ± 4.1 <sup>*,a</sup>	85.0 ± 5.6 <sup>*,a,b</sup>
Max Force (N) <sup>S,T</sup>	117.9 ± 6.1	144.9 ± 4.5 <sup>a</sup>	167.2 ± 4.2 <sup>a</sup>	168.1 ± 10.0 <sup>a</sup>	81.1 ± 6.3*	100.5 ± 2.3*	101.5 ± 3.9*	144.5 ± 7.1 <sup>a,b,c</sup>
Post-yield displacement (mm) <sup>S</sup>	0.42 ± 0.02	0.40 ± 0.04	0.36 ± 0.04	0.31 ± 0.06	0.33 ± 0.03*	0.32 ± 0.01	0.30 ± 0.02	0.28 ± 0.2
Energy-to-fracture (mJ) <sup>S,T</sup>	53.6 ± 6.2	62.9 ± 5.3	56.3 ± 3.2	55.6 ± 9.3	29.0 ± 2.8*	38.6 ± 1.8*	36.5 ± 2.8*	46.8 ± 4.8 <sup>a</sup>
Elastic Modulus (GPa) <sup>T</sup>	4.31 ± 0.34	5.58 ± 0.38	7.67 ± 0.35 <sup>a,b</sup>	6.96 ± 0.56 <sup>a</sup>	3.42 ± 0.64	5.55 ± 0.56 <sup>a</sup>	6.74 ± 0.63 <sup>a</sup>	6.25 ± 0.70 <sup>a</sup>
Ultimate Stress (MPa) <sup>S,T</sup>	160.3 ± 8.7	171.8 ± 5.8	196.0 ± 6.1 <sup>a</sup>	199.8 ± 9.7 <sup>a</sup>	124.8 ± 10.3*	171.7 ± 5.3 <sup>a</sup>	174.9 ± 6.9 <sup>a</sup>	194.5 ± 9.9 <sup>a</sup>
<b>Femoral Neck Fracture</b>	2 Weeks (n = 8)	6 Weeks (n = 8)	10 Weeks (n = 7)	16 Weeks (n = 9)	2 Weeks (n = 7)	6 Weeks (n = 8)	10 Weeks (n = 8)	16 Weeks (n = 9)
Max Force (N) <sup>S</sup>	87.2 ± 7.1	102.9 ± 4.2	103.0 ± 5.1	104.1 ± 8.8	56.9 ± 2.3*	72.6 ± 2.8*	86.9 ± 6.6 <sup>a</sup>	82.7 ± 4.9 <sup>a</sup>

<b>Torsion</b>	<b>Control</b>				<b>SCI</b>			
	2 Weeks (n = 8)	6 Weeks (n = 8)	10 Weeks (n = 8)	16 Weeks (n = 9)	2 Weeks (n = 8)	6 Weeks (n = 8)	10 Weeks (n = 8)	16 Weeks (n = 9)
Rotational Stiffness (Nmm/θ) <sup>S,T</sup>	1387 ± 54	1692 ± 145	2458 ± 130 <sup>a,b</sup>	2971 ± 107 <sup>a,b,c</sup>	636 ± 67*	1078 ± 74 <sup>*,a</sup>	1281 ± 91 <sup>*,a</sup>	1901 ± 116 <sup>*,a,b,c</sup>
Max Torque (Nmm) <sup>S,T</sup>	334.9 ± 19.0	428.7 ± 38.1	486.1 ± 17.4 <sup>a</sup>	595.0 ± 44.8 <sup>a,b,c</sup>	198.1 ± 21.0*	306.9 ± 12.8 <sup>*,a</sup>	290.4 ± 18.2 <sup>*,a</sup>	432.9 ± 15.4 <sup>*,a,b,c</sup>
Energy-to-fracture (mJ) <sup>S,T</sup>	54.1 ± 6.2	71.1 ± 11.1	60.2 ± 3.7	76.4 ± 11.1	48.5 ± 7.9	50.0 ± 3.8	38.5 ± 3.6*	66.2 ± 8.2 <sup>c</sup>
Rigidity Modulus (GPa) <sup>S,T</sup>	2.11 ± 0.17	2.25 ± 0.18	3.33 ± 0.18 <sup>a,b</sup>	4.07 ± 0.20 <sup>a,b</sup>	1.6 ± 0.06*	2.28 ± 0.24 <sup>a</sup>	3.00 ± 0.21 <sup>a</sup>	3.90 ± 0.35 <sup>a,b,c</sup>
Ultimate Shear Stress (MPa) <sup>S,T</sup>	70.7 ± 4.2	73.8 ± 2.6	78.6 ± 3.6	94.6 ± 6.7 <sup>a,b</sup>	56.7 ± 3.6*	70.4 ± 7.13	70.1 ± 4.6	83.7 ± 3.9 <sup>a</sup>

<sup>S</sup> Significant effect of SCI, <sup>T</sup> significant effect of time post-injury, <sup>S-T</sup> significant injury-time post injury interaction; ANOVA p < 0.05.

\* SCI different from Control at same timepoint post-injury; p < 0.05.

<sup>a</sup> Different from 2 weeks, <sup>b</sup> different from 6 weeks, <sup>c</sup> different from 10 weeks post-injury; p < 0.05.

## **Chapter 5 Discussion**

Many previous studies have shown that traumatic SCI leads to rapid and significant detrimental effects to the phenotype of long bones in the paralysed limbs of adults (Eser et al., 2004; Coupaud et al., 2009). These changes result in an increased fracture risk to these bones, particularly around the knee (distal femur, proximal tibia). In this study, the time course effects on the structural, mechanical and material properties of the femur (particularly the distal femur) were examined on a T9 transection rat model of spinal cord injury. Four different time point (2, 6, 10 and 16 weeks) post-surgery groups were assessed, with age-matched sham-operated controls,  $n = 8$  for each group.

Numerous rodent SCI models of osteoporotic bone loss exist (Zhang et al., 2014). Contusion SCIs closely recreate the histopathologic appearance of injuries seen in most human SCI cases (Basso et al., 1996), but in these rodent models of contusion SCI there are a significant number of spontaneous recoveries (Hooshmand et al., 2014), however this is far less common in the human SCI population. Therefore, the model of SCI used here was transection, as it leads to a more complete and permanent SCI, with minimal chance of recovery, thus providing more consistent outcome measures.

### ***5.1 Development of Global Analysis Tool***

Two approaches were used to characterise the morphometry of the distal femur; i) a developed 2D slice-by-slice approach by custom-made MATLAB scripts, followed by ii) more targeted conventional 3D  $\mu$ CT analysis described by Bouxsein et al. (2010).

A 2D slice-by-slice approach was developed here and used to analyse the morphometry of trabecular and cortical bone throughout the distal femur (40 to 100% bone length from the proximal end). Resultant morphometric parameters are comparable to those attained

from conventional  $\mu$ CT analysis (Appendix C.1). The slice-by-slice approach differs in two important ways from more conventional 2D  $\mu$ CT morphometric analysis: i) no limitation is imposed on the size of the VOI, and ii) the final integration step that leads to the reporting of morphometric parameters as averages is omitted. The first difference means that the VOI is limited only by the scan coverage of the bone (in this case the distal 60% of the bone length). This removes the bias introduced when subsample VOIs are selected for analysis without prior knowledge of the bone's overall architecture and allows for quantification of the entire trabecular structure. The second difference means that instead of just reporting the average of the morphometric parameter of interest within the selected VOI, it can be expressed as a function of bone length. This allows for comparison of multiple sites along the bone length and information on spatial variability and directionality of morphometric parameters is maintained. Also, the quantification of morphometry on a percentage bone length basis (rather than the conventional fixed-length basis) allows for comparisons between bones of different lengths, ensuring comparison between biomechanically similar regions (bone functional units/compartments). Clinically this is also the preferred method for standardising measurement regions for patients with SCI, using peripheral Quantitative Computed Tomography (pQCT) (Eser et al., 2004). This approach has promise since it has been shown conclusively that bone's response to altered mechanical environment is site-specific (Rittweger et al., 2010). Thus, it can be used to survey entire bones, identifying interesting regions for more computationally expensive (3D) analyses.

The application of approaches like this has been previously shown in the literature. Wu et al. (2015) used a slice-by-slice approach to localise differences in the trabecular architecture of lumbar vertebrae of ovariectomised (OVX) and sham-operated rats. The region identified as containing the largest microstructural differences between the two

groups was further analysed using more expensive computational techniques (3D morphometric and finite element analysis). While Galea et al. (2015) used a slice-by-slice approach to quantify the cortical bone geometry of entire mouse tibiae from several different experimental groups; including aged, OVX and disuse. They noted site-specific differences between groups that would not have been picked up using the standard procedure of analysis of morphometry at narrow cross-sectional sites.

This is the first study to develop scripts to perform brute-force slice-by-slice analysis, to help automate the process. It is also the first study to apply these techniques to both cortical and trabecular bone. Thus, it provides a unique perspective on the trabecular bone contained at the end of a long bone and identifies regions within the fracture-prone distal femur that warrant further 3D analysis. This technique is applicable to other load bearing long bones (tibia, humeri, radii, ulna), other types of imaging modality and other types of experimental design, including the effects of target rehabilitation strategies, gene knockout and pharmacological intervention. What follows is a summary of the effects SCI-induced osteoporosis has on the distal femur of a rat model of SCI.

## ***5.2 Longitudinal Bone Growth***

Longitudinal bone growth occurs at the ends of load bearing long bones through endochondral ossification, by the hypertrophy of growth plate chondrocytes, secretion of matrix proteins and subsequent matrix calcification. So, measuring the bone length allows the assessment of whether complete SCI affects longitudinal bone growth. For SCI to alter longitudinal bone growth, it must affect these growth processes (Rauch, 2005). Our results indicate that longitudinal bone growth has not been affected by the SCI, as there was no difference in femoral or tibial bone lengths (and thus growth rates) at any of the



four-time points post-surgery between SCI and control groups. Our results for early time points post-SCI are in accordance with several rat SCI studies (Jiang et al., 2007a; Liu et al., 2008; Yarrow et al., 2014; Beggs et al., 2015) where no difference in longitudinal length of the tibia and/or femur was observed over a range of ages (6 weeks to 5 months of age) and in the early stages post-SCI (3 to 4 weeks). However, Lin et al. (2015) found that femoral longitudinal bone growth was significantly reduced in 4-month old rats with SCI duration of 16 weeks, although their study was conducted on five contusion-SCI rats, this lower number of animals and the chance of a degree of recovered function in the hindlimbs of contusion models means that the study has a reduced chance of detecting a true effect than this study.

95% of SCI patients are adults, where the skeleton is skeletally mature and epiphyseal plates have completely ossified, so longitudinal bone growth has ceased, so this effect cannot be studied in people (Parent et al., 2011). On the other hand, it has been observed that young children with SCI generally exhibit inhibited longitudinal bone growth in the paralysed long bones (Duval-Beaupereet al., 1983). Pubertal hormones are known to affect longitudinal bone growth (Finkelstein et al., 1999), but male rats reach puberty around 5 to 7 weeks of age (Sengupta, 2011). To understand what is happening in the rat, and why it appears different to the clinical situation a histological examination of the rodent growth plate would be necessary.

### ***5.3 Muscle and Bone Mass***

Rapid and significant reductions in both long bone wet mass and associated muscle mass were observed after SCI. By 2 weeks post-surgery a 36% decrease in gastrocnemius mass had occurred; atrophy had reduced muscle mass as it adapted to the lack of mechanical stimulation. The mass accumulation rate of the gastrocnemius at all other time points

post-SCI was significantly less than for age-matched controls, so that growth-related muscle modelling added less mass while SCI and control bones grew to comparable lengths.

Without intervention (e.g. exercise-regime, functional electrical stimulation), it is believed that sublesional muscle (and bone) eventually reaches a new steady state at some point during the chronic stage of injury. Due to the confounding effects of growth, it is very hard to tell whether this had happened in the gastrocnemius muscle (i.e. it had adapted to its new conditions) of rats by 2 weeks post-SCI, and whether the subsequent increases in muscle mass are purely associated with growth-related modelling. Performing histology on these muscles could help elucidate how rapidly this muscle adapts to mechanical use changes after SCI. The concomitant reductions in bone wet mass (both femur and tibia) did not occur as rapidly as for muscle. It took until 6 weeks post-SCI for the most significant differences between SCI and control groups to become apparent.

These rapid and substantial decreases in muscle and bone masses within the paralysed hindlimbs are consistent with other rat SCI studies (Liu et al., 2008; Minematsu et al., 2016). Results from the human SCI population are in accordance with the rapid muscle loss seen here. In patients with complete SCI, average muscle cross-sectional areas have been 18% to 46% lower at 6 weeks post-SCI compared to able-bodied control subjects (Castro et al., 1999), and overall sublesional skeletal muscle can atrophy by 30 to 60% depending on the muscle type and completeness of injury (Qin, et al., 2010). The time-lag between peak muscle atrophy and peak bone loss is also seen clinically. Our results are also in accordance with (Biggin et al., 2013), who performed currently the only pQCT study evaluating BMD and morphology changes in children after SCI. After an initial loss of bone associated with the SCI, abnormalities in both muscle and bone growth and

development were seen. To explore the discrepancy in bone wet masses,  $\mu$ CT morphometric and densitometric analyses were performed on the trabecular and cortical bone of distal femur (100 – 40% bone length).

#### ***5.4 Trabecular Bone Distributions***

The global analysis of trabecular bone morphometry developed and implemented here, quantified for what is believed the first time the distribution of morphometric parameters (BA/TA, Tb.N<sub>2D</sub>, Tb.Th<sub>2D</sub> and Tb.Sp<sub>2D</sub>) throughout the entire distal femur (from the epiphyses, through the growth plate complex, metaphyseal primary and secondary spongiosa). It also for the first time allowed the quantification of the effects of growth and SCI on these global distributions. Previous rodent  $\mu$ CT studies of SCI-induced osteoporosis have limited their morphometric analysis to a single area, most commonly a VOI containing secondary spongiosa. This standard procedure is used because it limits new bone growth and excludes primary spongiosa which is actively modelling, thus restricting the analysis to the predominantly remodelling secondary spongiosa (Erben, 1996). Not limiting the analysis to solely the metaphyseal secondary spongiosa allowed the identification of site-specific changes throughout the structure, which otherwise would have been missed. This is important when considering SCI since the distal femur is the most common location for fracture.

##### ***5.4.1 Bone Growth – Control Femurs***

The variation of trabecular bone quantity (BA/TA) and quality (Tb.N<sub>2D</sub>, Tb.Th<sub>2D</sub> and Tb.Sp<sub>2D</sub>) distributions for representative “normal” distal femurs are shown in Figure 4.3. They highlight how trabecular bone is distributed throughout a normal rat femur. Prominent features include: i) the rarefication of metaphyseal trabecular bone with distance from the growth plate and ii) the more uniform density of trabecular bone within

the enclosed epiphyses, despite its cross-sectional shape varying more substantially. These structural differences reflect the differences in biomechanical function of the two trabecular compartments. The principle function of epiphyseal trabecular bone is to act as a natural shock absorber at the joint, and that of the metaphyseal trabecular bone is to transmit the load to the cortical shaft. The variations of these distributions with growth for 2 and 16-week post-surgery control rats are shown in Figure 4.5 (in terms of age this represents the trabecular transformation between 14 and 28 weeks of age). To understand what the morphometric distributions in Figure 4.5 highlight, the developmental changes within the distal femur trabecular construct must be understood.

#### *5.4.1.1 Metaphyseal Trabecular Bone*

Considering first the changes to metaphyseal trabecular bone between 2 and 16-week groups. In this thesis the metaphyseal trabecular bone compartment was defined as the regions between 88 and 60% bone length. As a long bone increases in length, new bone (both cortical and trabecular) is formed at the growth plate-metaphysis junction (here defined as the region between 89 and 92% bone length). At the opposite end of the metaphyseal trabecular structure, the metaphyseal-diaphysis junction, trabeculae are resorbed, and metaphyseal cortical bone is incorporated into the diaphysis. This process is observed in Figure 4.5A and quantified by the trabecular extent (Tb.E) which is a novel parameter defined and calculated from the trabecular BA/TA distribution. Tb.E quantifies how far metaphyseal trabecular bone extends into the medullary cavity from the distal growth plate. There is no difference in the gradients or extent of the metaphyseal BA/TA distributions. This means in these healthy femurs there was no difference in the normalised area fraction of trabecular bone or the extent of the trabecular structure. That is, there were concomitant increases in the total area (TA) (which here is equivalent to marrow area) and trabecular bone area (BA) as the femurs grew from 2 to 16-week

groups, furthermore in terms of percentage bone length, Tb.E remained unchanged ( $23.5 \pm 0.6\%$  and  $22.7 \pm 0.6\%$  bone length) for 2 and 16-week groups respectively). In absolute terms this equated to the 16-week Tb.E being approximately 1mm longer than 2-week Tb.E, in line with the increased length.

Despite the overall percent Tb.E and BA/TA of the metaphyseal trabecular structure remaining unchanged with growth, increases in the amount of trabecular bone and thus changes to its microstructure were observed. These changes were a fine-tuned increase in thickness and decrease in number of trabeculae as the femur grew between 2 and 16-week groups. This is in accordance with normal bone growth (Rauch, 2005). The metaphyseal region contains both primary spongiosa (newly formed trabeculae consisting of a mix of cartilage and bone) adjacent to the growth plate, and secondary spongiosa (more mature trabeculae bone). With age and distance from the growth plate the cartilage component is gradually removed and primary spongiosa thicken, transforming into secondary spongiosa, observed by the increase in metaphyseal Tb.Th<sub>2D</sub> (Figure 4.5C).

The decrease in Tb.N<sub>2D</sub> can be explained and observed by the Tb.Th<sub>2D</sub> mapped cross-sections (Figure 4.6). With increasing distance from the growth plate (i.e. during growth) we see trabeculae that were initially located at the centre of the bone are thinned out and gradually resorbed (as long as longitudinal bone growth continues). While peripheral metaphyseal trabeculae have a different fate, their main function is to transfer load to the cortex, becoming thicker and thicker the further away they are from the centre of the bone (eventually coalescing with the cortex, until longitudinal growth ceases). This suggests that is predominantly resorption of central trabeculae that leads to the reduction of trabecular number with growth, as the metaphyseal trabeculae adapt to transmit larger loads in the larger animal.

#### *5.4.1.2 Epiphyseal Trabecular Bone*

Unlike metaphyseal trabecular bone, there was a significant increase in epiphyseal trabecular BA/TA between 2 and 16-week groups. This means that after increases in total area were accounted for, the volume fraction of trabeculae bone increased within the epiphyseal compartment as the bone grew. In the most distal regions this was characterised by thickening of trabeculae, while in the more proximal regions, it was characterised by a combined increase in number and decrease in average thickness of trabeculae. This decrease in average thickness was biased by an increased number of thin trabeculae as observed in Figure 4.6, particularly in peripheral regions, thus thick trabeculae remained within the condyles.

A possible explanation as to why distal epiphyseal trabecular BA/TA increased via increased Tb.Th between 2 and 16-week control groups, while metaphyseal BA/TA remained constant, can be ascertained from the continued longitudinal bone growth observed. As previously stated, longitudinal bone growth occurs at the junction of the growth plate-metaphysis and results in elongation of the shaft; there is no elongation of the epiphyseal region, which is trapped between its thin cortical shell and growth plate. The epiphyseal trabecular structure is therefore essentially stationary, meaning that if this study was longitudinal in design, 2 and 16-week epiphyseal trabecular VOIs would contain the same trabecular structures. This is not the case for metaphyseal VOIs due to the lifecycle starting at the growth plate-metaphysis junction and ending at the metaphysis-diaphysis junction. Thus, epiphyseal trabeculae are can continually thicken to a certain point (resulting in increases BA/TA), which explains why epiphyseal trabeculae in growing long bones are on average thicker than metaphyseal trabeculae. Now that we have an overview of “normal” trabecular bone growth in the distal femur, the effects of SCI on age-matched femurs can be considered.

#### *5.4.2 Effects of SCI on Trabecular Bone*

The global analysis of distal femoral trabecular bone quantified the time-dependent response to SCI. At 2 weeks post-SCI there was a large-scale, site-specific decrease in trabecular BA/TA over the most distal regions (98 - 80% bone length) compared to control. The most severe decreases in BA/TA were observed in the proximal regions contiguous and adjacent with the growth plate (88 – 80% bone length), characterised by significant decreases in the number of trabeculae, but the remaining trabeculae were also on average thinner. These changes were primarily observed in centrally located trabeculae, although peripheral trabeculae were also affected (Figure 4.10). Less severe decreases in BA/TA were observed in the thicker epiphyseal trabecular bone. This decrease was characterised by a thinning of trabeculae, no significant resorption (decrease in number) was observed. The final observation extracted from the 2-week post-SCI distributions is that overall extent (Tb.E) of the distal femoral trabecular structure remained unchanged (Figure 4.9). These most proximal regions (70 – 80% bone length) did not experience significant reductions in BA/TA, but significant reductions in trabecular thickness were apparent (Figure 4.7 and 4.10).

The observation that the most severe bone loss at 2 weeks post-SCI occurred in the regions within and close to the growth plate is in accordance with the growing rat model of ovariectomy (OVX) (Iwaniec & Turner, 2013), no similar arguments have been put forth for SCI models. Similar to this study, growing OVX models exhibit elevated trabecular bone turnover. This trabecular osteopenia is primarily due to altered bone growth. Specifically, increased resorption of calcified growth plate cartilage is observed, resulting in decreased amounts of primary spongiosa, which serves as the template for future bone growth, thus the potential for future trabecular bone acquisition is prematurely halted. So OVX has reduced the net addition of trabecular bone in the

growing skeleton. This argument can be applied to the growing SCI model, since it is the same regions that have been most significantly affected in the early stages post-injury, from which future growth occurs.

The fact that the structure of trabecular bone at earlier times influences the construction of future bone during growth can be seen in action in the later time points (Appendix F for 6 and 10 weeks, Figure 4.7 for 16 weeks), where the BA/TA of newly formed trabecular bone (during growth) contiguous to the growth plate is always significantly decreased compared to age-matched control. At these later time points the difference in BA/TA is characterised more so by decreased trabecular number than decreased trabecular thickness. This indicates that the amount of cartilaginous template from which primary spongiosa is secreted had decreased, thus the number of trabeculae formed is reduced. Histology should be performed on these regions to confirm this is the case, because a second explanation could be that less primary spongiosa is being created due to less demand because of the change in loading environment post-SCI.

Alongside the decrease in amount of primary spongiosa being formed, this work has produced the novel observation that extent of the metaphyseal trabecular structure was significantly reduced compared to age-matched control by 6 weeks post-SCI (Figure F.1). This observation to the best of my knowledge is not noted anywhere in SCI literature. It may be an artefact of growth or could be a result of SCI-induced remodelling. A biomechanical explanation for this decrease in extent of metaphyseal trabecular bone into the shaft is that the loads that this trabecular bone now must transfer to the cortical shaft have diminished drastically, such that the strain-stimuli particularly on the more proximally-located trabeculae are so low that they get completely resorbed.



### ***5.5 3D Trabecular Morphometric Analysis***

The site-specific differences between regions within the distal femoral trabecular structure highlighted by the 2D trabecular graphs, motivated further study of three trabecular VOIs which from proximal to distal locations were; metaphyseal secondary spongiosa (MSS) (85 – 89% bone length), metaphyseal primary spongiosa (MPS) (81 – 85% bone length) and epiphyseal secondary spongiosa (ESS) (93 – 97% bone length).

#### ***5.5.1 Site-specific Differences***

This analysis confirmed several observations made with the slice-by-slice approach regarding site-specific differences and growth and development highlight in the trabecular distributions. In 2-week control distal femurs, the MPS compartment had the highest volume fraction trabecular bone out of the three trabecular compartments, it contained by far the highest number of trabeculae, but they were on average the thinnest. While the adjacent MSS compartment had by far the lowest BV/TV, compared to the MPS compartment these trabeculae were thicker, but there were much fewer of them, which was primarily due to resorption of central trabeculae alongside the thickening of peripheral trabeculae, resulting in a central cavity in the proximal region. This was quantified by the compartment on average having by far the largest trabecular separation (Figure 4.13). While at 2 weeks the ESS compartment had much higher trabecular BV/TV than MSS, but not quite as high as MPS, its microstructure was again vastly different than the other two compartments, consisting of a low number (compared to MPS) of much thicker trabecular struts. These differences can be observed in Figures 4.13, 4.17 & 4.20. Further observations acquired through 3D analysis were that at 2 weeks the high number of thin trabeculae within the MSS compartment had the highest connectivity of the three

compartments. While the thick trabeculae within the ESS compartment had by far the lowest surface area to volume ratio.

### *5.5.2 The Structural Effects of Growth*

The growth dependent changes to the microarchitecture of the trabecular bone in these three anatomically-different locations were further elucidated with 3D analysis. This section details the changes observed between 2, 6, 10 and 16-week post-surgery control groups. The ESS compartment was the only compartment to show growth-related increases in the amount of trabecular bone (BV) and BV/TV, primarily resulting from increased trabecular number (Figure 4.19A and 4.19B). The average trabecular thickness remained the same, indicating that older trabeculae also thickened steadily with time (Figure 4.19C). The increase in BV/TV was such that by 6 weeks it was comparable with MPS levels. In MSS, the trabeculae thickened with time, particularly in peripheral locations, while the central cavity increased in size (Figure 4.13). In the MPS there was also a transition to fewer but thicker trabeculae (Figure 4.16), but they were more uniformly located throughout the VOI (Figure 4.17). The decrease in number of trabeculae was such that by 16 weeks ESS and MPS contained approximately the same number. The MSS results were in accordance with those found in growing rodents, while ESS and MPS data could not be found in the literature. These results were also in accordance with the increase in trabecular thickness rather than number observed in the long bones of growing children, as growing bones adapt to increases in mechanical demands (Ryan et al., 2017).

3D analysis also revealed that there was a general decrease in trabecular connectivity for all three compartments as the femur grew, with the MSS compartment experiencing a drastic decrease as primary spongiosa transitioned to secondary spongiosa (Figures

4.14A, 4.18A and 4.21A). All three compartments also exhibited a decrease in BS/BV, primarily explained by concomitant trabeculae thickening (Figure 4.14B, 4.18B and 4.21B). For metaphyseal VOIs, no changes in the average rod to plate-likeness of trabeculae was observed with time, while there was potentially a transition to more plate-like trabeculae in the epiphyses (Figures 4.15A, 4.18C and 4.21C). These changes are consistent with previous observations characterising the variation of SMI, where it is noted that generally compared to rod-like structures, plate-like structures have higher BV/TV characterised by increased thickness (Hildebrand & Rüegsegger, 1997). While in growing children an increase in plate-like structures (decrease in SMI) is expected, particularly in high strain regions (Ryan et al., 2017).

The degree of anisotropy (DA) for both metaphyseal compartments was found to decrease with time (Figure 4.15B and 4.18D), this is not in agreement with observations in growing children, where DA is found generally to increase with age (Ryan et al., 2017). An interpretation of this is that, as trabecular bone matures, its quantity and quality (including structural orientation) become better adapted to the loading environment. However, Tanck et al. (2001) while studying bone growth and development in pig tibiae found a lag between the deposition of new trabecular bone and increases in DA. They suggested that the initial response to increased loads/growth is to add bone and then refine the mass later into a more efficient, anisotropic structure. An alternative reason could be the VOIs themselves over which DA was calculated. The large voids (cavities) present particularly in the central regions of the MSS compartment may have biased the DA value. Thus, the general increase in Tb.Sp found with age may have led to the overall decrease in DA (more isotropic). Future investigations should be limited to cubic VOIs within dense trabecular regions.

### 5.5.3 *The Structural Effects of SCI*

All three trabecular compartments in SCI animals underwent rapid loss of trabecular bone after transection of the spinal cord at thoracic level T9. By 2 weeks post-SCI MSS, MPS and ESS compartments experienced an absolute decrease in the amount of trabecular bone (BV) of  $2.66 \pm 0.77 \text{ mm}^3$ ,  $3.91 \pm 0.43 \text{ mm}^3$  and  $2.54 \pm 0.88 \text{ mm}^3$  respectively. Thus, the MPS compartment experienced the most severe absolute decrease in amount of trabecular bone compared to age-matched control, concomitant with this compartment having the highest BS/BV, but all three compartments experienced comparable absolute losses. This decrease in BV was due to a combination of suppressed bone appositional growth (evidenced by the decreased marrow cavity area and similar bone lengths) and SCI-induced bone loss. When this value is normalised to the total volume of the compartment (TV), which considers both longitudinal (z-axis) and appositional (x-y axis) effects, the resulting trabecular bone volume fraction (BV/TV) is acquired. The concomitant decreases in BV/TV for MSS, MPS and ESS compartments were  $59 \pm 3\%$ ,  $54 \pm 3\%$  and  $23 \pm 2\%$  respectively (Figures 4.11, 4.16A and 4.19A). Thus, when normalised the MSS compartment experienced the most severe decrease in volume fraction of trabecular bone compared to control, although this reduction was comparable to MPS.

For both metaphyseal trabecular bone compartments these decreases in BV and BV/TV were characterised by decreases in both average trabecular number and thickness (Figures 4.12 and 4.16), while epiphyseal decreases were characterised by decreased thickness, indicating that the thicker epiphyseal trabeculae were only thinned, not entirely resorbed (Figure 4.19). Thus, the connectivity of the epiphyseal compartment remained intact (on level with control), while the connectivity and geometric fractal properties of both metaphyseal compartments significantly diminished. The trabecular thinning apparent in all three compartments (and removal of trabeculae in metaphyseal compartments)

resulted in concomitant increases in the bone surface to volume ratio. There was also a concomitant transformation of all three trabecular compartments into more rod-like configurations (Table 4.1).

By 6 weeks post-SCI only the MSS compartment experienced a further significant decrease in BV compared to age-matched control (Table 4.1). This further net decrease meant that there were further detrimental effects of SCI on this compartment. There was no time 0 control in this study, therefore isolating this decrease to whether it was due to further SCI-induced trabecular bone loss or depressed trabecular bone growth alone was not possible. The only conclusion that can be made is that it is a combination of both, but the relative contributions of each process are not entirely known. Accounting for the total volume of SCI and control VOIs, indicates that bone loss was a significant component, thus the difference was not just due to suppressed bone growth.

ESS and MPS compartments behaved rather differently. Neither of these compartments experienced further decreases in trabecular BV. By 6 weeks post-SCI in the ESS compartment there was an overall net gain in both trabecular BV and BV/TV. These increases meant that the balance between detrimental effects of SCI and trabecular bone growth on the compartment were tipped in favour of growth (net bone gain). While the MPS did not undergo further significant decreases or increases in net BV acquisition or BV/TV (Table 4.1). This illustrates that there were site-specific and time-specific differences in the effects of SCI on the three trabecular compartments.

By 16 weeks post-SCI there was a significant net overall gain in the amount of trabecular bone compared to earlier (2 and/or 6-week SCI) groups in all three compartments. Thus, by 16 weeks post-SCI, the balance had tipped from the detrimental effects of SCI to bone growth in all three compartments. From 6 weeks post-SCI and onwards, the remaining

trabeculae within all three compartments of the SCI rat femur thickened with time, but at different rates. Only in the ESS compartment was there an increase in the number of trabeculae with time post-SCI, but this was significantly less than the increases seen with time in control ESS compartments. There was a continued decrease in number of trabeculae in the MPS compartment consistent with the continued longitudinal growth, as the remaining primary spongiosa transformed into secondary spongiosa, while no further change in trabecular number was observed in the MSS compartment. The surface to volume ratio of trabeculae continued to decrease consistent with these microstructural changes, but there was no significant change in the overall rod-like to plate-likeness of any compartment (Table 4.1).

These changes resulted in a monotonic decrease in connectivity with time post-SCI for all three compartments. The decrease in ESS connectivity remained in line with that of control, such that there was no significant difference at any time point between SCI and control groups. The connectivity of both metaphyseal compartments behaved asymptotically with time post-SCI, such that there was no difference in connectivity between 10 and 16-week groups. After the initial offset in connectivity for MPS between SCI and control, further rate of loss of connectivity was approximately the same, while there was continued loss of trabecular connectivity in MSS while the control group was more resistant to loss (Table 4.1).

In summary, overall the ESS trabecular compartment was structurally the most resistant to SCI-induced remodelling and suppression of bone growth at all time points post-SCI. The structural reason for this is that these trabeculae were on average significantly thicker than trabeculae within the two metaphyseal compartments. Thus, they offered less surface area per unit volume for bone resorption to occur on and the structure's overall connectivity was maintained as trabeculae were only thinned, not perforated. This result

was in accordance with Lin et al. (2015), who performed the only other rodent study of SCI-induced osteoporosis that characterised the effects of SCI on epiphyseal and metaphyseal trabeculae bone sites. In 4-month old rats that were given T9 contusion injury for a duration of 16 weeks, they observed a much milder deterioration of epiphyseal compared to metaphyseal trabecular bone. A 19% decrease in epiphyseal BV/TV was observed, characterised predominantly by trabecular thinning. In the only pQCT study of children with SCI (n = 19), the 4% tibia epiphyseal trabecular site was examined and a decrease in trabecular vBMD compared to healthy children was observed. Seven children also had a second scan performed in the chronic stages of SCI ( $3.2 \pm 1.0$  years later), and further reductions in trabecular vBMD Z-score and absolute vBMD were observed indicating a protracted lack of bone development in these children. This finding agrees with what was observed here in the growing rat model of SCI. The epiphyseal site is the most commonly assessed trabecular-rich region in studies of adults with SCI. At this site significant reductions in trabecular vBMD are observed within the first year (Coupaud et al., 2015), before a new steady state is reached 3 – 8 years post-SCI (Eser et al., 2004; Frotzler et al., 2008).

The metaphyseal trabecular compartments were less structurally-resistant to SCI (induced bone loss and suppressed bone growth). At 2 weeks post-SCI, both MPS and MSS trabecular compartments were overall much more severely affected. The overall decrease in trabecular bone volume fraction was comparable between the two compartments, both characterised by resorption and thinning of trabeculae, resulting in overall less connected structures compared to controls. While by 16 weeks post-SCI compared to age-matched controls the effect of SCI could be differentiated, with the MSS compartment being the most severely affected. However, this was more due to decreased growth-related changes

in primary spongiosa, rather than any further bone loss or growth suppression (Figures 4.11 and 4.16)

MSS sites are the most common trabecular site investigated in rat studies. Only Lin et al. (2015) also quantified the effects of SCI-induced osteoporosis on the MPS compartment. In 4-month old rats with subsequent SCI of 16 weeks duration, severe decreases in trabecular BV/TV of 65% and 56% in MSS and MPS sites, respectively, were observed compared to age-matched controls. Both characterised by significant reductions in trabecular thickness and number. They concluded that the MSS compartment exhibited the most drastic bone loss. Our study which used similar aged rats (10 to 12 weeks old, with DOI 2, 6, 10 and 16 weeks), observed 55% and 30% decreases in BV/TV for MSS and MPS respectively in the 16-week SCI group compared to control. Thus, our results agree with Lin et al. (2015), in that compared to control it appears that the MSS was most severely affected by SCI. But the earlier time point groups quantified here tell us that this may not be the case, as there were no further decreases in BV/TV after 2 weeks, and that the difference was due to growth-related changes particularly in the MPS compartment, where primary spongiosa transformed into secondary spongiosa (characterised by continued decreases in Tb.N and increases in Tb.Th).

The other rat studies examining MSS have looked at a range of SCI durations from 10 days, most commonly 3 weeks, while one study that examined the effects at 6 months; all were conducted on young growing rats (Jiang et al., 2007a; Jiang et al., 2007b; Liu et al., 2008; Morse et al., 2008; Yarrow et al., 2014; Beggs et al., 2015; Lin et al., 2015). Similarly, they all reported striking decreases in trabecular BV/TV in the range of 36% to 76% compared to time matched controls, characterised by significant decreases in average thickness and number. However, no significant correlation can be made between



BV/TV and duration of injury due to confounding factors that exist between studies.

Table 5.1 lists many of the main factors, with examples from several studies.

**Table 5.1.** Comparison of main confounding variables in  $\mu$ CT studies of bone loss in rat SCI models.

<b>Study Parameter</b>	<b>Morse et al. (2008)</b>	<b>Yarrow et al. (2015)</b>	<b>Lin et al. (2015)</b>	<b>Current study (2019)</b>
Rat	Sprague-Dawley	Sprague-Dawley	Fischer 344	<b>Wistar</b>
Sex	Male	Female	Male	<b>Male</b>
Injury type	Contusion	Contusion	Contusion	<b>Transection</b>
Age at SCI	7 weeks	16 weeks	4 months	<b>10 - 12 weeks</b>
Time since SCI*	10 days	7 & 14 days	16 weeks	<b>2, 6, 10 &amp; 16 weeks</b>
Control used?	Yes	Yes	Yes	<b>Yes</b>
Shams used?	No	No	No	<b>Yes</b>
Trabecular VOI	3.4mm	1.5 – 5.5 mm <sup>+</sup>	2.5 – 4 mm	
Voxel size ( $\mu$ m)	17	19.2	15	<b>6.89</b>

\*The time post-injury that  $\mu$ CT was performed.

<sup>+</sup> Format: (distance above distal growth plate) – (end of VOI).

Two rat  $\mu$ CT studies quantified the time course changes of metaphyseal trabecular bone in the proximal tibia MSS at acute periods post-SCI in young growing rats (Minematsu et al., 2014; 2016), the results from both are in accordance with our results. The first study used 8-week old rats that underwent low thoracic transection SCI, which were subsequently sacrificed at 1, 3 and 5-weeks post-SCI. In the 1-week post SCI group a significant decrease in trabecular BV and BV/TV characterised by significantly decreased Tb.N and Tb.Th compared to control. Further reductions in BV were seen up to 3 weeks post-SCI. By 5 weeks of age growth-related increases in trabecular thickness were observed in both control and SCI groups, but no mention of growth was made in the discussion. These studies confirm our observation that the SCI-induced decreases of trabecular bone quantity and quality are very rapidly. However, the localisation of

whether and when a potential steady-state has been reached in terms of the deleterious effects of SCI on trabecular bone is made significantly harder due to the background of bone growth.

Trabecular-rich metaphyseal sites are much less commonly assessed than epiphyseal sites in human SCI pQCT studies. The one study that analysed trabecular bone loss in the metaphysis observed a significant decrease in trabecular vBMD as early as one year, and further decreases were seen until a trabecular vBMD steady-state was achieved by 4 years post-SCI, at approximately 50% of healthy controls (Dudley-Javoroski & Shields, 2012).

Therefore, the decreases in amount and volume fraction of trabecular bone in the growing rat model of SCI (compared to control) are similar to that observed in the adult human SCI population. But as shown, the confounding effect of suppressed bone growth is a contributing factor that does not exist for the adult SCI population. The fact that this confounding factor is not accounted for in the rodent studies of SCI-induced osteoporosis mentioned, i.e. that the observed changes between SCI and control groups are assumed to be due to SCI-induced bone loss, means that the majority of conclusions made in these studies do not describe the complete picture (Jiang et al., 2007a; Jiang et al., 2007b; Liu et al., 2008; Morse et al., 2008; Yarrow et al., 2014; Beggs et al., 2015; Lin et al., 2015). The main reason this may not have been addressed in these studies is that they are single time point cross-sectional studies. In comparison, in our multi-timepoint cross-sectional study the effects of suppressed bone growth become self-evident.

## ***5.6 Cortical Bone Distributions***

This is the first animal study to analyse the morphological effects of SCI over large regions of cortical bone (40 – 85% bone length). The majority of  $\mu$ CT studies in this research area limit cortical morphometric analysis to the midshaft, very few analyse the more clinically-relevant (for SCI) metaphysis. This is important because results presented here indicate that measurements from the midshaft region do not generalise well to the distal end (Figure 4.24). This global analysis of cortical bone quantifies a time-dependent response to SCI, where at 2 weeks (and 6 weeks) it is the more distal regions where the most pronounced decreases are seen compared to control (Figure 4.26).

## ***5.7 3D Cortical Morphometric Analysis***

Considering the clear differences observed between distal and shaft regions highlighted by the 2D cortical distribution graphs, the distal-metaphyseal (81 – 85% bone length) and mid-diaphyseal (58 – 62% bone length) VOIs were selected for further 3D analysis.

### ***5.7.1 Appositional Bone Growth***

By studying the 2, 6, 10 and 16-week sham control groups (i.e. 14, 18, 22 and 28 weeks of age rats), “normal” growth and age-related effects can be observed in the femur. Cortical area (Ct.Ar) is a measure of mass accumulation, i.e. the amount of bone. This increased monotonically between 2, 6, 10 and 16-week groups in the mid-diaphyseal and distal-metaphyseal cortical bone VOIs, both of which started to plateau in the older groups (Figures 4.27B and 4.28B). Even so, the absolute gains in amount of bone in the different regions were significantly different, with the mid-diaphyseal VOI accruing almost three times as much bone between 2 and 16-week groups than the distal-metaphyseal VOI.

The increase in the amount of cortical bone is instigated by bone formation and/or resorption on periosteal and/or endocortical surfaces. Tt.Ar (or Ps.Pm) and Ma.Ar (or Ec.Pm) are measures reflecting this activity on the periosteal and endocortical surfaces, respectively. Periosteal expansion was observed with age for both the mid-diaphysis and distal-metaphysis, with peak Tt.Ar being reached at 6 weeks post-surgery (Figures 4.27C and 4.28C). In contrast, endocortical activity was different for the mid-diaphysis and distal-metaphysis. Marrow expansion was observed for the distal-metaphysis between 2 and 6 weeks, while no statistical changes in marrow area were observed for the mid-diaphysis (Figures 4.27D and 4.28D). Metaphyseal Ct.Ar increased with age through a combination of periosteal expansion and endocortical resorption (expansion of the marrow cavity), while diaphyseal Ct.Ar increased through periosteal expansion.

For the metaphysis the spatial distribution of bone as measured by the polar moment of area did not significantly change with age, but the eccentricity did, suggesting that growth had caused a redistribution of mass around the bone's centre of gravity into a less symmetric and less circular configuration (Figures 4.27E and G). This helps explain why there was no overall change in average thickness, as by inspecting Figures 4.29, certain regions of the metaphysis had thickened while others had thinned. For the diaphysis there was a tendency for polar moment of area to increase (similarly to Tt.Ar) between 2 and 16 weeks (Figures 4.28C and E).

The mid-diaphyseal changes observed were a result of rapid radial growth through bone formation on the periosteal surface and bone drift, which tapered off in the older groups. While the distal-metaphyseal changes result in an almost constant cortical thickness over the periods monitored. This might appear surprising, but it is a consequence of the growth process (longitudinal bone growth). The age of the metaphyseal cortical bone depends on the rate of growth. It is conceivable that growth makes it problematic for this bone to

adapt to its constantly-changing mechanical needs. These results and interpretations are consistent with clinical observations that metaphyseal cortical thickness remains relatively constant in young children during growth, once longitudinal bone growth has stopped, metaphyseal bone strength can catch up to requirements, thus metaphyseal cortical bone rapidly thickens during adolescence (Rauch & Schönau, 2005).

### *5.7.2 Effects of SCI on Cortical Bone*

3D analysis of both mid-diaphyseal and distal-metaphyseal cortical bone confirmed the observation that at the earliest time point assessed post-SCI (2 weeks) metaphyseal cortical bone was more severely affected than diaphyseal, both in terms of percentage and absolute decreases in Ct.Ar, where losses of 17% ( $0.7 \pm 0.19 \text{ mm}^2$ ) and 9% ( $0.45 \pm 0.16 \text{ mm}^2$ ) were observed, respectively, compared to control. This difference was at least in part due to the difference in relative bone surface to bone volume ratio (BS/BV), where the metaphysis had a 37% higher BS/BV compared to the diaphysis, equating to a larger surface area for bone turnover to occur on. This result compares well with human SCI, in a study by Rittweger et al. (2010) who performed pQCT scans of the tibia at every 5% bone length, in 9 men with chronic SCI (DOI between 9 and 32 years) and age, height and weight matched able-bodied controls. They noted wide-spread effects of SCI, where volumetric bone mineral content was significantly lower at all sites in SCI compared to controls but was more pronounced at the proximal and distal ends compared to the shaft. The theory proposed for this discrepancy between distal and shaft bone losses was the same as in our rodent model, namely that bone's adaptive response is a consequence of the surface area available for bone turnover, thus the reduced BS/BV ratio at the mid-diaphysis results in a less pronounced adaptive response than at the distal-metaphysis.

### 5.7.2.1 Diaphyseal Bone

The acute (2-weeks) post-surgery mid-diaphyseal decrease in Ct.Ar was characterised by a reduction in average thickness, which by 10 weeks post-surgery was characterised by a 23% and 16% decrease in total and marrow areas respectively (Figure 4.28), indicating that the periosteal and endocortical expansion evident in the growing control groups was suppressed here. The cortical thinning is consistent with what is observed in clinical studies of SCI, but the mechanism of this thinning is different. Adults with SCI experience cortical bone loss through endocortical thinning (marrow expansion), before new geometric and densitometric steady-states are eventually reached (typically a number of years) post-SCI (Eser et al., 2004; Frotzler et al., 2008). The results presented here are a combination of the initial loss of bone (associated with SCI-induced remodelling) and abnormal bone growth/development. Our results compares well with Biggin et al. (2013), who assessed the morphology of bone in children with SCI (age at injury  $6.6 \pm 4.1$  years). Cross-sectionally they observed, compared to healthy control children, children with SCI (average DOI  $5.6 \pm 3.6$  years before scan) had significantly reduced cortical and total cross-sectional area of the tibial mid-diaphysis. Our observation of reduced eccentricity of the femoral mid-diaphysis in 10 and 16-week SCI groups of rats compared to controls (Figure 4.28G), is also in accordance with Biggin et al. (2013) clinical study, which quantified and noted a transformation in the tibial diaphysis shape from its usual teardrop appearance to a more circular shape. This result is in keeping with the lack of directional muscle-driven bone stimulation after paralysis.

Analysis of 2, 6 and 10-week post-surgery SCI groups revealed that cortical area did not significantly increase over this period, but the marrow area did significantly decrease and there was a general reduction in total area, indicating that there was a significant redistribution of bone material in the diaphysis to a more-slender configuration. This 10-

week period appears to be dominated by the confounding effects of SCI and bone growth. This again is in agreement with Biggin et al. (2013) who performed a second scan on seven of the children with SCI  $3.2 \pm 1.0$  years later, they observed no statistical difference in the amount of bone or its density weighted polar moment of area between the two scans. By 16 weeks post-surgery the growth-related process of increasing cortical area through increasing total area appears, resulting in a significant increase in the polar moment of area (Figure 4.28E). An interpretation of this would be that a steady-state has been reached in terms of the SCI's effects on the bone, and now appositional growth is the dominant process. There currently appears to be no data in the literature to support this hypothesis in animal or patient studies.

An interesting observation is the rather rapid rate of diaphyseal appositional bone growth present between 10 and 16-weeks SCI groups (Figures 4.28B and C). Over this period there is no significant appositional growth in the control groups. On its own this would be quite a surprising result but given that bone formation is still significantly active between 10 and 16 weeks (as indicated by the increase in longitudinal length) it is not that surprising that rapid appositional growth is possible after SCI in the growing skeleton, once the initial SCI-induced remodelling has decreased.

#### *5.7.2.2 Metaphyseal Bone*

The acute (2-weeks) post-SCI distal-metaphyseal decrease in Ct.Ar was characterised by decreased Tt.Ar and Ma.Ar, a consequence of suppression of appositional bone growth and/or SCI induced bone loss. This resulted in decreased polar moment of area compared to age-matched controls. Overall these changes persisted for all later time point groups, resulting in the metaphyseal region having a more-slender spatial configuration, but the

cortical thickness remained comparable to that of control values in 6, 10 and-16 weeks post-surgery groups (Figure 4.27).

There is a lack of clinical literature on the effects of SCI on metaphyseal cortical bone. This is because in this region the cortex is very thin and due to the partial volume effect is not directly quantifiable with pQCT systems (Rauch & Schönau, 2005), let alone the clinical standard densitometry technique (DXA). Rat SCI studies of metaphyseal cortical bone have only looked at the acute stages of injury (DOI 10 days to 3 weeks) (Jiang et al., 2006; Morse et al., 2008; Yarrow et al., 2014). All three of these studies on growing rats reported significant reductions in cortical thickness, which is in accordance with our earliest time point (2 weeks post-SCI), but the mechanisms for this reduction were not fully quantified, with only one study observing a suppression in growth (Jiang et al., 2006). Further work is needed in this area, since it is the metaphysis that is most prone to fracture after SCI.

### ***5.8 Porosity***

A unique feature of this study was the characterisation of cortical porosity, which has not been characterised in previous rat  $\mu$ CT studies of SCI-induced osteoporosis. The resolution used (6.89  $\mu$ m) was enough to resolve large scale porosity in distal-metaphyseal cortical bone, but not in the mid-diaphysis. Smaller canals associated with lacunar-canalicular porosity are not detected and vascular porosity is underestimated due to partial volume effects. Nevertheless, quantification of porosity at the metaphysis revealed interesting results. Firstly, a significant reduction in pore volume fraction with time is seen in the control group (Figure 4.32). This is in accordance with the increased porosity seen in young growing paediatric bone, compared to skeletally mature bone (Ogden, 1984). Secondly, at 2 weeks post-surgery, compared to age-matched controls a



significant increase in porosity in metaphyseal cortical bone of the SCI rats is seen, which at later time points reaches similar or significantly reduced levels compared to their age-matched controls. An explanation for this, which would need confirmation through histomorphometry, is that immediately after SCI bone multicellular unit (BMU) creation increases. At 2 weeks post-SCI the consequence of the resorption phase of the recently recruited BMUs is observed. Thus, BMUs make transient pores within the bone, and when BMU creation declines as the bone adapts to its new disuse-related environment, a certain portion of the pores are filled back in. This would be a possible consequence of a BMU's activation-resorption-formation sequence. Secondary evidence for increased porosity is seen in the reduced BMD (both areal – from DXA, and volumetric – from CT) values observed in densitometric studies of the SCI population. Thirdly, there is an indication that the porosity quantified is linked to vasculature, since in all 8 groups over 90% of the porosity is contributed to by open pores, that is pores that are not fully enclosed by bone (i.e. is connected to outside space), as opposed to closed pores.

The relationship between blood flow, vascularisation, porosity and bone formation/resorption currently has not been fully elucidated. There are conflicting results in the literature. Short periods of disuse (7 to 14 days) have been associated with significantly decreased bone blood flow and increased vascular resistance (Lucas, 1987), while other studies have reported that rapidly induced osteoporosis from transection injured and orchidectomy rats have shown increased blood flow within the paralysed limbs (Verhas et al., 1980; Schoutens et al., 1984).

### ***5.9 Tissue Mineral Density***

Cortical tissue mineral density (TMD) as opposed to the more commonly used bone mineral density (BMD) was quantified here. The difference is that BMD refers to the

overall mineral density of a VOI, so it is the combined mineral density of both soft and bone tissue, while TMD quantifies the mineral density of only the bone tissue within the VOI. TMD was determined for the entire cortical VOI (40 – 85% bone length). Several interesting TMD-related results are seen. Firstly, there was a trend of decreasing cortical TMD with distance from the midshaft in both control and SCI femurs, to the point where in several groups distal-metaphyseal cortical bone had significantly lower TMD than mid-diaphyseal cortical bone (Figures 4.31 A and B). This trend has been noted in a  $\mu$ CT and Raman spectroscopy study of rat and human cortical bone (Buckley et al., 2014; Wong et al., 1995). The explanation given for this is that older bone is more mineralised than younger bone. This assumption holds for the rat femoral cortex since Haversian remodelling is minimal, thus the difference in location of a bone cross-section along the diaphysis reflects the difference in age, thus mid-diaphyseal bone is older than distal-metaphyseal bone, and thus more mineralised. Secondly, there was a slight trend of increased TMD with time post-surgery for both control and SCI groups (Figure 4.31B), which is in line with what is seen in the growing skeleton (Kalu et al., 1989; Willingham et al., 2010). Thirdly, at all four time-points assessed, there was no significant difference in TMD between control and SCI groups. This is in accordance with a preliminary Vicker's microhardness test performed on the diaphyseal bone for 10-week control and 10-week SCI femurs (both n = 5) (data not presented), where no significant difference was observed in this geometry independent measure of material hardness. Only one rat study of SCI-induced osteoporosis has quantified cortical TMD, their result agreed with ours where no significant difference was observed in mid-diaphyseal cortical TMD between control and SCI rats (Lin et al., 2015).

## ***5.10 Mechanical Tests***

Three-point bend and torsion tests were conducted on the right and left femora respectively of all groups. These modes of testing were chosen since they reflect the types of loading long bones are subjected to *in vivo* and when a long bone fractures, this failure often is due to both bending and torsional forces. In three-point bending, the failure location is predetermined by the location of central actuator (60% bone length) and is highly dependent on the bone's orientation (P-A here), while in torsion the mechanical properties of the entire diaphyseal bone within the gauge length are tested and failure occurs at the weakest point along this length, and the observed failure mode of a spiral fracture is seen clinically.

### ***5.10.1 Three Point Bend***

Maximum load before fracture and stiffness (the amount of elastic deformation the mid-diaphyseal undergoes during loading) significantly increased for the control group between 2 and 10-weeks post-surgery, with no further changes by 16 weeks (Figure 4.35). This agrees with Jiang et al. (2007b), who performed three-point bend tests on the femurs of three sets of 6-week old sham-operated rats at 2 and 6 weeks, and 6 months post-surgery. They observed a significant increase in maximum load between 2 and 6-weeks groups, but between 6 weeks and 6 months post sham surgery no differences were observed, unfortunately their study did not perform any geometrical measures of the diaphysis. In our study, maximum load and stiffness both correlated strongly with mid-diaphyseal Ct.Ar, Tt.Ar and polar moment of area and the correlation between each parameter pair was significant (Figure 4.36). These findings support the concept that the strength of the mid-diaphysis increases as it grows appositionally, and when this growth slows so does the concomitant increases in strength. This is in accordance with the

increased strength and stiffness and concomitant geometric changes seen with age in the tibiae and femora of growing rats and mice (Mustafy et al., 2018; Willinghamm et al., 2010). Post-yield displacement (PYD) and work to fracture in contrast did not show any significant growth-related changes. PYD is the distance between yielding and fracture, where the mechanical properties of bone are permanently altered. It is thus a measure of brittleness/ductility. A change in PYD would reflect a change in tissue-level properties of bone, thus this result is in accordance with the non-significant change observed in TMD with age. This is not in agreement with growing mice studies, where sharp decreases in PYD are observed during growth (Brodt et al., 1999; Willinghamm et al., 2010), which is generally attributed to increased mineralisation and collagen cross-links with age (Wang et al., 2002). The non-significant decrease in PYD observed here may be due to only examining a short period of time (14 weeks) in already substantially grown bone. Work to fracture is an integrative measure that is the area under the force-displacement curve, it is a function of the three previous measures reflecting the energy absorbed before fracture. The non-significant change seen here is in agreement with Jiang et al. (2007b) and in growing mice studies where it is associated with growth-related PYD changes (Willinghamm et al., 2010).

By 2 weeks post-SCI there was a significant reduction in all four whole-bone mechanical properties (stiffness, maximum load, PYD and energy to fracture) compared to control (Figure 4.35, Table 4.5). There was no significant change in any whole-bone mechanical property between 2 and 10-week SCI groups. These results, particularly in stiffness and maximum load agreed with the non-significant changes to diaphyseal morphology over the same period. While by 16 weeks, there was a significant increase in stiffness and maximum load compared to 10-week group, so much so that no significant difference exists between SCI and control groups. This change was also in agreement with the

diaphyseal morphology, where a rather rapid rate of diaphyseal appositional bone growth was observed between 10 and 16-week SCI groups, and all time point post-SCI groups correlated positively with mid-diaphyseal Ct.Ar, Tt.Ar and polar moment of area. Grouping all 4 control and SCI groups together and performing a linear regression analysis further increased the correlation coefficients, as shown for the maximum load versus mid-diaphyseal cortical area (Figure 3.36). This supports the concept that it is predominantly the detrimental effects on the amount and spatial distribution of diaphyseal cortical bone caused by SCI-induced osteoporosis in the growing rat, that have caused the changes in whole-bone mechanical properties, as opposed to changes to the bone material itself measured in this thesis by TMD.

The significant reduction in maximum load and stiffness of the mid-diaphysis observed at 2 weeks post-SCI is in accordance with all rodent studies of SCI-induced osteoporosis that quantify three-point bend-derived mechanical properties of the diaphysis (Jiang et al., 2006; Liu et al., 2008; Beggs et al., 2015) in the early stages of injury (3 to 4 weeks post-SCI). Only Jiang et al. (2007b) looked at longer durations of SCI (DOI 3, 6 weeks, and 6 months), unlike in our study where by 16 weeks post-SCI no significant difference existed between SCI and control groups, in their study the percentage difference between maximum load and work to fracture of the age-matched control and SCI groups remained almost constant between the three time points post-surgery. No measures of cortical geometry were obtained by Jiang et al. (2007b), the only piece of evidence found in their study that could be used to explain this discrepancy is the femoral wet mass. In our study, between 2 and 16-week groups femoral mass increased by 48% and 31% for control and SCI groups respectively, while between 3-week and 6-month groups in Jiang et al. (2007b) femoral mass increased by 12% and 17% for control and SCI groups respectively. This is an indication that the 6-week old rats used in Jiang et al. (2007b) may have been

more skeletally mature than our rats, thus the appositional growth seen by increased Ct.Ar between our 10 and 16-week SCI groups, which correlates well with increases in stiffness and strength, may have not been as prominent for them.

The three-point bend-derived material level properties elastic modulus and ultimate stress significantly increased with time post-surgery for both control and SCI groups, but these properties did not significantly differ between any age-matched control or SCI group (Figure 4.37). These results were in accordance with the cortical TMD results, but not in agreement with the rodent SCI studies that determined the elastic modulus and ultimate stress for the mid-diaphysis of either the femur or tibia (Jiang et al., 2006; Liu et al., 2008). In both cross-sectional studies, the reported elastic modulus and ultimate stress in young (6-week old) male rats with duration of SCI of 3 or 4 weeks was significantly reduced compared to age-matched controls. Again, there are several differences between our studies, in terms of these tissue level properties, this study computed geometry independent measures of moment of area, while these quoted studies assumed the geometry of bone cross-sections to be hollow ellipses. The material-level properties derived from whole-bone tests make many assumptions (e.g. the bone is made of a homogeneous, linear-elastic, prismatic material that is long in proportion to its depth) and provides an average value for the entire region tested. To answer the question of whether the material-level properties of bone are affected by SCI more deeply, further tests such as direct mechanical measurements of bone for example through nanoindentation, atomic force microscopy or reference point indentation, or through compositional analysis with for example ash content or Raman spectroscopy should be conducted.

### 5.10.2 Torsion Tests

Maximum torque (torsional load to failure), rotational stiffness, modulus of rigidity and ultimate torsional stress (strength of bone tissue when loaded in torsion) all monotonically increased for the control group between 2 and 16-weeks post-surgery (Figure 4.40). This is in accordance with the literature where increases are seen for growing rats, but in adult rats no significant changes with age are observed (Ekeland et al., 1981). A difference between bending and torsional whole bone properties was observed between 10 and 16-week control groups, where bending-derived maximum load and stiffness plateaued, but maximum torque and rotational stiffness continued to increase. At first glance this may be unexpected, since as observed in Figure 4.25 the polar moment of area was found to be lowest in the mid-diaphyseal regions (55 – 75% bone length), which included the three-point bend location (58 – 62% bone length). This would suggest that we may expect the destructive three-point bend and torsion tested bones to fracture in approximately the same locations. But torsion tests the mechanical properties of the entire bone within the gauge length, which depends not just on the amount and spatial distribution of bone, but also its material properties. The cortical TMD distributions (Figure 4.31A), follow an opposite trend to J, i.e. TMD decreases distally from the mid-diaphysis. Thus, the structurally weakest bone cross-sections may not occur at the mid-diaphysis but more distally. This agrees with the observation that torsion fractures were in supracondylar regions (60 - 85%) bone length. These regions, particularly the more distal regions are metaphyseal, which in growing bones such as these continues to thicken, while diaphyseal appositional growth may have stopped (Rauch, 2005), this would thus explain why whole-bone torsional mechanical continued to increase. To further test this hypothesis, a torsional rigidity (GJ) distribution could be determined, which is the product of the shear modulus and polar moment of area (Villa-Camacho et al., 2014). It considers both

material and geometric properties, therefore it would be more suitable for identifying the weakest cross-section, thus region most probable to fracture under torsion.

By 2 weeks post-SCI there was a significant reduction in maximum torque and rotational stiffness compared to control, this difference between SCI and control groups was either maintained or increased at later time points. These results are somewhat in accordance with those of Sugawara et al. (1998), which was the only study found in the literature that performed a torsion test on the femoral shaft of SCI rats (in this case 60 day old male rats, with T9 transection SCI, with DOI of 8 or 24 weeks). They observed a significant decrease in maximum torque to that of age-matched control only at 24 weeks post-SCI, which was strongly correlated with reduced cortical bone area and polar moment of area.

Rotational stiffness monotonically increased between 2 and 16-weeks post-SCI groups and maximum torque also showed overall significant increases between 2 and 16-week groups, unlike bending derived stiffness and maximum load. Both whole-bone mechanical properties correlated significantly better with distal-metaphyseal Ct.Ar and J than mid-diaphyseal Ct.Ar and J, again indicating that the fracture site was more distal than that of three-point bend.

The torsion-derived material level properties rigidity modulus and ultimate torsional stress significantly increased with time post-surgery for both control and SCI groups, but these properties only significantly differed for 2-week control or SCI groups (Figure 4.41). This is in accordance with Sugawara et al. (1998), who observed no difference in maximum shear stress of the femoral diaphysis between 8 or 24 week post-SCI rats. Overall these results along with three-point bend derived properties, TMD and preliminary Vicker's microhardness tests suggest that the reduction in diaphyseal bone strength is not due to changes in bone material properties, but due to geometric changes.



### *5.10.3 Femoral Neck Fracture*

There is a lower incidence of femoral neck fracture in patients with SCI than at the distal femur or proximal tibia (Frotzler et al., 2015), which coincides with the lower losses of BMD in the femoral neck than that of the proximal tibia (Biering-Sorensen et al., 1988). There was a significant decrease in peak fracture force of the femoral neck between 2 and 6-week post-surgery control and SCI groups, but this decrease was insignificant between for 10 and 16-week groups (Figure 4.43). This result is in accordance with Sugawara et al. (1998) who observed an insignificant loss of femoral neck strength at 8 and 24 weeks post-SCI.  $\mu$ CT scans of the femoral neck were not performed, so the effects of SCI-induced bone loss and suppressed bone growth could not be observed to further elucidate what is occurring.

### *5.11 CTX-I*

CTX-I is a bone resorption marker of the collagen degradation product type I collagen. It provides an evaluation of whole-body bone resorption and was used here to assess the role of bone resorption in SCI-induced osteoporosis. We observed that the CTX-I level and hence bone remodelling was significantly up at 2 weeks post-SCI and decreased with time (Figure E.1). In the 6-week SCI and control groups CTX-I level was approximately the same, this was true for all later time point groups. The result of increased CTX-I level at 2 weeks post-surgery compared to control was in accordance with findings obtained by Beggs et al. (2015). They observed a 50% increase ( $p < 0.05$ ) in increase CTX-I level in more skeletally mature (5 months old) rats with SCI duration of 2 weeks. In another study conducted on younger rats (6 weeks of age), the bone resorption marker N-terminal cross-linking telopeptide of type I collagen (NTX-I) was found to be significantly higher ( $p < 0.001$ ) 3 weeks post-SCI (Jiang et al, 2006). Our result of no significant difference in

CTX-I level at the latest time point post-surgery was in accordance with Lin et al. (2015). In 4-month old rats they found that after 16 weeks of T13 contusion SCI the bone resorption marker Tartrate-resistant acid phosphatase (TRAP) was not significantly different to age matched control. No intermediary bone resorption marker data between 4 and 16-weeks post-surgery could be found in the literature.

The bone resorption markers CTX-I, NTX-I, pyridinoline and deoxypyridinoline (DPD) have been found to be elevated after SCI in patients (Ludwig et al., 2007), with increased bone resorption markers being observed as early as 2 weeks post-SCI, peaking around 4 months post-SCI (Giangregorio et al., 2006), remaining elevated for at least 6 months – 2 years post-SCI (Roberts et al., 1998; Sabour et al., 2014). The time points assessed in our study were not enough to reveal details seen in clinical studies, such as the sharp increase then gradual decrease in the early stages of SCI, but the overall trend of CTX-I decreasing into the chronic stage of injury was observed, but at very different timescales compared to patients.

### ***5.12 Limitations***

As previously discussed, the use of growing rats as a model of adult SCI-induced bone loss is a significant limitation. Future studies should be conducted on more skeletally-mature rats. To overcome the shortcomings associated with a growing model, ideally a 10-month old rat should be used, with trabecular bone taken from MSS sites. 10 months is ideal because a skeletally mature animal is used, without age-related bone loss.

A second major limitation is the cross-sectional as opposed to longitudinal experimental design of the study. That is the use of different animals for each time point; using 2, 6, 10 and 16-week post-surgery SCI and control groups, instead of following up the same SCI and control animals at the 4-time points, allowing architectural changes in the same bone

to observed. Although, this would require use of an *in vivo*  $\mu$ CT scanner, resulting in lower resolution scans of the distal femur.

A third major limitation is the material-level properties of bone were indirectly obtained. TMD is determined from the average X-ray attenuation of bone, and three-point and torsion derived moduli only provide estimates of material properties. More direct methods such as ash content and back scattered electron microscopy should be used for mineralisation assessment, and micro/nano indentation tests on small machined bone sections for modulus determination.

## Chapter 6 Conclusions and Future Work

This thesis characterised changes in the microarchitecture, mechanical and material properties of the femur during growth and spinal cord injury (SCI) in a T9 transection rat model using a range of techniques and analysis methods. Additionally, for the  $\mu$ CT data, a 2D “slice-by-slice” analysis method for highlighting site-specific changes in bone was developed and validated.

### 6.1 Conclusions

The main conclusions from this thesis are:

- The 2D “slice-by-slice”  $\mu$ CT analysis technique developed and used here is a useful surveying tool that allows the identification of local regions of interest that may warrant further investigation.
- The microarchitecture of trabecular bone significantly varies between anatomical sites in the distal femur, which may be linked to the different loading environments and mechanical functions.
- Bone microarchitecture both trabecular (e.g. BV/TV and Tb.Th) and cortical (e.g. Ct.Ar and Ct.Th), and cortical mechanical (stiffness and strength) and material (TMD) properties increased with growth as the bone adapts to a continually changing loading environment.
- In the growing rat femur, metaphyseal trabecular bone is more affected by SCI-induced structural damage than epiphyseal trabecular bone
- SCI has decreased the spatial distribution of both trabecular (BV, BV/TV, Tb.Th and Tb.N) and cortical bone (Ct.Ar, Ct.Th, J) in site-specific ways, but the bone material itself (TMD) does not appear to be affected.

- The slenderer spatial configuration of cortical bone after SCI primarily explains the reduced whole-bone mechanical properties observed.
- If the aim of a therapy is to prevent SCI-induced osteoporosis, then it must be start as soon as feasibly possible after injury.

## ***6.2 Future Work***

Further investigations that have the potential to improve our understanding of SCI-induced osteoporosis (and thus how to intervene and treat it) range from additional imaging studies in animal models to intervention studies in the clinical population.

Imaging-based approaches could provide further characterisation of changes in bone quality and material distribution, in the rat model. For example, by combining histological techniques with staining to visualise the changes that occur at and around the growth plate. The growth plate and effects of longitudinal bone growth could further be investigated with use Goldner's trichrome staining. This would allow for the demonstration of normal chondrocyte organisation in control rats and the effects of SCI-induced osteoporosis on endochondral ossification processes in SCI rats (Morse et al., 2008).

To validate the hypothesis that the differences between trabecular and cortical bone parameters between and within control and SCI groups are due to changes in modelling and remodelling processes, histology and histomorphometry should be performed and variables such as osteoblast and osteoclast surfaces and bone formation rates calculated.

To characterise the compositional response of bone after SCI, Fourier Transform Infra-Red (FTIR) and/or Raman spectroscopy can be used. They generate information for example on collagen maturity, mineralisation, crystal size, carbonate substitution. Other

tools such as Sirius red staining for collagen and ashing of cortical bone would provide further information on the bone matrix's mineral content.

To further study porosity, a multimodal and multiscale image analysis could be performed. This would involve combining scan data from different resolution scales/imaging modalities and scan coverages, thus allowing the linking of porosity information across different length scales. For example, whole bone coverage would be achieved with  $\mu$ CT at a resolution for example of 10  $\mu$ m, this would be combined with higher resolution data from other techniques such as nanoCT and scanning electron microscopy on sections of the same bone. Overall this combined information could be used to quantify and model the overall bone porosity.

For further characterisation of the mechanical properties of the bone after SCI, in particular to assess the fracture-prone distal femur, a modified A-P compression and bending test that assesses metaphyseal cortical bone (as opposed to the commonly tested mid-shaft) could be performed, as conducted by Yarrow et al. (2014).

Quantifying the biomarkers of the activity of different cell types (e.g. osteoblasts and osteoclasts) would be recommended to identify time-points at which the relative rates of bone formation and resorption are most affected by SCI, to help identify the most appropriate time-window for intervention to attenuate bone loss. A PINP (total procollagen type 1 N-terminal propeptide) or similar assay used as an evaluation of whole-body bone formation would complement the CTX-I assay performed here.

Finally, a refined animal model is recommended, to better reflect the stage of skeletal development that most patients with SCI are in at the time of injury. If the goal is to study SCI-induced osteoporosis in a model that mimics as closely as reasonably possible the

bone loss observed in the adult human SCI model, a more skeletally mature rat must be used, accompanied by time 0 control rats.

## **Appendix A - Trabecular Morphometric Parameters**

This appendix discusses all 3D and 2D trabecular morphometric parameters used in this thesis to characterise the effects of SCI-induced osteoporosis on the distal femur are discussed in depth here. 3D trabecular morphometric parameters are calculated directly from binarised, surface-rendered volumetric models acquired from  $\mu$ CT scans (Figure 3.27A). 2D trabecular morphometric parameters are calculated for each slice in the dataset and plotted as a function of percentage bone length (Figure 3.27B). All parameters described follow the standard nomenclature recommended by the American Society of Bone and Mineral Research (Bouxsein et al., 2010).

### ***A.1 Metric Parameters***

#### ***A.1.1 Bone Volume, Total Volume & Bone Volume Fraction***

Bone volume (BV) represents the volume of binarised objects within the volume of interest (VOI). In 3D analysis it is determined through use of the volumetric-marching cubes algorithm, where the surface-rendered model of trabecular bone is infilled from its surface with tetrahedrons (Müller & Rüegsegger, 1995), while in slice-by-slice (2D) analysis it is derived simply by counting binarised voxels. Total (or tissue) volume (TV) represents the total volume of the VOI. The ratio of these two indices gives the bone volume fraction (BV/TV), the amount of the VOI occupied by bone. In 2D analysis trabecular BA/TA is defined as the ratio of the total number of pixels representing trabecular bone to the total number of medullary cavity pixels, as depicted in Figure A.1. It represents the fraction of each medullary cross-section that is occupied by mineral bone tissue.



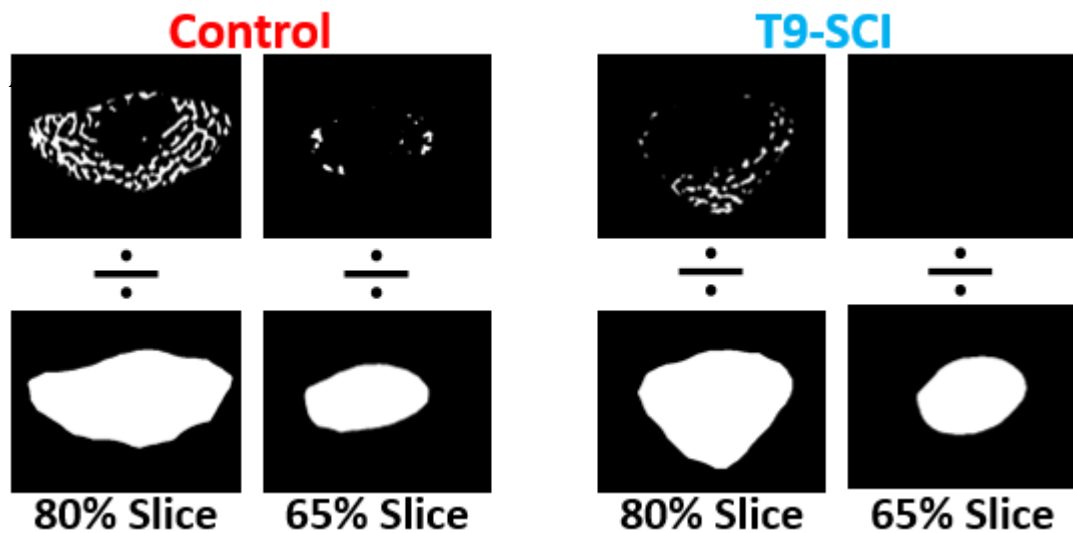


**Figure A.1.** Schematic of trabecular bone area fraction (BA/TA). For representative A) 10-week control and B) 10-week SCI femurs at 80% and 65% bone length from the proximal end.

#### *A.1.2 Bone Surface Area & Bone Surface to Volume Ratio*

Bone surface area (BS) is determined by a marching-cubes algorithm, where a triangular surface configuration defines the free surfaces of the bone dataset (Lorenson & Cline, 1987) (Figure A.2). It is the total area of the triangles that is reported. These triangles form one side of the outer most tetrahedrons used for 3D BV/TV calculations. Bone surface to volume ratio (BS/BV) is then the ratio of solid bone surface to bone volume within the VOI.

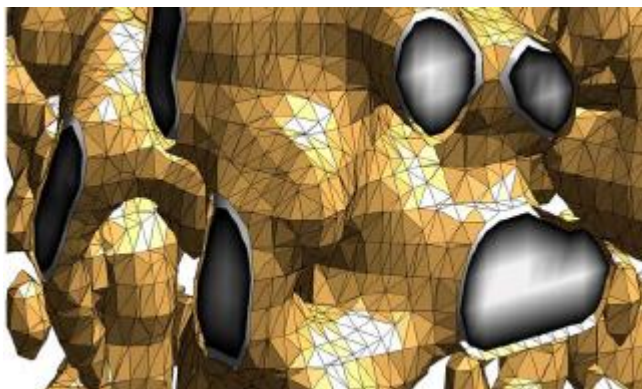


**Figure A.2.** Schematic representation of the triangulation of 3D trabecular bone surfaces for bone surface area calculation. From Bayarri (2010).

### *A.1.3 Trabecular Thickness, Separation & Number*

To acquire a mean trabecular thickness (Tb.Th), first a local thickness is defined for all points within the structure. For a given point, the local thickness is defined as the diameter of the largest sphere that includes the point and entirely fits within the structure (Figure A.3A). The mean thickness of the structure is then the volume-weighted average of all the local thicknesses. Trabecular separation (Tb.Sp) is determined with the same technique, just applied to the inverse of the structure i.e. the empty (marrow) space (Hildebrand and Rüegsegger, 1997a; Remy and Thiel, 2002) (Figure A.3B). In 2D, Tb.Th<sub>2D</sub> (and Tb.Sp<sub>2D</sub>) are determined by fitting largest circles at every point of the structure (or inverse structure) in each cross-section. In 3D trabecular number (Tb.N) is a structure linear density, i.e. it is the inverse of the number of intersections made by trabecular structures per unit length, it represents the average number of trabecular encountered per mm of the VOI (Equation A.1).

$$Tb.N = \frac{1}{(Tb.Th + Tb.Sp)} \quad (A.1)$$

Similarly, in 2D Tb.N<sub>2D</sub> was determined from 2D measurements of trabecular spacing, where Tb.Th<sub>2D</sub> and Tb.Sp<sub>2D</sub> are determined by circle-fitting.

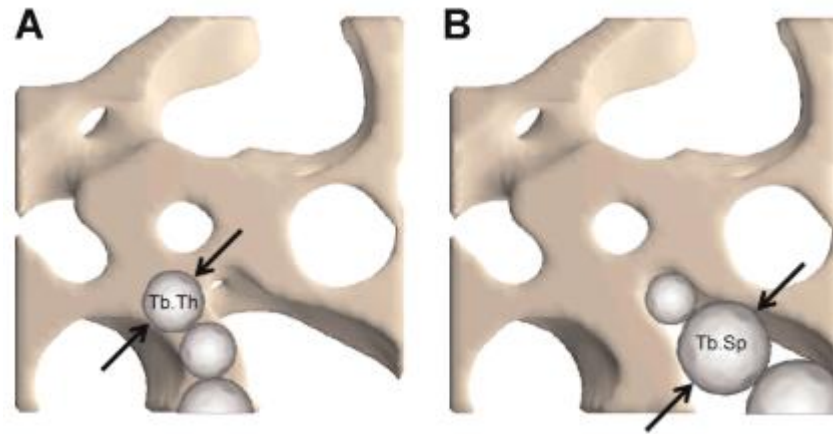


**Figure A.3.** Schematic of the algorithm used to determine A) trabecular thickness and B) trabecular separation. From Bouxsein et al. (2010).

## ***A.2 Non-metric Parameters***

The competence of trabecular structures depends not only on metric quantities such as the amount of bone material, but also on its overall complexity, which includes its connectedness, orientation and distribution. There are several inherently non-metric indices that have been developed to quantify this competency, many of which are used in this thesis.

### ***A.2.1 Trabecular Bone Pattern Factor***

Trabecular bone pattern factor (Tb.Pf) is a parameter closely related to connectivity. The idea is that all structures can be described by the relation between their concave and convex surfaces, which can be used as a proxy for connectivity, since a large number of convex structures would indicate that the structure is poorly connected, while a large number of concave structures would indicate a well-connected structure (Figure A.4B) (Hahn et al., 1992). This relationship between concave and convex elements within trabecular bone is estimated by the measurement of the area (A) and perimeter (P) before

(A1 and P1) and after (A2 and P2) a simple one-pixel dilation. Tb.Pf is then defined as the quotient of the difference between these two sets of measurements (Equation A.2).

$$Tb.Pf = \left( \frac{P1 - P2}{A1 - A2} \right) \quad (A.2)$$

The dilation leads to artificial thickening of trabeculae, meaning that there is always an increase in area, so the denominator is negative. The numerator on the other hand can either be positive or negative. In the case of a concave surface the perimeter will decrease thus the numerator would be positive, while for convex surfaces the perimeter would increase, thus the numerator would be negative (Figure A.4A). So, a larger Tb.Pf results from cases where there are more convex than concave elements. This parameter was first developed for the early detection of post-menopausal osteoporosis, where there are minimal changes to BV/TV. It was found to be very sensitive to minimal modifications of the trabecular lattice, that result for instance in perforations/isolated trabecular, i.e. more convex structures, which decrease the overall stability of the structure (Figure A.4B). Determination of Tb.Pf in 3D is achieved by replacing areas (A1 and A2) and perimeters (P1 and P2) with surfaces (S1 and S2) and volumes (V1 and V2), also instead of a single pixel dilation, a single voxel dilation is performed between measurements.

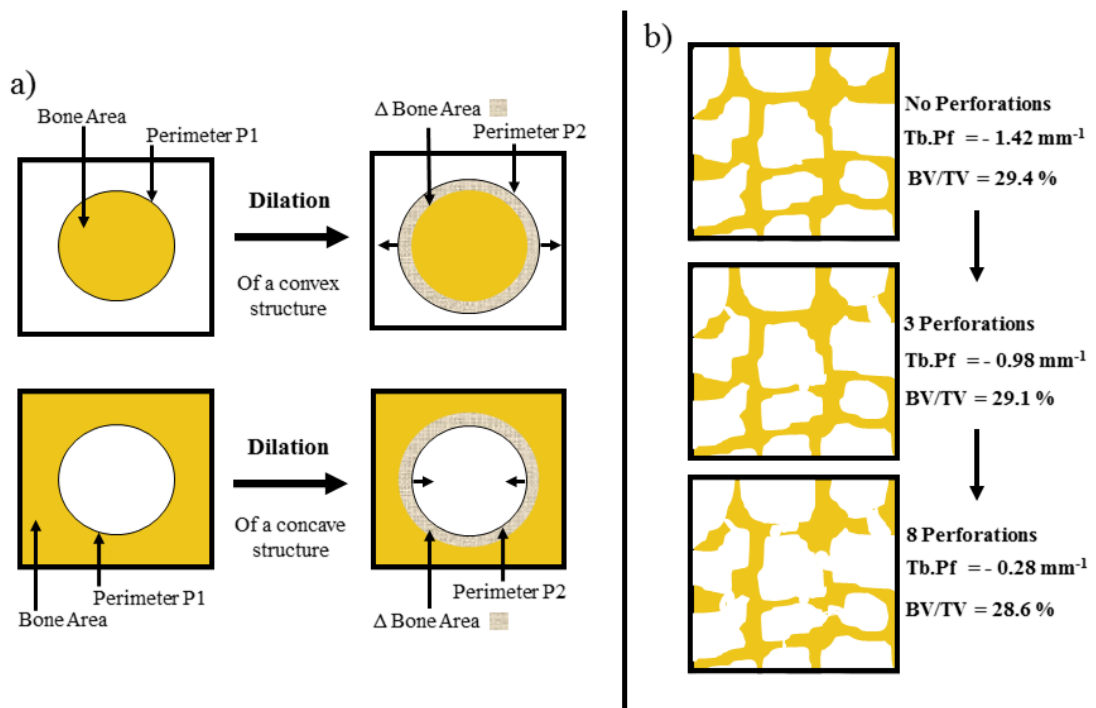


**Figure A.4.** Trabecular pattern factor (Tb.Pf). A) Schematic showing the effect a single pixel dilation has on the area and perimeter of convex and concave shapes. (A higher ratio of concave structures would lead to a lower Tb.Pf value). B) indicates how a change in structure due to perforation of individual trabeculae in 2D affects Tb.Pf. Redrawn from Hahn et al. (1992).

### A.2.2 Structure Model Index

Structure model index (SMI) was developed to quantify the overall representative form of trabecular bone in terms of the number of plates and rods that it is composed of (Hildebrand and Rüegsegger, 1997b). This is based on the commonly used, and highly subjective classification system that characterises the deterioration of trabecular bone on the extent of its conversion from a plate-like to rod-like trabeculae architecture (Parfitt et al., 1983) seen in osteoporosis. Rod-like trabecular structures are typically lower density and form open (perforated) cells (Figure A.5A), while plate-like trabecular structures are typically higher density and form more closed cells (Figure A.5B) (Gibson, 1985). SMI is closely related to Tb.Pf, it is a mathematical model that relates the volume and surface to a form-dependent quantity, and a linear measure relating to thickness. In this model

SMI values of 0, 3 and 4 correspond to an ideal plate, cylinder (rod) and sphere respectively. The SMI value reported for 3D trabecular bone VOIs will vary between 0 and 3. The interpretation of the results is that the real architecture a mixture of both rod and plate like trabeculae.

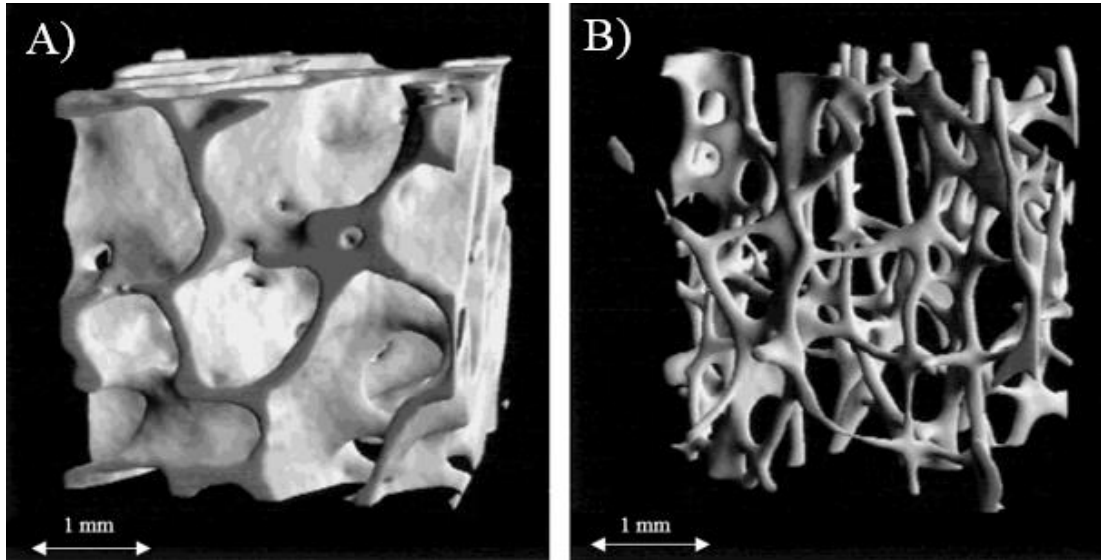


**Figure A.5.**  $\mu$ CT images of A) high BV/TV trabecular bone with plate-like architecture (SMI = 0.16) from the femoral head, B) low BV/TV trabecular bone with rod-like architecture (SMI = 2.5) from the lumbar spine. Adapted from Hildebrand et al. (1999).

### A.2.3 Fractal Dimension

Trabecular bone, like many other biological structures (e.g. the bronchial and cardiovascular systems), is irregular in shape. It contains features such as branches and enclosed cavities that increase its overall complexity. Fractal geometry was established by Mandelbrot to help quantify the complexity found in nature (Mandelbrot, 1982). Fractal structures tend to have a feature termed self-similarity, i.e. the repetition of features over different spatial scales. Take the fractal shape the Sierpinski triangle (Figure A.6).

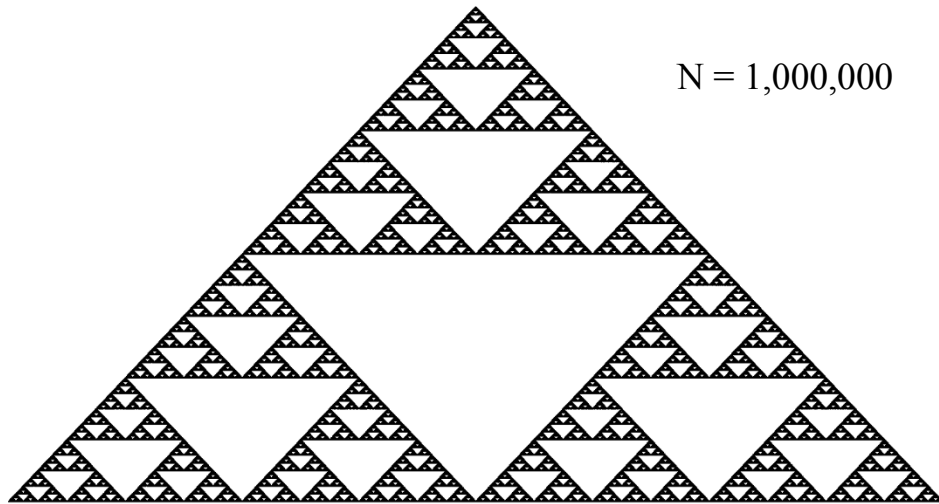


**Figure A.6.** The Sierpinski triangle plotted with 1,000,000 black points.

On the scale presented the Sierpinski triangle may be considered a single triangular structure, but it can be decomposed into three identical triangles, each half the size of the original, i.e. if any one of the three were enlarged by a factor of 2, we would obtain an exact copy of the original. So, the Sierpinski triangle contains 3 self-similar copies of itself, with magnification factor 2. We can go further because it also contains 9 self-similar copies with magnification factor 4, 27 self-similar copies with magnification factor 8 and so proceed ad infinitum (it may be divided into  $3^n$  self-similar copies each with  $2^n$  magnification factor).

The fractal dimension is an alternative way to define the dimension of a self-similar object. It is quantified here using the box- (cube-) counting (or Kolmogorov) method (Chappard et al., 2001). In 2D, a binarised slice is divided into a grid of non-overlapping equal side squares (Figure A.7). The total number of squares  $N$  of side-length  $\epsilon$  required to completely encapsulate the trabecular bone present in the slice is recorded. This step of dividing the slice into a grid is then repeated by varying  $\epsilon$  between 2 and 100 pixels.

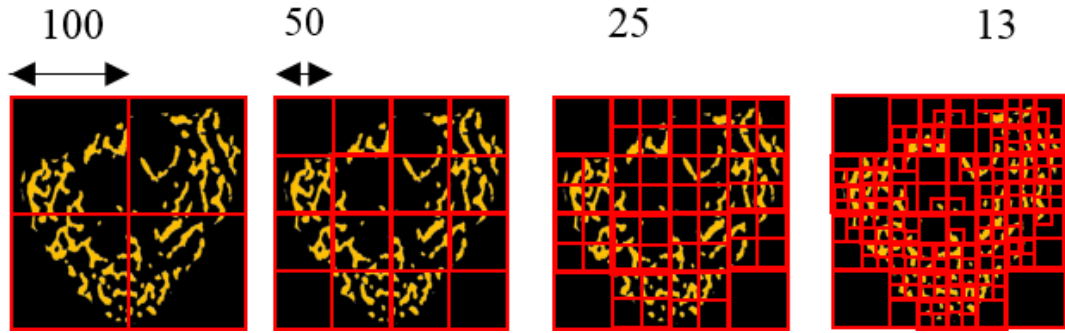


**Figure A.7.** Schematic of the box-counting (Kolmogorov) method employed to determine the fractal dimension. Only boxes of length  $\epsilon$  are counted ( $N$ ).

A log-log plot of the number of squares containing trabecular bone ( $N$ ) against the square side-length ( $\epsilon$ ) is then made. The reported fractal dimension value is the gradient of the subsequent linear regression line (Equation A.3). The same principle holds for the 3D fractal dimension used here, except the 3D VOI replaces the slice and an analogous cube-counting method is used instead of the box-counting method described. Using this technique, the fractal dimension of a line, square and cube would be 1, 2 and 3 respectively. So, this fractal dimension analysis on 3D trabecular bone VOIs yields values between 2 and 3.

$$\log(N) = -FD \log(\epsilon) + \log(\alpha) \quad (\text{A.3})$$

#### *A.2.4 Degree of Anisotropy and Structural Orientation*

Anisotropy is the attribute of directional dependence. This implicitly implies different attributes in different directions. For trabecular bone the anisotropy/isotropy referred to in this thesis is the presence/absence of preferentially aligned bone orientations. It is characterised by the degree of anisotropy (DA), which is defined as a difference when measured along orthogonal axes. Mean intercept length (MIL) and eigen-analyses are the techniques used to quantify DA (Harrigan & Mann, 1984; Whitehouse, 1974).



#### A.2.4.1 Mean Intercept Length

Isotropy is the attribute of uniformity in all orientations, i.e. no directional dependence. Lines passing through more isotropic biphasic structures would make similar numbers of intercepts between solid and non-solid phases regardless of orientation (Figure A.8A). Now consider a more anisotropic biphasic structure, i.e. a group of solid objects aligned approximately in the vertical, lines passing through this structure with orientation parallel to the vertically aligned structures would make minimal interceptions between the two phases, but if the orientation of the lines was perpendicular, then there would be many more interceptions (Figure A.8B). The mean intercept length (MIL) of a unit line ( $L$ ) at different orientations ( $\omega$ ) can then be used as a measure of isotropy (anisotropy),

$$MIL(\omega) = L/I(\omega) \quad (\text{A.4})$$

where  $I$  represents the number of interceptions.

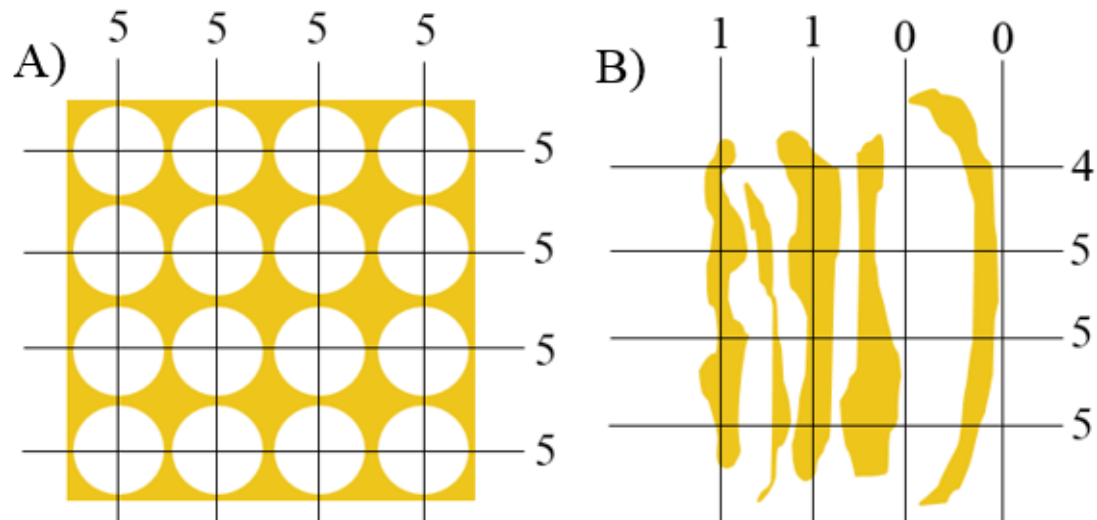


**Figure A.8.** Schematics of A) an isotropic trabecular-like structure and B) an anisotropic trabecular-like structure in cross-section. For the more isotropic structure vertical and horizontal test lines make approximately the same number of interceptions, while for the more anisotropic structure vertical test lines make few interceptions while perpendicular test lines make many more interceptions. Numbers signify the number of intersections per line.

In 3D, a spherical VOI is defined that fully encapsulated the trabecular bone VOI. A grid of test lines each separated by 10 voxels is projected through the VOI, over 1024 3D angles (Figure A.9). For each line within the grid the MIL is defined as the length of the line, divided by the number of intercepts made within the biphasic VOI. For each orientation ( $\omega$ ) the MIL is calculated as the mean for all lines within the grid.

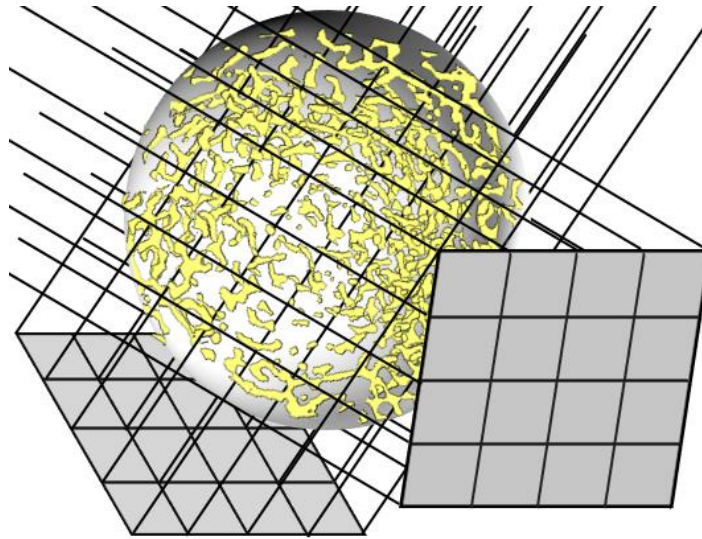


**Figure A.9.** Schematic of the 3D MIL analysis. A grid of test lines is projected through the spherical volume of trabecular bone over many 3D orientations. (A small test grid and only two orientations are shown). The MIL for each orientation is determined as the mean of lines in the grid.

#### *A.2.4.2 Ellipsoid Fitting and Eigen Analysis*

The average MIL at each orientation is plotted as a radius from the origin at the angle of 3D orientation in polar coordinates (Figure A.10). If the VOI was purely isotropic, a sphere of radius MIL would perfectly encapsulate the MIL distribution. Anisotropic MIL distributions therefore deviate from a spherical distribution, with elongation occurring in directions of longest MIL.

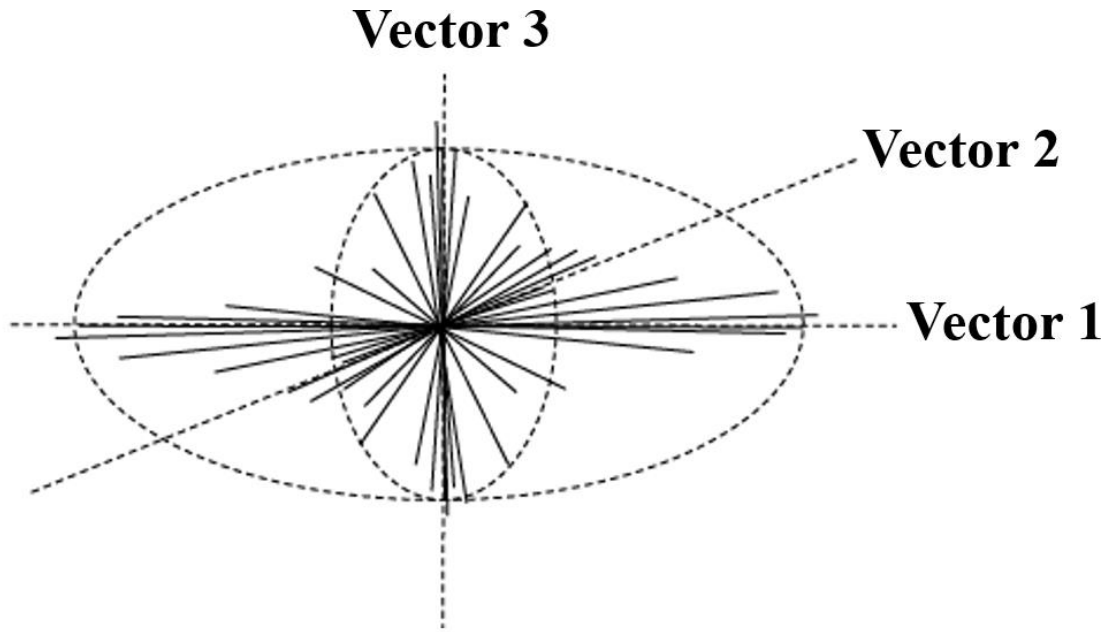


**Figure A.10.** Visualisation of the MIL distribution. A least-squares fitting procedure is applied to fit an ellipsoid to the distribution. The ellipsoid is described by its three main orthogonal axes and can be defined as a 3 x 3 second rank tensor, the columns of which are eigenvectors that describe the vector's three orientations.

The surface of this MIL distribution, i.e. the locus of the end points of the MIL vectors is then approximated by an idealised ellipsoid, which is statistically fitted by a multivariable linear least squares fitting procedure (Li and Griffiths, 2004). The surface of this ellipsoid has a general formula of the form;

$$An_1^2 + Bn_2^2 + Cn_3^2 + Dn_1n_2 + En_1n_3 + Fn_2n_3 = 1/MIL^2 \quad (\text{A.5})$$

where  $A$  to  $F$  are coefficients of the ellipsoid and  $n_1$ ,  $n_2$  and  $n_3$  are direction cosines between principal MILs and the base vectors in the coordinate system. This equation can be written as:

$$1/MIL^2 = \mathbf{n} \cdot [\mathbf{M}] \cdot \mathbf{n} \quad (\text{A.6})$$

where  $\mathbf{n}$  is a unit vector in the direction of the principal MIL measurements and  $[\mathbf{M}]$  is a second rank tensor of material anisotropy, whose components in terms of the ellipsoid coefficients are:

$$[M] = \begin{bmatrix} A & D/2 & E/2 \\ D/2 & B & F/2 \\ E/2 & F/2 & C \end{bmatrix} \quad (\text{A.7})$$

The six constants of this MIL tensor i.e. the ellipsoid coefficients, specify the shape and size of the ellipsoid and the directions of its principal axes (the longest MIL and orthogonal major and minor axes) (Harrigan & Mann, 1984). The expression given by Equation A.7 represents three simultaneous equations for each of the direction cosines. These equations are solved to determine the principal eigenvectors ( $\mathbf{e}_1$ ,  $\mathbf{e}_2$  and  $\mathbf{e}_3$ ), which determine three principle MIL vector orientations and eigenvalues ( $\lambda$ ), which determine their magnitudes.

This decomposition of the MIL 3D distribution has the unavoidable effect of assuming the trabecular bone VOI is orthotropic (i.e. the structure varies along three orthogonal axes of rotational symmetry). This is acceptable for the current purpose since it provides a description of the trabecular microstructure in terms of the orientation of its principal axes, and the ratios of their magnitudes, so the absolute values are not of interest (Harrigan & Mann, 1984).

The information provided by this analysis is therefore the orientation of the principal direction of trabecular bone orientation, and its two orthogonal axes provided by the eigenvectors and the degree of anisotropy (DA), which is defined as:

$$DA = \left( 1 - \left[ \frac{\lambda_{min}}{\lambda_{max}} \right] \right) \quad (\text{A.8})$$

Where  $DA = 0$  indicates pure isotropy and 1 is total anisotropy.

### A.2.5 Connectivity Density

Connectivity is a topological descriptor of networks such as trabecular bone. It is a measure of the maximum number of trabecular struts that can be removed without the overall structure splitting into two separate pieces (Odgaard & Gundersen, 1993). It is calculated by the Euler characteristic,  $\chi$ :

$$\chi = \beta_0 - \beta_1 + \beta_2 \quad (\text{A.9})$$

The  $\beta$ 's are the first three Betti numbers.  $\beta_0$  represents the number of bone structures, it is 1 if the entire structure is fully connected.  $\beta_1$  represents the connectivity (number of redundant connections).  $\beta_2$  represents the number of enclosed cavities (marrow cavities fully surround by bone). The connectivity analysis performed assumes that the dataset contains: i) a trabecular structure that is fully connected ( $\beta_0 = 1$ ) and ii) there are no isolated marrow cavities ( $\beta_2 = 0$ ). To achieve this, all structures are removed except the largest trabecular and marrow structures. Thus, the Euler characteristic is calculated on a volume that contains one connected bone and one connected marrow phase. Thus Equation A.9 becomes:

$$\chi = 1 - \beta_1 \quad (\text{A.10})$$

The connectivity density (Conn.D) is then determined by dividing this connectivity estimate by the total volume of the dataset (Toriwaki & Yonekura, 2002).

$$\text{Conn. } D = \frac{\beta_1}{TV} \quad (\text{A.11})$$

Edge effects are corrected for by assuming all open ends of trabeculae located at edges are considered connected. Being a topological quantity, Conn.D does not supply any information about the size, shape or distribution of the connections, thus it should not be used on its own.

## Appendix B – Cortical Morphometric Parameters

The 2D morphometric parameters described below were quantified for each slice in the dataset and plotted as a function of percentage bone length.

### *B.1 Cortical Thickness (Ct.Th)*

In 3D Ct.Th was determined by the same maximum sphere-fitting algorithm used to determine Tb.Th (Section A.1.3). In 2D Ct.Th<sub>2D</sub> was here defined as the average distance between the outer (periosteal) and inner (endosteal) bone perimeters in each binarised cross-section. Ct.Th<sub>2D</sub> was determined at four measurement points (0, 90°, 180° and 270°) (Figure B.1), the slice was then rotated by 2° about its centroid and Ct.Th<sub>2D</sub> was measured again at the same four measurement sites. Full coverage was achieved with 44 rotations. To minimise quantisation error, each original unrotated cross-section was duplicated 44 times so that each slice was rotated only once, but through each of the 45 different angles.

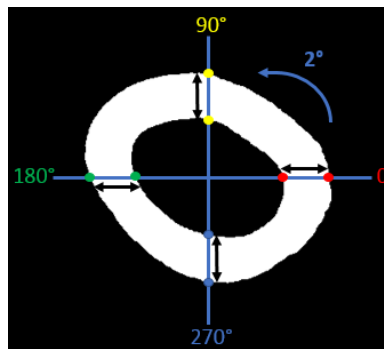


**Figure B.1.** Representative cortical cross-section, depicting the cortical thickness calculation. It was determined as the difference between each set of points at the four orientations depicted, a rotation of 2° was then applied and four more measurements were taken, further 2° rotations were applied until complete coverage was achieved.

## ***B.2 Cortical, Total and Marrow Areas (Ct.Ar, Tt.Ar and Ma.Ar)***

In 3D Ct.Ar, Tt.Ar and Ma.Ar were determined by using the volumetric-marching cubes algorithm used to determine bone volume (BV) (Section A.1.1). The volumes were then converted to areas (Equation B.1):

$$Area = \frac{Volume}{number\ of\ slices \times slice\ thickness} \quad (B.1)$$

In 2D Ct.Ar<sub>2D</sub>, Tt.Ar<sub>2D</sub> and Ma.Ar<sub>2D</sub> were determined by calculating the total number of pixels representing each area in the cross-section (Figure B.2). To acquire Figure B.2A, a filling procedure was applied to the cross-section to stretch over any pores (holes under a certain radius, i.e. 15 pixels), so the reported Ct.Ar<sub>2D</sub> ignores pores. To acquire Figure B.2B, the same filling procedure was applied, but with a much larger radius (e.g. 200 pixels). To acquire Figure B.2C, the XOR Boolean operator was applied to A) and B).

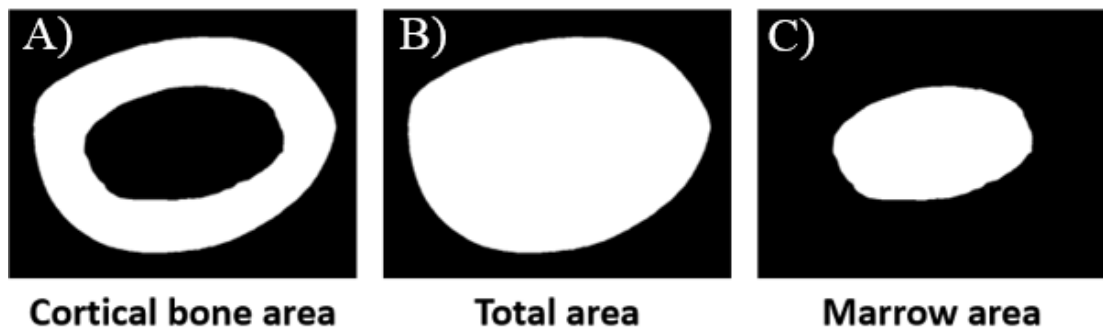


**Figure B.2.** A) Representative cortical midshaft cross-section (cortical bone area), B) filling procedure applied to depict total area enclosed by the periosteum, C) XOR Boolean operator applied to show the marrow area.

### ***B.3 Periosteal and Endocortical Perimeters (Ps.Pm and Ec.Pm)***

Perimeters were calculated in 2D. For 3D analysis, the perimeter of each cross-sectional slice in the VOI was determined and the average reported. Counting border pixels is not an effective way to determine perimeters, it would underestimate the boundary length. This is because it considerably reduces the information pertaining to the contour of the original object. This type of perimeter measure would consider all border pixels as equal distances apart (4-connectivity). A more realistic determination of perimeter would be achieved using 8-connectivity, which counts the diagonal lengths between pixels. These lengths are  $\sqrt{2}$  times longer than the horizontal and vertical lengths and account for the exact pixel centre to pixel centre lengths of our segmented binarised representations of the original bone. This approximates the boundary to straight lines at orientations 0, 45° and 90°, which is not a true representation of the bone. To reduce this orientation dependency different weightings have been proposed for diagonal and vertical (and horizontal) lengths, and a count of the number of times the orientation changes (Proffitt & Rosen, 1979; Vossepoel & Smeulders, 1982). This is how MATLAB ‘regionprops’ perimeter function determines the perimeter. Ps.Pm is determined on Figure B.2B and the Ec.Pm on Figure B.2C.

### ***B.4 Polar Moment of Area (J)***

The polar moment of area was calculated in 2D (like the perimeter). The second moments of area were calculated without any assumption of the underlying geometry. Consider Figure B.3,  $I_{yy}$  symbolises the second moment of area relative to Y-axis, for digitised cross-sections it can be computed as the following summation over all bone pixels.

$$I_{yy} = \sum_{i=1}^N (\text{Pixel Area} \times (x_i - x_c)^2 + \text{Pixel MOA}) \quad (\text{B.2})$$



Where,  $Pixel\ Area = Pixel\ Width \times Pixel\ Height$ ,  $x_c$  is the X-axis coordinate of the bone cross-section centroid, the quantity  $x_i - x_c$  represents the distance from the Y-axis to the  $i^{th}$  pixel,  $Pixel\ Moment\ of\ Area = (Pixel\ Width)^4/12$ .  $I_{xx}$  and  $I_{yy}$ , the product moments of area, were calculated in a similar fashion.

The maximum and minimum second moments of area were derived with respects to the relative second moments of area, for example:

$$I_{max} = \frac{I_{xx} + I_{yy}}{2} + \sqrt{\left(\frac{I_{xx} - I_{yy}}{2}\right)^2 + I_{xy}^2} \quad (B.3)$$

The second polar moment of area follows

$$J = I_{max} + I_{min} \quad (B.4)$$

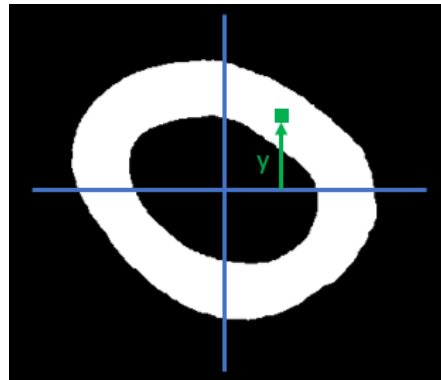


**Figure B.3.** Representative cortical cross-section, depicting the calculation of moments of area. Each pixel is a known distance from the centroid, thus allowing moments of area to be determined.

### B.5 Eccentricity (*Ecc*)

*Ecc* is also calculated in 2D. Here it measures the periosteal (outer) eccentricity as the departure from a circular shape. A circle is an ellipse with zero eccentricity, while a straight line has an eccentricity of one. It is calculated using Equation B.5:

$$Ecc = \sqrt{1 - \frac{b^2}{a^2}} \quad (\text{B.5})$$

where  $a$  is the semi-major axis and  $b$  the semi-minor axis.

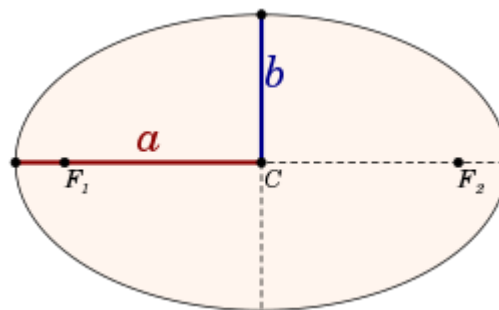


**Figure B.4.** Semi-major axis ( $a$ ) and semi-minor axis ( $b$ ) of an ellipse, along with the centre ( $C$ ) and both foci ( $F_1$  and  $F_2$ ) also labelled.

## Appendix C – Validation of 2D Morphometric Distributions

The 2D trabecular and cortical bone morphometric distributions calculated in this thesis were compared with the gold standard 2D average morphometric parameters calculated by CTAn (Version 1.16.10.0, Kontich, Belgium), for two reasons:

- i) To valid the methodological changes and custom MATLAB scripts written for this thesis,
- ii) To assess how adequately the “gold standard” 2D morphometric parameters (mean  $\pm$  standard error) describe trabecular and cortical bone compared with the 2D morphometric distributions.

### *C.1 Validation of Scripts*

The custom MATLAB scripts calculate 2D morphometric parameters for each slice in a VOI and plots them as a function of percentage bone length, while CTAn calculates the 2D morphometric parameters for each slice in a VOI and averages the values, reporting the mean. To validate the custom MATLAB scripts, a comparison was made with CTAn software. The following equation was used to do this:

$$Average_{2D\ Parameter} = \frac{\sum_{i=1}^N 2D\ Parameter_i}{N} \quad (C.1)$$

where,  $N$  is the number of slices making up the VOI,  $2D\ Parameter_i$  is the 2D morphometric value at the  $i^{th}$  slice. This equation therefore converts the 2D morphometric distributions into means, allowing comparison with CTAn. For 10-week control group trabecular (81 – 85% bone length) and cortical (62 – 58% bone length) VOIs, both MATLAB-determined and CTAn-determined 2D morphometric parameters were compared (Table C.1).

**Table C.1.** Comparison of MATLAB- and CTAn-determined morphometric parameters for the 10-week control group. Data presented as mean  $\pm$  SE.

2D Parameter	MATLAB-determined	CTAn-determined
BA/TA (%)	28.2 $\pm$ 2.3	28.2 $\pm$ 2.3
<b>Tb.Th<sub>2D</sub> (mm)</b>	<b>0.06 <math>\pm</math> 0.01</b>	<b>0.07 <math>\pm</math> 0.01</b>
<b>Tb.Sp<sub>2D</sub> (mm)</b>	<b>0.15 <math>\pm</math> 0.02</b>	<b>0.26 <math>\pm</math> 0.03</b>
<b>Tb.N<sub>2D</sub> (mm<sup>-1</sup>)</b>	<b>3.9 <math>\pm</math> 0.3</b>	<b>3.2 <math>\pm</math> 0.3</b>
<b>Ct.Th<sub>2D</sub> (mm)</b>	<b>0.65 <math>\pm</math> 0.3</b>	<b>0.76 <math>\pm</math> 0.3</b>
Ct.Ar <sub>2D</sub> (mm <sup>2</sup> )	6.1 $\pm$ 0.1	6.1 $\pm$ 0.1
Tt.Ar <sub>2D</sub> (mm <sup>2</sup> )	9.0 $\pm$ 0.2	9.0 $\pm$ 0.2
Ma.Ar <sub>2D</sub> (mm <sup>2</sup> )	2.9 $\pm$ 0.2	2.9 $\pm$ 0.2
Ps.Pm (mm)	11.6 $\pm$ 0.4	11.6 $\pm$ 0.4
Ec.Pm (mm)	18.3 $\pm$ 0.5	18.3 $\pm$ 0.5
J (mm <sup>4</sup> )	12.1 $\pm$ 0.7	12.1 $\pm$ 0.7

**Bold text** shows parameters where differences were seen between the two approaches.



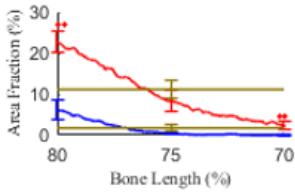
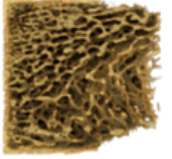
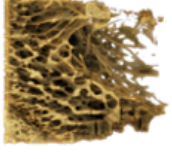
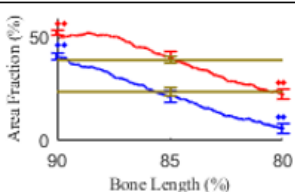


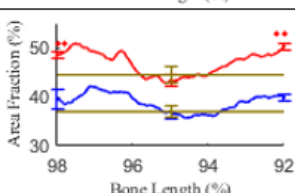
For trabecular BA/TA and the cortical parameters Ct.Ar<sub>2D</sub>, Tt.Ar<sub>2D</sub>, Ma.Ar<sub>2D</sub>, Ps.Pm, Ec.Pm, and J the two approaches returned the exact same values (Table C.1). While for Tb.Th<sub>2D</sub>, Tb.Sp<sub>2D</sub>, Tb.N<sub>2D</sub> and Ct.Th<sub>2D</sub> the values determined by the two approaches were different but not significantly so. The difference existed because the methods used to calculate the parameters were different (but both valid). These parameters were calculated assuming a plate model in CTAn (Parfitt et al., 1987), while in the MATLAB scripts they are calculated as geometry independent measures (Appendices A & B).

### ***C.2 Comparison of Methods***

To assess how well the gold standard 2D average trabecular BA/TA (mean  $\pm$  standard error) describes the trabecular bone within VOIs (10% bone length for metaphyseal trabecular bone, 6% bone length for epiphyseal trabecular bone), it was compared with the 2D average trabecular BA/TA distribution, over the same VOIs for both 10-week control and SCI groups (Table C.2). The gold standard 2D average trabecular BA/TA did not adequately describe the variation in trabecular bone quantity within trabecular

compartments. For example, in the 90 - 90% VOI the recorded gold standard average BA/TA was 25% lower ( $p < 0.001$ ) than at the distal-most end and 74% higher ( $p < 0.0001$ ) than at the proximal-most end of the VOI, for control. A similar but greater discrepancy was observed in the SCI VOI, where BA/TA was 43% lower ( $p < 0.001$ ) at the distal-most end and 294% higher ( $p < 0.0001$ ) at the proximal-most end of the VOI, compared to the gold standard average value. Similar trends were observed for other trabecular morphometric parameters (data not shown).

**Table C.2.** Comparison of the 2D slice-by-slice approach with the integrated gold standard approach for trabecular bone area fraction (BA/TA), for both 10-week control (CTL) and SCI groups. Data presented as mean  $\pm$  SE.

Volume of Interest <sup>a</sup>		Distribution vs. Gold Standard <sup>b</sup>	Distribution		Gold Standard		
Control	SCI		Length (%)	BA/TA (%)	BA/TA (%)		
				CTL	SCI	CTL	SCI
			70	<b>2.3</b> $\pm$ <b>1.3</b>	0.0 $\pm$ 0.0	11.2 $\pm$ 2.3	1.7 $\pm$ 0.8
			75	8.3 $\pm$ 2.5	0.5 $\pm$ 0.3	p = 0.032	
			80	<b>22.7</b> $\pm$ 2.6	6.1 $\pm$ 2.4		
			80	<b>22.7</b> $\pm$ 2.6	<b>6.1</b> $\pm$ <b>2.4</b>	39.5 $\pm$ 1.7	24.0 $\pm$ 1.9
			85	40.8 $\pm$ 2.5	21.7 $\pm$ 2.6	p = 0.0001	
			90	<b>52.6</b> $\pm$ 1.2	<b>41.5</b> $\pm$ 1.6		
			92	<b>50.2</b> $\pm$ 0.6	39.9 $\pm$ 0.7	44.5 $\pm$ 0.7	37.0 $\pm$ 1.3
			95	43.3 $\pm$ 1.1	37.0 $\pm$ 1.4	p = 0.0004	
			98	<b>48.6</b> $\pm$ 0.7	39.5 $\pm$ 2.1		

<sup>a</sup> 3D visualisations of representative  $\mu$ CT 10% bone length metaphyseal trabecular VOIs, and 6% epiphyseal trabecular bone VOIs for both control and SCI at 10-weeks post-surgery.

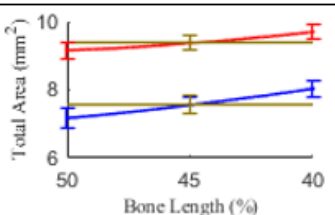
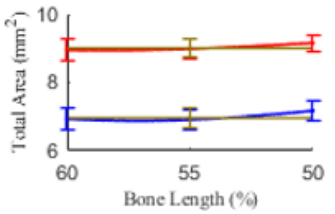
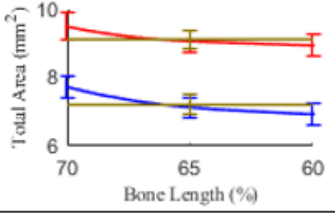
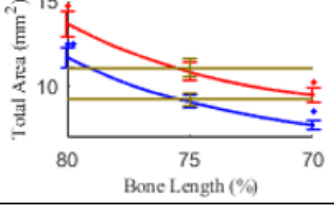
<sup>b</sup> Graphical comparison of the average trabecular BA/TA distribution against the gold standard integrated value. control in red, SCI in blue and corresponding gold standards in gold.

**Bold text** refers to a significant difference between slice-by-slice approach and gold standard ( $p < 0.05$ ).

To assess how well the cortical bone is described by the gold standard 2D average cortical morphometric parameters within VOIs (each 10% bone length), the average Tt.Ar was compared with the 2D average Tt.Ar distribution over the same VOI for both 10-week control and SCI groups (Table C.3). For the diaphysis (70 – 40% bone length) the variability of Tt.Ar was adequately described by the gold standard with the 10% bone length VOIs. It was only more distally (70 - 80%) where the Tt.Ar varies at a faster rate

per unit length, that the gold standard does not perform adequately. For control the gold standard average 2D Tt.Ar was 26% lower ( $p < 0.001$ ) than at the most-distal end and 15% higher ( $p < 0.01$ ) than at the most-proximal end of the 10% bone length VOI. Whilst for (70 - 80%) SCI VOI the gold standard Tt.Ar was 26% lower ( $p < 0.001$ ) than at the most-distal end and 10% lower ( $p < 0.01$ ) than at the most-proximal end of the 10% bone length VOI. All other cortical morphometric parameters displayed a similar trend when compared with the gold standard, i.e. statistical differences were detected in the most distal (70 - 80%) VOI (data not shown).

**Table C.3.** Comparison of the 2D slice-by-slice approach with the integrated gold standard approach for total cortical bone cross-sectional area inside the periosteal envelope (Tt.Ar), for both 10-week control and SCI groups. Data presented as mean  $\pm$  SE.

Volume of Interest <sup>a</sup>	Distribution			Gold Standard	
	Length (%)	Tt.Ar (mm <sup>2</sup> )		Tt.Ar (mm <sup>2</sup> )	
		CTL	SCI	CTL	SCI
	40	9.7 $\pm$ 0.2	8.0 $\pm$ 0.2	9.2 $\pm$ 0.2	7.6 $\pm$ 0.3
	45	9.4 $\pm$ 0.2	7.6 $\pm$ 0.2	p = 0.0003	
	50	9.2 $\pm$ 0.2	7.2 $\pm$ 0.3		
	50	9.2 $\pm$ 0.2	7.2 $\pm$ 0.3	9.0 $\pm$ 0.3	7.0 $\pm$ 0.3
	55	9.0 $\pm$ 0.3	6.9 $\pm$ 0.3	p = 0.0005	
	60	9.0 $\pm$ 0.3	6.9 $\pm$ 0.3		
	60	9.0 $\pm$ 0.3	6.9 $\pm$ 0.3	9.1 $\pm$ 0.3	7.2 $\pm$ 0.3
	65	9.1 $\pm$ 0.3	7.1 $\pm$ 0.3	p = 0.0015	
	70	9.5 $\pm$ 0.4	7.7 $\pm$ 0.3		
	70	<b>9.5<math>\pm</math>0.4</b>	<b>7.7<math>\pm</math>0.3</b>	11.1 $\pm$ 0.6	9.3 $\pm$ 0.4
	75	10.9 $\pm$ 0.5	9.1 $\pm$ 0.4	p = 0.0199	
	80	<b>13.7<math>\pm</math>0.7</b>	<b>11.7<math>\pm</math>0.6</b>		

<sup>a</sup> Graphical comparison of the total area distribution against the gold standard integrated value. Control in red, SCI in blue and corresponding gold standards in gold.

**Bold text** refers to a significant difference ( $p < 0.05$ ) between slice-by-slice approach and gold standard.



## Appendix D – Material Level Torsional Properties

The torsion test evaluates the torsional properties of the entire femoral cortex within the gauge length. Typically, a simplified beam theory approach is used to analyse these tests, where it is assumed that the bone is prismatic and analysed as a tube with constant cross-section. The errors introduced by this approach are significant when comparing bones of different sizes (Levenston et al., 1994). Femurs have a geometry that varies with length, thus a non-prismatic approach was used here based on Levenston et al. (1994). The prismatic equations for the rigidity modulus ( $G$ ) (Equation D.1) and the ultimate shear stress ( $\tau_{max}$ ) (Equation D.2) were adapted by including the geometries of every  $n$ th equally spaced  $\mu$ CT slice within the gauge length to get the effective rigidity modulus ( $G_E$ ) (Equation D.3) and effective ultimate shear stress ( $\tau_{maxE}$ ) (Equation D.4). The more slices used the better the approximation (Figure D.1).

$$G = \frac{TL}{\theta J} \quad (D.1)$$

$$\tau_{max} = \frac{T_{max}r}{J} \quad (D.2)$$

$$G_E = \frac{T}{\theta} \sum_{i=1}^n \frac{L_i}{J_i} \quad (D.3)$$

$$\tau_{maxE} = T_{max} \sum_{i=1}^n \frac{r_i}{J_i} \quad (D.4)$$

Where  $T/\theta$  is the rotational stiffness,  $L$  the gauge length,  $J$  the second polar moment of area,  $T_{max}$  the maximum torque and  $r$  the distance from the centroid of the cross-section to the outermost point. Each left femur that underwent torsion testing was  $\mu$ CT scanned at 6.89  $\mu$ m resolution. For each scan the bone within the gauge length was acquired and

$n$  slices every 50 slices apart were used to calculate  $r_i$  and  $J_i$ .  $n$  ranged from 33 to 57 depending on the gauge length (Figure D.2). Further details of this implementation can be seen in the Appendix of Levenston et al. (1994)

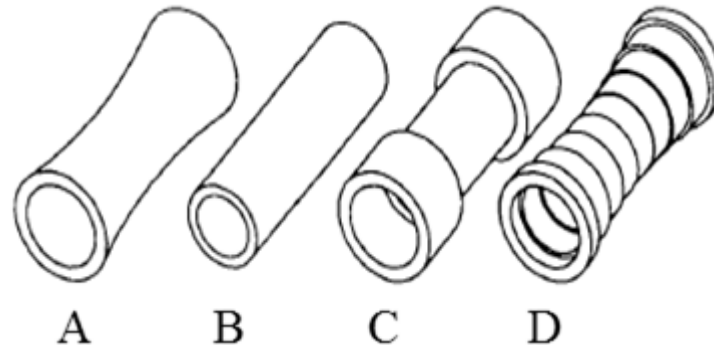


**Figure D.1.** Schematic representations of models used to approximate the femoral diaphysis within the gauge length. A) Actual representation, B) prismatic approach (conventional), C) three and D) nine equally spaced cross-sections. Adapted from Levenston et al. (1994).

$$n = 1, 2, \dots$$

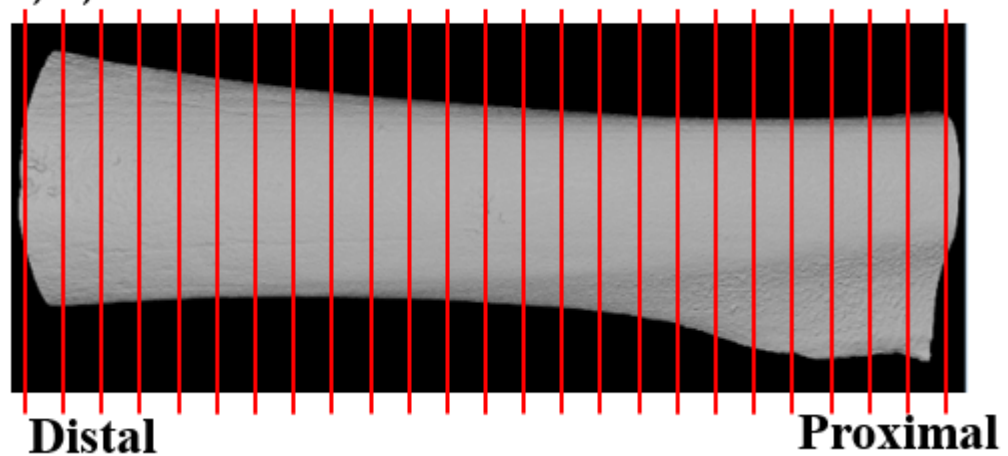


**Figure D.2.** Schematic of multi-prismatic approach. Torsion tested cortical bone within the gauge length VOI. Red lines give examples of the equally spaced cross-sections used to calculate  $G_E$  and  $\sigma_{maxE}$ .

## **Appendix E – CTX-I Experiment**

In collaboration with Dr Carmen Huesa (Edinburgh Musculoskeletal Group, University of Edinburgh) a C-terminal telopeptide crosslinks (CTX-I) Enzyme immunoassay (EIA) (RatLaps™ (CTX-1) EIA, Immunodiagnostic Systems, Tyne & Wear, UK) was performed for the quantification of degradation products of type I collagen (CTX-I) in rat blood serum. These degradation products are released during the osteoclastic resorption of bone (Rosen et al., 2000).

### **Methodology**

Blood serum CTX-I was determined by EIA according to the manufacturer's recommended procedures. The rats were fasted for 6 hours prior to sacrifice, blood was collected at time of sacrifice via descending aorta exsanguination. Blood was collected for all rats. Serum was aliquoted into 20 µl samples.

### **Results**

At 2 weeks post-SCI, the bone resorption marker CTX-I was found to be increased by 47% ( $p < 0.01$ ) compared to control group (Figure E.1). This was the only timepoint where there was a significant difference in CTX-I between age-matched control and SCI groups. For SCI groups, CTX-I decreased monotonically with time point post-surgery group, between 2 and 16 weeks there was a 68% ( $p < 0.0001$ ) decrease. For control groups, CTX-I decreased between 6 and 16 weeks by 59% ( $p < 0.001$ ).

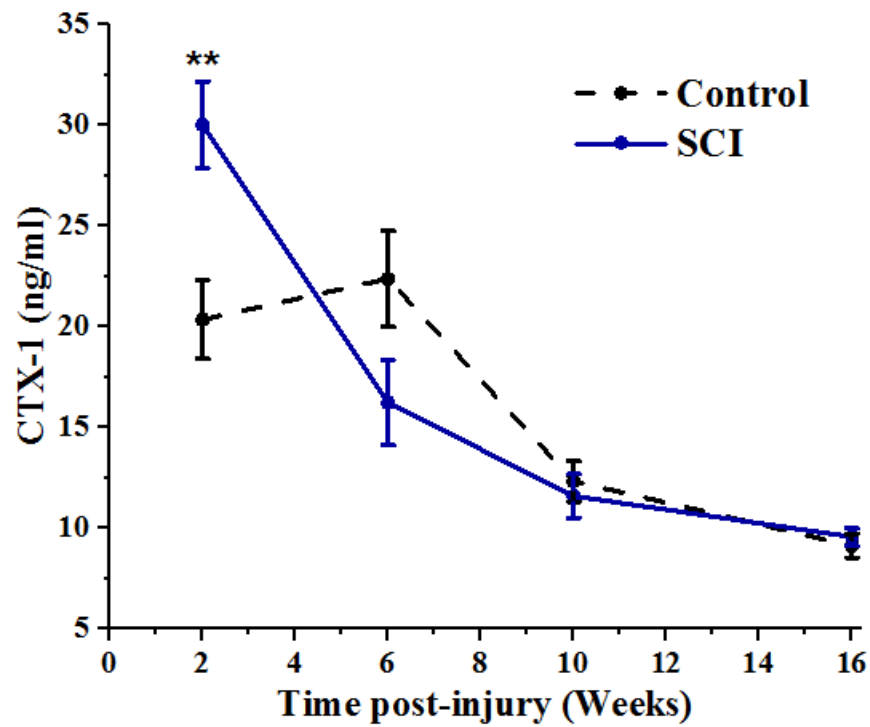


**Figure E.1.** Blood serum CTX-I levels for 2, 6, 10 and 16-week control (black dashed line) and SCI (blue line) groups. Data shown as mean ± SE. \*\* indicates  $p < 0.001$ .

**Table E.1.** Blood serum CTX-I levels for 2, 6, 10 and 16-week control and SCI groups.

		2 Weeks	6 Weeks	10 Weeks	16 Weeks
CTX-I (ng/ml) <sup>S,T,S- T</sup>	<b>Control</b>	20.37 ± 1.96	22.38 ± 2.38	12.34 ± 1.01 <sup>a,b</sup>	9.14 ± 0.59 <sup>a,b</sup>
	<b>SCI</b>	30.02 ± 2.16*	16.24 ± 2.11 <sup>a</sup>	11.61 ± 1.08 <sup>a</sup>	9.59 ± 0.44 <sup>a,b</sup>

<sup>S</sup> Significant effect of SCI, <sup>T</sup> significant effect of time post-injury, <sup>S-T</sup> significant injury-time post injury interaction; ANOVA  $p < 0.05$ .

\* SCI different from control at same timepoint post-injury;  $p < 0.05$ .

<sup>a</sup> Different from 2 weeks, <sup>b</sup> different from 6 weeks, <sup>c</sup> different from 10 weeks post-injury;  $p < 0.05$ .

## Appendix F – Effects of Growth on Trabecular Compartments

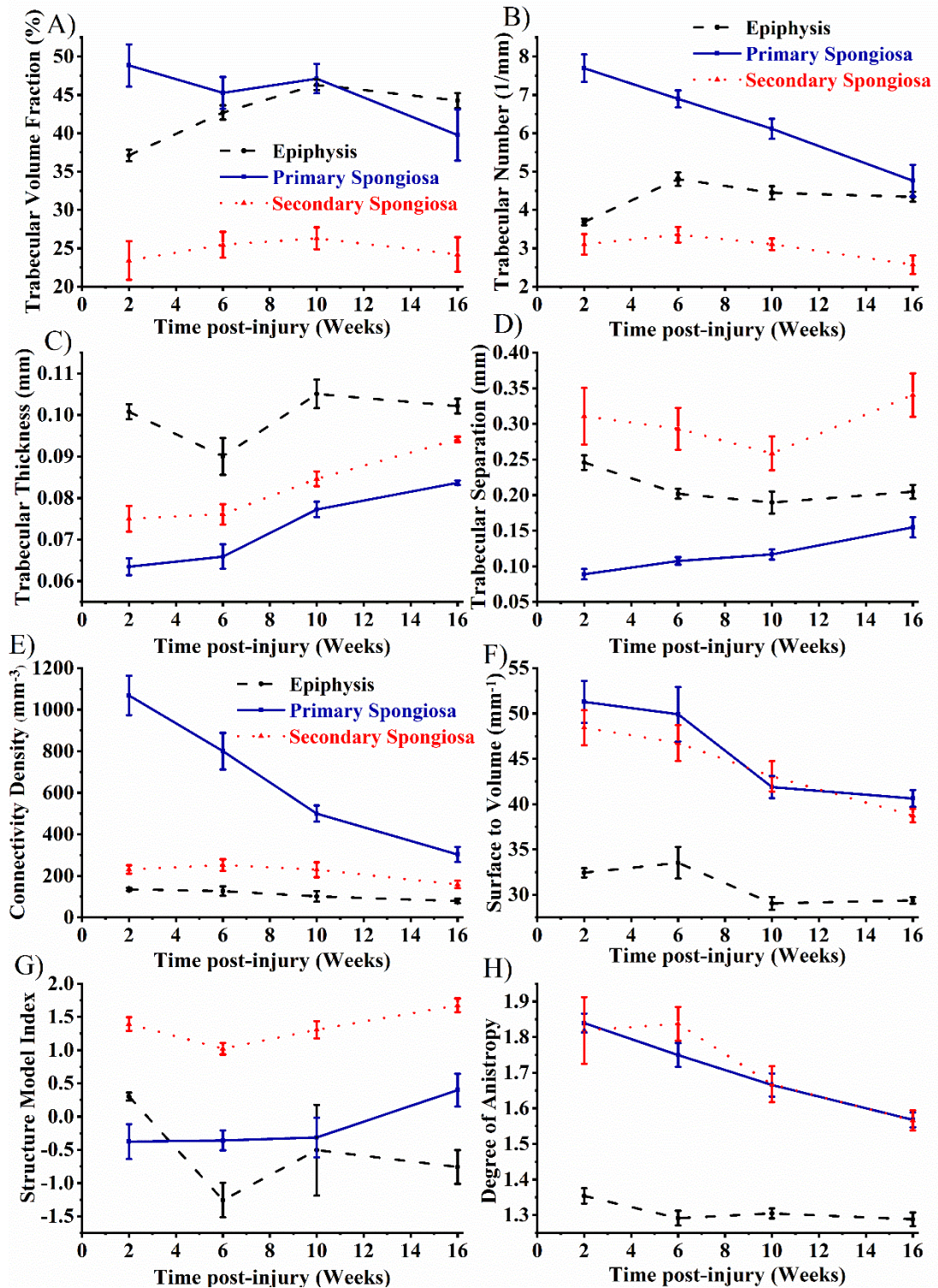


**Figure F.1.** The effects of growth between 2 and 16-week control groups on the epiphyseal secondary spongiosa, metaphyseal primary spongiosa and metaphyseal secondary spongiosa VOIs. A) Trabecular volume fraction (BV/TV), B) Trabecular Number (Tb.N), C) Trabecular Thickness (Tb.Th), D) Trabecular Separation (Tb.Sp), E) connectivity density (Conn.D), F) specific bone surface to volume (BS/BV), G) structure model index (SMI) and H) degree of anisotropy (DA).

## References

- Alexandre, C., & Vico, L. (2011). Pathophysiology of bone loss in disuse osteoporosis. *Joint Bone Spine*, 78(6), 572–576. <http://doi.org/10.1016/j.jbspin.2011.04.007>
- b-cube AG, S. (2019). No Title. Retrieved March 5, 2019, from [http://www.b-cube.ch/images/stories/morphometry\\_spacing.gif](http://www.b-cube.ch/images/stories/morphometry_spacing.gif)
- Barbier, A., Martel, C., de Vernejoul, M. C., Tirode, F., Nys, M., Mocaer, G., ... Lacheretz, F. (1999). The visualization and evaluation of bone architecture in the rat using three-dimensional X-ray microcomputed tomography. *Journal of Bone and Mineral Metabolism*, 17(1), 37–44. <http://doi.org/10.1007/s007740050061>
- Barnes, G. T. (1982). Radiographic mottle: A comprehensive theory. *Medical Physics*, 9(5), 656–667. <http://doi.org/10.1118/1.595126>
- Basso, D. M., Beattie, M. S., & Bresnahan, J. C. (1996). Graded histological and locomotor outcomes after spinal cord contusion using the NYU weight-drop device versus transection. *Experimental Neurology*, 139(2), 244–256. <http://doi.org/10.1006/exnr.1996.0098>
- Battaglino, R. A., Lazzari, A. A., Garshick, E., & Morse, L. R. (2013). Spinal Cord Injury-Induced Osteoporosis: Pathogenesis and Emerging Therapies. *Current Osteoporosis Reports*, 10(4), 278–285. <http://doi.org/10.1007/s11914-012-0117-0>.Spinal
- Bauman, W. A., Zhang, R. L., Morrison, N., & Spungen, A. M. (2009). Acute suppression of bone turnover with calcium infusion in persons with spinal cord injury. *Journal of Spinal Cord Medicine*, 32(4), 398–403. <http://doi.org/10.1080/10790268.2009.11754393>

- Beggs, L. A., Ye, F., Ghosh, P., Beck, D. T., Conover, C. F., Balaez, A., ... Yarrow, J. F. (2015). Sclerostin inhibition prevents spinal cord injury-induced cancellous bone loss. *Journal of Bone and Mineral Research*, 30(4), 681–689.  
<http://doi.org/10.1002/jbmr.2396>
- Behari, J. (1991). Solid state bone behaviour. *Progress in Biophysics and Molecular Biology*, 56(1), 1–41. [http://doi.org/10.1016/0079-6107\(91\)90006-E](http://doi.org/10.1016/0079-6107(91)90006-E)
- Biering-Sørensen, F., Bohr, H. H., & Schaadt, O. P. (1990). Longitudinal study of bone mineral content in the lumbar spine, the forearm and the lower extremities after spinal cord injury. *European Journal of Clinical Investigation*, 20(3), 330–335.  
<http://doi.org/10.1111/j.1365-2362.1990.tb01865.x>
- Biering-Sorensen, F., Bohr, H., & Schaadt, O. (1988). Bone mineral content of the lumbar spine and lower extremities years after spinal cord lesion. *Paraplegia*, 26(5), 293–301. <http://doi.org/10.1038/sc.1988.44>
- Biggin, A., Briody, J. N., Ramjan, K. A., Middleton, A., Waugh, M. C. A., & Munns, C. F. (2013). Evaluation of bone mineral density and morphology using pQCT in children after spinal cord injury. *Developmental Neurorehabilitation*, 16(6), 391–397. <http://doi.org/10.3109/17518423.2012.762590>
- Bolanowski, W., Śmiszkiewicz-Skwarska, A., Polguy, M., & Jédrzejewski, K. S. (2005). The occurrence of the third trochanter and its correlation to certain anthropometric parameters of the human femur. *Folia Morphologica*, 64(3), 168–175.
- Bolotin, H. H., & Sievänen, H. (2001). Inaccuracies Inherent in Dual-Energy X-Ray Absorptiometry in Vivo Bone Mineral Density Can Seriously Mislead Diagnostic / Prognostic Interpretations of Patient-Specific Bone Fragility. *Journal of Bone and Mineral Research*, 16(5), 799–805. <http://doi.org/10.1359/jbmr.2001.16.5.799>

- Bolotin, H. H., Sievänen, H., & Grashuis, J. L. (2003). Patient-Specific DXA Bone Mineral Density Inaccuracies: Quantitative Effects of Nonuniform Extraosseous Fat Distributions. *Journal of Bone and Mineral Research*, 18(6), 1020–1027. <http://doi.org/10.1359/jbmr.2003.18.6.1020>
- Bonewald, L. F. (2011). The amazing osteocyte. *Journal of Bone and Mineral Research*, 26(2), 229–238. <http://doi.org/10.1002/jbmr.320>
- Boutroy, S., Bouxsein, M. L., Munoz, F., & Delmas, P. D. (2005). In Vivo assessment of trabecular bone microarchitecture by high-resolution peripheral quantitative computed tomography. *The Journal of Clinical Endocrinology & Metabolism*, 90(12), 6508–6515. <http://doi.org/10.1210/jc.2005-1258>
- Bouxsein, M. L. (2003). Bone quality: where do we go from here? *Osteoporosis International*, 14(Supplement 5), S118–S127. <http://doi.org/10.1007/s00198-003-1489-x>
- Bouxsein, M. L., Boyd, S. K., Christiansen, B. A., Guldberg, R. E., Jepsen, K. J., & Müller, R. (2010). Guidelines for assessment of bone microstructure in rodents using micro-computed tomography. *Journal of Bone and Mineral Research*, 25(7), 1468–1486. <http://doi.org/10.1002/jbmr.141>
- Brodt, M. D., Ellis, C. B., & Silva, M. J. (1999). Growing C57Bl/6 Mice Increase Whole Bone Mechanical Properties by Increasing Geometric and Material Properties. *Journal of Bone and Mineral Research*, 14(12), 2159–2166. <http://doi.org/10.1359/jbmr.1999.14.12.2159>
- Buckley, K., Kerns, J. G., Parker, A. W., Goodship, A. E., & Matousek, P. (2014). Millimeter-Scale Mapping of Cortical Bone Reveals Organ-Scale Heterogeneity. *Applied Spectroscopy*, 68(4), 510–514. <http://doi.org/10.1366/13-07296>



- Buckwalter, J. A., Glimcher, M. J., Cooper, R. R., & Recker, R. (1995). Bone biology. Part II: Formation, form, modeling, remodeling, and regulation of cell function. *The Journal of Bone and Joint Surgery (Instructional Course Lecture)*, 77(8), 1276–1289.
- Buie, H. R., Campbell, G. M., Klinck, R. J., MacNeil, J. A., & Boyd, S. K. (2007). Automatic segmentation of cortical and trabecular compartments based on a dual threshold technique for in vivo micro-CT bone analysis. *Bone*, 41(4), 505–15. <http://doi.org/10.1016/j.bone.2007.07.007>
- Burr, D. B., & Allen, M. R. (2013). *Basic and Applied Bone Biology* (1st ed.). Academic Press.
- Castro, M. J., Apple, D. F., Staron, R. S., Campos, G. E. R., & Dudley, G. A. (1999). Influence of complete spinal cord injury on skeletal muscle within 6 mo of injury. *The Journal of Applied Physiology*, 86(1), 350–358. <http://doi.org/10.1152/jappl.1999.86.1.350>
- Center, N. S. C. I. S. (2019). *Spinal Cord Injurt Facts and Figures at a Glance*. Birmingham, AL: University of Alabama at Birmingham,.
- Chantraine, A., Nusgens, B., & Lapiere, C. M. (1986). Bone remodeling during the development of osteoporosis in paraplegia. *Calcified Tissue International*, 38(6), 323–327. <http://doi.org/10.1007/BF02555744>
- Chappard, D., Legrand, E., Haettich, B., Chalès, G., Auvinet, B., Eschard, J. P., ... Audran, M. (2001). Fractal dimension of trabecular bone: comparison of three histomorphometric computed techniques for measuring the architectural two-dimensional complexity. *Journal of Pathology*, 195(4), 515–521. <http://doi.org/10.1002/path.970>

- Chappard, D., Retailleau-Gaborit, N., Legrand, E., Baslé, M. F., & Audran, M. (2005). Comparison insight bone measurements by histomorphometry and  $\mu$ CT. *Journal of Bone and Mineral Research*, 20(7), 1177–1184.  
<http://doi.org/10.1359/JBMR.050205>
- Choi, H. (2005). Respiratory abnormalities resulting from midcervical spinal cord injury and their reversal by serotonin 1A agonists in conscious rats. *Journal of Neuroscience*, 25(18), 4550–4559. <http://doi.org/10.1523/JNEUROSCI.5135-04.2005>
- Cirnigliaro, C. M., Myslinski, M. J., La Fountaine, M. F., Kirshblum, S. C., Forrest, G. F., & Bauman, W. A. (2017). Bone loss at the distal femur and proximal tibia in persons with spinal cord injury: imaging approaches, risk of fracture, and potential treatment options. *Osteoporosis International*, 28(3), 747–765.  
<http://doi.org/10.1007/s00198-016-3798-x>
- Compston, J. (2006). Bone quality: what is it and how is it measured? *Arquivos Brasileiros de Endocrinologia e Metabologia*, 50(4), 579–585.  
<http://doi.org/http://dx.doi.org/10.1590/S0004-27302006000400003>
- Cormack, A. M. (1963). Representation of a function by its line integrals, with some radiological applications. *Journal of Applied Physics*, 34(9), 2722–2727.  
<http://doi.org/10.1063/1.1729798>
- Cormack, A. M. (1964). Representation of a function by its line integrals, with some radiological applications. II. *Journal of Applied Physics*, 35(10), 2908–2913.  
<http://doi.org/10.1063/1.1713127>
- Coupaud, S., Gislason, M. K., Purcell, M., Sasagawa, K., & Tanner, K. E. (2017). Patient-specific bone mineral density distribution in the tibia of individuals with

chronic spinal cord injury, derived from multi-slice peripheral Quantitative Computed Tomography (pQCT) — A cross-sectional study. *Bone*, 97, 29–37. <http://doi.org/10.1016/j.bone.2016.12.014>

Coupaud, S., McLean, A. N., & Allan, D. B. (2009). Role of peripheral quantitative computed tomography in identifying disuse osteoporosis in paraplegia. *Skeletal Radiology*, 38(10), 989–995. <http://doi.org/10.1007/s00256-009-0674-1>

Coupaud, S., McLean, A. N., Purcell, M., Fraser, M. H., & Allan, D. B. (2015). Decreases in bone mineral density at cortical and trabecular sites in the tibia and femur during the first year of spinal cord injury. *Bone*, 74, 69–75. <http://doi.org/10.1016/j.bone.2015.01.005>

Dauty, M., Perrouin Verbe, B., Maugars, Y., Dubois, C., & Mathe, J. F. (2000). Supralesional and sublesional bone mineral density in spinal cord-injured patients. *Bone*, 27(2), 305–309. [http://doi.org/10.1016/S8756-3282\(00\)00326-4](http://doi.org/10.1016/S8756-3282(00)00326-4)

Dawson, A. B. (1925). The age order of epiphyseal union in the long bones of the albino rat. *The Anatomical Record*, 31(1), 1–17. <http://doi.org/10.1002/ar.1090310102>

Day, M. (2018). Distal Femur Fractures. Retrieved November 28, 2019, from <https://www.orthobullets.com/trauma/1041/distal-femur-fractures>

Depypere, M. (2013). *MicroCT imaging of bone architecture and vasculature*. Katholieke Universiteit Leuven.

Doube, M., Kłosowski, M. M., Arganda-Carreras, I., Cordelières, F. P., Dougherty, R. P., Jackson, J. S., ... Shefelbine, S. J. (2010). BoneJ: Free and extensible bone image analysis in ImageJ. *Bone*, 47(6), 1076–1079.

<http://doi.org/10.1016/j.bone.2010.08.023>

- Drake, M. T., Srinivasan, B., Mödder, U. I., Peterson, J. M., McCready, L. K., Riggs, B. L., ... Khosla, S. (2010). Effects of parathyroid hormone treatment on circulating sclerostin levels in postmenopausal women. *Journal of Clinical Endocrinology and Metabolism*, *95*(11), 5056–5062. <http://doi.org/10.1210/jc.2010-0720>
- Dudley-Javoroski, S., & Shields, R. K. (2012). Regional cortical and trabecular bone loss after spinal cord injury. *Journal of Rehabilitation Research and Development*, *49*(9), 1365–76. <http://doi.org/10.1682/JRRD.2011.12.0245>
- Duval-Beaupere, G., Lougovoy, J., Trocellier, L., & Lacert, P. (1983). Trunk and Leg Growth in Children with Paraplegia caused by Spinal Cord Injury. *Paraplegia*, *21*, 339–350. <http://doi.org/10.1038/sc.1983.58>
- Ekeland, A., Engesæter, L. B., & Langeland, N. (1981). Mechanical properties of fractured and intact rat femora evaluated by bending, torsional and tensile tests. *Acta Orthopaedica Scandinavica*, *52*(6), 605–613. <http://doi.org/10.3109/17453678108992155>
- Erben, R. G. (1996). Trabecular and endocortical bone surfaces in the rat: Modeling or remodeling? *The Anatomical Record*, *246*(1), 39–46. [http://doi.org/10.1002/\(SICI\)1097-0185\(199609\)246:1<39::AID-AR5>3.0.CO;2-A](http://doi.org/10.1002/(SICI)1097-0185(199609)246:1<39::AID-AR5>3.0.CO;2-A)
- Eser, P., Frotzler, A., Zehnder, Y., Wick, L., Knecht, H., Denoth, J., & Schiessl, H. (2004). Relationship between the duration of paralysis and bone structure: a pQCT study of spinal cord injured individuals. *Bone*, *34*(5), 869–80. <http://doi.org/10.1016/j.bone.2004.01.001>
- Feldkamp, L. A., Davis, L. C., & Kress, J. W. (1984). Practical cone-beam algorithm.

*Journal of the Optical Society of America A*, 1(6), 612–619.

<http://doi.org/10.1364/JOSAA.1.000612>

Feldkamp, L. A., Goldstein, S. A., Parfitt, A. M., Jesion, G., & Kleerekoper, M. (1989).

The direct examination of three-dimensional bone architecture in vitro by computed tomography. *Journal of Bone and Mineral Research*, 4(1), 3–11.

<http://doi.org/10.1002/jbmr.5650040103>

Finkelstein, J. S., Klibanski, A., & Neer, R. M. (1999). Comment on Normal

Volumetric Bone Mineral Density and Bone Turnover in Young Men with Histories of Constitutional Delay of Puberty. *The Journal of Clinical*

*Endocrinology & Metabolism*, 9(1), 3400–3406.

<http://doi.org/https://doi.org/10.1210/jcem.84.9.6011-2a>

Frey-Rindova, P., de Bruin, E. D., Stüssi, E., Dambacher, M. A., & Dietz, V. (2000).

Bone mineral density in upper and lower extremities during 12 months after spinal cord injury measured by peripheral quantitative computed tomography. *Spinal*

*Cord*, 38(1), 26–32. <http://doi.org/10.1038/sj.sc.3100905>

Frost, H. M. (1964). *The Laws of Bone Structure*. Springfield, Illinois.: C.C. Thomas.

Frost, H. M. (1987). The mechanostat: a proposed pathogenic mechanism of

osteoporoses and the bone mass effects of mechanical and nonmechanical agents.

*Bone and Mineral*, 2(2), 73–85.

Frost, H. M. (2000). The Utah paradigm of skeletal physiology: an overview of its

insights for bone, cartilage and collagenous tissue organs. *Journal of Bone and*

*Mineral Metabolism*, 18(6), 305–316. <http://doi.org/10.1007/s007740070001>

Frost, H. M. (2003). Bone's mechanostat: a 2003 update. *The Anatomical Record. Part*

A, *Discoveries in Molecular, Cellular, and Evolutionary Biology*, 275A(2), 1081–1101. <http://doi.org/10.1002/ar.a.10119>

Frost, H. M. (2004). *The Utah Paradigm of Skeletal Physiology: Volume 1 Bone and Bones and Associated Problems*. Greece: International Society of Musculoskeletal and Neuronal Interactions.

Frotzler, A., Berger, M., Knecht, H., & Eser, P. (2008). Bone steady-state is established at reduced bone strength after spinal cord injury: A longitudinal study using peripheral quantitative computed tomography (pQCT). *Bone*, 43(3), 549–555. <http://doi.org/10.1016/j.bone.2008.05.006>

Frotzler, A., Cheikh-Sarraf, B., Pourtehrani, M., Krebs, J., & Lippuner, K. (2015). Long-bone fractures in persons with spinal cord injury. *Spinal Cord*, 53(9), 1–4. <http://doi.org/10.1038/sc.2015.74>

Galea, G. L., Hannuna, S., Meakin, L. B., Delisser, P. J., Lanyon, L. E., & Price, J. S. (2015). Quantification of alterations in cortical bone geometry using site specificity software in mouse models of aging and the responses to ovariectomy and altered loading. *Frontiers in Endocrinology*, 6(52), 1–11. <http://doi.org/10.3389/fendo.2015.00052>

Garland, D. E., Adkins, R. H., Kushwaha, V., & Stewart, C. (2004). Risk factors for osteoporosis at the knee in the spinal cord injury population. *The Journal of Spinal Cord Medicine*, 27(3), 202–206. <http://doi.org/10.1080/10790268.2004.11753748>

Garland, D. E., Adkins, R. H., & Stewart, C. A. (2008). Five-year longitudinal bone evaluations in individuals with chronic complete spinal cord injury. *Journal of Spinal Cord Medicine*, 31(5), 543–550. <http://doi.org/10.1080/10790268.2008.11753650>

- Garland, D. E., Adkins, R. H., Stewart, C. A., Ashford, R., & Vigil, D. (2001). Regional osteoporosis in women who have a complete spinal cord injury. *The Journal of Bone and Joint Surgery*, 83(8), 1195–1200.
- Garland, D. E., Stewart, C. A., Adkins, R. H., Hu, S. S., Rosen, C., Liotta, F. J., & Weinstein, D. A. (1992). Osteoporosis after spinal cord injury. *Journal of Orthopaedic Research*, 10(3), 371–378. <http://doi.org/10.1002/jor.1100100309>
- Giangregorio, L., & McCartney, N. (2006). Bone Loss and Muscle Atrophy in Spinal Cord Injury: Epidemiology, Fracture Prediction, and Rehabilitation Strategies, 29(5), 489–500.
- Gibson, L. J. (1985). The mechanical behaviour of cancellous bone. *Journal of Biomechanics*, 18(5), 317–328. [http://doi.org/10.1016/0021-9290\(85\)90287-8](http://doi.org/10.1016/0021-9290(85)90287-8)
- Gong, J. K., Arnold, J. S., & Cohn, S. H. (1964). Composition of trabecular and cortical bone. *The Anatomical Record*, 149(3), 325–331. <http://doi.org/10.1002/ar.1091490303>
- Gupta, H. S., & Zioupos, P. (2008). Fracture of bone tissue: The “hows” and the “whys.” *Medical Engineering and Physics*, 30(10), 1209–1226. <http://doi.org/10.1016/j.medengphy.2008.09.007>
- Hadjidakis, D. J., & Androulakis, I. I. (2006). Bone remodeling. *Annals of the New York Academy of Sciences*, 1092(1), 385–396. <http://doi.org/10.1196/annals.1365.035>
- Hahn, M., Vogel, M., Pompesius-Kempa, M., & Delling, G. (1992). Trabecular bone pattern factor - A new parameter for simple quantification of bone microarchitecture. *Bone*, 13(4), 327–330. [http://doi.org/10.1016/8756-3282\(92\)90078-B](http://doi.org/10.1016/8756-3282(92)90078-B)

- Harrigan, T. P., Jasty, M., Mann, R. W., & Harris, W. H. (1988). Limitations of the continuum assumption in cancellous bone. *Journal of Biomechanics*, *21*(4), 269–275. [http://doi.org/10.1016/0021-9290\(88\)90257-6](http://doi.org/10.1016/0021-9290(88)90257-6)
- Harrigan, T. P., & Mann, R. W. (1984). Characterization of microstructural anisotropy in orthotropic materials using a second rank tensor. *Journal of Materials Science*, *19*(3), 761–767. <http://doi.org/10.1007/BF00540446>
- Herman, G. T. (1979). Correction for Beam Hardening in Computed-Tomography. *Physics in Medicine and Biology*, *24*(1), 81–106. <http://doi.org/10.1088/0031-9155/24/1/008>
- Hessle, L., Stordalen, G. A., Wenglén, C., Petzold, C., Tanner, E. K., Hessle, L., ... Wengle, C. (2013). The Skeletal Phenotype of Chondroadherin Deficient Mice. *PloS One*, *8*(6), 1–11. <http://doi.org/10.1371/journal.pone.0063080>
- Hildebrand, T., & Rüegsegger, P. (1997). A new method for the model-independent assessment of thickness in three-dimensional images. *Journal of Microscopy*, *185*(1), 67–75. <http://doi.org/10.1046/j.1365-2818.1997.1340694.x>
- Hildebrand, T., & Rüegsegger, P. (1997). Quantification of bone microarchitecture with the structure model index. *Computer Methods in Biomechanics and Biomedical Engineering*, *1*(1), 15–23. <http://doi.org/10.1080/01495739708936692>
- Hodgson, S. F., Clarke, B. L., Wermers, R., Hefferan, T., & Yaszemski, M. (2010). Bone Histology and Histopathology for Clinicians: A Primer. Mayo Foundation for Medical Education and Research and American Association of Clinical Endocrinologists.
- Hooshmand, M. J., Galvan, M. D., Partida, E., & Anderson, A. J. (2014).



- Characterization of recovery, repair, and inflammatory processes following contusion spinal cord injury in old female rats: is age a limitation? *Immunity & Ageing*, *11*(1), 1–13. <http://doi.org/10.1186/1742-4933-11-15>
- Hounsfield, G. N. (1973). Computerized transverse axial scanning (tomography): Part 1. Description of system. *The British Journal of Radiology*, *46*(552), 1016–1022. <http://doi.org/10.1259/0007-1285-46-552-1016>
- Hsieh, Y.-F., & Turner, C. H. (2001). Effects of loading frequency on mechanically induced bone formation. *Journal of Bone and Mineral Research*, *16*(5), 918–924. <http://doi.org/10.1359/jbmr.2001.16.5.918>
- Iwaniec, U. T., & Turner, R. T. (2013). Animal Models for Osteoporosis. In 4th (Ed.), *Osteoporosis* (4th ed., pp. 939–961). Academic Press. <http://doi.org/10.1016/B978-0-12-415853-5.00039-X>
- Järvinen, T. L. N., Kannus, P., & Sievänen, H. (2008). Bone quality: Emperor 's new clothes. *Journal of Musculoskeletal Neuronal Interactions*, *8*(1), 2–9.
- Jee, W. S. S. (2004). In Memoriam Tribute to Harold M. Frost M.D: 1921-2004. *Journal of Musculoskeletal & Neuronal Interactions*, *19*(12), 2091–2092. <http://doi.org/10.1359/jbmr.2004.19.12.2091>
- Jee, W. S. S., & Yao, W. (2001). Overview: animal models of osteopenia and osteoporosis. *Journal of Musculoskeletal & Neuronal Interactions*, *1*(3), 193–207.
- Jepsen, K. J., Silva, M. J., Vashishth, D., Guo, X. E., & van der Meulen, M. C. H. (2015). Establishing biomechanical mechanisms in mouse models: Practical guidelines for systematically evaluating phenotypic changes in the diaphyses of long bones. *Journal of Bone and Mineral Research*, *30*(6), 951–966.

<http://doi.org/10.1002/jbmr.2539>

- Jiang, S.-D., Dai, L.-Y., & Jiang, L.-S. (2006). Osteoporosis after spinal cord injury. *Osteoporosis International*, *17*(2), 180–192. <http://doi.org/10.1007/s00198-005-2028-8>
- Jiang, S.-D., Jiang, L.-S., & Dai, L.-Y. (2006). Spinal cord injury causes more damage to bone mass, bone structure, biomechanical properties and bone metabolism than sciatic neurectomy in young rats. *Osteoporosis International*, *17*(10), 1552–1561. <http://doi.org/10.1007/s00198-006-0165-3>
- Jiang, S.-D., Jiang, L.-S., & Dai, L.-Y. (2007a). Changes in bone mass, bone structure, bone biomechanical properties, and bone metabolism after spinal cord injury: a 6-month longitudinal study in growing rats. *Calcified Tissue International*, *80*(3), 167–75. <http://doi.org/10.1007/s00223-006-0085-4>
- Jiang, S.-D., Jiang, L.-S., & Dai, L.-Y. (2007b). Effects of spinal cord injury on osteoblastogenesis, osteoclastogenesis and gene expression profiling in osteoblasts in young rats. *Osteoporosis International*, *18*(3), 339–349. <http://doi.org/10.1007/s00198-006-0229-4>
- Jiang, S.-D., Shen, C., Jiang, L.-S., & Dai, L.-Y. (2007). Differences of bone mass and bone structure in osteopenic rat models caused by spinal cord injury and ovariectomy. *Osteoporosis International*, *18*(6), 743–750. <http://doi.org/10.1007/s00198-006-0299-3>
- Kalu, D., Liu, C., Hardin, R., & Hollis, B. (1989). The aged rat model of ovarian hormone deficiency bone loss. *Endocrinology*, *124*(1), 7–16. <http://doi.org/10.1210/endo-124-1-7>

- Kanis, J. A., Borgstrom, F., De Laet, C., Johansson, H., Johnell, O., Jonsson, B., ...  
Khaltaev, N. (2005). Assessment of fracture risk. *Osteoporosis International*,  
16(6), 581–589. <http://doi.org/10.1007/s00198-004-1780-5>
- Karsenty, G., & Wagner, E. F. (2002). Reaching a genetic and molecular understanding  
of skeletal development. *Developmental Cell*, 2(4), 389–406.  
[http://doi.org/10.1016/S1534-5807\(02\)00157-0](http://doi.org/10.1016/S1534-5807(02)00157-0)
- Katz, J. L. (1971). Hard tissue as a composite material-I. Bounds on the elastic  
behavior. *Journal of Biomechanics*, 4(5), 455–473. [http://doi.org/10.1016/0021-9290\(71\)90064-9](http://doi.org/10.1016/0021-9290(71)90064-9)
- Kiratli, B. J., Smith, A. E., Nauenberg, T., Kallfelz, C. F., & Perkas, I. (2000). Bone  
mineral and geometric changes through the femur with immobilization due to  
spinal cord injury. *Journal of Rehabilitation Research and Development*, 37(2),  
225–233.
- Kuhn, J. L., Goldstein, S. A., Feldkamp, L. A., Goulet, R. W., & Jasion, G. (1990).  
Evaluation of a microcomputed tomography system to study trabecular bone  
structure. *Journal of Orthopaedic Research*, 8(6), 833–42.  
<http://doi.org/10.1002/jor.1100080608>
- Laib, A., Häuselmann, H. J., & Rüdiger, P. (1998). In vivo high resolution 3D-QCT  
of the human forearm. *Technology and Health Care*, 6.5(6), 329–337.
- Lanyon, L. E., & Rubin, C. T. (1984). Static vs dynamic loads as an influence on bone  
remodeling. *Journal of Biomechanics*, 17(12), 897–905.  
[http://doi.org/10.1016/0021-9290\(84\)90003-4](http://doi.org/10.1016/0021-9290(84)90003-4)
- Lee, B. B., Cripps, R. A., Fitzharris, M., & Wing, P. C. (2013). The global map for

traumatic spinal cord injury epidemiology: update 2011, global incidence rate.

*Spinal Cord*, 52(2), 110–116. <http://doi.org/10.1038/sc.2012.158>

Lelovas, P. P., Xanthos, T. T., Thoma, S. E., Lyritis, G. P., & Dontas, I. A. (2008). The laboratory rat as an animal model for osteoporosis research. *Comparative Medicine*, 58(5), 424–30.

Levenston, M. E., Beaupre, G. S., & van der Meulen, M. C. H. (1994). Improved method for analysis of whole bone torsion tests. *Journal of Bone and Mineral Research*, 9, 1459–1465. <http://doi.org/10.1002/jbmr.5650090919>

Lin, T., Tong, W., Chandra, A., Hsu, S.-Y., Jia, H., Zhu, J., ... Qin, L. (2015). A comprehensive study of long-term skeletal changes after spinal cord injury in adult rats. *Bone Research*, 3, 1–9. <http://doi.org/10.1038/boneres.2015.28>

Liskova, M., & Hert, J. (1971). Reaction of bone to mechanical stimuli. 2. Periosteal and endosteal reaction of tibial diaphysis in rabbit to intermittent loading. *Folia Morphologica*, 19(3), 301–317.

Liu, D., Zhao, C.-Q., Li, H., Jiang, S.-D., Jiang, L.-S., & Dai, L.-Y. (2008). Effects of spinal cord injury and hindlimb immobilization on sublesional and supralesional bones in young growing rats, 43(1), 119–125.  
<http://doi.org/10.1016/j.bone.2008.03.015>

Lorensen, W. E., & Cline, H. E. (1987). Marching cubes: A high resolution 3D surface construction algorithm. *ACM Siggraph Computer Graphics*, 21(4), 163–169.  
<http://doi.org/10.1145/37401.37422>

Lu, P., Graham, L., Wang, Y., Wu, D., & Tuszynski, M. (2014). Promotion of survival and differentiation of neural stem cells with fibrin and growth factor cocktails after

severe spinal cord injury. *Journal of Visualized Experiments*, 89, 1–9.

<http://doi.org/10.3791/50641>

Lucas, P. (1987). Reversible Reduction in Bone Blood Flow in Streptozotocin-Diabetic

Rats. *Experientia*, 43, 894–895. <http://doi.org/10.1007/BF01951655>

Mandelbrot, B. (1982). *The Fractal Geometry of Nature*. New York: WH Freeman.

Martin, R. B. (2000). Toward a unifying theory of bone remodeling. *Bone*, 26(1), 1–6.

[http://doi.org/10.1016/S8756-3282\(99\)00241-0](http://doi.org/10.1016/S8756-3282(99)00241-0)

McCarthy, I. D., Bloomer, Z., Gall, A., Keen, R., & Ferguson-Pell, M. (2012). Changes

in the structural and material properties of the tibia in patients with spinal cord

injury. *Spinal Cord*, 50(4), 333–337. <http://doi.org/10.1038/sc.2011.143>

McCaughey, E. J., Purcell, M., Mclean, A. N., Fraser, M. H., Bewick, A., Borotkanics,

R. J., & Allan, D. B. (2016). Changing demographics of spinal cord injury over a

20-year period: a longitudinal population-based study in Scotland. *Spinal Cord*,

54(4), 270–276. <http://doi.org/10.1038/sc.2015.167>

McManus, M. M., & Grill, R. J. (2011). Longitudinal evaluation of mouse hind limb

bone loss after spinal cord injury using novel, in vivo, methodology. *Journal of*

*Visualized Experiments*, (58), 1–8. <http://doi.org/10.3791/3246>

Mellon, S. J., & Tanner, K. E. (2012). Bone and its adaptation to mechanical loading: a

review. *International Materials Reviews*, 57(5), 235–255.

<http://doi.org/10.1179/1743280412Y.0000000008>

Melton, L. J., Chrischilles, E. A., Cooper, C., Lane, A. W., & Riggs, B. L. (1992).

Perspective how many women have osteoporosis? *Journal of Bone and Mineral*

*Research*, 7(9), 1005–1010. <http://doi.org/10.1002/jbmr.5650070902>

- Minaire, P., Meunier, P., Edouard, C., Bernard, J., Courpron, P., & Bourret, J. (1974). Quantitative histological data on disuse osteoporosis - Comparison with biological data. *Calcified Tissue Research*, 17(1), 57–73. <http://doi.org/10.1007/BF02547214>
- Minematsu, A., Nishii, Y., Imagita, H., & Sakata, S. (2014). Time Course of Changes in Trabecular Bone Microstructure in Rats with Spinal Cord Injury. *Journal of Life Sciences*, 8(6), 522–528.
- Minematsu, A., Nishii, Y., Imagita, H., Takeshita, D., & Sakata, S. (2016). Whole-body vibration can attenuate the deterioration of bone mass and trabecular bone microstructure in rats with spinal cord injury. *Spinal Cord*, 54(8), 597–603. <http://doi.org/10.1038/sc.2015.220>
- Morse, L. R., Sudhakar, S., Danilack, V., Tun, C., Lazzari, A., Gagnon, D. R., ... Battaglino, R. A. (2012). Association between sclerostin and bone density in chronic spinal cord injury. *Journal of Bone and Mineral Research*, 27(2), 352–359. <http://doi.org/10.1002/jbmr.546>
- Morse, L., Teng, Y. D., Pham, L., Newton, K., Yu, D., Liao, W.-L., ... Battaglino, R. (2008). Spinal cord injury causes rapid osteoclastic resorption and growth plate abnormalities in growing rats (SCI-induced bone loss in growing rats). *Osteoporosis International*, 19(5), 645–52. <http://doi.org/10.1007/s00198-007-0494-x>
- Mosley, J. R., & Lanyon, L. E. (1998). Strain rate as a controlling influence on adaptive modeling in response to dynamic loading of the ulna in growing male rats. *Bone*, 23(4), 313–318. [http://doi.org/10.1016/S8756-3282\(98\)00113-6](http://doi.org/10.1016/S8756-3282(98)00113-6)
- Müller, R., Hildebrand, T., & Rüegsegger, P. (1994). Non-invasive bone biopsy: A new method to analyse and display the three-dimensional structure of trabecular bone.

*Physics in Medicine and Biology*, 39(1), 145–164. <http://doi.org/10.1088/0031-9155/39/1/009>

Müller, R., & Rüeegsegger, P. (1995). Three-dimensional finite element modelling of non-invasively assessed trabecular bone structures. *Medical Engineering and Physics*, 17(2), 126–133. [http://doi.org/10.1016/1350-4533\(95\)91884-J](http://doi.org/10.1016/1350-4533(95)91884-J)

Müller, R., van Campenhout, H., van Damme, B., van der Perre, G., Dequeker, J., Hildebrand, T., & Rüeegsegger, P. (1998). Morphometric analysis of human bone biopsies: A quantitative structural comparison of histological sections and micro-computed tomography. *Bone*, 23(1), 59–66. [http://doi.org/10.1016/S8756-3282\(98\)00068-4](http://doi.org/10.1016/S8756-3282(98)00068-4)

Mustafy, T., Londono, I., & Villemure, I. (2018). Can the contralateral limb be used as a control during the growing period in a rodent model? *Medical Engineering and Physics*, 58, 31–40. <http://doi.org/10.1016/j.medengphy.2018.04.013>

O'Connor, J. A., Lanyon, L. E., & MacFie, H. (1982). The influence of strain rate on adaptive bone remodelling. *Journal of Biomechanics*, 15(10), 767–781. [http://doi.org/10.1016/0021-9290\(82\)90092-6](http://doi.org/10.1016/0021-9290(82)90092-6)

Odgaard, A., & Gundersen, H. J. G. (1993). Quantification of connectivity in cancellous bone, with special emphasis on 3D reconstructions. *Bone*, 14(2), 173–182. [http://doi.org/10.1016/8756-3282\(93\)90245-6](http://doi.org/10.1016/8756-3282(93)90245-6)

Ogden, J. A. (1984). The uniqueness of growing bones. In C. . J. Rockwood, K. E. Wilkins, & R. E. King (Eds.), *Fractures in Children* (Vol 3, pp. 1–86). Philadelphia: J.B. Lippincott.

Parent, S., Mac-Thiong, J.-M., Roy-Beaudry, M., Sosa, J. F., & Labelle, H. (2011).

Spinal Cord Injury in the Pediatric Population: A Systematic Review of the Literature. *Journal of Neurotrauma*, 28(8), 1515–1524.

<http://doi.org/10.1089/neu.2009.1153>

Parfitt, A. M. (2002). Targeted and nontargeted bone remodeling: Relationship to basic multicellular unit origination and progression. *Bone*, 30(1), 5–7.

[http://doi.org/10.1016/S8756-3282\(01\)00642-1](http://doi.org/10.1016/S8756-3282(01)00642-1)

Parfitt, A. M., Drezner, M. K., Glorieux, F. H., Kanis, J. A., Malluche, H., Meunier, P.

J., ... Recker, R. R. (1987). Bone histomorphometry: Standardization of nomenclature, symbols, and units. Report of the ASBMR histomorphometry

nomenclature committee. *Journal of Bone and Mineral Research*, 2(6), 595–610.

<http://doi.org/10.1002/jbmr.5650020617>

Parfitt, A. M., Mathews, C. H. E., Villanueva, A. R., Kleerekoper, M., Frame, B., &

Rao, D. S. (1983). Relationships between surface, volume, and thickness of iliac trabecular bone in aging and in osteoporosis. Implications for the microanatomic

and cellular mechanisms of bone loss. *The Journal of Clinical Investigation*, 72(4),

1396–1409. <http://doi.org/10.1172/JCI111096>

Pelker, R. R., Friedlaender, G. E., Markham, T. C., Panjabi, M. M., & Moen, C. J.

(1984). Effects of freezing and freeze-drying on the biomechanical properties of rat bone. *Journal of Orthopaedic Research*, 1(4), 405–11.

<http://doi.org/10.1002/jor.1100010409>

Pemberton, G. D., Childs, P., Reid, S., Nikukar, H., Tsimbouri, P. M., Gadegaard, N.,

... Dalby, M. J. (2015). Nanoscale stimulation of osteoblastogenesis from mesenchymal stem cells: nanotopography and nanokicking. *Nanomedicine*

(London, England), 10(4), 547–60. <http://doi.org/10.2217/nnm.14.134>



- Picard, S., Lapointe, N. P., Brown, J. P., & Guertin, P. A. (2008). Histomorphometric and densitometric changes in the femora of spinal cord transected mice. *The Anatomical Record*, 291(3), 303–307. <http://doi.org/10.1002/ar.20645>
- Proffitt, D., & Rosen, D. (1979). Metrication errors and coding efficiency of chain-encoding schemes for the representation of lines and edges. *Computer Graphics and Image Processing*, 10(4), 318–332. [http://doi.org/10.1016/S0146-664X\(79\)80041-6](http://doi.org/10.1016/S0146-664X(79)80041-6)
- Qin, W., Bauman, W. A., & Cardozo, C. (2010). Bone and muscle loss after spinal cord injury: Organ interactions. *Annals of the New York Academy of Sciences*, 1211(1), 66–84. <http://doi.org/10.1111/j.1749-6632.2010.05806.x>
- Qingde Li, & Griffiths, J. G. (2004). Least squares ellipsoid specific fitting. *Geometric Modeling and Processing*, 335–340. <http://doi.org/10.1109/GMAP.2004.1290055>
- Radon, J. (1986). On the determination of functions from their integral values along certain manifolds. *IEEE Transactions on Medical Imaging*, 5(4), 170–176. <http://doi.org/10.1109/TMI.1986.4307775>
- Rauch, F. (2005). Bone Growth in Length and Width: The Yin and Yang of Bone Stability. *Journal of Musculoskeletal & Neuronal Interactions*, 5(3), 194–201.
- Rauch, F., & Schönau, E. (2005). Peripheral quantitative computed tomography of the distal radius in young subjects – new reference data and interpretation of results. *Journal of Musculoskeletal & Neuronal Interactions*, 5(2), 119–126. <http://doi.org/10.1007/PL00005830>
- Reiter, A. L., Volk, A., Vollmar, J., Fromm, B., & Gerner, H. J. (2007). Changes of basic bone turnover parameters in short-term and long-term patients with spinal

cord injury. *European Spine Journal*, 16, 771–776. <http://doi.org/10.1007/s00586-006-0163-3>

Remy, E., & Thiel, E. (2002). Medial axis for chamfer distances: computing look-up tables and neighbourhoods in 2D or 3D. *Pattern Recognition Letters*, 23(6), 649–661. [http://doi.org/10.1016/S0167-8655\(01\)00141-6](http://doi.org/10.1016/S0167-8655(01)00141-6)

Rho, J. Y., Kuhn-Spearing, L., & Zioupos, P. (1998). Mechanical properties and the hierarchical structure of bone. *Medical Engineering and Physics*, 20(2), 92–102. [http://doi.org/10.1016/S1350-4533\(98\)00007-1](http://doi.org/10.1016/S1350-4533(98)00007-1)

Rittweger, J., Goosey-Tolfrey, V. L., Cointy, G., & Ferretti, J. L. (2010). Structural analysis of the human tibia in men with spinal cord injury by tomographic (pQCT) serial scans. *Bone*, 47(3), 511–518. <http://doi.org/10.1016/j.bone.2010.05.025>

Roberts, D., Lee, W., Cuneo, R. C., Wittmann, J., Ward, G., Flatman, R., ... Hickman, P. E. (1998). Longitudinal Study of Bone Turnover after Acute Spinal Cord Injury. *The Journal of Clinical Endocrinology & Metabolism*, 83(2), 415–422. <http://doi.org/10.1210/jcem.83.2.4581>

Robling, A. G., Duijvelaar, K. M., Geevers, J. V., Ohashi, N., & Turner, C. H. (2001). Modulation of appositional and longitudinal bone growth in the rat ulna by applied static and dynamic force. *Bone*, 29(2), 105–113. [http://doi.org/10.1016/S8756-3282\(01\)00488-4](http://doi.org/10.1016/S8756-3282(01)00488-4)

Rosen, H., Moses, A., Gatter, J., Iloputaife, I., Ross, D., SL, L., & Greenspan, S. (2000). Serum CTX: a new marker of bone resorption that shows treatment effect more often than other markers because of low coefficient of variability and large changes with bisphosphonate therapy. *Calcified Tissue International*, 66(2), 100–103.

- Rowland, J. W., Hawryluk, G. W. J., Kwon, B., & Fehlings, M. G. (2008). Current status of acute spinal cord injury pathophysiology and emerging therapies: promise on the horizon. *Neurosurgical Focus*, *25*(5:E2), 1–17.  
<http://doi.org/10.3171/FOC.2008.25.11.E2>
- Rubin, C. T., & Lanyon, L. E. (1984). Regulation of bone formation by applied dynamic loads. *Journal of Bone and Joint Surgery*, *66*(3), 397–402.  
[http://doi.org/10.1007/978-1-4471-5451-8\\_134](http://doi.org/10.1007/978-1-4471-5451-8_134)
- Rubin, C. T., & Lanyon, L. E. (1985). Regulation of bone mass by mechanical strain magnitude. *Calcified Tissue International*, *37*(4), 411–417.  
<http://doi.org/10.1007/BF02553711>
- Rubin, C. T., & Mcleod, K. J. (1994). Promotion of bony ingrowth by frequency-specific, low-amplitude mechanical strain. *Clinical Orthopaedics and Related Research*, *298*, 165–174. <http://doi.org/10.1097/00003086-199401000-00022>
- Ryan, T. M., Raichlen, D. A., & Gosman, J. H. (2017). Structural and Mechanical Changes in Trabecular Bone during Early Development in the Human Femur and Humerus. In C. J. Percival & J. T. Richtsmeier (Eds.), *Building Bones: Bone Formation and Development in Anthropology* (1st ed., pp. 281–303). Cambridge: Cambridge University Press.
- Sabo, D., Blaich, S., Wenz, W., Hohmann, M., Loew, M., & Gerner, H. J. (2001). Osteoporosis in patients with paralysis after spinal cord injury. *Archives of Orthopaedic and Trauma Surgery*, *121*(2001), 75–78.  
<http://doi.org/10.1007/s004020000162>
- Sabour, H., Javidan, A. N., Latifi, S., Larijani, B., Shidfar, F., Vafa, M. R., ... Razavi, E. (2014). Bone biomarkers in patients with chronic traumatic spinal cord injury.

- The Spine Journal*, 14(7), 1132–1138. <http://doi.org/10.1016/j.spinee.2013.07.475>
- Salmon, P. L., & Liu, X. (2014). MicroCT bone densitometry: Context sensitivity, beam hardening correction and the effect of surrounding media. *The Open Access Journal of Science and Technology*, 2, 1–25. <http://doi.org/10.11131/2014/101142>
- Schoenau, E., & Frost, H. M. (2002). The “Muscle-Bone Unit” in Children and Adolescents. *Calcified Tissue International*, 70(5), 405–407. <http://doi.org/10.1007/s00223-001-0048-8>
- Schoutens, A., Verhas, M., L’Hermite-Baleriaux, M., L’Hermite, M., Verschaeren, A., Dourov, N., ... Tricot, A. (1984). Growth and Bone Haemodynamic Response to Castration in Male rats. Reversibility by Testosterone. *Acta Endocrinologica*, 107(3), 428–432.
- Seeman, E. (2003). Invited review: Pathogenesis of osteoporosis. *Journal of Applied Physiology*, 95(5), 2142–2151. <http://doi.org/10.1152/jappphysiol.00288.2003>
- Sengupta, P. (2011). A scientific review of age determination for a laboratory rat: How old is it in comparison with human age? *Biomedicine International*, 2(2), 81–89.
- Sezer, N. (2015). Chronic complications of spinal cord injury. *World Journal of Orthopedics*, 6(1), 24–33. <http://doi.org/10.5312/wjo.v6.i1.24>
- Shields, R. K., Schlechte, J., Dudley-Javoroski, S., Zwart, B. D., Clark, S. D., Grant, S. A., & Mattiace, V. M. (2005). Bone mineral density after spinal cord injury: A reliable method for knee measurement. *Archives of Physical Medicine and Rehabilitation*, 86(10), 1969–1973. <http://doi.org/10.1016/j.apmr.2005.06.001>
- Silva, M. J., Brodt, M. D., Wopenka, B., Thomopoulos, S., Williams, D., Wassen, M. H., ... Bank, R. A. (2006). Decreased Collagen Organization and Content Are

Associated With Reduced Strength of Demineralized and Intact Bone in the SAMP6 Mouse. *Journal of Bone and Mineral Research*, 21(1), 78–88.  
<http://doi.org/10.1359/jbmr.050909>

Siris, E. S., Chen, Y.-T., Abbott, T. A., Barrett-Connor, E., Miller, P. D., Wehren, L. E., & Berger, M. L. (2004). Bone Mineral Density Thresholds for Pharmacological Intervention to Prevent Fractures. *Archives of Internal Medicine*, 164(10), 1108–1112. <http://doi.org/10.1001/archinte.164.10.1108>

Sugawara, H., Linsenmeyer, T. A., Beam, H., & Parsons, J. R. (1998). Mechanical properties of bone in a paraplegic rat model. *Journal of Spinal Cord Medicine*, 21(4), 302–308. <http://doi.org/10.1080/10790268.1998.11719539>

Tan, C. O., Battaglino, R. a, & Morse, L. R. (2013). Spinal Cord Injury and Osteoporosis: Causes, Mechanisms, and Rehabilitation Strategies. *International Journal of Physical Medicine & Rehabilitation*, 1, 1–10.  
<http://doi.org/10.4172/2329-9096.1000127>

Tanck, E., Homminga, J., van Lenthe, G. H., & Huiskes, R. (2001). Increase in bone volume fraction precedes architectural adaptation in growing bone. *Bone*, 28(6), 650–654. [http://doi.org/10.1016/S8756-3282\(01\)00464-1](http://doi.org/10.1016/S8756-3282(01)00464-1)

Thompson, D. (1942). *On growth and form*. New York: Cambridge University Press.

Toriwaki, J., & Yonekura, T. (2002). Euler Number and Connectivity Indexes of a Three Dimensional Digital Picture. *Forma*, 17, 183–209.

Turner, C. H. (1998). Three Rules for Bone Adaptation to Mechanical Stimuli. *Bone*, 23(5), 399–407. [http://doi.org/10.1016/S8756-3282\(98\)00118-5](http://doi.org/10.1016/S8756-3282(98)00118-5)

Turner, C. H., Forwood, M. R., & Otter, M. W. (1994). Mechanotransduction in bone:

do bone cells act as sensors of fluid flow? *The FASEB Journal*, 8(11), 875–878.

<http://doi.org/10.1096/fasebj.8.11.8070637>

Turner, C. H., Owan, I., & Takano, Y. (1995). Mechanotransduction in bone: role of strain rate. *American Journal of Physiology*, 269(3), E438–E442.

<http://doi.org/10.1152/ajpendo.1995.269.3.E438>

Turner, S. (2001). Animal models of osteoporosis - Necessity and Limitations.

*European Cells and Materials*, 1, 66–81. <http://doi.org/10.22203/eCM.v001a08>

Umemura, Y., Ishiko, T., Yamauchi, T., Kurono, M., & Mashiko, S. (1997). Five jumps per day increase bone mass and breaking force in rats. *Journal of Bone and*

*Mineral Research*, 12(9), 1480–1485. <http://doi.org/10.1359/jbmr.1997.12.9.1480>

*US Department of Health and Human Services Bone health and osteoporosis: A report of the Surgeon General*. (2004).

Väänänen, H. K., Liu, Y., Lehenkari, P., & Uemara, T. (1998). How do osteoclasts resorb bone? *Materials Science and Engineering: C*, 6(4), 205–209.

[http://doi.org/10.1016/S0928-4931\(98\)00052-6](http://doi.org/10.1016/S0928-4931(98)00052-6)

Varzi, D., Coupaud, S. a. F., Purcell, M., Allan, D. B., Gregory, J. S., & Barr, R. J.

(2015). Bone morphology of the femur and tibia captured by statistical shape modelling predicts rapid bone loss in acute spinal cord injury patients. *Bone*, 81,

495–501. <http://doi.org/10.1016/j.bone.2015.08.026>

Vashishth, D., Tanner, K. E., & Bonfield, W. (2001). Fatigue of cortical bone under combined axial-torsional loading. *Journal of Orthopaedic Research*, 19(3), 414–

420. [http://doi.org/10.1016/S0736-0266\(00\)00036-X](http://doi.org/10.1016/S0736-0266(00)00036-X)

Verhas, M., Martinello, Y., Mone, M., Heilporn, A., Bergmann, P., Tricot, A., &

- Schoutens, A. (1980). Demineralization and Pathological Physiology of the Skeleton in Paraplegic Rats. *Calcified Tissue International*, 30(1), 83–90.  
<http://doi.org/10.1007/bf02408611>
- Vestergaard, P., Krogh, K., Rejnmark, L., & Mosekilde, L. (1998). Fracture rates and risk factors for fractures in patients with spinal cord injury. *Spinal Cord*, 36(11), 790–796. <http://doi.org/10.1038/sj.sc.3100648>
- Villa-Camacho, J. C., Iyoha-Bello, O., Behrouzi, S., Snyder, B. D., & Nazarian, A. (2014). Computed tomography-based rigidity analysis: a review of the approach in preclinical and clinical studies. *Bonekey Rep*, 3, 587.  
<http://doi.org/10.1038/bonekey.2014.82>
- Vossepoel, A. M., & Smeulders, A. W. M. (1982). Vector code probability and metrication error in the representation of straight lines of finite length. *Computer Graphics and Image Processing*, 20(4), 347–364. [http://doi.org/10.1016/0146-664X\(82\)90057-0](http://doi.org/10.1016/0146-664X(82)90057-0)
- Wang, X., Shen, X., Li, X., & Mauli Agrawal, C. (2002). Age-related changes in the collagen network and toughness of bone. *Bone*, 31(1), 1–7.  
[http://doi.org/10.1016/S8756-3282\(01\)00697-4](http://doi.org/10.1016/S8756-3282(01)00697-4)
- Warden, S. J., Bennell, K. L., Matthews, B., Brown, D. J., McMeeken, J. M., & Wark, J. D. (2002). Quantitative ultrasound assessment of acute bone loss following spinal cord injury: A longitudinal pilot study. *Osteoporosis International*, 13(7), 586–92. <http://doi.org/10.1007/s001980200077>
- Warden, S. J., & Turner, C. H. (2004). Mechanotransduction in the cortical bone is most efficient at loading frequencies of 5-10 Hz. *Bone*, 34(2), 261–270.  
<http://doi.org/10.1016/j.bone.2003.11.011>

- Whitehouse, W. J. (1974). The quantitative morphology of anisotropic trabecular bone. *Journal of Microscopy*, 101(2), 153–168. <http://doi.org/10.1111/j.1365-2818.1974.tb03878.x>
- WHO. (1994). Assessment of fracture risk and its application to screening for postmenopausal osteoporosis: report of a WHO study group. *World Health Organization Technical Report Series*, 843, 1–129.
- Willinghamm, M. D., Brodt, M. D., Lee, K. L., Stephens, A. L., Ye, J., & Silva, M. J. (2010). Age-related changes in bone structure and strength in female and male BALB/c Mice. *Calcified Tissue International*, 86(6), 470–483. <http://doi.org/10.1007/s00223-010-9359-y>
- Wilmet, E., Ismail, A., Heilporn, A., Welraeds, D., & Bergmann, P. (1995). Longitudinal study of the bone mineral content and of soft tissue composition after spinal cord section. *Paraplegia*, 33, 674–677. <http://doi.org/10.1038/sc.1995.141>
- Wolff, J. (1891). *Das Gesetz der Transformation der Knochen*. Berlin, Germany: Springer-Verlag.
- Wolff, J. (1986). *The Law of Bone Remodelling*. Berlin: Springer-Verlag.
- Wolkowski, B., Snead, E., Wesolowski, M., Singh, J., Pettitt, M., Chibbar, R., & Montgomery, J. (2015). Assessment of freeware programs for the reconstruction of tomography datasets obtained with a monochromatic synchrotron-based X-ray source. *Journal of Synchrotron Radiation*, 22(4), 1130–1138. <http://doi.org/10.1107/S1600577515008437>
- Wong, F. S. L., Elliott, J. C., Anderson, P., & Davis, G. R. (1995). Mineral Concentration Gradients in Rat Femoral Diaphyses Measured by X-Ray



Microtomography. *Calcified Tissue International*, 56, 62–70.

<http://doi.org/10.1007/BF00298746>

Wu, Y., Adeeb, S., & Doschak, M. R. (2015). Using Micro-CT Derived Bone Microarchitecture to Analyze Bone Stiffness – A Case Study on Osteoporosis Rat Bone. *Frontiers in Endocrinology*, 6, 1–7.

<http://doi.org/10.3389/fendo.2015.00080>

Yarrow, J. F., Ye, F., Balaez, A., Mantione, J. M., Otzel, D. M., Chen, C., ...

Vandenborne, K. (2014). Bone loss in a new rodent model combining spinal cord injury and cast immobilization. *Journal of Musculoskeletal & Neuronal Interactions*, 14(3), 255–266.

Zehnder, Y., Lüthi, M., Dieter, M., Knecht, H., Perrelet, R., Neto, I., ... Lippuner, K.

(2004). Long-term changes in bone metabolism, bone mineral density, quantitative ultrasound parameters, and fracture incidence after spinal cord injury: a cross-sectional observational study in 100 paraplegic men. *Osteoporosis International*, 15(3), 180–189. <http://doi.org/10.1007/s00198-003-1529-6>

Zhang, Z., Zhang, Y. P., Shields, L. B. E., & Shields, C. B. (2014). Technical comments on rodent spinal cord injuries models. *Neural Regeneration Research*, 9(5), 453–455. <http://doi.org/10.4103/1673-5374.130052>